



A National Center of Excellence in Advanced Technology Applications

ISSN 1520-295X

Methodologies for Post-Earthquake Building Damage Detection Using SAR and Optical Remote Sensing: Application to the August 17, 1999 Marmara, Turkey Earthquake

by

Charles K. Huyck, Beverley J. Adams, Sungbin Cho,
Ronald T. Eguchi, Babak Mansouri and Bijan Houshmand

ImageCat, Inc.

Union Bank of California Building
400 Oceangate, Suite 1050
Long Beach, California 90802

Technical Report MCEER-04-0004

June 15, 2004

This research was conducted at ImageCat, Inc. and was supported primarily by the Earthquake Engineering Research Centers Program of the National Science Foundation under award number EEC-9701471.

NOTICE

This report was prepared by ImageCat, Inc. as a result of research sponsored by the Multidisciplinary Center for Earthquake Engineering Research (MCEER) through a grant from the Earthquake Engineering Research Centers Program of the National Science Foundation under NSF award number EEC-9701471 and other sponsors. Neither MCEER, associates of MCEER, its sponsors, ImageCat, Inc., nor any person acting on their behalf:

- a. makes any warranty, express or implied, with respect to the use of any information, apparatus, method, or process disclosed in this report or that such use may not infringe upon privately owned rights; or
- b. assumes any liabilities of whatsoever kind with respect to the use of, or the damage resulting from the use of, any information, apparatus, method, or process disclosed in this report.

Any opinions, findings, and conclusions or recommendations expressed in this publication are those of the author(s) and do not necessarily reflect the views of MCEER, the National Science Foundation, or other sponsors.

**Methodologies for Post-Earthquake
Building Damage Detection Using SAR and
Optical Remote Sensing**

**Application to the August 17, 1999 Marmara,
Turkey Earthquake**

by

Charles K. Huyck,¹ Beverley J. Adams,² Sungbin Cho,³
Ronald T. Eguchi,⁴ Babak Mansouri⁵ and Bijan Houshmand⁶

Publication Date: June 15, 2004

Submittal Date: February 13, 2004

Technical Report MCEER-04-0004

NSF Master Contract Number EEC 9701471

- 1 Senior Vice President, ImageCat, Inc., Long Beach, California
- 2 Project Scientist, ImageCat, Inc., Long Beach, California
- 3 Senior Project Scientist, ImageCat, Inc., Long Beach, California
- 4 President/CEO, ImageCat, Inc., Long Beach, California
- 5 Ph.D. Student, Department of Civil Engineering, University of Southern California, Los Angeles
- 6 MCEER Consultant, Santa Monica, California

MULTIDISCIPLINARY CENTER FOR EARTHQUAKE ENGINEERING RESEARCH
University at Buffalo, State University of New York
Red Jacket Quadrangle, Buffalo, NY 14261

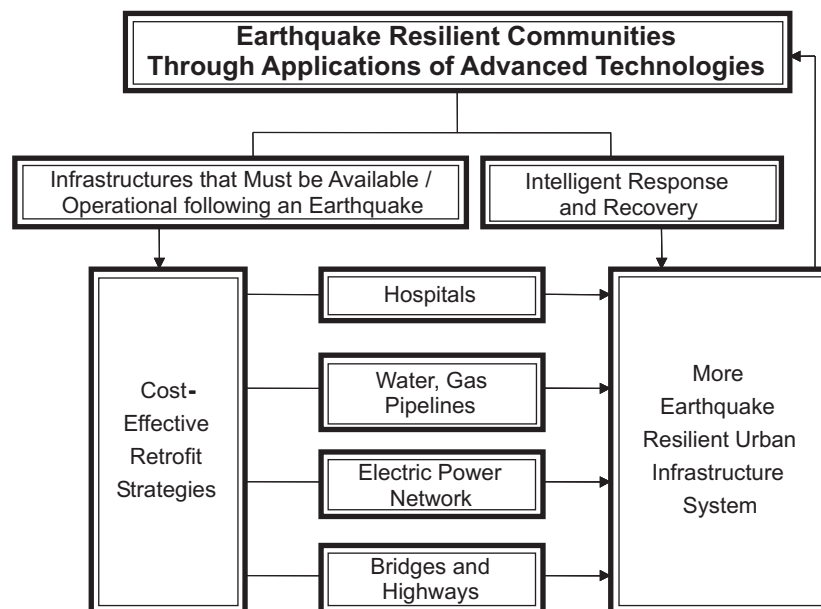
Preface

The Multidisciplinary Center for Earthquake Engineering Research (MCEER) is a national center of excellence in advanced technology applications that is dedicated to the reduction of earthquake losses nationwide. Headquartered at the University at Buffalo, State University of New York, the Center was originally established by the National Science Foundation in 1986, as the National Center for Earthquake Engineering Research (NCEER).

Comprising a consortium of researchers from numerous disciplines and institutions throughout the United States, the Center's mission is to reduce earthquake losses through research and the application of advanced technologies that improve engineering, pre-earthquake planning and post-earthquake recovery strategies. Toward this end, the Center coordinates a nationwide program of multidisciplinary team research, education and outreach activities.

MCEER's research is conducted under the sponsorship of two major federal agencies: the National Science Foundation (NSF) and the Federal Highway Administration (FHWA), and the State of New York. Significant support is derived from the Federal Emergency Management Agency (FEMA), other state governments, academic institutions, foreign governments and private industry.

MCEER's NSF-sponsored research objectives are twofold: to increase resilience by developing seismic evaluation and rehabilitation strategies for the post-disaster facilities and systems (hospitals, electrical and water lifelines, and bridges and highways) that society expects to be operational following an earthquake; and to further enhance resilience by developing improved emergency management capabilities to ensure an effective response and recovery following the earthquake (see the figure below).



A cross-program activity focuses on the establishment of an effective experimental and analytical network to facilitate the exchange of information between researchers located in various institutions across the country. These are complemented by, and integrated with, other MCEER activities in education, outreach, technology transfer, and industry partnerships.

The study described in this report explores how remote sensing technology can bring significant benefits to post-earthquake response and recovery activities, through improved urban damage detection. The Marmara, Turkey earthquake of August 17, 1999 is used as a testbed, as one of the first earthquakes where a temporal sequence of 'before' and 'after' optical and radar imagery was available. The authors present a series of qualitative and quantitative methodological procedures and algorithms, which can be used to characterize the location, severity and extent of building damage. This study paves the way for subsequent research, employing very high-resolution imagery acquired by the new generation of optical satellites. Finally, since many of the illustrations rely on color to convey meaning, and the report is printed in black and white, a full-color version is included on a CD-ROM.

ABSTRACT

Each year, natural disasters such as earthquakes bring death, destruction and hardship to millions of people around the World (ISDR, 2002). In a bid to minimize these costs, research is increasingly focusing on disaster risk reduction. Through funding from the National Science Foundation, the Multidisciplinary Center for Earthquake Engineering Research has identified ‘Earthquake Response and Recovery’ as a thrust area. The stated goal is *‘to improve the speed with which appropriate response, restoration and recovery activities are undertaken, and the quality of the decisions that are made in the immediate and longer-term post-impact period’* (MCEER, 2003).

This report represents the culmination of several years of research by ImageCat Inc., which was undertaken with the broad aim of *‘Identifying ways in which post-earthquake response and recovery activities can be improved through the integration of remote sensing technology’*. The earthquake on 17th August 1999, which struck the Marmara region of Turkey, is employed as a test bed for addressing this aim. In addition to extreme urban damage across an extensive geographic area, Marmara was one of the first earthquakes where a temporal sequence of high resolution optical and radar imagery was available.

A combination of qualitative and quantitative methodological procedures is employed for characterizing the: (a) location; (b) severity; and (c) extent of urban building damage, using remote sensing imagery. This is achieved using indices of change recorded between images acquired before and after the Marmara earthquake. Visual assessment proves to be a useful tool for characterizing the signature of building damage on remote sensing imagery. Graph-based damage profiles, bi-variate damage plots and damage probability curves are used to distinguish between levels of building damage, ranging from 0-100% of collapsed structures. Theoretical foundations of data fusion are reviewed and associated techniques are shown to be a useful supplement to the damage detection methodology. Methods of measurement, feature and decision fusion are shown to enhance the distinction between and ability to predict damage states.

ACKNOWLEDGEMENTS

The authors gratefully acknowledge the financial support of the National Science Foundation (CMS-0085273) and the Multidisciplinary Center for Earthquake Engineering Research (NSF Award Number EEC-9701471) in this study.

We would like to thank Professors Masanobu Shinozuka and Kathleen Tierney for their guidance and enthusiastic support in helping this research team adapt these new and emerging technologies for earthquake loss estimation. Additionally, we acknowledge the help and support of the following individuals and organizations:

Professor Fumio Yamazaki, of the University of Tokyo and Dr. Masashi Matsuoka of the Earthquake Disaster Mitigation Research Center (EDM);

Suha Ulgen from Imagins in Istanbul, for dedicating his time while the research team was in Turkey to help collect data from the devastating Marmara, Turkey earthquake;

The Architectural Institute of Japan (AIJ), in joint effort with the Japanese Geotechnical Institute (JGS) and the Japan Society of Civil Engineers (JSCE), for use of observed building damage data in Golcuk, Turkey;

European Space Agency, for providing ERS SAR data;

and NIK Insaat Ticaret Ltd. of Istanbul, Turkey, for providing SPOT data of Golcuk.

TABLE OF CONTENTS

SECTION	TITLE	PAGE
1.0	INTRODUCTION	1
2.0	CHANGE DETECTION METHODOLOGY	9
2.1	Overview of Remote Sensing Data	9
2.1.1	Synthetic Aperture Radar, or SAR	11
2.1.2	Optical	18
2.2	Overview of Change Detection	19
3.0	IMPLEMENTATION	25
3.1	Study Sites	25
3.1.1	Golcuk	26
3.1.2	Adapazari	28
3.2	Ground Truth Data	28
3.2.1	Damage Observations	29
3.2.2	Damage Maps	32
3.3	SAR Remote Sensing	39
3.3.1	Pre-processing	42
3.3.2	Intensity	45
3.3.3	Intensity Difference	53
3.3.4	Correlation	56
3.3.5	Coherence	63
3.4	Optical Remote Sensing	66
3.4.1	Pre-processing	67
3.4.2	Intensity	68
3.4.3	Difference	71
3.4.4	Correlation	72
3.5	Summary of Key Findings	75
4.0	PRELIMINARY DAMAGE ALGORITHMS	77
4.1	SAR Damage Profiles	78
4.1.1	Intensity Difference	78
4.1.2	Correlation	82
4.1.3	Coherence	88
4.2	Optical Damage Profiles	91
4.2.1	Difference	91
4.2.2	Correlation	95
4.3	Bi-variate Damage Plots	97
4.4	Damage Probability Curves	101
4.5	Summary of Key Findings	104

TABLE OF CONTENTS (CONTINUED)

SECTION	TITLE	PAGE
5.0	DATA FUSION	107
5.1	Introduction	107
5.2	Measurement Level Fusion	116
5.3	Feature Level Fusion	117
5.4	Performance-Weighted Decision Fusion	119
5.4.1	Model Calibration	119
5.4.2	Model Validation	128
5.5	Summary of Key Findings	129
6.0	SUMMARY OF KEY FINDINGS	133
6.1	Overview of Findings	133
6.2	Recommendations	135
7.0	REFERENCES	137

LIST OF ILLUSTRATIONS

Note that color illustrations are included on the CD-ROM located on the back cover of the report.

FIGURE	TITLE	PAGE
1-1	Summary of previous research addressing the remote sensing of urban building damage.	3
2-1	Schematic representation of data acquisition using a ‘synthetic aperture’ radar.	11
2-2	Complex representation of SAR data.	12
2-3	Schematic representation of radar return from various ground surface.	13
2-4	Schematic representation of the scanning configuration for a SAR sensor.	14
2-5	Schematic representation of layover and foreshortening.	17
2-6	Flow chart summarizing general methodological procedures involved in damage detection.	21
2-7	Schematic representation of change detection using: (a) subtraction; (b) correlation (or coherence); and (c) block correlation statistics.	24
3-1	Landsat 5 RGB image acquired on August 18, 1999, covering Izmit Bay and Lake Sapanca – north-western Turkey near Anatolian fault.	27
3-2	Photo mosaic, showing damage sustained in Golcuk and surrounding areas, during the 1999 Marmara earthquake	30
3-3	Photo mosaic, showing damage sustained in Adapazari during the Marmara earthquake.	33
3-4	Map of Golcuk showing street network used as a basis for defining the the 70 zones employed in damage assessment.	34
3-5	Map showing the surveyed area of building damage in Golcuk.	36
3-6	Map of Adapazari, showing the districts used a basis for aggregating damage statistics collected by the Turkish Government.	37
3-7	Map showing building damage in central Adapazari.	38
3-8	Adapazari building validation points, fused with a vector layer showing the 16 Government-defined sample areas and Landsat 5 imagery.	38
3-9	Flowchart summarizing processing stages involved in damage detection using ERS SAR data.	41
3-10	Internal geometric distortions inherent in the SAR imaging process.	43
3-11	SAR intensity data for Golcuk, showing images ‘before’ (a-b) and ‘after’ (c-d) the Marmara earthquake. Image histograms (e-h) record DN value distribution within the 70 zones.	47
3-12	SAR intensity data for Golcuk, acquired ‘before’ and ‘after’ the 1999 Marmara earthquake, fused with SPOT 4 panchromatic imagery.	48
3-13	SAR intensity data for Adapazari, acquired ‘before’ (a-b) and ‘after’ (c-d) the Marmara earthquake. Image histograms (e-h) record DN value distribution within the 16 zones.	50
3-14	SAR intensity data for Adapazari acquired ‘before’ and ‘after’ the 1999 Marmara earthquake, fused with Landsat 5 imagery.	51

LIST OF ILLUSTRATIONS (CONTINUED)

Note that color illustrations are included on the CD-ROM located on the back cover of the report.

FIGURE	TITLE	PAGE
3-15	SAR intensity difference maps for Golcuk: (a-f) baseline; and (b-e) ‘before’-‘after’ pairings. Image histograms (g-h) record the DN value distribution within the 70 zones.	54
3-16	SAR intensity difference maps for Adapazari: (a-f) baseline; and (b-e) ‘before’-‘after’ pairings. Image histograms (g-h) record the DN value distribution within the 16 zones.	55
3-17	SAR sliding window-based intensity correlation map, for Golcuk: (a-f) baseline and (b-e) ‘before’-‘after’ pairings. Image histograms (g-h) show the distribution of DN values within the 70 zones.	58
3-18	SAR sliding window-based intensity correlation maps for Adapazari: (a-f) baseline and (b-e) ‘before’-‘after’ pairings. Image histograms (g-h) show the distribution of DN values within the 16 zones.	60
3-19	SAR block correlation statistics for Golcuk, computed using: (a,f) baseline and (b-e) ‘before’-‘after’ pairings.	61
3-20	SAR block correlation statistics for Adapazari, computed using: (a,f) baseline and (b-e) ‘before’-‘after’ pairings.	62
3-21	Golcuk coherence maps, computed for: (a,f) baseline and (b-e) ‘before’-‘after’ pairings. Image histograms (g-h) show the distribution of DN values within the 70 zones.	64
3-22	Adapazari coherence maps, computed for: (a,f) baseline and (b-e) ‘before’-‘after’ pairings. Image histograms (g-h) show the distribution of DN values within the 16 zones.	65
3-23	Flowchart summarizing stages involved in damage detection using high-resolution optical imagery acquired by the SPOT 4 sensor.	67
3-24	Panchromatic SPOT 4 coverage of Golcuk.	69
3-25	Near-infrared (band4) SPOT 4 coverage of Golcuk.	69
3-26	False color composite for SPOT data acquired ‘after’ the Marmara earthquake. Western regions of Golcuk are clearly affected by the presence of smoke in the upper atmosphere, which is detected at near middle infrared wavelengths.	70
3-27	Color-coded difference values for Golcuk, computed using pre processed SPOT 4 (a) panchromatic and (b) infrared coverage of Golcuk, acquired on 7/15/99 and 8/20/99. Results are overlaid with the ‘after’ panchromatic image.	72
3-28	Optical sliding window-based correlation statistics, computed using: (a) panchromatic; and (b) infrared SPOT 4 images.	74
3-29	Optical block correlation statistics for Golcuk computed using (a) panchromatic; and (b) infrared SPOT 4 images.	74

LIST OF ILLUSTRATIONS (CONTINUED)

Note that color illustrations are included on the CD-ROM located on the back cover of the report.

FIGURE	TITLE	PAGE
4-1	Damage profile for Golcuk, showing: (a) the mean difference in SAR intensity values $\text{dif}[B2,A1]$ as a function of building damage state (A-E); (b) Comparison between damage profile $\text{dif}[B2,A1]$ and baseline profiles $\text{dif}[B1,B2]$ and $\text{dif}[A1,A2]$; (c) damage profiles adjusted for radiometric offset.	80
4-2	(a) Damage profile for Adapazari, showing the mean difference in SAR intensity values $\text{dif}[B2,A1]$ as a function of building damage state (A-E); (b) Comparison between damage profile $\text{dif}[B2,A1]$ and baseline profiles $\text{dif}[B1,B2]$ and $\text{dif}[A1,A2]$.	81
4-3	(a) Damage profile for Golcuk, showing mean sliding window correlation values $\text{cor}[B2,A1]$ as a function of building damage state (A-E); (b) Comparison between damage profile $\text{cor}[B2,A1]$ and baseline profiles $\text{cor}[B1,B2]$ and $\text{cor}[A1,A2]$.	83
4-4	(a) Damage profile for Adapazari, showing mean sliding window correlation values $\text{cor}[B2,A1]$ as a function of building damage state (A-E); (b) Comparison between damage profile $\text{cor}[B2,A1]$ and baseline profiles $\text{cor}[B1,B2]$ and $\text{cor}[A1,A2]$.	84
4-5	(a) Damage profile for Golcuk, showing mean block correlation values $\text{bk_cor}[B2,A1]$ as a function of building damage state (A-E); (b) Comparison between damage profile $\text{bk_cor}[B2,A1]$ and baseline profiles $\text{bk_cor}[B1,B2]$ and $\text{bk_cor}[A1,A2]$. Error bars represent 1 standard deviation about the mean.	86
4-6	(a) Damage profile for Adapazari, showing mean block correlation values $\text{bk_cor}[B2,A1]$ as a function of building damage state (A-E); (b) Comparison between damage profile $\text{bk_cor}[B2,A1]$ and baseline profiles $\text{bk_cor}[B1,B2]$ and $\text{bk_cor}[A1,A2]$.	87
4-7	(a) Damage profile Golcuk, showing mean coherence values $\text{coh}[B2,A1]$ as a function of building damage state (A-E); (b) Comparison between damage profiles $\text{coh}[B2,A1]$ and baseline profiles $\text{coh}[B1,B2]$ and $\text{coh}[A1,A2]$.	89
4-8	(a) Damage profile for Adapazari, showing mean coherence values $\text{coh}[B2,A1]$ as a function of building damage state (A-E); (b) Comparison between damage profile $\text{coh}[B2,A1]$ and baseline profiles $\text{coh}[B1,B2]$ and $\text{coh}[A1,A2]$.	90
4-9	Damage profiles for Golcuk, showing the association between building damage state (A-E) and average difference between ‘before and ‘after’ for SPOT 4 (a) panchromatic and (b) infrared bands.	93

LIST OF ILLUSTRATIONS (CONTINUED)

Note that color illustrations are included on the CD-ROM located on the back cover of the report.

FIGURE	TITLE	PAGE
4-10	Damage profiles for Golcuk, showing the association between building damage state (A-E) and average sliding window-based correlation between ‘before’ and ‘after’ for SPOT 4 (a) panchromatic and (b) infrared bands.	95
4-11	Damage profiles for Golcuk, showing the association between building damage state (A-E) and average block correlation between ‘before’ and ‘after’ for SPOIT 4 (a) panchromatic and (b) infrared bands.	96
4-12	Bi-variate building damage plots for Golcuk, showing mean and standard deviation in difference and block correlation for: (a) panchromatic; and (b) infrared SPOT 4 data.	99
4-13	Bi-variate building damage plots for Golcuk, showing mean and standard deviation in difference and sliding window-based correlation, for: (a) panchromatic; and (b) infrared SPOT 4 data.	100
4-14	Hypothetical example of building damage observations and change statistics, demonstrating the approach used to generate damage probability curves.	102
4-15	Damage probability curves, showing association between block correlation recorded on panchromatic SPOT 4 coverage of Golcuk, and mean percentage of damage observations categorized as minor (G1-G3) and severe (G4-G5).	103
5-1	Conceptual representation of the generic data fusion processing architecture, comprising measurement, feature and decision level approaches.	109
5-2	Schematic representation of bi-variate sensor (SAR and optical) data fusion, for post-earthquake building damage assessment.	118
5-3	Schematic representation of calibration and validation phases of an <i>a priori</i> performance-weighted decision fusion approach to building damage classification.	118
5-4	Division of Golcuk ground truth zones into calibration and validation datasets.	121
5-5	Damage models for the 10 indices of change recorded using SPOT and SAR remote sensing coverage.	122
5-6	Performance matrices for the 10 measures of change recorded using SPOT optical and ERS SAR imagery of Golcuk acquired before and after the 1999 Marmara earthquake.	127

LIST OF TABLES

TABLE	TITLE	PAGE
1-1	Logistical framework diagram, outlining the aim, objectives and research design for this study.	7
2-1	Summary characteristics of commercial optical and SAR satellite systems.	10
3-1	Summary of damage to building structures and human casualties resulting from the 1999 Marmara earthquake.	26
3-2	Damage evaluation based on the European Macro-seismic Scale (EMS98) (Courtesy of Architectural Institute of Japan (AIJ).	35
3-3	Specification of SAR imagery acquired ‘before’ (B) and ‘after’ (A) the 1999 Marmara earthquake.	39
3-4	Specification of optical SPOT and Landsat imagery for Golcuk and Adapazari.	66
5-1	Characterization of measurement, feature, and decision level techniques of data fusion.	113
5-2	Subdivision of Golcuk zone-based damage observations into calibration and validation datasets.	119
5-3	Statistical summary of linear regression functions used to model the relationship between remote sensing indices of change and percentage building collapse.	126
5-4	Predictive capability of SPOT and SAR indices of change for damage classification, recorded <i>individually</i> and using <i>performance-weighted</i> decision fusion.	129

SECTION 1

INTRODUCTION

Each year, natural disasters such as earthquakes bring death, destruction and hardship to millions of people around the World. In a bid to minimize these costs, research is increasingly focusing on disaster risk reduction. Through funding from the National Science Foundation, the Multidisciplinary Center for Earthquake Engineering Research has identified ‘Earthquake Response and Recovery’ as a thrust area. The stated goal is *‘to improve the speed with which appropriate response, restoration and recovery activities are undertaken, and the quality of the decisions that are made in the immediate and longer-term post-impact period’* (MCEER, 2003).

The recent United Nations review, published as part of the International Strategy for Risk Reduction, observes that science and technology play key roles in developing tools and methodologies for disaster risk reduction (ISDR, 2002, p. 17). With respect to large magnitude earthquakes that strike populous regions, advanced technologies have important contributions to make in the immediate response period, early recovery period, and as a key component of longer-term mitigation programs. The research presented here is concerned with short-term response; more specifically rapid damage assessment in urban environments, where the human and economic costs are particularly high.

In the aftermath of an earthquake, damage assessment facilitates the prioritization and coordination of relief efforts. Local damage maps optimize response times by directing emergency teams to the *location* of damaged buildings. In terms of prioritizing these response efforts, the *severity* of damage is judged from the spatial distribution of these buildings, coupled with observed damage states. Broadening the assessment to a regional scale reveals damage *extent*, which enables the scaling of relief efforts, and determines whether the situation warrants international aid.

Determining the location, severity and extent of building damage as part of a post-earthquake damage assessment has traditionally been undertaken using field survey techniques. However, from experience, this approach proves time consuming, fraught with danger due to aftershocks, and subject to accessibility issues when telecommunication links and transportation networks are

disrupted. Exploratory studies suggest that *satellite remote sensing* is an alternative approach to damage assessment, which if integrated into existing reconnaissance practices, brings important benefits into play:

- ✓ **Overview of damage:** The imagery used for damage assessment spans a large geographic area, including numerous urban settlements within a single frame.
- ✓ **Near-global coverage:** Earth-orbiting satellites support damage assessment throughout the World, including both developed and lesser developed nations, where the effects of natural disasters may be particularly acute.
- ✓ **Supplements existing maps:** Satellite imagery provides an easily interpreted visual representation of damage, in the context of surrounding urban areas. This capability is particularly useful for lesser developed regions, where map coverage and geographic databases are often limited.
- ✓ **Low risk:** For international emergency response and aid organizations, decisions concerning the scale of relief efforts can be safely made in the immediate aftermath of an earthquake event, at a time when ground based assessment is extremely dangerous.
- ✓ **Resilient communication:** When the usual communication channels are down, satellite connections remain active.
- ✓ **Independent of time and weather:** Synthetic aperture radar (SAR) satellites offer 24/7, all weather monitoring. SAR imagery can be acquired under the cover of darkness and in cloudy conditions.
- ✓ **Fast response:** Satellites will ultimately provide real-time post-disaster information.
- ✓ **Loss estimation:** The damage assessment provides input data for initial loss estimates.

Figure 1-1 summarizes the scope of prior research concerning the remote sensing of urban building damage caused by earthquake events. In theoretical terms, a basic distinction can be drawn between *direct* approaches, where damage is recorded through its signature within the imagery versus *indirect* indicators, using a surrogate measure such as nighttime lighting levels (Hashitera *et al.*, 1999). Within the realm of direct damage detection, studies are based on either *mono-* or *multi-temporal* analysis. While the former distinguishes between the appearance of damaged and non-damaged structures within a given scene (see, for example, Mitomi *et al.*, 2000, 2001, 2002), the latter infers damage in terms of change between a temporal sequence of images. Multi-temporal damage detection is an extremely active research area, where considerable progress is attributable to collaborative efforts between ImageCat, Inc. from the U.S., and the Earthquake Disaster Management Center (EDM) in Japan.

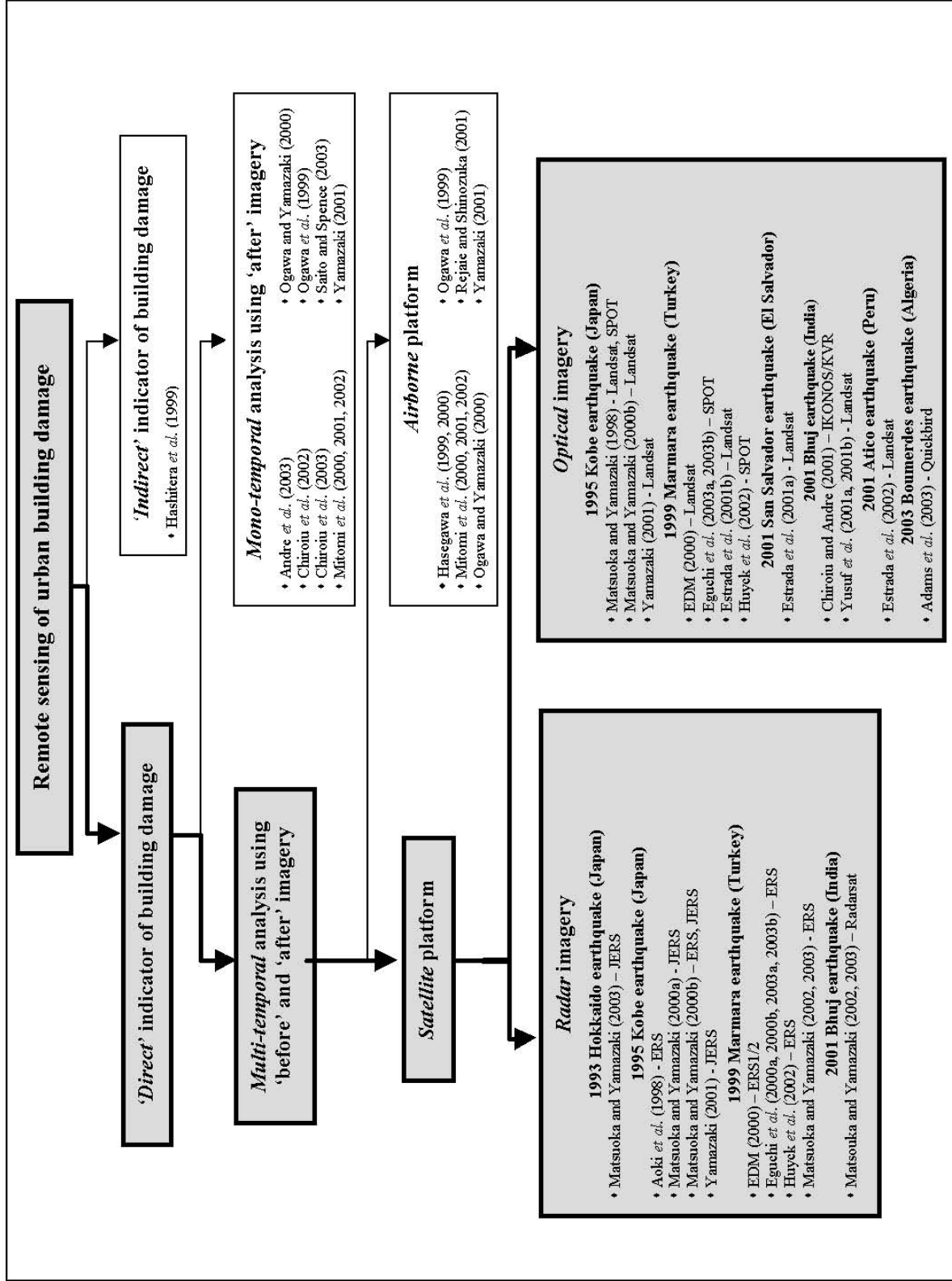


FIGURE 1-1 Summary of previous research addressing the remote sensing of urban building damage.

A number of intermediary reports document progress made with the development of qualitative and quantitative approaches to damage detection based on satellite imagery (see Eguchi *et al.*, 2000a, 2000b, 2003a, 2003b; also Matsuoka and Yamazaki, 2000a, 2000b, 2002, 2003). These studies employ optical and radar coverage. Optical sensors such as SPOT and Landsat are widely used in earth observation. Images are easy to interpret as they depict the ground surface as it appears to the human eye. Although more difficult to interpret as it records surface geometry, radar imagery has the advantage of 24/7, all weather viewing capability. As shown in Figure 1-1, both types of imagery have been implemented for a range of earthquakes including the 1995 Kobe, 1999 Marmara and 2001 Bhuj events.

The present report represents the culmination of several years of research by ImageCat Inc., which was undertaken with the broad aim of *identifying ways in which post-earthquake response and recovery activities can be improved through the integration of remote sensing technology*. The occurrence of an extreme earthquake on 17th August 1999 in the Marmara region of Turkey provided a suitable test bed for addressing this aim. In addition to extreme urban damage across an extensive geographic area, Marmara was one of the first earthquakes where high-resolution images were recorded by both synthetic aperture radar (SAR) and optical satellite sensors, before and after the event. A further advantage was the availability of results for a ground-based damage survey, which offered a means of validation.

Returning to the fundamental requirements of damage assessment in the aftermath of an earthquake, identifying the *location*, *severity* and *extent* of damage are key concerns. However, it is important to recognize that the successful integration of remote sensing into response and recovery activities requires more than just a theoretical understanding. It depends on the formalization of practical methodological procedures, which will ultimately provide the basis for automated damage detection algorithms. The research documented in this report sets out to bridge this gap between theory and practice, with the stated objective of:

Objective 1: To develop methodological procedures for characterizing the: (a) location; (b) severity; and (c) extent of urban building damage, using remote sensing imagery.

In recognition of the respective benefits associated with multi-source imagery for post-earthquake monitoring, methodological development includes both optical and radar coverage. To date, these datasets have been analyzed in isolation. However, with a view to optimizing the accuracy and robustness of future damage detection algorithms, it is important to recognize that overall performance may be improved when these datasets are analyzed in combination. Data fusion techniques are emerging in the literature as a useful mechanism for increasing the information yield from remote sensing imagery. To determine whether this is the case for building damage detection, a second objective of this research is identified as:

Objective 2: To determine whether multi-sensor data fusion improves the performance of building damage detection methodologies.

The logistical framework diagram in Table 1-1 outlines the research design used to address each of these objectives. Section 2 of this report introduces the general theory of multi-temporal building damage detection, using satellite remote sensing imagery. To assist the non-remote sensing specialist, this includes an overview of remote sensing technology and practice, which introduces optical and SAR data. Having furnished readers some understanding of the analytical process and datasets involved, Section 3 and Section 4 describe the implementation of damage detection theory for the Marmara earthquake. Following descriptions of selected study sites and available ground truth data, Section 3 documents the initial stages of data processing. This is followed by visual interpretation and evaluation of the datasets and derived measures of change, as an important step towards locating urban building damage based on its remotely sensed signature (Objective 1a). Now that readers should be familiar with the appearance of building damage on optical and SAR imagery, Section 4 goes on to present quantitative methods for characterizing damage severity (Objective 1b). Consistency between the damage algorithms for several study areas indicates whether the damage assessment is reliable across a wide geographic extent (Objective 1c).

It is envisaged that empirically-based ‘preliminary damage algorithms’ will ultimately provide the basis for automated building damage detection. While Section 4 focuses on the performance of individual measures derived from optical and SAR coverage, Section 5 investigates whether damage detection capability is likely to be optimized when they are analyzed in combination.

Following an introduction to the theory of data fusion, SAR and optical indices are combined using measurement- and decision-level procedures. A summary of key findings from the preceding analysis is presented in Section 6, together with recommendations for future research.

Table 1-1 Logistical framework diagram, outlining the aim, objectives and research design for this study.
To identify ways in which post-earthquake response and recovery activities can be improved through the integration of remote sensing technology.

GENERAL AIM	To identify ways in which post-earthquake response and recovery activities can be improved through the integration of remote sensing technology.			
SPECIFIC OBJECTIVE	1a. To develop methodological procedures for characterizing the location of urban building damage	1b. To develop methodological procedures for characterizing the severity of urban building damage	1c. To develop methodological procedures for characterizing the extent of urban building damage	2. To determine whether the performance of damage detection methodologies is improved by integrating remote sensing datasets
APPROACH	Use qualitative and quantitative methods of analysis to characterize urban building damage on SAR and optical remote sensing coverage	Establish graphical associations between multi-temporal changes measured on remote sensing coverage, and the concentration of building damage	Determine whether damage characteristics and preliminary algorithms show consistency between different urban settlements	Compare the predictive capability of empirical damage algorithms using indices of change individually and in combination
DATA REQUIRED	<ul style="list-style-type: none"> ♦ SAR imagery of study sites, acquired before and after the Marmara earthquake ♦ Optical imagery of study sites, acquired before and after the Marmara earthquake ♦ Maps showing the distribution of collapsed buildings. 	<ul style="list-style-type: none"> ♦ Aggregated indices of change, derived from optical and SAR imagery ♦ Area-based measures for the percentage of severely damaged or collapsed buildings, as a function of total damage observations 	<ul style="list-style-type: none"> ♦ Preliminary damage algorithms for several geographically distributed urban areas that recorded building damage following the Marmara earthquake 	<ul style="list-style-type: none"> ♦ Indices of change computed using optical and SAR imagery ♦ Corresponding ground truth data for the percentage of collapsed buildings
SOURCES OF DATA	<ul style="list-style-type: none"> ♦ Satellite imagery of urban areas where buildings collapsed following the Marmara earthquake ♦ Ground survey for urban areas recording the location of damaged buildings 	<ul style="list-style-type: none"> ♦ Satellite imagery of urban areas where buildings collapsed following the Marmara earthquake ♦ Ground survey for urban areas recording the location of damaged buildings 	<ul style="list-style-type: none"> ♦ Satellite imagery of urban areas where buildings collapsed following the Marmara earthquake ♦ Ground survey for urban areas recording the location of damaged buildings 	<ul style="list-style-type: none"> ♦ Satellite imagery of urban areas where buildings collapsed following the Marmara earthquake ♦ Ground survey for urban areas recording the location of damaged buildings
HOW TO ADDRESS OBJECTIVE	Visually identify significant changes between pre- and post-earthquake images that may be linked to building damage. Compare with the appearance of lesser- and non-damaged areas. Compute indices of change using optical and SAR imagery. Map indices of change and validate against observations of building damage.	Compute the percentage of collapsed buildings within a designated spatial unit. Aggregate indices of change into corresponding spatial units. Use graphical display to generate preliminary damage algorithms, showing empirical associations between indices of change and the concentration of collapsed buildings.	Compare graphical associations recorded in preliminary damage algorithms for several urban areas affected by the earthquake.	Using regression analysis, compute empirical relations between building damage and individual remote sensing indices of change. Assess the predictive capability of each model. Use data fusion techniques to complete the same prediction. Compare the performance of both approaches.

SECTION 2

CHANGE DETECTION METHODOLOGY

As noted in Section 1, the application of remote sensing technologies for post-disaster building damage assessment is an emerging focus of earthquake engineering research. This section of the report serves as an introduction to the general theory of multi-temporal urban change detection, which will be used to determine the location, severity and extent of building damage sustained in several Turkish cities following the 1999 Marmara earthquake. Section 2.1 presents an overview of optical and SAR remote sensing imagery, including background information and a brief discussion of their respective benefits and limitations for disaster monitoring. Section 2.2 then reviews the change detection methodology implemented by the ImageCat research team.

2.1 Overview of Remote Sensing Data

Defined by Lillesand and Keifer (1994, p.1) as *'the science and art of obtaining useful information about an object, area or phenomenon through the analysis of data acquired by a device that is not in contact with the object, area, or phenomenon under investigation'*, remote sensing offers a detailed yet synoptic representation of the earth's surface, which can be used to monitor major incidents, such as large fires, extensive flooding and hurricane wind damage (see, for example, CEOS, 2001). In addition, high-resolution imagery acquired by earth-orbiting satellite systems, has increasingly been used to study the effects of earthquakes (see, for example, Table 1-1). Table 2-1 summarizes the characteristics of commercial optical and synthetic aperture radar (SAR) sensors, the imagery from which could be used to assess earthquake damage in urban areas. Each satellite system has a specific spectral, spatial, and temporal resolution, relating to: altitude; coverage; wavebands; and revisit time. These factors ultimately determine which sensors are optimized for detecting damage arising from earthquakes, such as the 1999 event in Marmara, Turkey. The following section provides an introduction to both optical and SAR systems, describing how they work, what they record, and noting the key advantages and disadvantages.

TABLE 2-1 Summary characteristics of commercial optical and SAR satellite systems.

Satellite/Platform	Sensor	Altitude (km)	Coverage (km x km)	Wavebands (μm or GHz)	Spatial Resolution	Repeat cycle
Landsat-5 (launched 3/1/84)	Optical (TM)	700	170 x 185	1: 0.45-0.52 2: 0.52-0.6 3: 0.63-0.69 4: 0.76-0.9 5: 1.55-1.75 6: 10.4-12.5 7: 2.08-2.35	30m 30m 30m 30m 30m 120m 30m	16 days
Landsat-7 (launched 4/15/99)	Optical (TM)	700	170 x 185	1: 0.45-0.515 2: 0.525-0.605 3: 0.63-0.69 4: 0.75-0.90 5: 1.55-1.75 6: 10.4-12.5 7: 2.09-2.35 Pan: 0.52-0.9	30m 30m 30m 30m 30m 60m 30m 15m	16 days
SPOT 4 (launched 3/24/98)	Optical (HRV)	830	60 x 60	1 (green): 0.5-0.59 2 (red): 0.61-0.68 3 (nir): 0.79-0.89 4 (mir): 1.58-1.75 Pan: 0.61-0.68	20m 20m 20m 20m 10m	26 days
Spot 5 (launched 5/4/02)	Optical (HRG)	810	60 x 60	1 (green): 0.5-0.59 2 (red): 0.61-0.68 3 (nir): 0.79-0.89 4 (mir): 1.58-1.75 Pan: 0.48-0.71	10m 10m 10m 10m 2.5/5m	26 days
IRS-1C (launched 12/28/95) IRS-1D (launched 9/29/97)	Optical (LISS/PAN)	817 824-874	70 x 70 70 x 70	2 (green): 0.52-0.58 3 (red): 0.62-0.68 4 (nir): 0.77-0.86 5 (mir): 1.55-1.7 Pan: 0.5-0.75	23.5m 23.5m 23.5m 23.5m 5.8m	24 days
Ikonos (launched 9/24/02)	Optical	680	13 x 13	1 (blue): 0.45-0.5 2 (green): 0.52-0.6 3 (red): 0.63-0.69 4 (nir): 0.76-0.9 Pan: 0.45-0.9	4m 4m 4m 4m 1m	1.5-2.9 days (at 40° latitude)
Quickbird (launched 10/18/01)	Optical	600	16.5 x 16.5	1 (blue): 0.45-0.52 2 (green): 0.52-0.6 3 (red): 0.63-0.69 4 (nir): 0.76-0.89 Pan: 0.45-0.9	2.5-4m 2.5-4m 2.5-4m 2.5-4m 0.61-1m	1-4 days (depending on latitude)
ERS 1 (launched 6/17/91) ERS 2 (launched 4/20/95)	SAR	785	100 x 100	C-band: 5.3GHz	30m (I -mode) 10m (W -mode)	35 days
JERS1 (expired 10/11/98)	SAR	570	75 x 75	L-band: 1.3 GHz	18m	44 days
Radarsat1 (launched 11/4/95)	SAR	800	100 x 100 50 x 50	C-band: 5.3GHz	25m (S-mode) 8m (F-mode)	1-6 days (depending on latitude)
Radarsat2 (launches 2004)	SAR	798	100 x 100 20 x 20	C-band 5.3GHz	28m (S-mode) 3m (UF-mode)	3 days

2.1.1 Synthetic Aperture Radar, or SAR

SAR sensors are active remote sensing devices, which provide their own source of illumination to a given target area. These imaging systems operate by transmitting and recording microwave signals through a sideways looking sensor or antenna. The term ‘synthetic aperture’ radar relates to the process of mathematically analyzing a sequence of these signals and the distance that the satellite platform has traveled, to synthesize the effect of a much larger antenna. The larger antenna has the effect of simulating a bigger camera lens, thereby enhancing the detail or resolution of the imaged scene. The schematic represented in Figure 2-1 demonstrates how the synthetic aperture is constructed by moving the real aperture (antenna) through a series of positions along the flight track. At each position, the return signal is recorded by the echo store. Combining these signals coherently, a procedure referred to as multi-signal processing, achieves a more detailed and crisper image than traditional real aperture sensors.

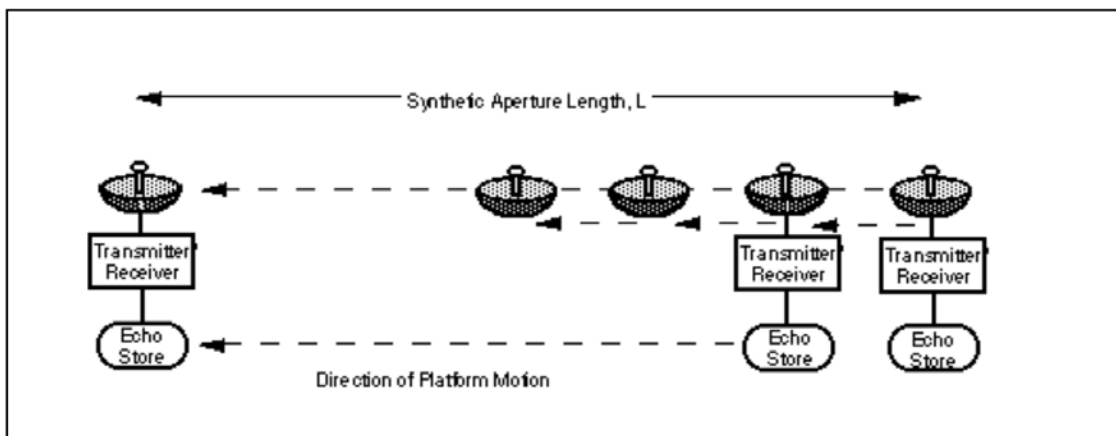


FIGURE 2-1 Schematic representation of data acquisition using a ‘synthetic aperture’ radar. The antenna is moved through a series of positions along the flight path and the return signals focused onto a single point (adapted from Freeman, 2000).

Characteristics of the earth’s surface are recorded as a series of echoes from the emitted signal. These are transmitted at a rate of approximately 1,500 pulses per second. SAR radar return falls within the wavelength range 1cm-1m, and the frequency range 300MHz-30GHz. It comprises two measurements: (1) phase or signal round-trip time; and (2) the signal strength. This information may be expressed in the form of complex numbers, comprising real and imaginary components. The phase or angle (ϕ), shown in Figure 2-2, is related to the time delay with

respect to a reference clock. Magnitude or intensity relates to the signal amplitude. Intensity (I) is computed according to Equation 2-1 (decibel scale), using both real and imaginary components:

$$\text{Intensity } (I) = 10 \cdot \log (\text{Real}^2 + \text{Imaginary}^2) \quad (2-1)$$

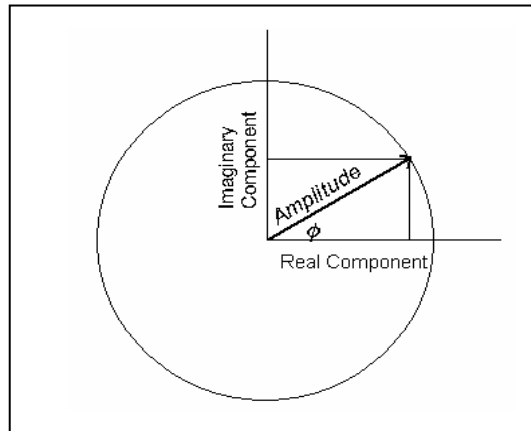


FIGURE 2-2 Complex representation of SAR data.

High amplitude values relate to extremely reflective features, where a large fraction of the radar energy is returned to the sensor. For low values, little energy is reflected. In general, backscatter varies with factors including: (1) the size and orientation of surface features; (2) surface material and roughness; (3) sensor observation or ‘look’ angle; and (4) moisture content within the target area.

In an urban context, buildings look particularly bright, as incoming radar pulses bounce back from the structures (see, for example, Figure 2-3). Right-angled geometrical shapes producing this characteristic return (such as the juncture between walls, roofs and pavements) are referred to as ‘corner reflectors’ (see, for example, Mansouri *et al.*, 2001). In contrast, city streets and freeways tend to appear dark, since the signal is mostly reflected away on contact with flat surfaces. Thus, a typical urban setting can be analyzed as an arrangement of various large corner reflectors (dihedrals and trihedrals) and flat planes. Building height, building material and surface roughness are other factors affecting the radar return. In the case of building height, Figure 2-3 demonstrates how features such as hilly terrain and tall buildings create a shadowing effect, which produces a lower return in the obscured area (see also Figure 2-5).

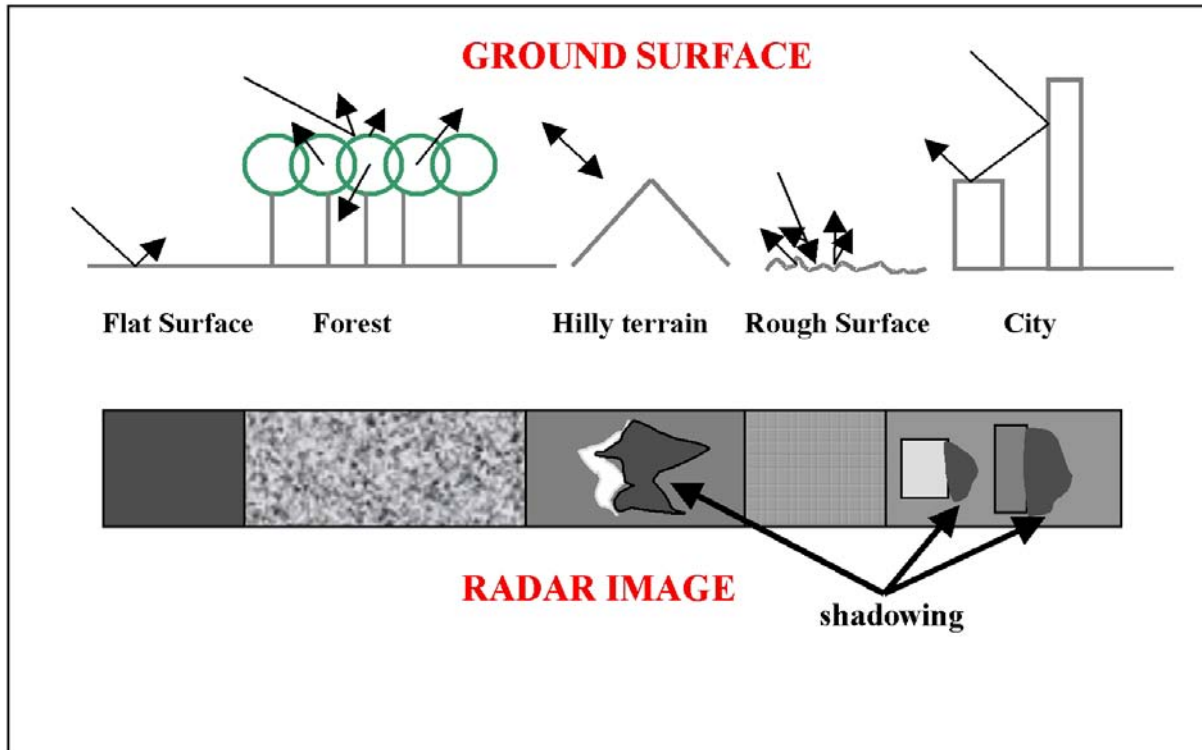


FIGURE 2-3 Schematic representation of radar return from various ground surface features.

The spatial resolution of SAR imagery is determined by several factors (see Oliver and Quegan, 1998). Along-track in the azimuth direction (see Figure 2-4), antenna size controls the interval between readings. As a rule of thumb, the azimuth resolution of a fully focused SAR sensor is approximately 0.5x the antenna length. Across-track (also termed ‘in range’), the interval is determined by the time interval over which samples of the return signal are averaged. This is proportional to the bandwidth of the signal, with a higher bandwidth synonymous with increased resolution. The sample interval often differs between along- and cross-track directions. Consequently, the data are initially posted with rectangular pixel dimensions, and then resampled to regular units. Where multiple or ‘repeat’ passes are made over a given location, any difference in the position of the satellite platform is referred to as the ‘sensor baseline’ distance. A shorter baseline leads to better image correlation.

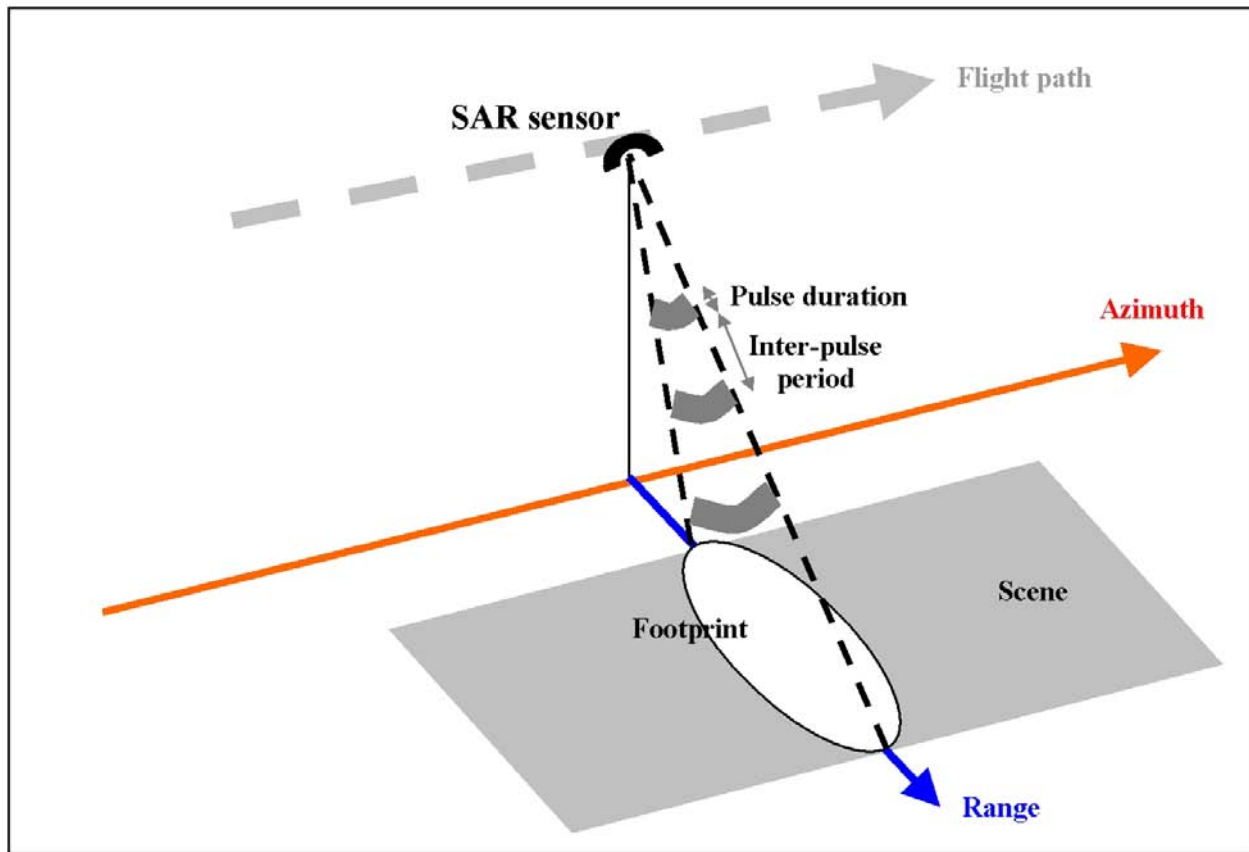


FIGURE 2-4 Schematic representation of the scanning configuration for a SAR sensor.

For change detection purposes, correlation and coherence are useful derivative datasets that can be obtained from SAR complex data. Correlation measures the change in intensity between a pair of SAR images, which are expressed as I_1 and I_2 in Equation 2-2. Values are computed using a sliding window. This procedure takes into account the cross-correlation of neighboring pixels that may include a similar target/object. In order to reduce the effect of random noise that is inherent to radar systems (due to thermal noise and random scatter at the receiver), this window size is larger than a single pixel.

$$\text{Correlation}(I_1, I_2) = \frac{\text{Covariance}(I_1, I_2)}{\text{Standard deviation}(I_1) \cdot \text{Standard deviation}(I_2)} \quad (2-2)$$

The expanded version of this formula (Equation 2-3) shows how the correlation coefficient r measures the degree of fit between a least-squares regression line and the sample data. X and Y are two N -element independent sample populations, with x_i and y_i data points that respectively

fall within the sliding windows of images I_1 and I_2 . Values fall within the range $[-1.0,1.0]$, indicating the degree of fit to a linear model. Where multi-temporal images are used, the resulting correlation matrix records higher values in areas where change is minimal, and lower values where significant differences are present. However, it is important to recognize that random noise is a limiting factor in SAR imagery, often leading to unexpectedly low correlation values. In addition to the sliding window approach, correlation can also be measured using block statistics. This approach is discussed further in Section 2.2.

$$r = \frac{\frac{1}{N-1} \sum_{i=0}^{N-1} \left(x_i - \left[\frac{\sum_{k=0}^{N-1} x_k}{N} \right] \right) \left(y_i - \left[\frac{\sum_{k=0}^{N-1} y_k}{N} \right] \right)}{\left[\frac{1}{N-1} \sum_{i=0}^{N-1} \left(x_i - \left[\frac{\sum_{k=0}^{N-1} x_k}{N} \right] \right)^2 \right]^{1/2} \left[\frac{1}{N-1} \sum_{i=0}^{N-1} \left(y_i - \left[\frac{\sum_{k=0}^{N-1} y_k}{N} \right] \right)^2 \right]^{1/2}} \quad (2-3)$$

Otherwise known as complex correlation, coherence measures the degree of similarity between the real and imaginary components in a temporal sequence of complex images. The standard formula for computing coherence is shown in Equation 2-4, with C_1 and C_2 representing co-registered complex images, and C^* the complex conjugate. The numerator in Equation 2-4 is the summation of the complex conjugate multiplications of pixels in a designated sliding window. While the window is necessary for computational purposes, this approach is particularly appropriate for SAR data, because a given object may be imaged or mapped within a number of neighboring pixels. The image significance of the object may be detected in adjacent pixels, due to subtle geometric differences in the respective data acquisition configurations. The optimal window size is determined by the trade off between dimensions of the target object, computation time, and the smoothing effect associated with larger windows.

$$\text{Coherence}(C_1, C_2) = \frac{\left| \sum C_1 C_2^* \right|}{\sqrt{\left(\sum C_1 C_1^* \right) \left(\sum C_2 C_2^* \right)}} \quad (2-4)$$

For change detection purposes, SAR sensors offer near-continuous coverage (see Table 2-1) for most areas of interest around the World. The area covered by each frame of imagery is sufficient

for urban monitoring. SAR remote sensing devices have several distinct advantages over optical systems. First, SAR is an active sensor, which operates in all weather and illumination conditions. The ability to penetrate cloud or smoke cover means that it can provide a timely overview of damage, when optical views are obscured. Second, SAR is capable of 3D imaging, enabling digital elevation models (DEM) to be produced for target areas using a technique known as interferometry (see Rodriguez and Martin, 1992; also Massonet and Rabaute, 1993). Although this approach is not employed in the present study, with an appropriate sequence of complex images, radar interferometry can reveal minute ground displacements across an extensive area (see, for example, Gabriel *et al.*, 1989; also Peltzer and Rosen, 1995).

There are potential limitations associated with satellite-based SAR systems. Diffuse backscatter from targets causes noise-like speckle, rendering objects on the surface below indistinct. Providing that suitable datasets are available, the level of speckle can be reduced using multi-look imagery. This is a form of averaging, where the same point on the ground is observed from a range of sensor positions. Another limitation is the sensitivity of SAR data to the relative position of objects with respect to the sensor. As the system is side-looking, shadowing has an obscuring effect (see Figure 2-3). As shown in Figure 2-5, layover and foreshortening are also issues. Layover occurs when the return from multiple ground surface features coincide. In the illustrated example, returns are simultaneously received for all points along line T₁. Together, these values determine the overall magnitude of response for the corresponding pixel on a SAR image. Foreshortening is less common in the urban environments studied here. The emitted wave reaches the base of a long gradual feature, prior to the top. On the associated image, the feature appears considerably shorter compared with its actual dimensions.

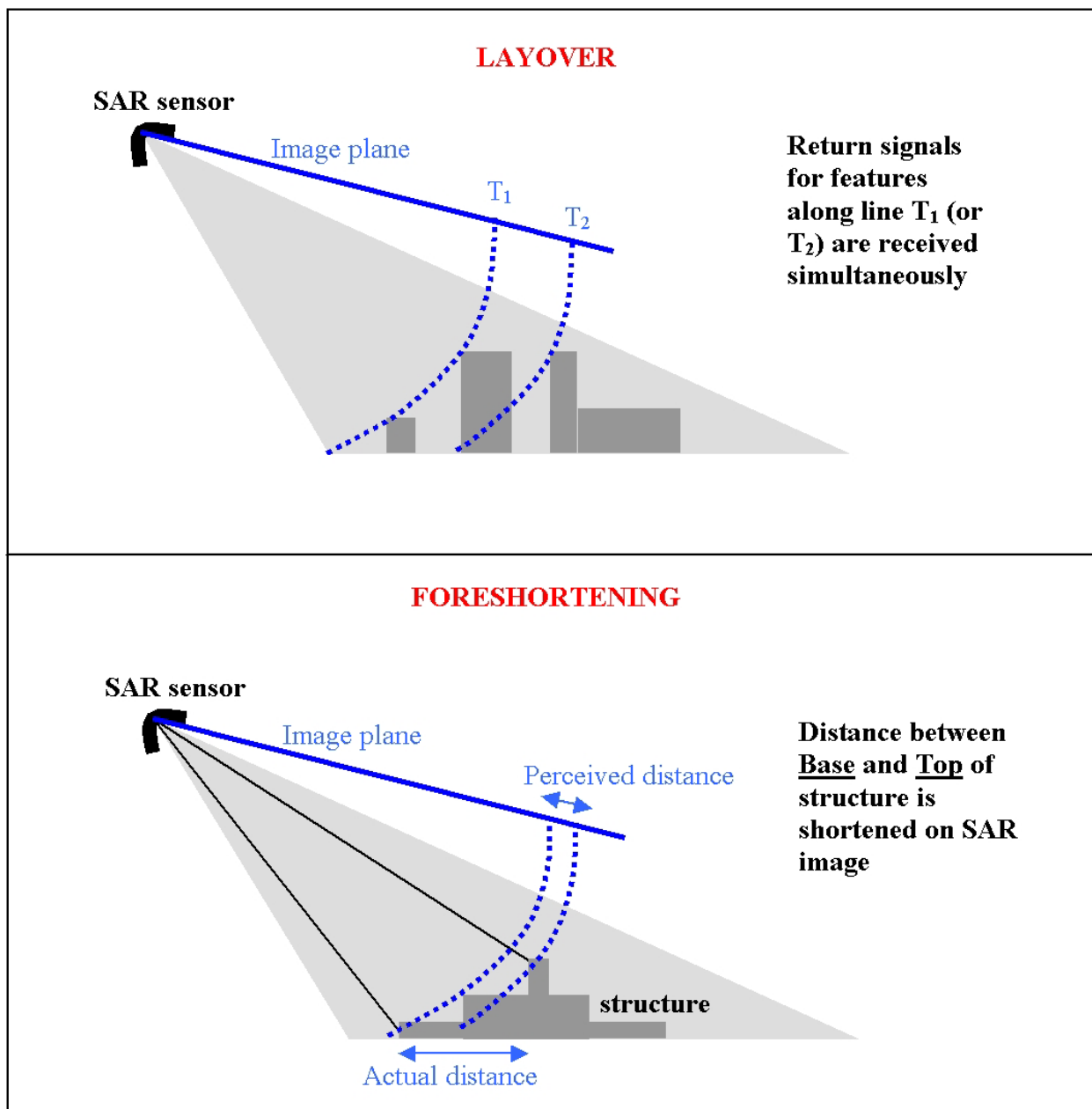


FIGURE 2-5 Schematic representation of layover and foreshortening. Layover is a common effect in urban environments, where tall buildings are concentrated.

2.1.2 Optical

The optical satellite sensors listed in Table 2-1, including: Landsat; SPOT; IRS; IKONOS; and Quickbird, are passive sensors that record reflectance characteristics of the earth's surface as it is illuminated by the sun. Optical devices operate at visible (0.38-0.72 μm), near- (0.72-1.30 μm) and mid-infrared (1.30-3.0 μm) wavelengths of the electromagnetic spectrum. Data is acquired in a series of 'bands'. Any system that records data in more than two bands is termed 'multispectral'. In 'hyperspectral' systems (for details, see Campbell, 1996) these bands are very narrow, with a width of $\sim 0.2\mu\text{m}$. In the visible region of the spectrum, bands span blue, green and red wavelengths. In some instances, reflectance from these wavelengths is combined into a single, wide panchromatic band.

The magnitude of reflectance in each band is received by the sensor, calibrated, and expressed as a digital number (DN). These values are usually recorded as 8- (e.g. SPOT 4) or 11-bit (e.g. IKONOS) data, which respectively fall in the range 0-255 DN and 0-2048 DN. Earth surface materials have different reflectance characteristics. These are determined at an atomic/molecular level, with the sensor detecting the colors associated with particular patterns of electronic excitation and vibration. The spectral characteristics of different materials are referred to as a 'spectral signature'. In general terms, dense urban areas tend to exhibit a moderate reflectance in green, red and infrared bands. In contrast, the signature for residential suburbs is often dominated by the near infrared, due to a comparative prevalence of vegetative cover. Water bodies, such as lakes, rivers and oceans reflect strongly at short wavelengths, but absorb in longer infrared bands.

The spatial resolution or ground coverage of each pixel is related to the altitude of the satellite platform. While low-resolution systems such as NOAA AVHRR and Meteosat present a holistic view of the earth's surface, the present study is concerned with change detection at a regional scale. Moderately high resolution systems, such as SPOT, depict the earth's surface in greater detail, enabling features of the urban landscape to be distinguished. The new generation of very high-resolution optical systems, such as Quickbird, has sub-meter pixels. However, their recent launch date limits data availability for previous earthquake events.

The temporal resolution of earth-orbiting systems reflects the interval between satellite overpasses. For satellites such as SPOT and Landsat, the frequency of data acquisition reflects altitude above the earth's surface (see Table 2-1). The revisit period for new high-resolution systems is more flexible, as they permit 'off-nadir' or sideways viewing.

The use of optical data for change detection has a number of advantages. First, the spectral characteristics of imagery are comparable to human vision, making it easy to understand and interpret. Furthermore, the distinction between earth surface materials is enhanced by the multi-band sensing capabilities. Compared with SAR devices, passive optical systems are subject to less noise/scatter. Near-nadir viewing SPOT and Landsat avoid issues such as foreshortening (see Figure 2-5), and widespread shadowing.

The primary limitations of optical data relate to its passive remote sensing strategy. Driven by solar radiation, optical systems are limited to daylight hours. Furthermore, they are at the mercy of weather and atmospheric conditions, being unable to image through clouds or the dense plumes of smoke that often accompany disasters.

2.2 Overview of Change Detection

Following extreme events, quick and accurate damage detection assessment can be the difference between life and death. Change detection techniques, based on high-resolution remote sensing data, provide an overview of the post-disaster scene, a method of rapid damage detection, and most importantly, a focus for rescue and recovery efforts. The following section initially describes the theory behind change detection, focusing on the capabilities of satellite data that enable it to successfully meet the key requirements for disaster response in urban environments. Important methodological issues underpinning change detection procedures are then discussed.

In simple terms, damage arising from a disaster is detected in the form of 'changes' between a temporal sequence of remote sensing images acquired 'before' and 'after' the event. This approach to change detection is quick, straightforward and can be performed using either SAR or optical data. While the approach is readily applicable to most extreme events (hurricanes, fires, terrorist attacks), here the focus is on damage caused by earthquakes in urban environments, where building and highway destruction is often severe.

In the case of SAR imagery, damage sustained by buildings may be detected as a pronounced change in the magnitude of radar return. Where buildings have collapsed, the degree of backscatter is expected to fall. When the buildings were standing, the radar return was bounced back from right angles to the sensor. After collapse, the right angles are destroyed and the signal is instead dispersed across the now uneven surface. The mechanism behind this change is well understood, with the importance of dihedral and trihedral right angle corner reflectors discussed in other publications (see, for example, Mansouri *et al.*, 2001). In the case of optical imagery, damage sustained by urban environments is detected as visible changes in the reflectance characteristics of surface materials. Structures look different where, for example, roofs and walls have collapsed and structures buckled. Submergence due to flooding, or extrusion caused by liquefaction, may further alter reflectance characteristics.

For damage detection purposes, the qualitative and quantitative characteristics of changes between remote sensing images acquired ‘before’ and ‘after’ an earthquake event need to be formally established. Visual inspection of these differences offers an overview of events and may provide an initial focus for recovery efforts. However, mathematical techniques promise a more detailed damage record, which will fully support the emergency response.

Figure 2-6 summarizes general methodological procedures underpinning damage detection algorithms developed by the research team. First, a catalogue of remote sensing data is acquired. As noted previously, this must include imagery recorded ‘before’ and ‘after’ the event. The minimum requirement is a single scene from each time frame, ideally acquired close to the event. Damage detection capabilities may be improved where a series of pre- and post- event images is available, as the distinction can then be made between earthquake related damage and extraneous changes. Establishing a ‘baseline’ encapsulates the effects of seasonality, shadowing and differences in illumination, which although causes of change, are distinct from direct damage to the built environment. It is important to note that this baseline image is fundamentally different to the ‘sensor baseline’, defined in Section 2.1.1 as the physical distance between satellite platforms as they cover the same target area.

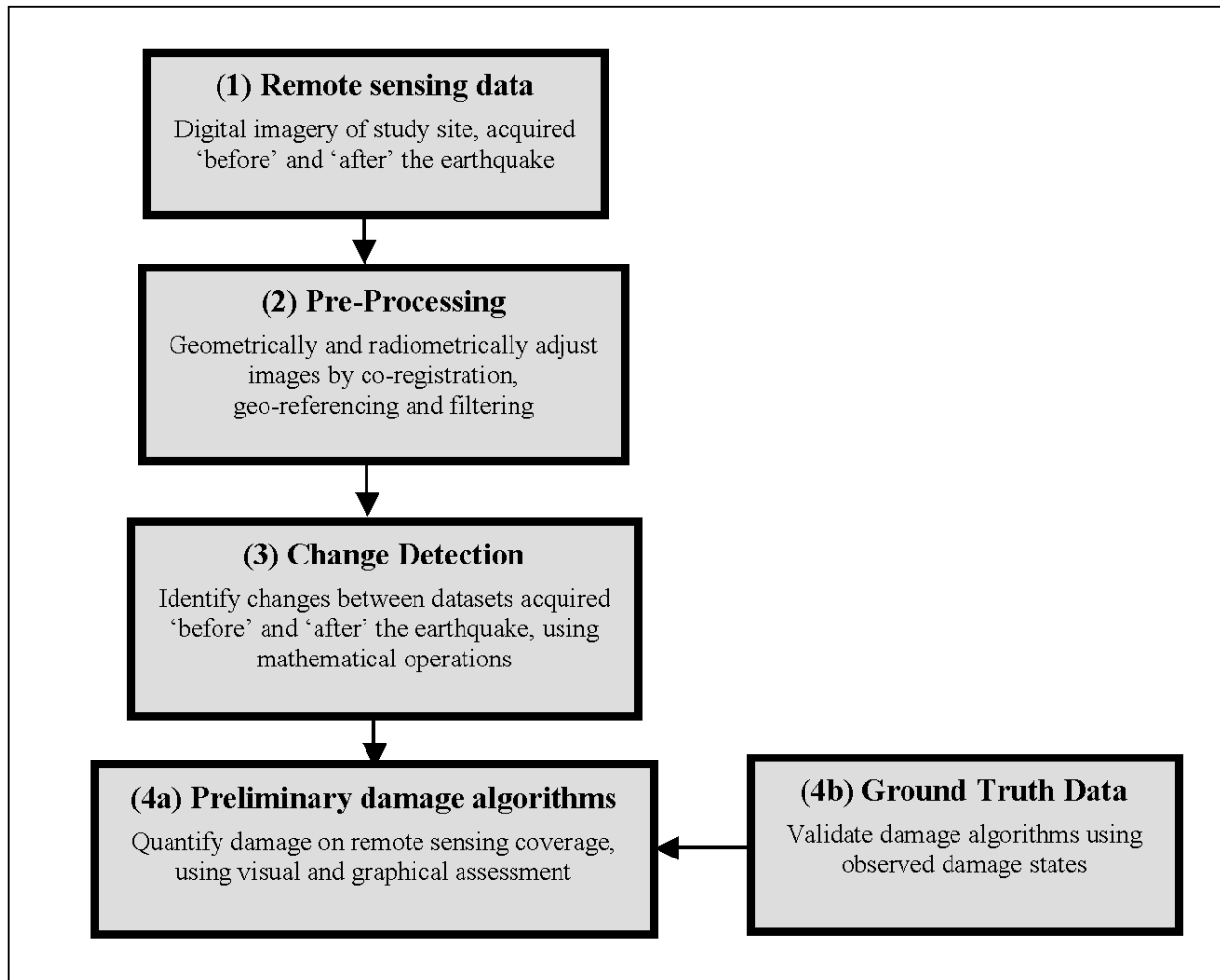


FIGURE 2-6 Flow chart summarizing general methodological procedures involved in damage detection. Sensor specific methodologies are provided in Section 3.

From Figure 2-6, the initial catalogue of imagery now requires pre-processing to: (1) remove geometric errors inherent in the data; and (2) register all scenes to a common geographic coordinate system. Spatial distortions specific to optical and SAR imagery are linked with systematic (sensor related) and non-systematic (platform and scene related) factors. These are described further with respect to ERS and SPOT datasets in Section 3.3 and Section 3.4. Most systematic distortions are removed at the source, prior to data delivery. However, additional correction procedures and fine-tuning may subsequently be performed, using automated and/or manual techniques.

Co-registration aligns multiple images of a given location, so that any object occupies the same position in all scenes (for details, see Campbell, 1996). Basic manual registration is performed in the image coordinate system (x,y), and is achieved using a network of ground control points (GCPs). These comprise distinctive ground surface features, such as the corners of buildings and highway intersections, which are readily distinguished on the imagery. In cases where coarse registration is sufficient (see, for example, Section 3.3.1), automated GCP selection may be performed, resulting in a set of arbitrary points. Given manually or automatically derived GCPs, a warping process comprising rotation, scaling and translation, is then performed using a mathematical transformation. One image is designated the ‘master’ and the others ‘slaves’. The complexity of polynomial function used to warp the slave to its master is reflected by its order. The most appropriate transformation order depends on the nature and degree of error present within the data. Automated template matching (for details see Section 3.3.1) may then be applied to fine tune the registration and establish an optimal fit between the scenes. This matching algorithm works by shifting the pair of images at pixel increments, until the correlation is maximized.

Geo-referencing typically accompanies the registration procedure. Here, a simple linear transformation establishes a common frame of reference, such as a real world coordinate system (latitude and longitude). Once displayed using a standard map projection, objects of interest within the suite of images should appear at corresponding geographic locations.

Changes between the ‘before’ and ‘after’ scenes can be computed using a range of mathematical operators, including: (1) subtraction; (2) division; (3) correlation; (4) coherence or complex

correlation; and (5) elevation change. The schematic representation in Figure 2-7a shows how subtraction is performed on a per-pixel basis. As discussed in the context of SAR imagery (see Section 2.1.1; also Equations 2-2 and 2-3), correlation and coherence are measured within a sliding window. Figure 2-7b demonstrates how the value of a central pixel is thereby determined. Correlation may also be calculated using block statistics, where as depicted in Figure 2-7c, each block of pixels determines a single value that is adopted by all pixels within that block. For both sets of computations, the baseline images derived from pairs of ‘before’ scenes may be used for comparative purposes, to distinguish changes due to environmental effects. The idea is to study the difference between a baseline ‘before’-‘before’ correlation or coherence scene, with respect to a ‘before’-‘after’ correlation/coherence image.

Although the approach is not investigated here, it is important to note that changes could also be computed through temporal differences in elevation. This calculation involves the subtraction of digital terrain models (DEM) generated using interferometric analysis of SAR data acquired ‘before’ and ‘after’ the event.

The final step of this methodological sequence forges empirical associations between changes identified in pre- and post-earthquake remote sensing coverage, and building damage states observed in the field. So called ‘ground truth’ damage data (see Section 3.2), incorporates both qualitative and quantitative information. In the context of earthquake damage assessment, qualitative resources include photographic records of damage sustained and descriptive text. As noted in Section 1, quantitative assessments comprise records of building damage state, together with estimates of damage extent. As imagery from the new generation of very high-resolution satellite sensors becomes widely available, damage assessment on a per building basis can now be undertaken remotely (Adams *et al.*, 2003; Saito *et al.*, 2004).

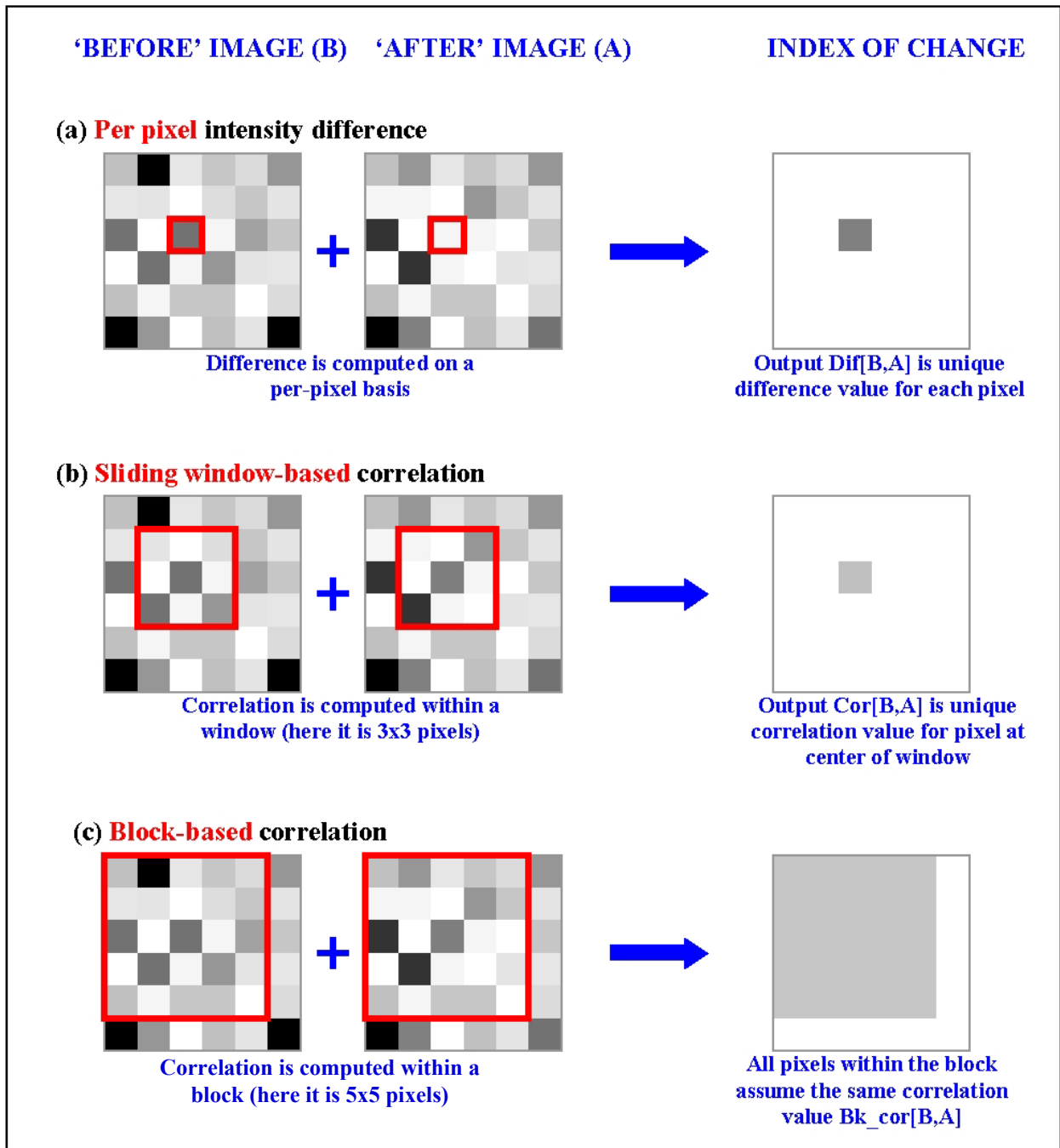


FIGURE 2-7 Schematic representation of change detection using: (a) subtraction; (b) correlation (or coherence); and (c) block correlation statistics.

SECTION 3

IMPLEMENTATION

This section of the report details implementation of the general change detection methodology introduced in Section 2, in the context of the Marmara earthquake (see also Huyck *et al.*, 2002; Eguchi *et al.*, 2003b). This devastating event hit north-western Turkey on 17th August, 1999, with a moment magnitude of 7.4 and surface wave magnitude of 7.8 on the Richter scale (Papageorgiou, 2000). The present study focuses on the cities of Golcuk and Adapazari, which were severely damaged during the earthquake. Details of these localities are given in Section 3.1. Section 3.2 describes the ground truth data collected for these areas. This is followed by separate accounts of the techniques employed for processing multi-temporal SAR and optical data, and deriving measures of change. Visual characteristics of each dataset are then presented, as a means of addressing Objective 1a (see Section 1.2). The qualitative damage assessment indicates whether *locations* of urban damage are distinguishable on remote sensing coverage.

3.1 Study Sites

The cities of Golcuk and Adapazari are situated on the seismic fault within the North Anatolian Fault Zone that triggered the Marmara earthquake. As described in the following sections and summarized in Table 3-1, urban damage was widespread, and included: subsidence; fire; and building collapse. The location of Golcuk and Adapazari is depicted by the multispectral composite Landsat image in Figure 3-1. This coverage was acquired on 18th September, 1999, approximately one month after the Marmara earthquake. Although of coarse resolution compared with optical systems such as SPOT 4 (see Table 2-1), the imagery provides a useful overview of the study localities. The image has been pre-processed and geo-referenced. On this red-green-blue (RGB) color composite, the Marmara Sea and Lake Sapanca appear dark, while coastlines are sharply visible. To the east of Adapazari, the River Sakarya also appears dark blue. Chains of mountain are evident around the main water bodies. The enlarged sub-scenes are annotated to highlight urban and rural areas, together with the main highways through each development. The RGB color-coding effectively separates mountainous and natural lands (maroon) from urban areas (blue) and the extensive agricultural lands surrounding both cities.

TABLE 3-1 Summary of damage to building structures and human casualties resulting from the 1999 Marmara earthquake. *Golcuk is situated in Kocaeli province and **Adapazari in Sakarya province. (Courtesy of EDM, 2000)

Province	BUILDING DAMAGE			CASUALTIES	
	Heavily damaged	Moderately damaged	Lightly damaged	Dead	Injured
Bolu	3,226	4,782	3,233	264	1,163
Bursa	32	109	431	263	333
Eskisehir	70	32	204	86	83
Istanbul	3,614	12,370	10,630	978	3,547
Kocaeli*	23,254	21,316	21,481	4,088	4,147
Sakarya**	20,104	11,381	17,953	2,627	5,084
Yalova	10,134	8,870	14,459	2,501	4,472
Total	60,434	58,860	68,391	10,807	18,829

3.1.1 Golcuk

The town of Golcuk is situated on the southern shore of Izmit Bay, with a latitude of 40.72° and longitude of 29.83°. Golcuk is the most densely populated urban center in Kocaeli province. Prior to the earthquake, Golcuk was estimated to have 130,000 inhabitants and 5,000 buildings (AIJ, 1999). Many of the buildings were constructed from reinforced concrete frames with unreinforced masonry infill (see Bruneau, 2000; also Aschheim, 2000). The epicenter of the earthquake was located 10km east of Golcuk, with the associated fault line running east-west to the north side of the city, near the coastline. Seismic activity is common in the region, with the event of 17th August 1999 being the eleventh large earthquake along the NAFZ since 1939 (Homan and Eastwood, 2001). Golcuk suffered severe building damage during the earthquake. 30-40% of structures experienced full or partial collapse (Coburn *et al.*, 1999, cited in Rathje, 2000). In general, medium-to-high-rise reinforced concrete buildings experienced much greater damage than masonry and low-rise structures.

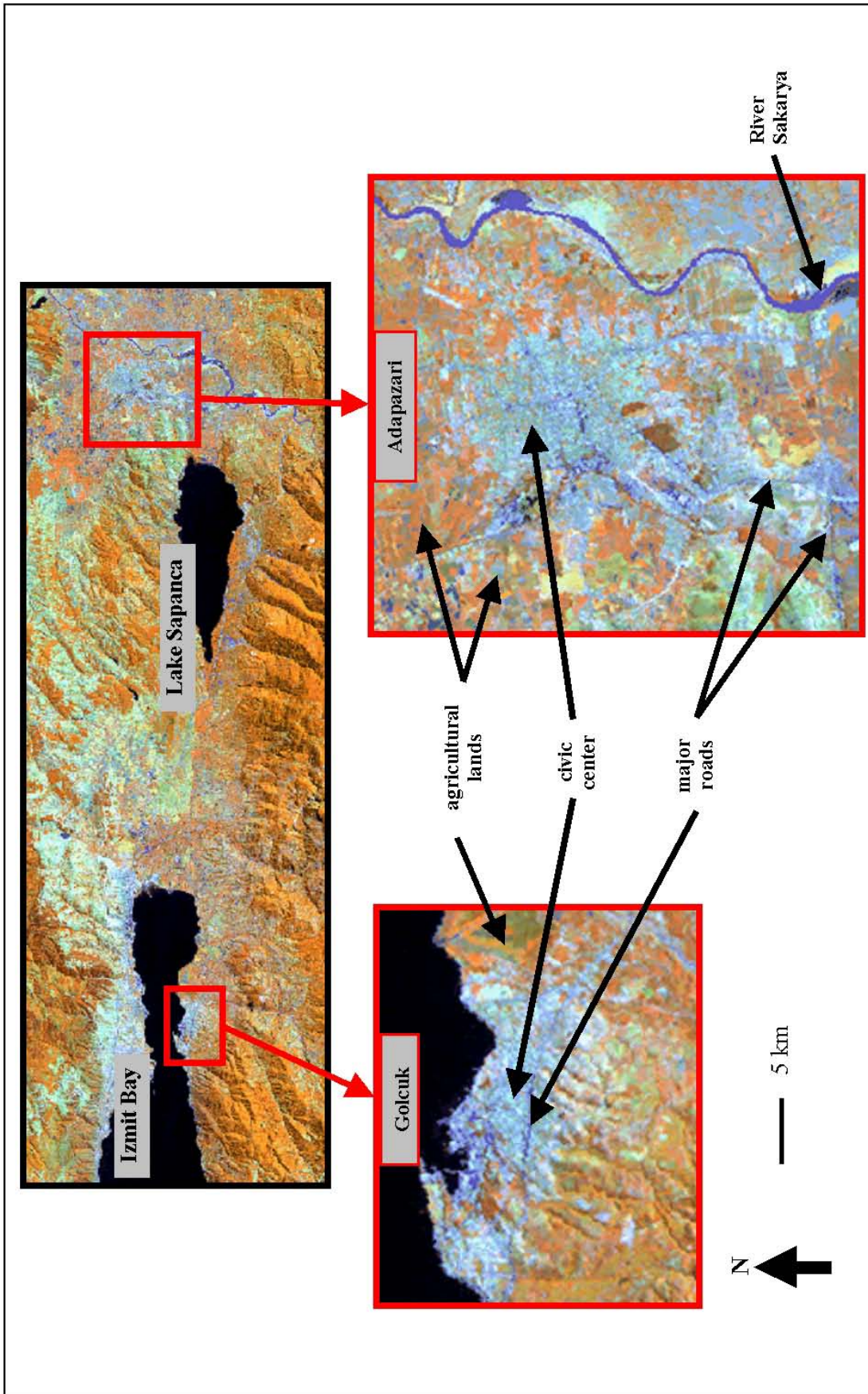


FIGURE 3-1 Landsat 5 RGB image (Red: band 4, Green: band 5, and Blue: band 3) acquired on August 18, 1999, covering Izmit Bay and Lake Sapanca – north-western Turkey near north Anatolian fault. Land use characteristics of the Golcuk and Adapazari study sites are shown (Data courtesy of ESA).

3.1.2 Adapazari

Adapazari is located 125 kilometers east of Istanbul, with a latitude and longitude of 40.78° and 30.40°, respectively. The area has a history of seismic activity (Homan and Eastwood, 2001), with large earthquakes occurring in 1894, 1943 and 1967 (Bray and Stewart, 2000). Within the province of Sakarya, Adapazari was most severely affected by the earthquake, with 27% of the building stock either severely damaged or destroyed by the event (Bray and Stewart, 2000). In portions of the city, as many as 70% of structures were severely damaged or collapsed (Aschheim, 2000). During the earthquake, surface rupture of up to 5.5m, intense ground motion and extensive liquefaction were experienced. The severity of damage may be traced to the location of this city (7km north of the fault rupture) and its position within a sedimentary basin of soft Holocene alluvium between two meandering rivers. While Adapazari originally had ~200,000 inhabitants, after the disaster, only 50,000-70,000 remained in the city (Webb, 2000). The Turkish Government reported that 20% of damaged structures were 3-5 story reinforced concrete and 56% 1-2 story timber/brick structures. (Bray and Stewart, 2000).

3.2 Ground Truth Data

In addition to the international emergency response teams dispatched to Turkey following the 1999 Marmara earthquake, research groups made reconnaissance trips to Golcuk and Adapazari, to record the location and severity of urban damage. The resulting information is published in several reports (AIJ, 2000; Youd *et al.*, 2000; EDM, 2000; Eguchi *et al.*, 2000b; MCEER, 2000). Selected datasets are employed for ground truthing purposes – using real observations and derived maps to assess the performance of damage detection methodologies. The main sources of ground truth data described further in the following sections comprise:

(1) Golcuk: Extensive surveys of building damage in the city, completed by The Architectural Institute of Japan (AIJ), in collaboration with Turkish Universities. Photographic record compiled by a multi-organizational team coordinated by R. Eguchi of ImageCat, Inc.

(2) Adapazari: Record of structural damage data compiled by the Turkish government, documented in Bray and Stewart (2000). Photographic record compiled by R. Andrews of Candle Corp. and a multi-organizational team coordinated by R. Eguchi of ImageCat, Inc.

3.2.1 Damage Observations

The photographic record introduced below, was acquired by the research team lead by R. Eguchi of ImageCat, Inc. Additional photographs were provided by R. Andrews of Candle Corp. This resource provides a useful overview of building damage sustained in urban areas of Golcuk and Adapazari. Quantitative measures of damage state used to produce the damage maps in Section 3.2.2 were based on observations similar to these.

The photo mosaic in Figure 3-2 demonstrates the extensive damage sustained throughout the Golcuk area. Aerial shots acquired from the window of a helicopter (Figure 3-2a-b) are indicative of the widespread and catastrophic collapse of apartment blocks. Prior to the earthquake event, these piles of rubble (see Figure 3-2c-e) were angular buildings, similar to the adjacent structures that are still standing. From a remote sensing perspective, destruction of this nature (which from Figure 3-2f is clearly not limited to apartment structures), has a strong spectral signature. In optical regions of the spectrum, it appears as a change in reflectance characteristics. Whereas roofing materials were the dominant feature recorded by the ‘before’ images, in instances where buildings collapsed during the earthquake, this signature is replaced by the comparatively bright white/gray reflectance characterizing piles of concrete. On SAR coverage, building collapse of this nature is recorded as a reduction in backscatter, as corner reflectors have been destroyed. The rough textured piles of rubble interact differently with the emitted SAR beam, acting as a diffuse scatterer. Partial roof collapse (Figure 3-2g) and tilting of structures (Figure 3-2h) should also produce changes in SAR return, as orientation relative to the platform is modified. In contrast, widespread pancaking (Figure 3-2h) that occurred where the lower floors collapsed because of insufficient shear strength and the upper layers fell down on top, is unlikely to be manifest in the optical/SAR coverage. In this instance, elevation data provided by SAR interferometry or lidar would be useful.

In addition to building damage, the earthquake caused several other forms of damage. Oil tanks ruptured at the Tupras refinery (Figure 3-2j), leaving fires burning. From Figure 3-26, the smoke that shrouded Golcuk for several days clearly affects the optical coverage. Had the smoke been thicker, the obscuring effect would have been more severe. Since active SAR sensors are unaffected by atmospheric pollutants, the signature of smoke is not evident in the ERS coverage.



FIGURE 3-2 Photo mosaic, showing damage sustained in Golcuk and surrounding areas, during the 1999 Marmara earthquake: (a-b) aerial view of extensive apartment collapse (Courtesy of R. Andrews); (c-e) ground-based perspective of debris piles accompanying apartment collapse; (f) damage sustained by other structures, such as a gas station. Building damage such as this is recorded as changes in optical and SAR remote sensing imagery, acquired before and after the earthquake.

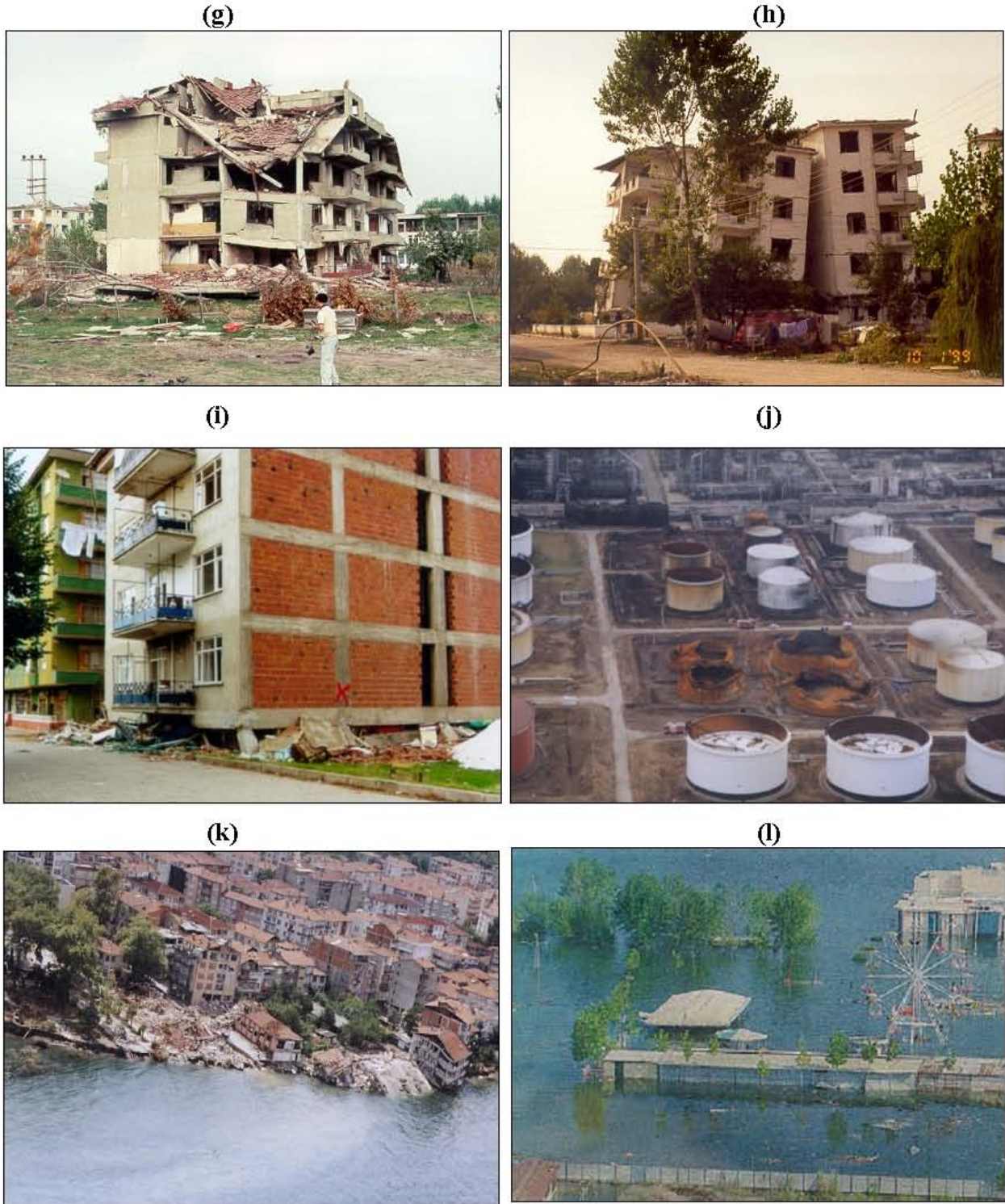


FIGURE 3-2 (cont.) Photo mosaic, showing damage sustained in Golcuk and surrounding areas, during the 1999 Marmara earthquake: (g) partial collapse with roof damage; (h) tilted housing structures; (i) pancaked first and second story; (j) aftermath of the burning Tupras oil refinery, which shrouded Golcuk for several days; and (k-l) zone of inundation by the Marmara Sea.

The earthquake also resulted in subsidence of land adjacent to the Marmara Sea. The effect of subsequent inundation within this area of Golcuk is depicted in Figure 3-2k-l. The fundamental difference between dry and inundated surface areas is likely to be manifested as an abrupt change in optical reflectance and radar backscatter between the ‘before’ and ‘after’ scenes.

The photo mosaic in Figure 3-3 illustrates the extensive urban damage that was experienced in Adapazari, due to the combined effects of ground shaking, liquefaction, and poor construction. Adapazari was among the most devastated locations, with severely damaged multi-story apartments. Figure 3-3a-b illustrates the extent of damage sustained. From a remote sensing perspective, buildings formerly appearing as strong corner reflectors on the SAR coverage are reduced to piles of rubble. Building debris is likely to appear brighter on the optical data, compared with non-damaged structures. As with Golcuk, a large number of concrete frame apartment buildings suffered partial to total collapse where the lower floor pancaked (Figure 3-3c). This soft first-story effect was also responsible for the presence of many tilted structures (Figure 3-3d-e). Tilting is more likely to be detected on SAR than optical coverage, since changes in orientation relative to the SAR sensor are strongly manifest in terms of backscatter. Since roof type and its reflectance characteristics remain constant, tilting is less likely to be recorded on the SPOT imagery. Finally, Figure 3-3f indicates that damage was not limited to residential areas. Here, the central pillars supporting a large temple collapsed, causing the structure to tilt and fall.

3.2.2 Damage Maps

For surveying damage in Golcuk, the AIJ team adopted a zone-based sampling strategy. As shown in Figure 3-4, administrative boundaries corresponding with the street network were used, effectively dividing the city into 70 survey regions. In a geospatial context, these polygons are treated as a ‘vector’ dataset. A building inventory survey was conducted within these areas. A number of attributes were recorded, including: building location; age; number of stories; and structure. However, for the present study, the most significant is damage level.

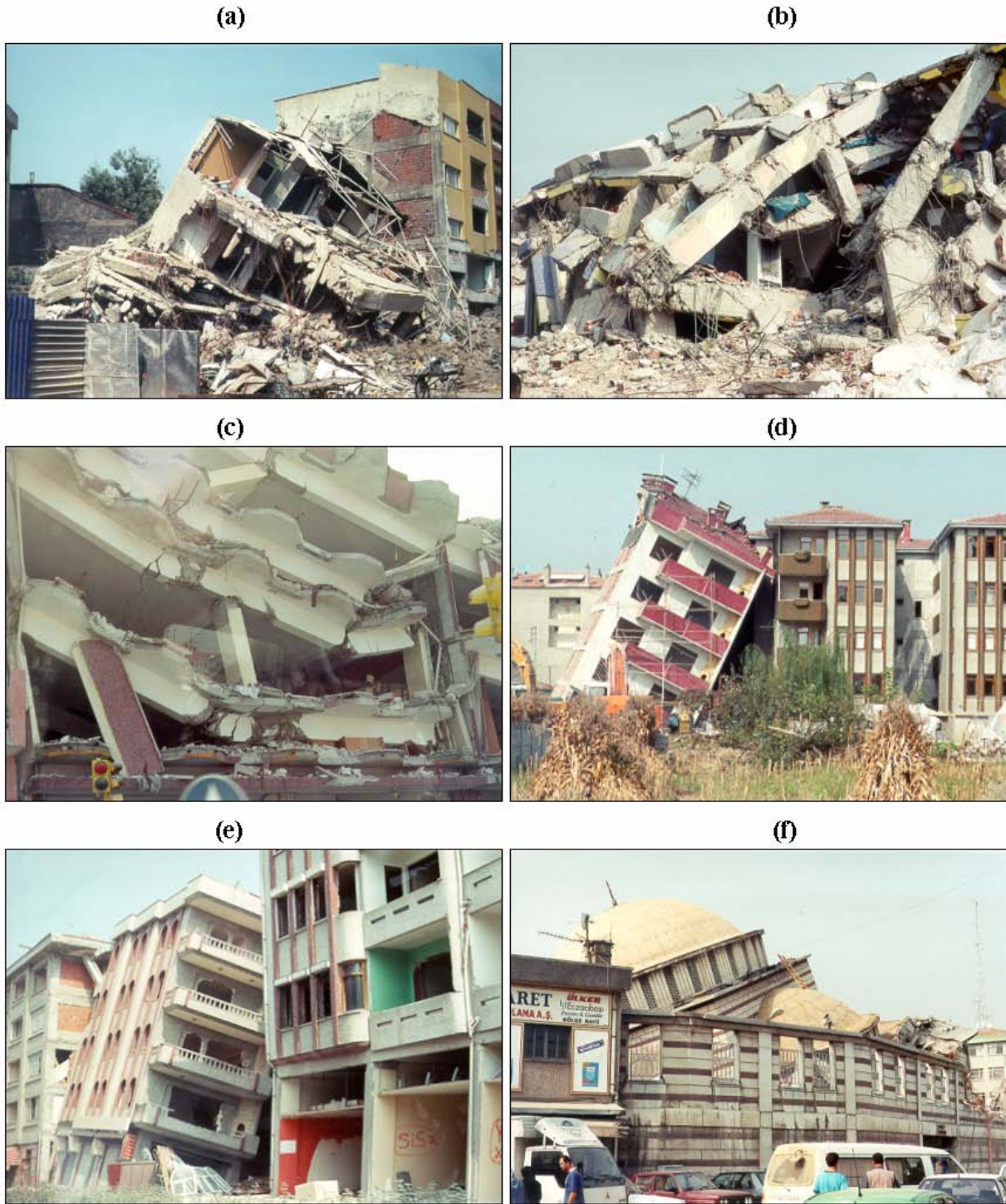


FIGURE 3-3 Photo mosaic, showing damage sustained in Adapazari during the Marmara earthquake: (a-b) extensive building collapse; (c) building collapse through pancaking of the floors; (d-e) severe tilting caused by collapse of the first floor; (f) building damage extends beyond residential structures to include religious centers. Building damage such as this is recorded as changes in optical and SAR remote sensing imagery, acquired before and after the earthquake.

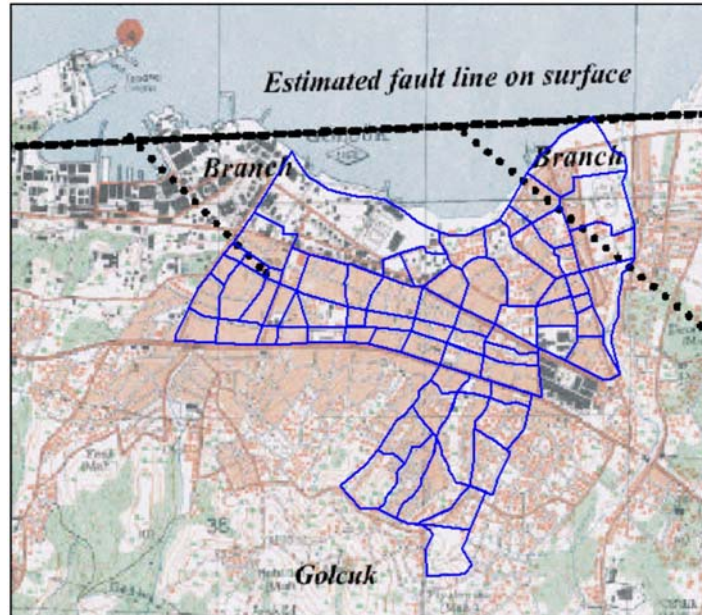


FIGURE 3-4 Map of Golcuk showing street network used as a basis for defining the 70 zones (shown in blue) employed in damage assessment.

The damage classification used by the AIJ team is a variation of the European Macro-seismic Scale (EMS98). As shown by Table 3-2, for masonry and reinforced concrete buildings, damage may fall into five categories:











- Grade 1: Negligible to slight damage
- Grade 2: Moderate damage
- Grade 3: Substantial to heavy damage
- Grade 4: Very heavy damage
- Grade 5: Destruction/collapse

The damage map in Figure 3-5 was created on the basis of 2746 buildings surveyed by AIJ (1999). This represents ~50% of the total sample. Various damage levels were observed in Golcuk. Approximately 13% of the buildings were classified as collapsed or near collapse. In turn, severely damaged buildings, including the collapsed structures, comprised some 16%. Damage rates for masonry were generally lower than for reinforced concrete. 25% of the medium-rise (four stories or higher) and 4% of low-rise (3 stories or lesser) buildings collapsed or were severely damaged (AIJ, 1999).

From the preceding photographic record, building *collapse* (Grade 5) leaves a strong visual signature on the urban landscape (see, for example, Figure 3-2a-e). This is to be expected given

the associated level of structural damage, as defined in Table 3-2. On the basis of corresponding definitions for lesser damage states, it is reasonable to assume that substantial, moderate and negligible damage (Grades 1-3) will record less pronounced signatures. From a remote sensing perspective, a number of authors (see Matsuoka and Yamazaki, 1998; Chiroiu and Andre, 2001 and Chiroiu *et al.*, 2002) observe that building collapse is more readily detected than these subordinate damage states. Consequently, the 70 polygons are classified and color-coded according to the percentage of collapsed buildings within the total set of observations. The class ranges follow a pseudo-exponential scale where ‘A’ relates to regions where 0-6.25% of buildings collapsed. ‘B’ indicates a range of 6.25-12.5%, while ‘C’ shows a range of 12.5-25%. ‘D’ reflects the severe case, where 25-50% of buildings collapsed. ‘E’ depicts the worst hit areas, where > 50% of observed buildings collapsed. In addition to this record of damage to the built environment, severe ground subsidence resulting in extensive flooding to the north-east of Golcuk is given a separate class ‘sunk’, denoted in blue.

**TABLE 3-2 Damage evaluation based on the European Macro-seismic Scale (EMS98).
(Courtesy of Architectural Institute of Japan (AIJ)).**

Classification of damage to masonry buildings		Classification of damage to buildings with reinforced concrete	
	Grade 1: Negligible to slight damage (no structural damage, slight non-structural damage) Hair-line cracks in very few walls. Fall of small pieces of plaster only. Fall of loose stones from upper parts of building in very few cases.		Grade 1: Negligible to slight damage (no structural damage, slight non-structural damage) Fine cracks in plaster over frame members or in walls at the base
	Grade 2: Moderate damage (slight structural damage, moderate non-structural damage) Cracks in many walls. Fall of fairly large pieces of plaster. Partial collapse of chimneys.		Grade 2: Moderate damage (slight structural damage, moderate non-structural damage) Cracks in columns and beams of frames and in structural walls. Cracks in partition and infill walls; fall of brittle cladding and plaster. Falling mortar from the joints of wall panels.
	Grade 3: Substantial to heavy damage (moderate structural damage, heavy non-structural damage) Large and extensive cracks in most walls. Roof tiles detach. Chimneys fracture at the roof line; failure of individual non-structural elements (partition, gable walls)		Grade 3: Substantial to heavy damage (moderate structural damage, heavy non-structural damage) Cracks in columns and beam column joints or frames at the base and at joints of coupled walls. Spalling of concrete cover buckling of reinforced rods. Large cracks in partition and infill walls, failure of individual infill panels.
	Grade 4: Very heavy damage (heavy structural damage, very heavy non-structural damage) Serious failure of walls; partial structural failure of roofs and floors.		Grade 4: Very heavy damage (heavy structural damage, very heavy non-structural damage) Large cracks in structural elements with compression failure of concrete and fracture of rebars; bond failure of beam reinforced bars; tilting of columns. Collapse of a few columns or of a single upper floor.
	Grade 5: Destruction (very heavy structural damage) Total or near total collapse.		Grade 5: Destruction (very heavy structural damage) Collapse of ground floor or parts (e.g. wings) of buildings.

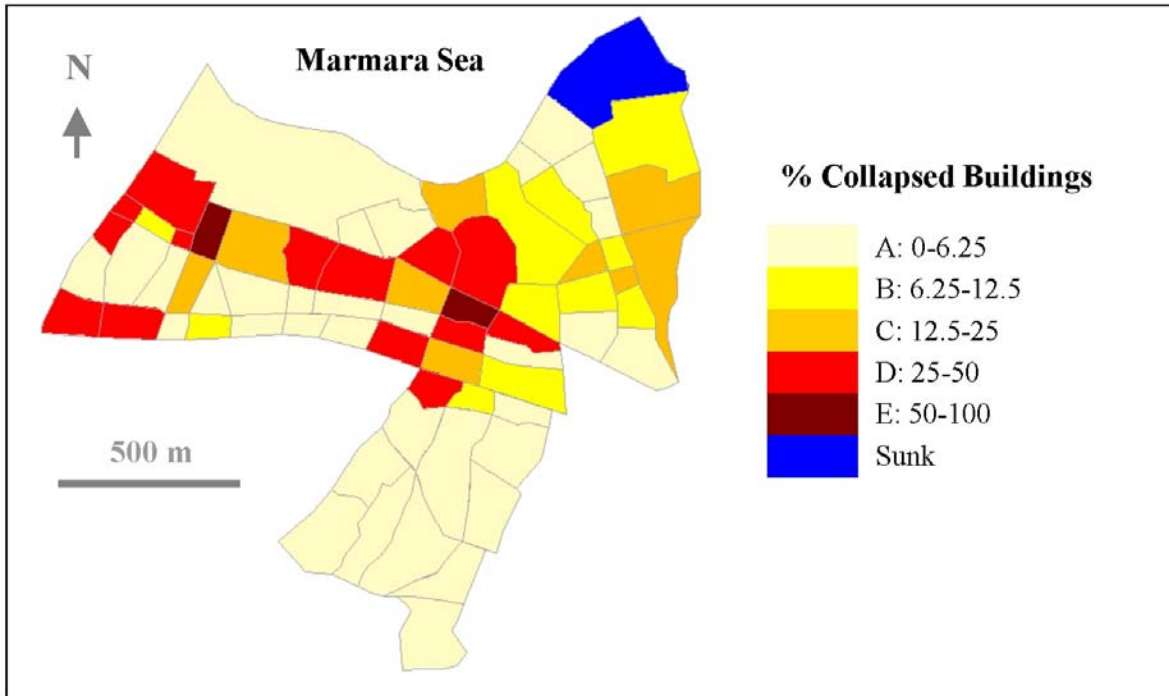


FIGURE 3-5 Map showing the surveyed area of building damage in Golcuk. The 70 sample areas are color-coded to represent the distribution of collapsed structures and location of subsided (sunk) area. (Data courtesy of AIJ, 1999).

Damage data compiled for Adapazari by the Turkish Government is presented in an aggregated form, divided into the 35 districts in Figure 3-6 that had been demarcated for planning purposes (see Bray and Stewart, 2000). Building damage within the central urban area is of particular interest. A subset of 16 zones relating to the civic center (see red vectors in Figure 3-7) is therefore carried forward to subsequent stages of the analysis. Surrounding zones, dominated by agricultural activity, are considered no further.

The survey employed a 4-level classification of building damage state, comprising:

- Grade 1: No damage
- Grade 2: Light damage
- Grade 3: Medium damage
- Grade 4: Collapse/heavy damage

To affirm the reliability of this dataset, a validation exercise was undertaken, using building damage observations recorded by the research team (Eguchi *et al.*, 2000). Figure 3-8 depicts the distribution of readings taken along streets throughout the civic center.

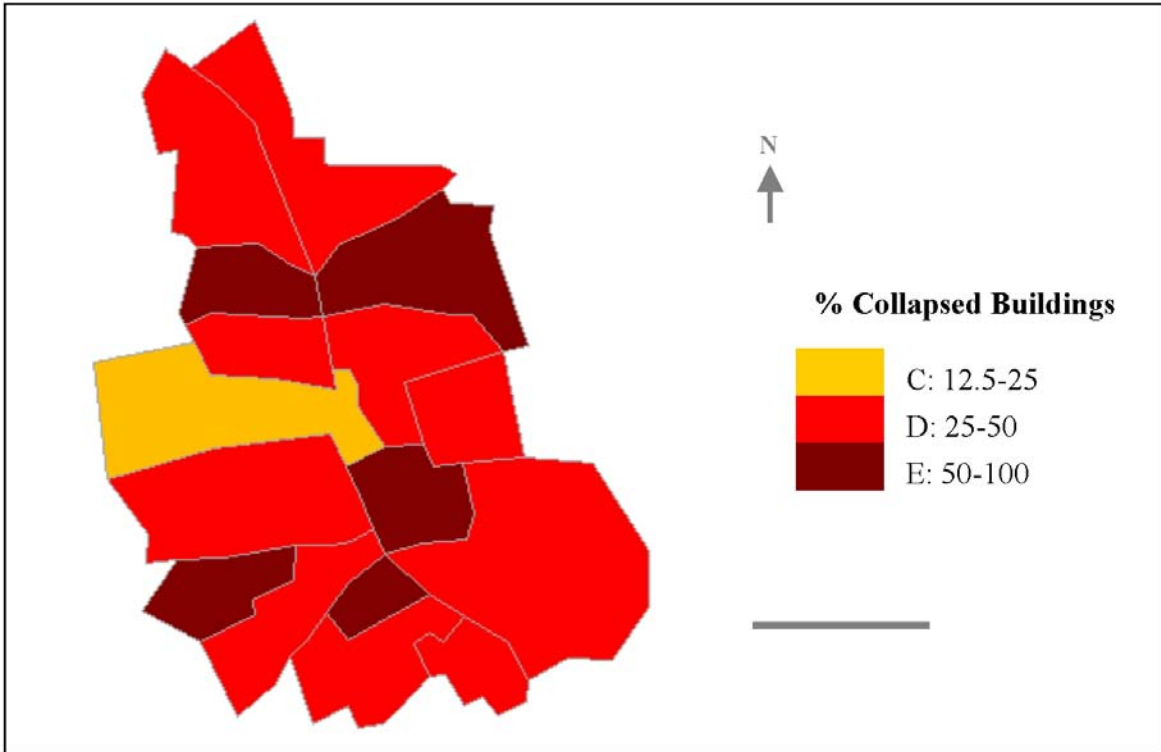


FIGURE 3-7 Map showing building damage in central Adapazari. The 16 sample areas defined by the Turkish Government are color-coded to represent the distribution of collapsed structures (based on data from Bray and Stewart, 2000).

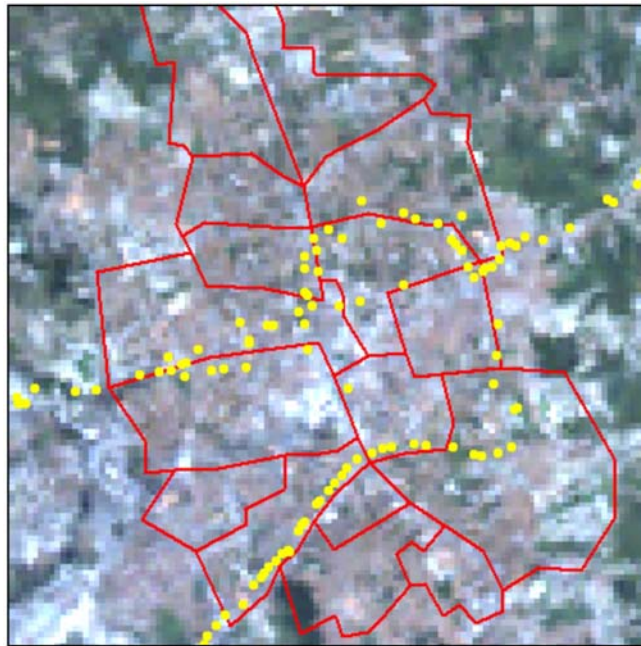


FIGURE 3-8 Adapazari building damage validation points (yellow), fused with a vector layer (red) showing the 16 Government-defined sample areas and Landsat 5 imagery.

3.3 SAR Remote Sensing

From the list of potential sensors in Table 2-1, ERS coverage was available for the Marmara earthquake (courtesy of the European Space Agency – ESA under a cooperative research agreement established after the 1999 Marmara, Turkey earthquake). The dataset includes imagery from both the ERS-1 and ERS-2 satellites, which operate in tandem. SAR data was acquired using the Active Microwave Instrument, which is a C-band (5.3 GHz) system. SLCI (Single Look Complex Image) coverage was obtained. These data are provided as two complex data streams, comprising ‘real’ and ‘imaginary’ components. Values are readily converted to the phase and magnitude of return (see Figure 2-2).

The ERS imagery has a nominal spatial resolution of 4m (along-track azimuth) by 20m (across-track range). It was acquired on two different dates ‘before’ (B1,B2) and ‘after’ (A1,A2) the earthquake. These datasets (see Table 3-3) were obtained at similar orbit positions and have the same frame number. The relative positions of the satellites, with respect to the ground surface below, results in short sensor baselines. This is advantageous because shorter baselines exhibit less baseline decorrelation. This is desirable for coherence, and although not undertaken here, interferometric studies. Furthermore, the acquisition of two ‘before’ images enables a baseline image to be produced, which could be used to normalize for extraneous (non-damage related) changes.

TABLE 3-3 Specification of SAR imagery acquired ‘before’ (B) and ‘after’ (A) the 1999 Marmara earthquake.

D	Acquisition Date	Satellite	Orbit	Frame	Coverage
B1	3/20/99	ERS 2	20459	2781	Golcuk/Adapazari
B2	4/24/99	ERS 2	20960	2781	Golcuk/Adapazari
A1	9/10/99	ERS 1	42637	2781	Golcuk/Adapazari
A2	9/11/99	ERS 2	22964	2781	Golcuk/Adapazari

The flowchart in Figure 3-9 summarizes the processing stages involved in implementing the change detection algorithm for ERS SAR data. The following section addresses key stages of pre-processing. The resulting intensity, coherence, correlation and power datasets are evaluated in Section 3.3.2 through Section 3.3.5, with a view to addressing Objective 1a (see Section 1) – characterizing the *location* of urban damage. The preliminary damage algorithms identified at the end of the flowchart, are presented in Section 4.

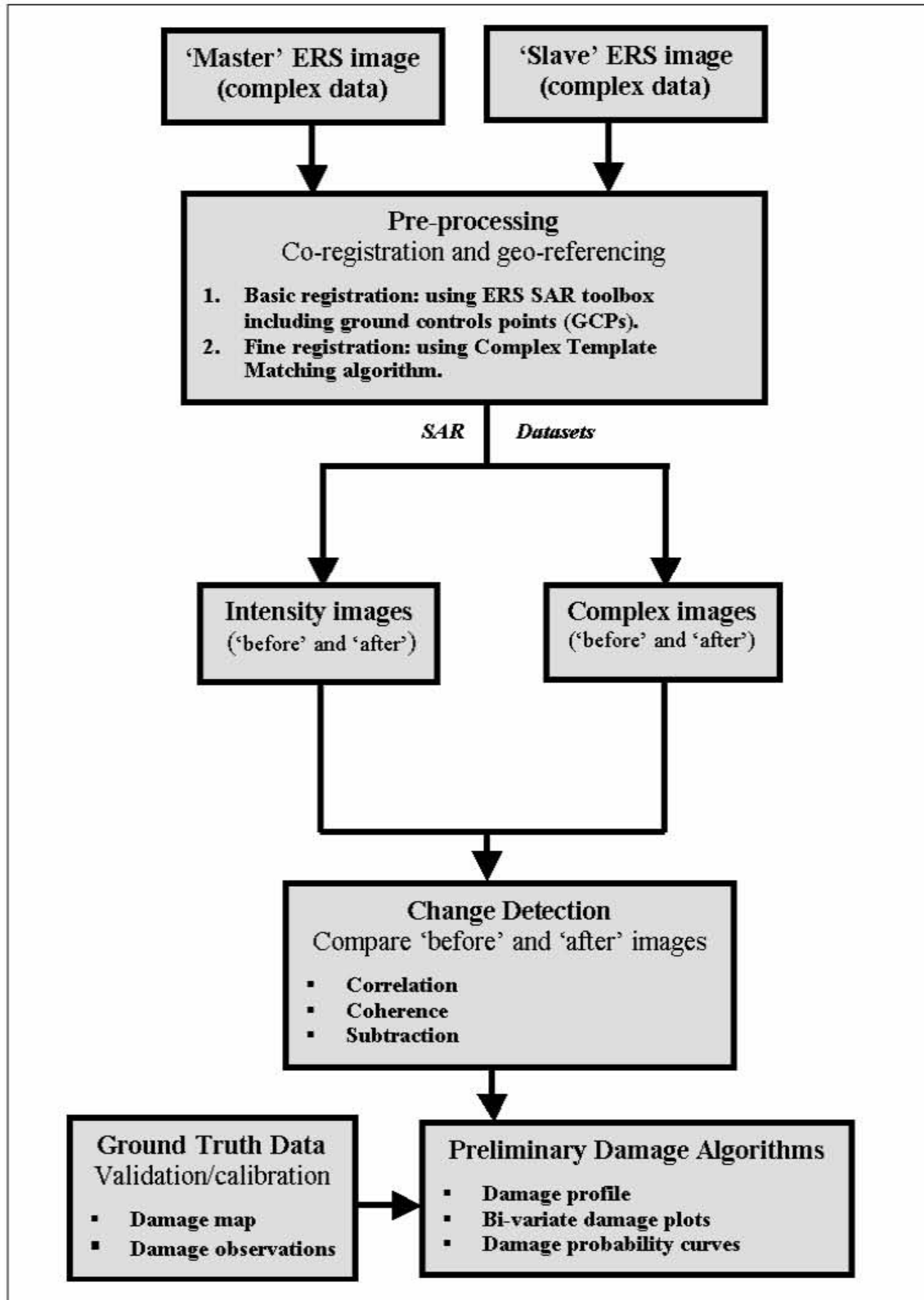


FIGURE 3-9 Flowchart summarizing processing stages involved in damage detection using ERS SAR data.

3.3.1 Pre-processing

The present change detection methodology is based on the use of multi-temporal remote sensing coverage, acquired ‘before’ and ‘after’ an earthquake event. In order to compare reflectance characteristics between scenes, acquired in this instance by ERS-1 and ERS-2, it is vital that they relate to the same geographic area. As described in Section 2.1.1, geometric inconsistencies are often present between images. These distortions are summarized below, followed by a comprehensive description of the steps taken to alleviate them during pre-processing.

To understand the nature of the geometric distortion present in SAR imagery, it is useful to establish sources of error as the imaging process unfolds. Errors are introduced in the range (across-track) and azimuth (along-track) during the basic imaging process. SAR systems operate by sending coherent signals and recording corresponding echoes. The range of the detected object is directly proportional to the time lapse between transmitting and receiving the signal. At a specific detection time, all signals with the same travel time/distance are assigned the same range. As shown by Figure 3-10, this results in circular distortion in the range direction, corresponding with lines of equidistance from the platform. In the azimuth direction, an accompanying parabolic distortion is exhibited, due to Doppler frequency shifts.

A number of geometric errors are introduced during data acquisition, which unless removed, may hinder the performance of damage detection algorithms. Significant processing errors relate to: (1) anomalous Doppler shift due to spacecraft attitude changes; (2) unreliable relative motion information (the Doppler rate), causing misregistration in the azimuth direction and blurred images; (3) the appearance of ‘ghosts’ where bright parts of an image are repeated at diminished intensity; (4) range migration due to rotation of the earth; and (5) minor altitude fluctuations. Look angle variations between different frames, relative frame shifts, earth model errors and global positioning errors may also introduce variations between the scenes.

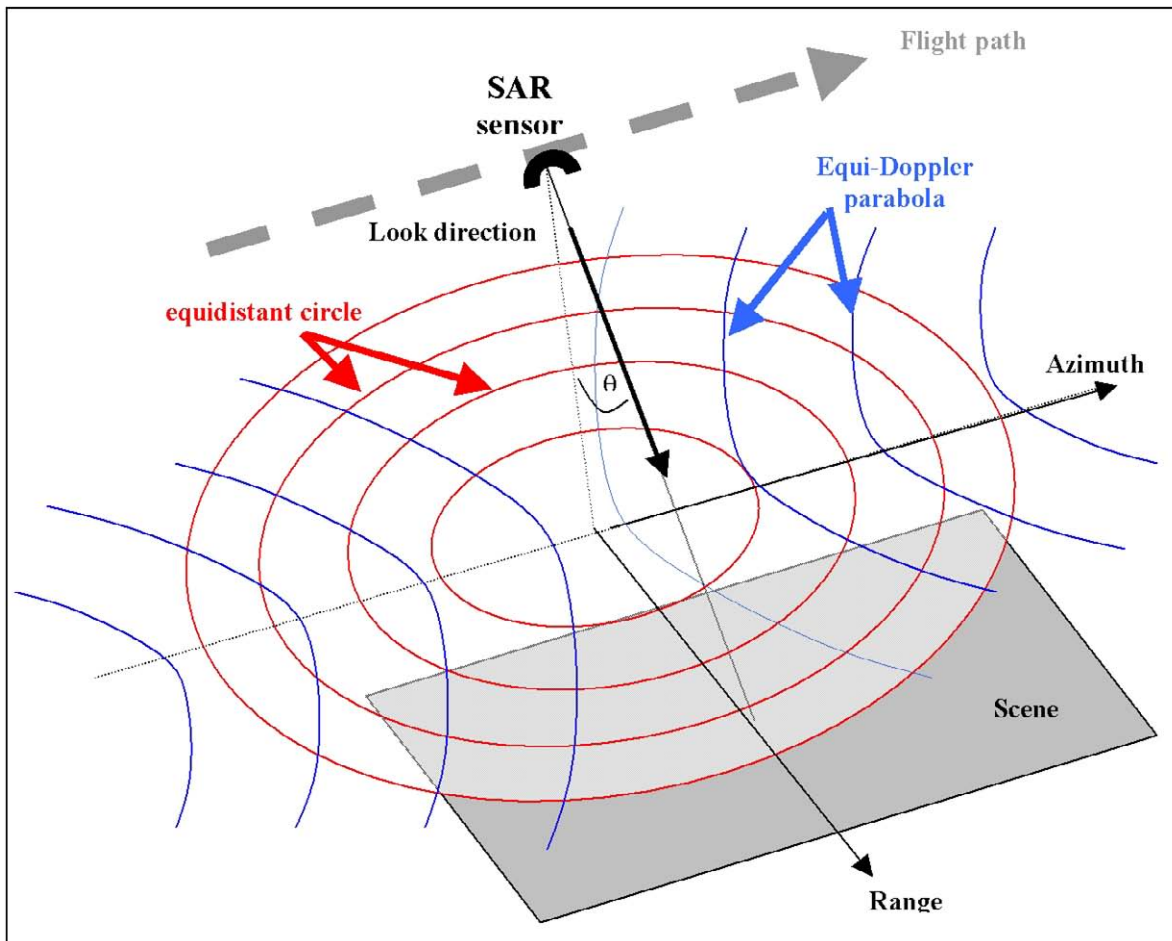


FIGURE 3-10 Internal geometric distortions inherent in the SAR imaging process (adapted from Elachi, 1987). Equidistant circles are mapped to the same range. Doppler shift separates cells in the azimuth direction.

Since coverage for the present study is far from nadir and limited in extent to a few kilometers, the SAR coordinate distortion is small between datasets acquired on different dates. Furthermore, the sources of error described above are well established and readily corrected using standard formulae. The ERS SLCI data had already been pre-processed to correct for these geometric distortions, and was delivered referenced with respect to the four corners and center geographic address of the scene. However, the complex data still requires proper geo-referencing, to determine the geographic coordinates of individual pixels. An initial coarse registration procedure geo-references the suite of images, by extracting the data for a designated area of interest and establishing a common coordinate system. This process was completed using a combination of ERS SAR Toolbox (Walker *et al.*, 1999, ESA, 2002), executable code provided by the European Space Agency (ESA) and ENVI (Environment for Visualizing Imagery)

software. SAR Toolbox code automatically extracted GCPs (in latitude and longitude), based on information about the satellite orbit parameters, together with a priori knowledge of latitude and longitude values and the extent of the scene. The imagery and GCPs were then exported to ENVI and registration performed. The resulting ERS scenes were posted at a spatial resolution of 4x20m.

Following this coarse registration, minor offsets are still present between the scenes. These are minimized by the second stage of registration fine tuning, using a complex template matching technique. For this purpose, a special software code was developed in Interactive Data Language (IDL) that performs minute relative horizontal and vertical shifts between a pair of SAR images. From the flow diagram in Figure 3-9, one complex image is designated the 'Master'. This dataset and its geographic attributes are treated as the reference, with no further adjustments made to the scene. The second image is designated the 'Slave'. For the present study, data acquired on 4-24-99 was consistently used as the Master, with remaining 3 dates becoming the Slaves. By shifting the Slave over the Master image at 1-pixel increments (in both horizontal and vertical directions), coherence values are computed within a sliding window. In this case, a 3x3 pixel window size was selected because: (1) preliminary tests indicate that a similar translation shift results for larger window sizes (5x 5, 7x7, and 9x9 were examined); (2) it is small enough for fast computation; and (3) it is large enough to be comparable with building sizes. A summation of coherence values $r_h > 0.5$ was then performed within the window, the best Master-Slave match occurring where the total is maximized.

Following the registration process, intensity difference, correlation, and coherence images were computed using the geo-referenced complex data. A 3x15 computation window, yielding a ground pixel size of 60x60m, was used to calculate correlation and coherence values. Finally, the output images were subset to smaller scenes, focusing on the study areas of Golcuk and Adapazari. Using ENVI software, the GCPs generated by SAR Toolbox were employed to extract and warp the datasets. These images were posted at 4x4 m resolution, and to ensure consistency, displayed using a common map projection (UTM zone 36) and datum (WGS-84).

To determine whether radiometric enhancement is likely to improve results obtained from SAR imagery, the influence of filtering and masking was tested for a sample of intensity and

correlation scenes. Preliminary findings indicate that Lee and median filters do little to improve the distinction between damage states. Masking out non-urban areas based on pixels identified in cross-power scenes proved to be problematic, because few pixels remained in some survey zones. Consequently, the datasets carried forward to subsequent stages of visualization and algorithmic development, received no further manipulation.

3.3.2 Intensity

Intensity images were derived from the pre-processed complex ERS SAR images (see Table 3-3) according to Equation 2-1. The 4x4m resolution datasets are displayed using a common map projection (UTM zone 36) and datum (WGS-84). The resulting ‘before’ and ‘after’ scenes for Golcuk and Adapazari are recorded in Figure 3-11 to Figure 3-14. To enhance visualization and enable a comparison to be drawn between brightness levels in the image sequence, the respective datasets are displayed using a radiometric contrast stretch. In the case of Golcuk, the accompanying histograms indicate that values are concentrated in the range $16 < I < 24$ DN. Linearly re-scaling these values across an 8-bit (0-255) grayscale range will significantly improve distinguishing capability. For Adapazari, the stretch spans $18 < I < 25$ DN.

Figure 3-11 depicts intensity responses for Golcuk, which are clearly subject to the speckle/noise that is typical of SAR data. Beyond this ‘salt and pepper’ effect, visual inspection of the study area indicates that at all dates, radar return is consistently high throughout the city center (denoted by the yellow vector overlay). The color intensity map in Figure 3-12 effectively illustrates this concentration of high return structures acting as corner reflectors. Central areas of the city appearing red (C1 in Figure 3-12a), have a particularly high return. Piers along the shoreline also exhibit a high radar return, looking bright in the grayscale and red in the color image. In contrast, flat surfaces, including the principal highway through the city, produce a low backscatter, and therefore look darker. In Figure 3-12, this low radar return (C2) is accentuated by reduced reflectance of the underlying SPOT scene. Less densely occupied areas and agricultural lands bordering the main civic center also record lower backscatter (C3), which in this instance, is due to the reduced number of corner reflectors. While return is generally lower across Izmit Bay, the intensified backscattering of turbulent waters in the upper part of Figure 3-11a-Figure 3-11d, suggests that SAR data are sensitive to wave scattering of the sea surface. In

visual terms, this signal is suppressed in the corresponding color overlay (C4), which is dominated by low reflectance in the SPOT coverage.

The intensity images for Adapazari (Figure 3-13) record a similar pattern of response. Throughout the central urban area, bright regions where return tends towards the maximum of $I=25$ DN, are synonymous with corner reflectors. The distribution of these features (C1) is presented as red and yellow responses in Figure 3-14. In this color composite, SAR coverage is fused with Landsat 5 imagery. The level of detail recorded by Landsat 5 is markedly reduced compared with the SPOT 4 Golcuk scene. The blocky appearance and difficulty distinguishing features such as roads (see, for example, C2) accompanies degradation in spatial resolution from 10m to 28.5m pixels. Areas exhibiting amplified return to the north of the urban center (C3), correspond with industrial premises. Returning to the grayscale images (Figure 3-13), a marked reduction in intensity towards the edge of the scene (see also C4) corresponds with agricultural land where corner reflectors are rare.

By drawing a visual comparison between the grayscale sequence of ‘before’ and ‘after’ scenes, in conjunction with the frequency histograms, it is possible to identify *scene-wide* trends. Throughout the urban areas of Golcuk and Adapazari, scene B1 is ubiquitously brighter than B2. From the corresponding histograms (Figure 3-11e-f and Figure 3-13e-f), in the former, a greater number of pixels fall towards the upper end of the DN scale. Histograms for the ‘after’ scenes (Figure 3-11g and Figure 3-11h) have a similar shape, but peak at a higher frequency. Overall, images A1 and A2 are generally brighter than those acquired before the earthquake. A fundamental offset between brightness levels in images acquired on different dates may arise for a number of reasons. It may reflect the temporal interval between data acquisition. In the case of B1 and B2, this is approximately 1 month; for A1 and A2 just one day. Changes in ambient conditions, such as atmospheric diffusion, may vary considerably over these time spans. Alternatively, the offset may be systematic, arising from variations in sensor incidence angle. *Localized* changes between the ‘before’ and ‘after’ datasets are more difficult to establish from visual inspection alone, due to high levels of noise inherent in the data. In theory, these should be more readily discerned using measures of change, such as intensity difference, correlation and coherence, the characteristics of which are documented in the following sections.

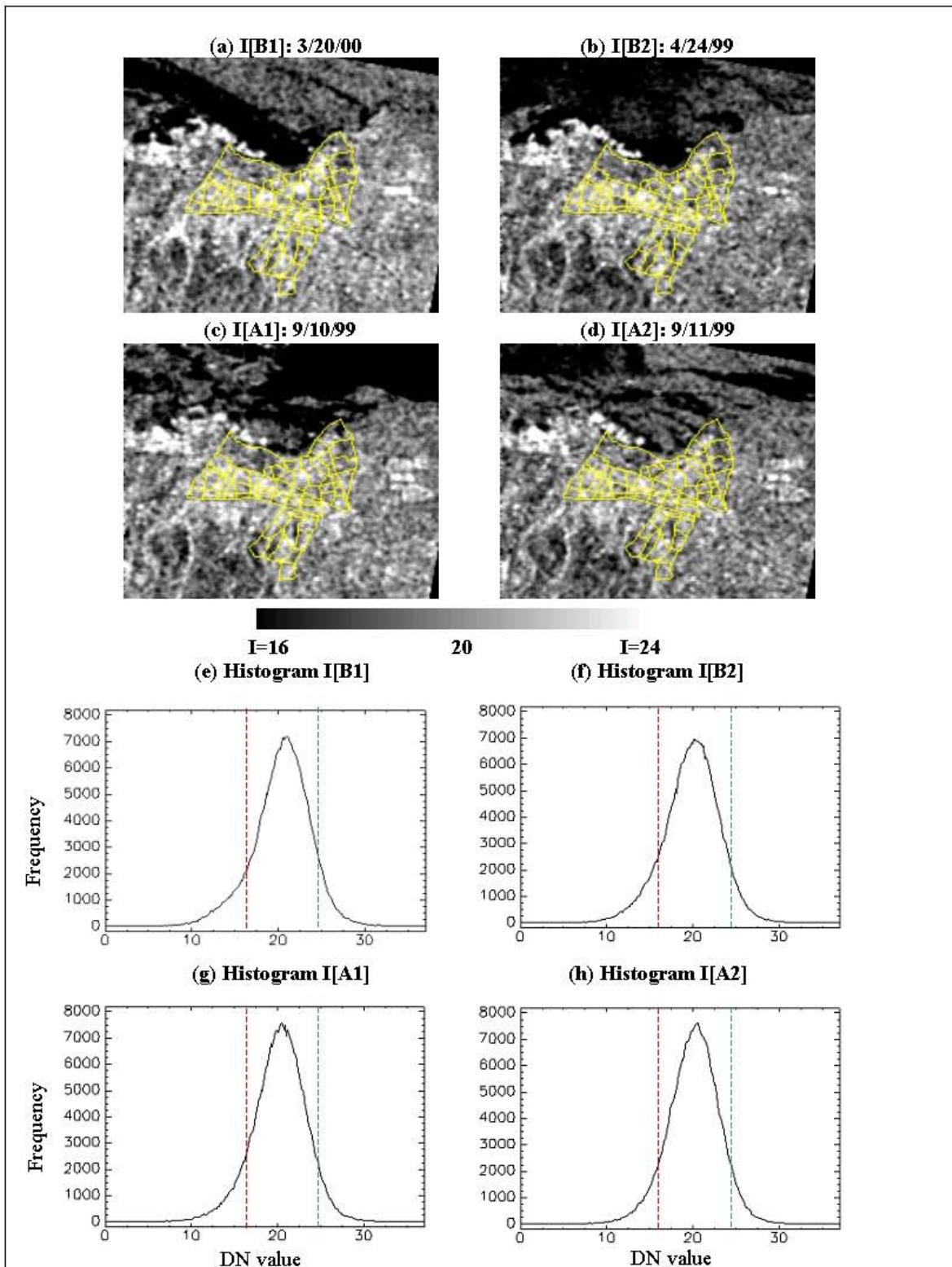


FIGURE 3-11 SAR intensity data for Golcuk, showing images ‘before’ (a-b) and ‘after’ (c-d) the Marmara earthquake, displayed using a linear contrast stretch from $16 < I < 24$ to optimize visual interpretation of features within the scene. Image histograms (e-h) record DN value distribution within the 70 zones. (Data courtesy of ESA).

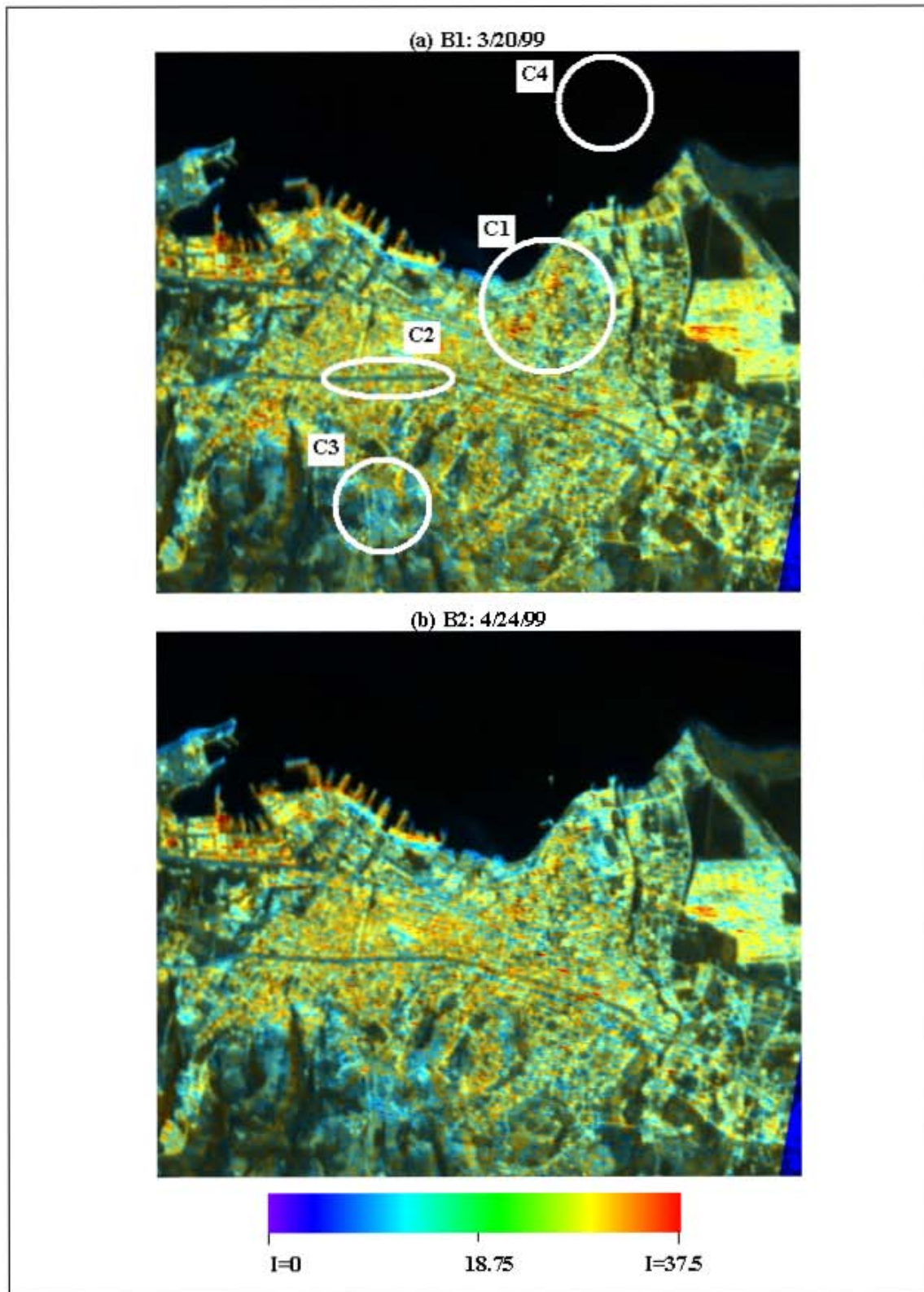
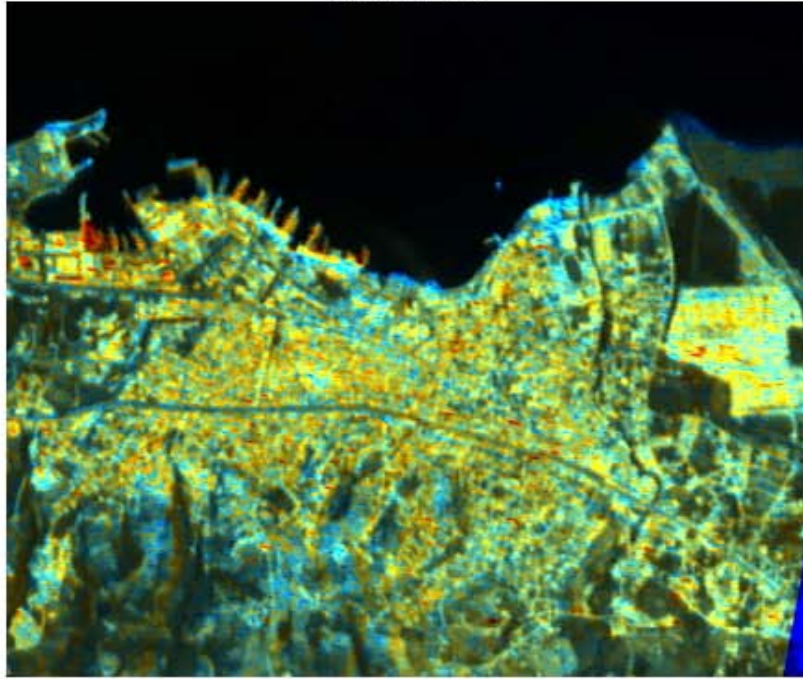


FIGURE 3-12 SAR intensity data for Golcuk acquired ‘before’ and ‘after’ the 1999 Marmara earthquake, fused with SPOT 4 panchromatic imagery. (Data courtesy of ESA and NIK). See text for explanation of symbols C1-C5.

(c) A1: 9/10/99



(d) A2: 9/11/99

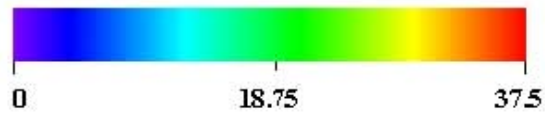
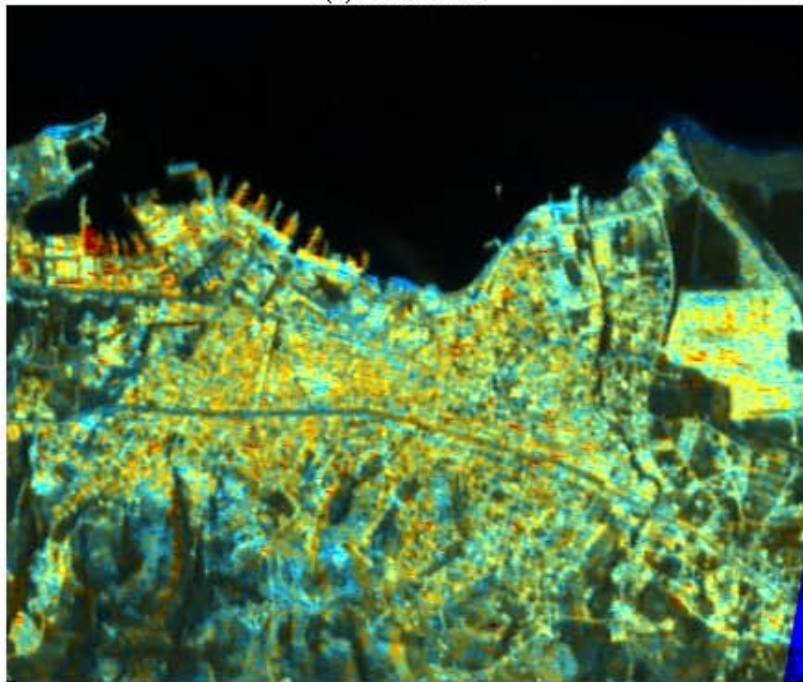


FIGURE 3-12 (cont.) SAR intensity data for Golcuk acquired ‘before’ and ‘after’ the 1999 Marmara earthquake, fused with SPOT 4 panchromatic imagery.

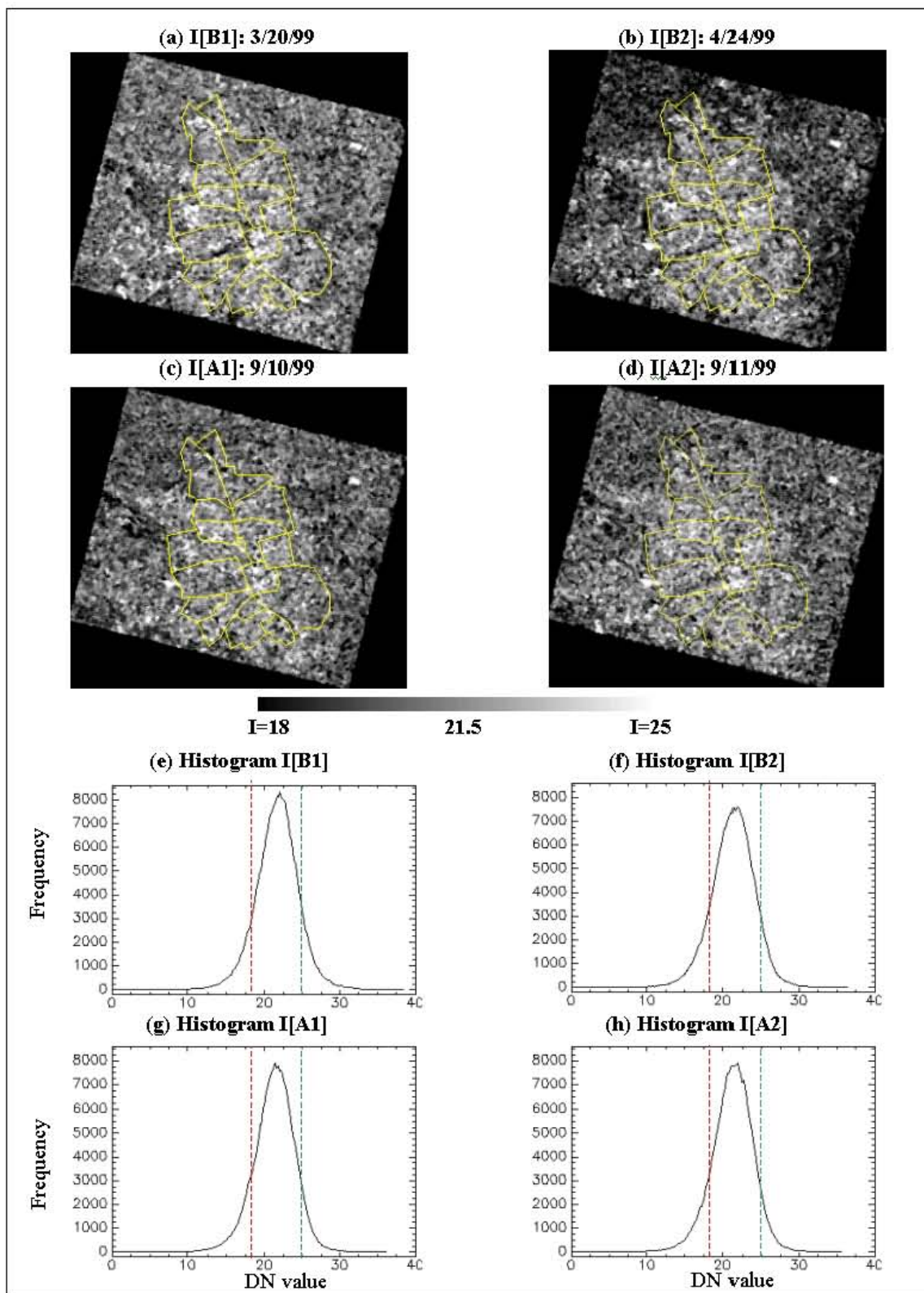


FIGURE 3-13 SAR intensity data for Adapazari, acquired ‘before’ (a-b) and ‘after’ (c-d) the Marmara earthquake, displayed using a linear contrast stretch $18 < I < 25$. Image histograms (e-h) record DN value distribution within the 16 zones. (Data courtesy of ESA).

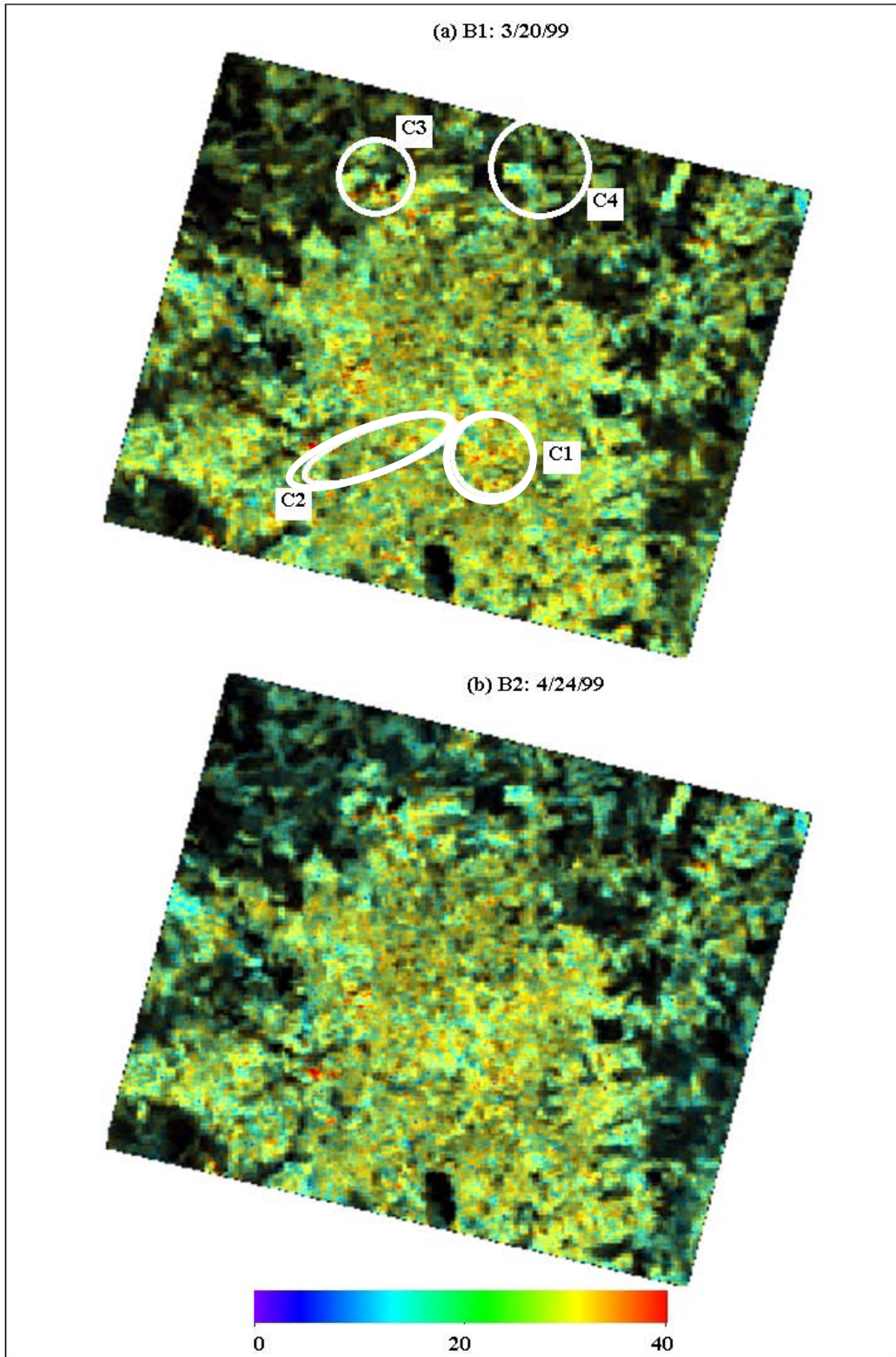


FIGURE 3-14 SAR intensity data for Adapazari acquired ‘before’ and ‘after’ the 1999 Marmara earthquake, fused with Landsat 5 imagery (Data courtesy of ESA and NIK). See text for explanation of symbols C1-C4.

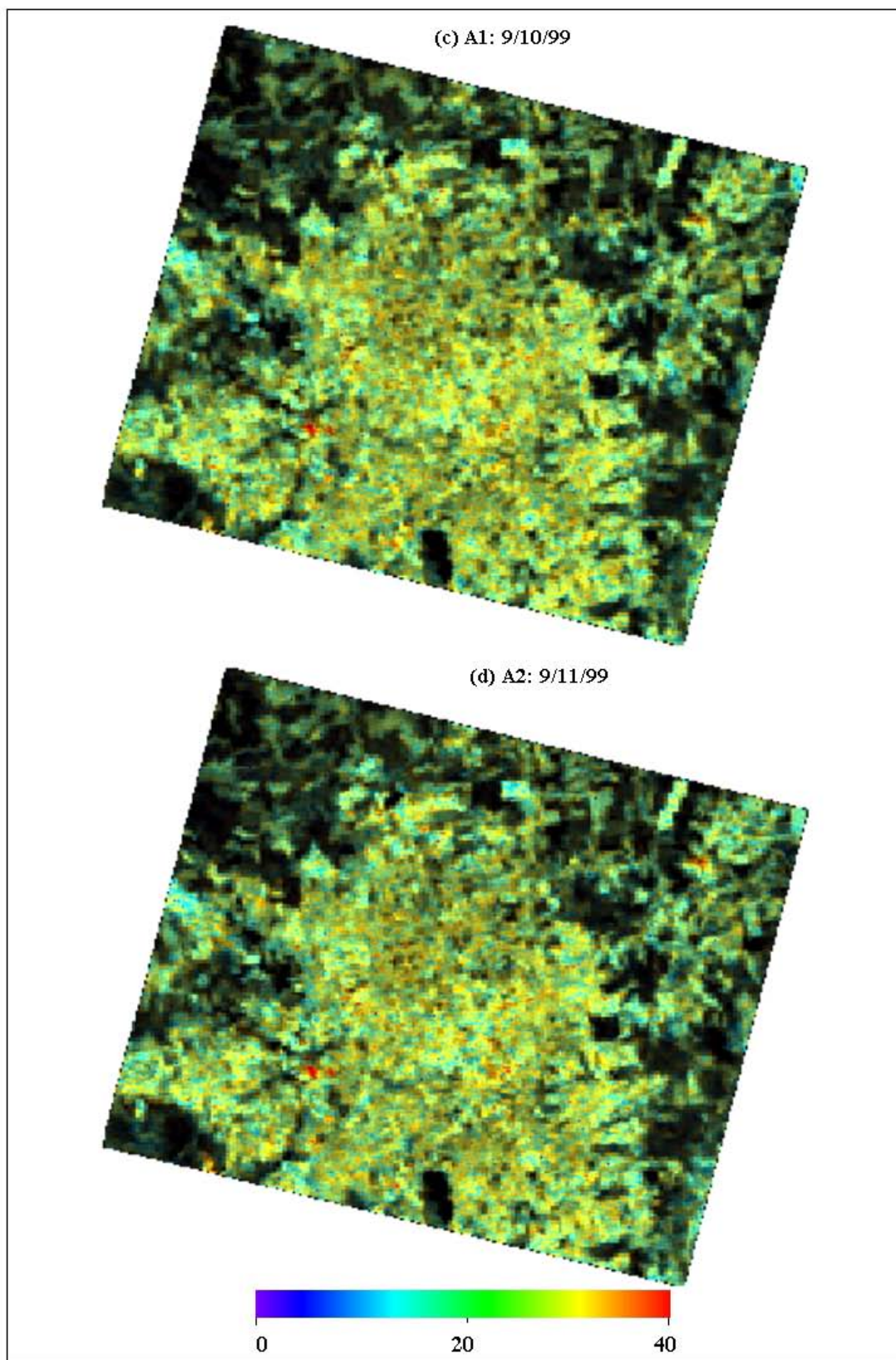


FIGURE 3-14 (cont.) SAR intensity data for Adapazari acquired ‘before’ and ‘after’ the 1999 Marmara earthquake, fused with Landsat 5 imagery.

3.3.3 Intensity Difference

The difference between intensity values recorded ‘before’ and ‘after’ the earthquake is a potentially useful qualitative measure for the damage detection algorithms in Section 4.1. A range of image pairings is possible, given the availability of several ‘before’ (B) and ‘after’ (A) scenes (see Table 3-3). For straightforward change, these permutations include: dif[B1,A1]; dif[B1,A2]; dif[B2,A1]; and dif[B2,A2] (for details of notation, see Figure 2-7). As discussed in Section 2.2, these pairings may be compared with baseline images, such as dif[B1,B2] or dif[A1,A2], in order to assess the influence of non earthquake-related change.

Difference values were computed by basic subtraction of the intensity images, posted at 4x4m resolution and projected to the standard map coordinate system (UTM zone 36 and datum WGS-84). The results for Golcuk and Adapazari in Figure 3-15 and Figure 3-16 are displayed using a linear contrast stretch across the range $-2 < \text{dif} < 6$ DN. In all cases, the difference images are subject to considerable noise. Viewing the difference data at a pixel level, it is difficult to discern scene-wide trends between the ‘before’-‘after’ and baseline pairings, or localized patterns in response that may be attributed to building damage. Improved distinguishing potential may accompany aggregation of the data at a coarser spatial scale. This is investigated further through the use of zone-based damage profiles in Section 4. From the frequency histograms in Figure 3-15g,h and Figure 3-16g,h, difference values are concentrated around zero. Unlike optical imagery where seasonal effects are a major cause of temporal variations (see Section 3.4.3), these difference images exhibit limited sensitivity to factors responsible for changes in radar return, such as surface texture, material type and sensor look angle.

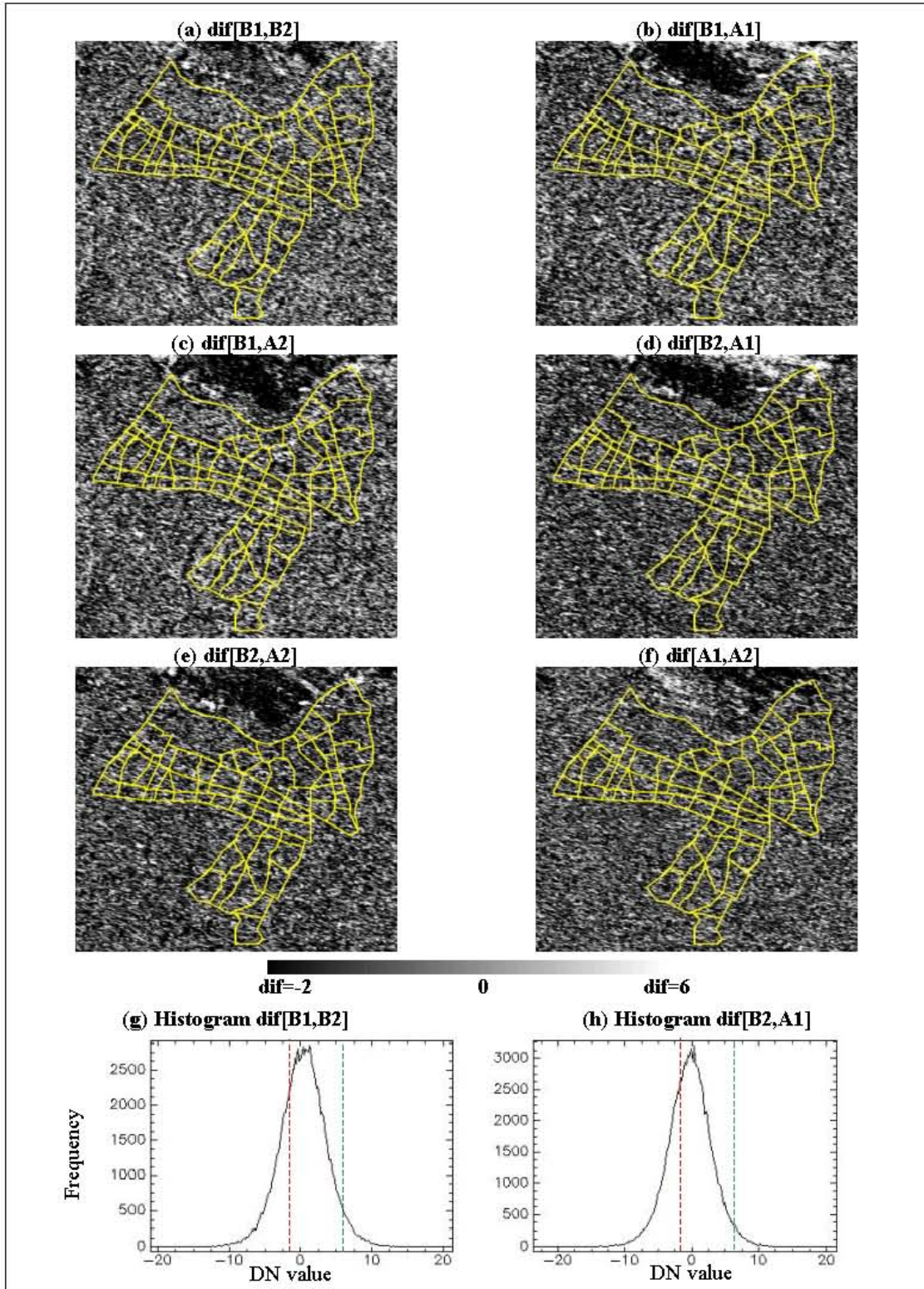


FIGURE 3-15 SAR intensity difference maps for Golcuk: (a-f) baseline; and (b-e) ‘before’-‘after’ pairings. Image B1 was acquired on 3/20/99, B2 on 4/24/99, A1 on 9/10/99 and A2 on 9/11/99. Bright areas represent positive and dark areas negative differences. Image histograms (g-h) record the DN value distribution within the 70 zones.

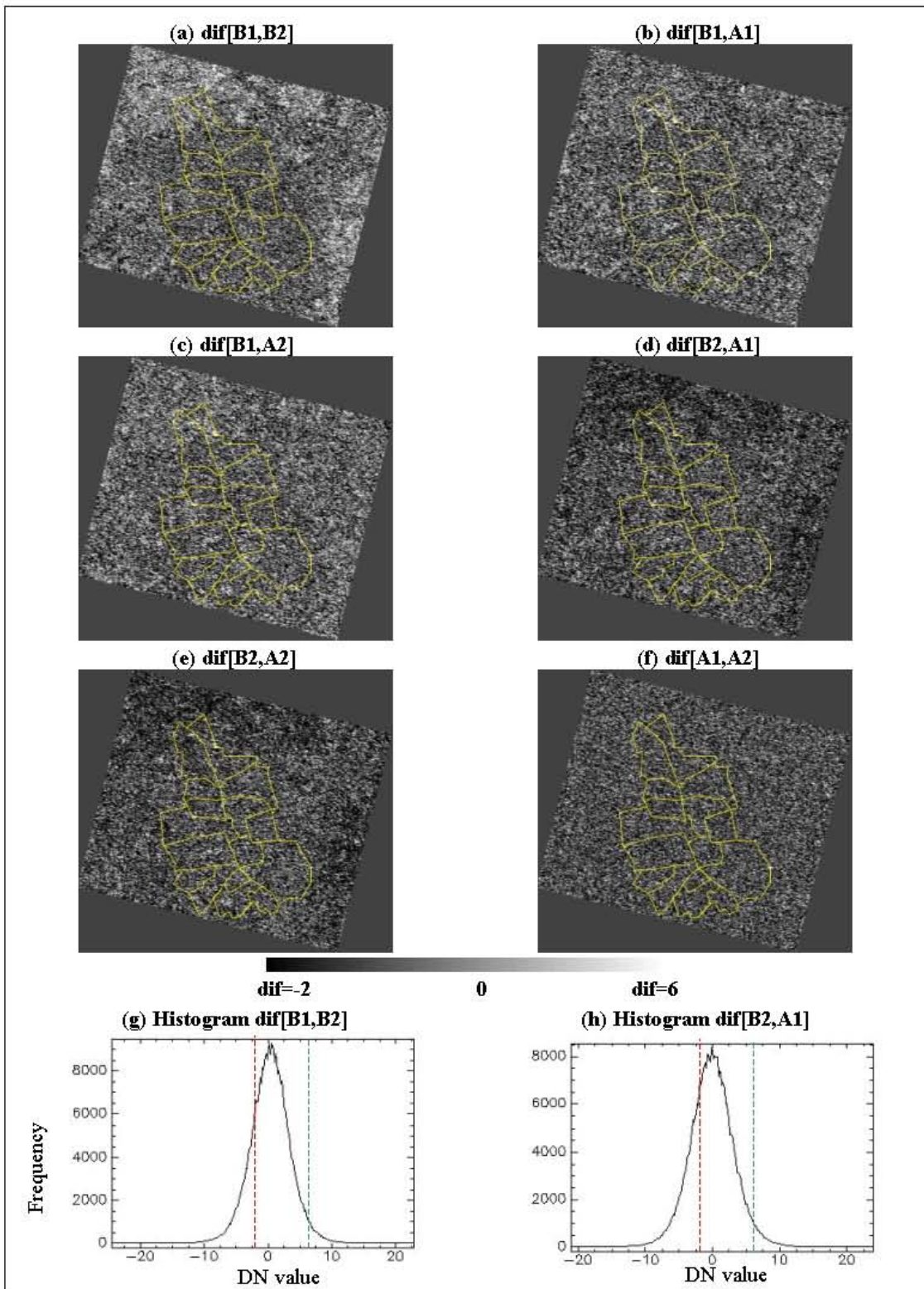


FIGURE 3-16 SAR intensity difference maps for Adapazari: (a-f) baseline; and (b-e) ‘before’-‘after’ pairings. Image B1 was acquired on 3/20/99, B2 on 4/24/99, A1 on 9/10/99 and A2 on 9/11/99. Bright areas represent positive and dark areas negative differences. Image histograms (g-h) record the DN value distribution within the 16 zones.

3.3.4 Correlation

The correlation between pairs of SAR intensity images is a potentially useful measure of temporal changes that can be used to locate earthquake building damage. Given the availability of several ‘before’ (B) and ‘after’ (A) scenes (see Table 3-3), a range of pairings is possible. For straightforward change between pre- and post-earthquake scenes, permutations include: $\text{cor}[B1,A1]$; $\text{cor}[B1,A2]$; $\text{cor}[B2,A1]$; and $\text{cor}[B2,A2]$. As discussed in Section 2.2, these pairings may also be compared with baseline scenarios, such as $\text{cor}[B1,B2]$ or $\text{cor}[A1,A2]$, which establish the nature of non-earthquake related changes.

Correlation analysis is performed here using several different techniques (see also Section 2.2): (1) sliding window-based correlation; and (2) block statistics. For the former window-based correlation, a sliding window of 3x15 pixels was selected. Given the pre-sampling spatial resolution of 20m across-track and 4m along-track, this relates to a square area of 60x60m, which is comparable with the scale of urban features, such as apartment buildings. Datasets resulting from this computation were posted at 4x4m resolution and projected to the standard map coordinate system (UTM zone 36 and datum WGS-84). For the latter approach, block correlation statistics were computed for the resampled 4x4m intensity scenes within a 40x40 pixel window. All pixels within these 160x160m blocks assume the resultant correlation value r_b .

Figure 3-17 and Figure 3-18 depict Golcuk and Adapazari correlation maps, produced by the sliding window-based approach, for all possible pairings of B and A. For visualization purposes, results for both cities have been thresholded at $0.2 < r_c < 0.6$. All intermediate values are displayed in an 8-bit grayscale (0-255) range, using a linear contrast stretch. The histograms in Figure 3-17g,h and Figure 3-18g,h indicate that this method of display spans only part of the full dynamic range of responses. Excluded values towards the lower end of the scale were found to correspond with background noise, and backscatter from other regions of the image, such as the surrounding rural belts, which are less relevant to the present study.

Figure 3-17a,f and Figure 3-18a,f show baseline values for Golcuk and Adapazari, where changes are attributable to extraneous effects (see also Section 3.3.3), rather than earthquake damage. In general terms, the scenes are brighter and sliding window-based correlation values

(r_c) higher than in the ‘before’-‘after’ pairings. The concentration of higher correlation values is due to the reduced temporal interval between the data sets (see Table 3-3). Of the baseline pairings, $\text{cor}[A1,A2]$ is brighter, with time lag of just 1 day. The input data for $\text{cor}[B1,B2]$ were acquired approximately 1 month apart. In comparison, the ‘before’-‘after’ pairings in Figure 3-17b-e and Figure 3-18b-e look relatively dark. As such, correlation levels are generally lower than in the baseline responses. Although there are scattered areas where r_c remains high, low correlation is evident throughout central urban areas, where building damage was sustained. Low correlation in rural areas is indicative of extraneous changes in ground surface return and systematic variations between sensor configurations at the time of imaging.

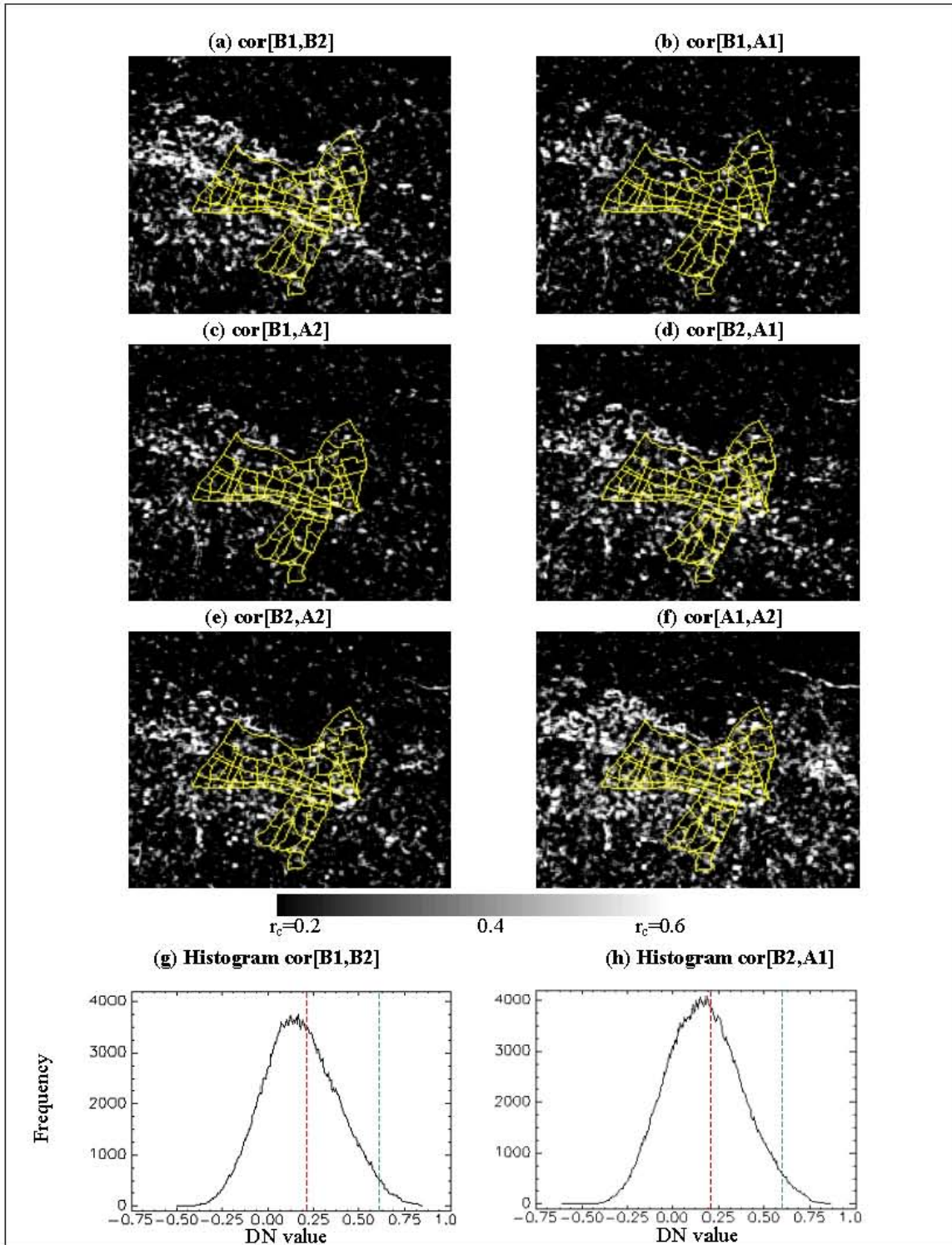


FIGURE 3-17 SAR sliding window-based intensity correlation maps, for Golcuk: (a,f) baseline; and (b-e) ‘before’-‘after’ pairings. Image B1 was acquired on 3/20/99, B2 on 4/24/99, A1 on 9/10/99 and A2 on 9/11/99. Bright areas record a high positive correlation, while dark areas denote low correlation and inconsistency between the scenes. Image histograms (g-h) show the distribution of DN values within the 70 zones.

Results obtained using block statistics are presented in Figure 3-19 and Figure 3-20, overlaid with base maps of the respective urban areas. The blocky appearance is due to the 160x160m unit of aggregation. Although preliminary tests suggested that this block size provides optimal distinguishing potential between building damage states, it is approaching the minimum area coverage of certain zones in Golcuk. For these smaller sample areas there is no guarantee that the block will fall centrally and any offset may compromise the accuracy of results.

For the present study, block values have been classified into classes of: low ($0 < r_b < 0.2$); moderate ($0.2 < r_b < 0.4$); high ($0.4 < r_b < 0.6$); and very high ($r_b > 0.6$) correlation. Several broad generalizations are warranted for the Golcuk and Adapazari results. First, block correlation values are typically higher than those obtained using the sliding window-based approach. This is due to the smoothing effect created by the larger sample area. Second, block correlation levels within the urban areas of both cities are consistently higher in the baseline scenes, compared with the 'before'-'after' permutations. This demonstrates that decorrelation accompanying the earthquake is considerable, compared with changes caused by extraneous baseline factors.

With emphasis on the *localized* characteristics of the datasets, a number of blocks within the civic centers of Golcuk and Adapazari record particularly low correlation for all combinations of B and A (see symbol C1 Figure 3-19b-e and Figure 3-20b-e). Comparison with the damage maps in Figure 3-5 and Figure 3-7 suggests that these low values coincide with building damage caused by the earthquake. In Golcuk, low correlation outside the urban area is concentrated around Izmit Bay (C2), where changing conditions of the water surface causes pronounced differences in backscatter. For Adapazari, low correlation is also recorded in rural areas, where agricultural activity may be responsible for seasonal changes in ground texture and material.

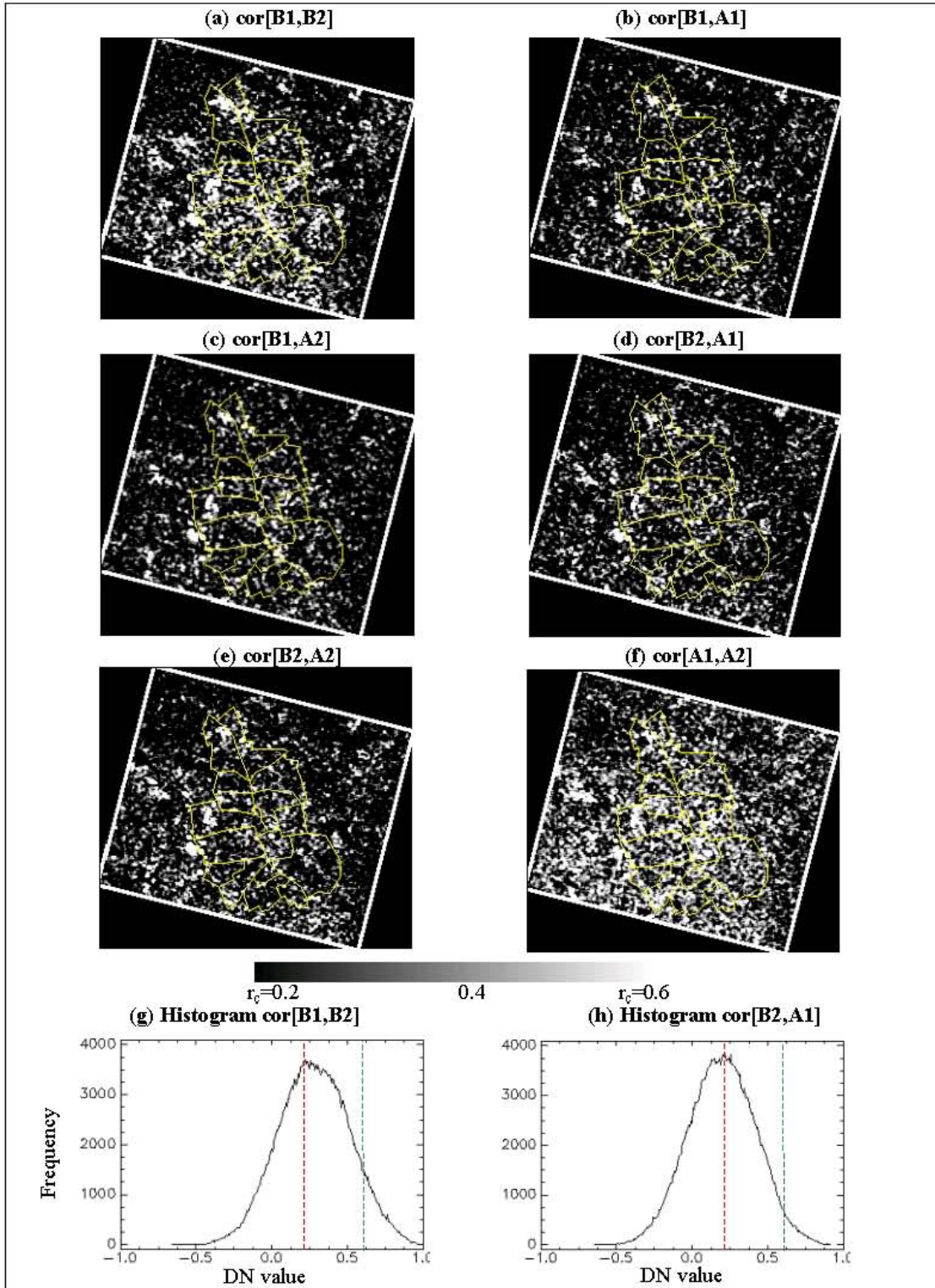


FIGURE 3-18 SAR sliding window-based intensity correlation maps, for Adapazari: (a,f) baseline; and (b-e) ‘before’-‘after’ pairings. Image B1 was acquired on 3/20/99, B2 on 4/24/99, A1 on 9/10/99 and A2 on 9/11/99. Bright areas record a high positive correlation, while dark areas denote low correlation and inconsistency between the scenes. Image histograms (g-h) show the distribution of DN values within the 16 zones.

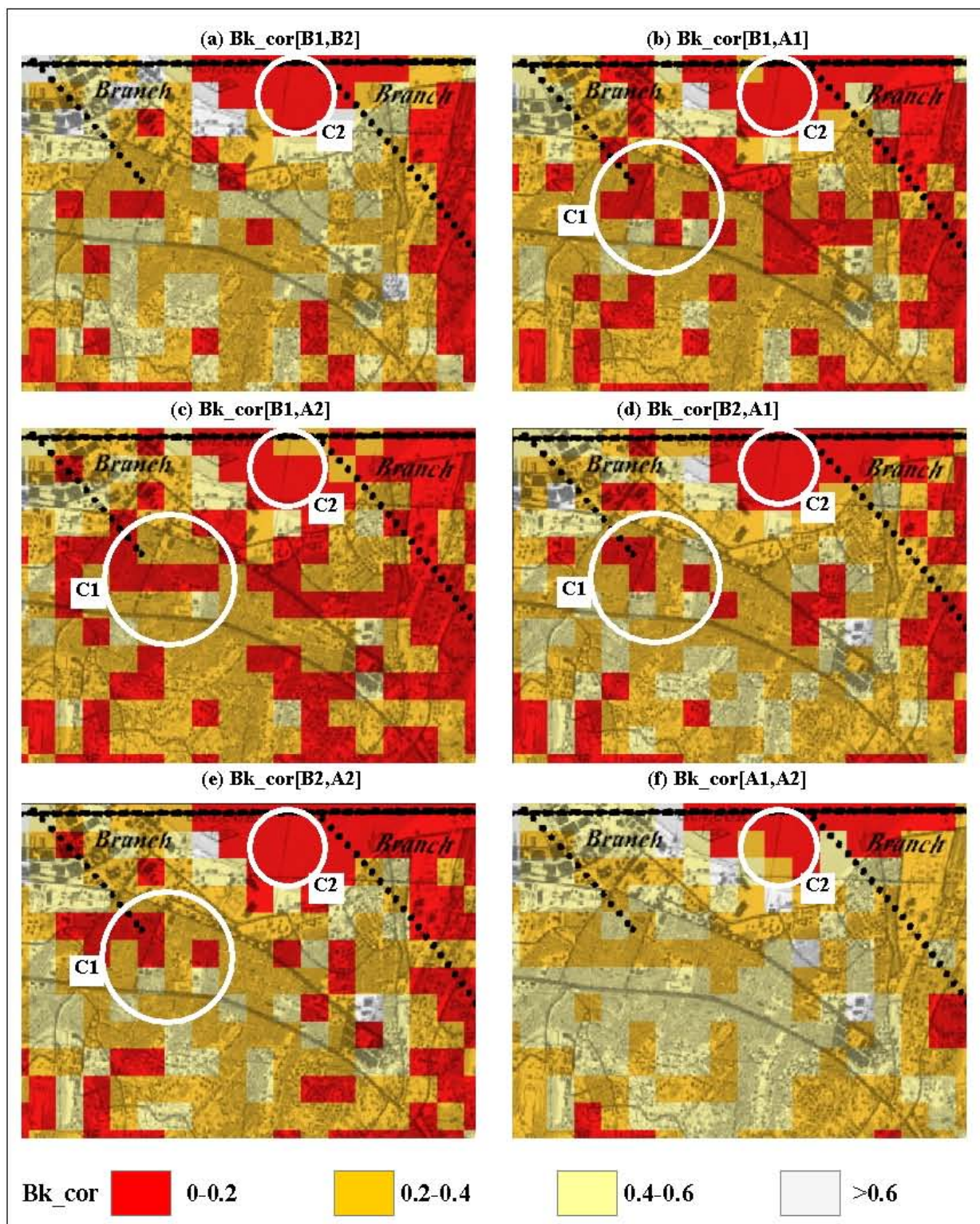


FIGURE 3-19 SAR block correlation statistics for Golcuk, computed using: (a,f) baseline and (b-e) 'before'-'after' pairings. Image B1 was acquired on 3/20/99, B2 on 4/24/99, A1 on 9/10/99 and A2 on 9/11/99. Low correlation (in red) is indicative of pronounced changes between the images. See text for explanation of symbols C1-C2.

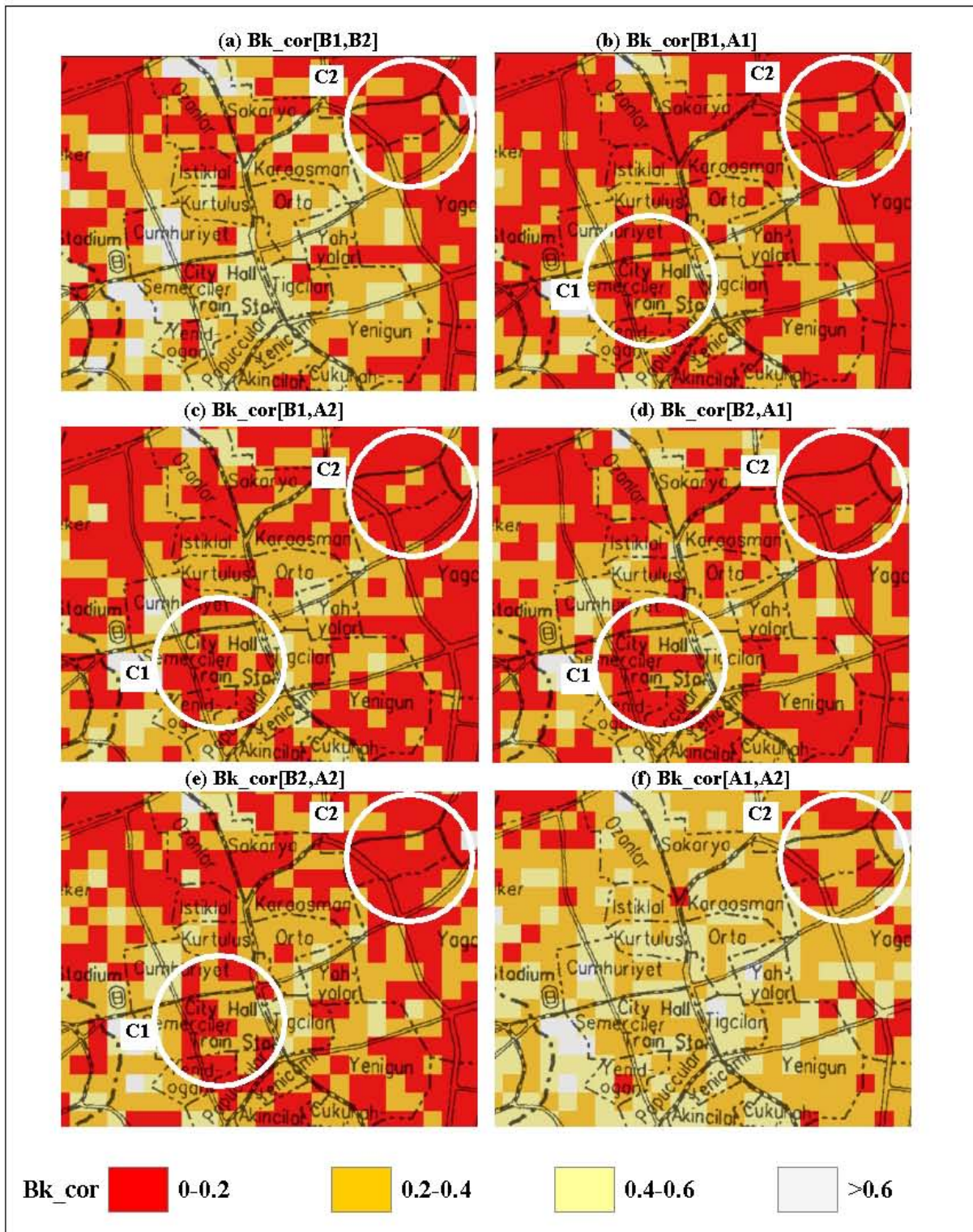


FIGURE 3-20 SAR block correlation statistics for Adapazari, computed using: (a,f) baseline and (b-e) ‘before’-‘after’ pairings. Image B1 was acquired on 3/20/99, B2 on 4/24/99, A1 on 9/10/99 and A2 on 9/11/99. Low correlation (in red) is indicative of pronounced changes between the images. See text for explanation of symbols C1-C2.

3.3.5 Coherence

Coherence maps were produced from the complex ERS datasets (Table 3-3), using the sliding window-based approach in Equation 2 and Equation 3. A number of image pairings are possible between the ‘before’ and ‘after’ scenes. The full range of ‘before’-‘after’ permutations include: $\text{coh}[B1,A1]$; $\text{coh}[B1,A2]$; $\text{coh}[B2,A1]$; and $\text{coh}[B2,A2]$. For comparative purposes, baseline combinations were calculated as: $\text{coh}[B1,B2]$; and $\text{coh}[A1,A2]$. A 15x3 sample window was used to calculate complex correlation (coherence) values, which given the nominal 4x20m spatial resolution of the data, produces an effective window size of 60x60m. The results were then projected to the standard map coordinate (UTM zone 36 and datum WGS-84), and resampled to a 4x4 m pixel size. The resulting scenes for Golcuk and Adapazari are depicted in Figure 3-21 and Figure 3-22.

For visualization, pixel values within the range $0.3 < r_h < 0.6$ are displayed using a grayscale linear contrast stretch. These display limits were selected in order to focus on changes in the backscatter within urban regions. Values towards the lower end of the frequency histogram (Figure 3-21g-h and Figure 3-22g-h) appear to correspond with low level noise, less densely populated regions bordering the civic center, and in the case of Golcuk, return from Izmit Bay.

Figure 3-21a,f and Figure 3-22a,f show the baseline coherence for Golcuk and Adapazari respectively, where changes are attributable to extraneous systematic and environmental effects, rather than earthquake damage. Compared with the various permutations of ‘before’ and ‘after’ images, these baseline images appear brighter, suggesting that coherence levels are generally higher. The particularly bright appearance of image $\text{coh}[A1,A2]$ can be traced to the temporal interval of just 1 day between constituent scenes. Low coherence is evident throughout both urban and rural areas in the ‘before’-‘after’ pairings (Figure 3-21b-e and Figure 3-22b-e). With localized trends between coherence values and earthquake damage proving difficult to discern by visual means, the quantitative algorithms in Section 4 promise additional insights into spatial correspondence between the magnitude of this index and building collapse.

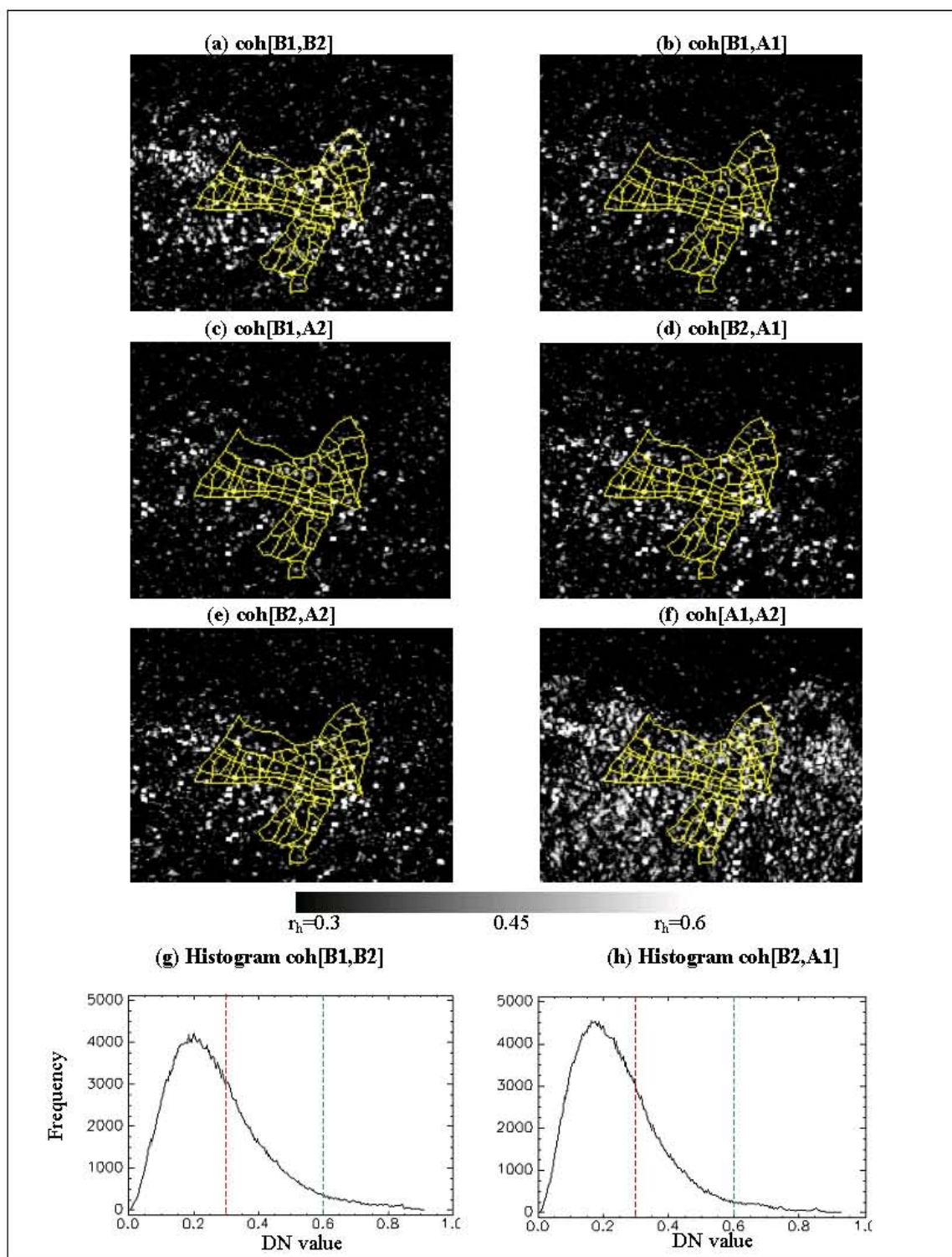


FIGURE 3-21 Golcuk coherence maps, computed for: (a,f) baseline and (b-e) ‘before’-‘after’ pairings. Image B1 was acquired on 3/20/99, B2 on 4/24/99, A1 on 9/10/99 and A2 on 9/11/99. Bright areas record a high coherence, while dark areas denote lower coherence and inconsistency between the scenes. Image histograms (g-h) show the distribution of DN values within the 70 zones.

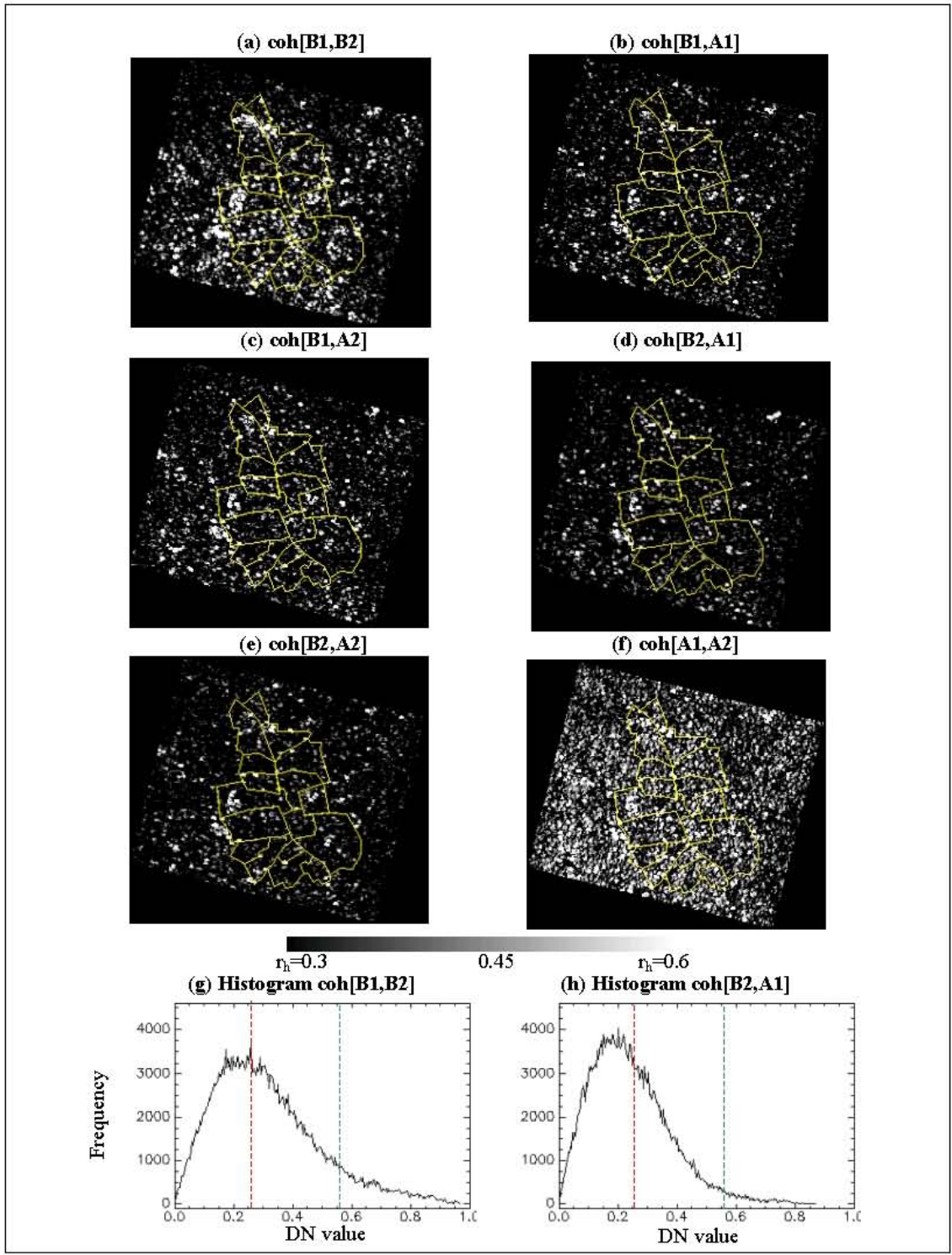


FIGURE 3-22 Adapazari coherence maps, computed for: (a,f) baseline and (b-e) ‘before’-‘after’ pairings. Image B1 was acquired on 3/20/99, B2 on 4/24/99, A1 on 9/10/99 and A2 on 9/11/99. Bright areas record a high coherence, while dark areas denote lower coherence and inconsistency between the scenes. Image histograms (g-h) show the distribution of DN values within the 16 zones.

3.4 Optical Remote Sensing

From the suite of optical satellite remote sensing devices listed in Table 2-1, coverage acquired by the SPOT HRVIR (high resolution visible and infrared) sensor (courtesy of NIK) offers an appropriate spectral, spatial and temporal resolution for regional change detection purposes. SPOT 4 records data in visible and near-infrared regions of the electromagnetic spectrum. Individual bands span green (0.50-0.59 μm), red (0.61-0.68 μm), infrared (0.79-0.89 μm) and middle-infrared (1.58-1.75 μm) wavelengths, with an associated spatial resolution of 20m. The panchromatic band spans wavelengths comparable to the red (0.61-0.68 μm), but depicts the earth's surface in much greater detail, with a spatial resolution of 10m. Unfortunately, a limited catalogue of imagery was available for areas affected by the Marmara earthquake. From a temporal perspective, coverage of Golcuk (see Table 3-4) promises an accurate representation of changes due to earthquake damage, since imagery was acquired on 15th July 1999, approximately one month prior to the event, and on 20th August, just 3 days afterwards.

Unfortunately, high-resolution SPOT 4 coverage could not be located for Adapazari. Landsat coverage of the entire region was available 'before' and 'after' the event (courtesy of NIK). Although this latter coverage is useful for visualization purposes (see Section 3.1.1), in view of the poor spatial resolution of 30m, the usefulness of this data for change detection is limited. In consequence, Adapazari is precluded from further analysis in sections of this report concerned with optical response.

TABLE 3-4 Specification of optical SPOT and Landsat imagery for Golcuk and Adapazari. SPOT 4 data for Golcuk was available both 'before' (B) and 'after' (A) the earthquake.

Acquisition Date	Satellite	Coverage
7/15/99 (B1)	SPOT 4	Golcuk
8/20/99 (A1)	SPOT 4	Golcuk
8/18/99	Landsat	Adapazari/Golcuk

The flow diagram in Figure 3-23 depicts the sequence of procedures involved in change detection for the SPOT 4 data. Key stages of pre-processing are addressed in the following section. Details of intensity and correlation datasets provided in Section 3.4.2 and Section 3.4.3

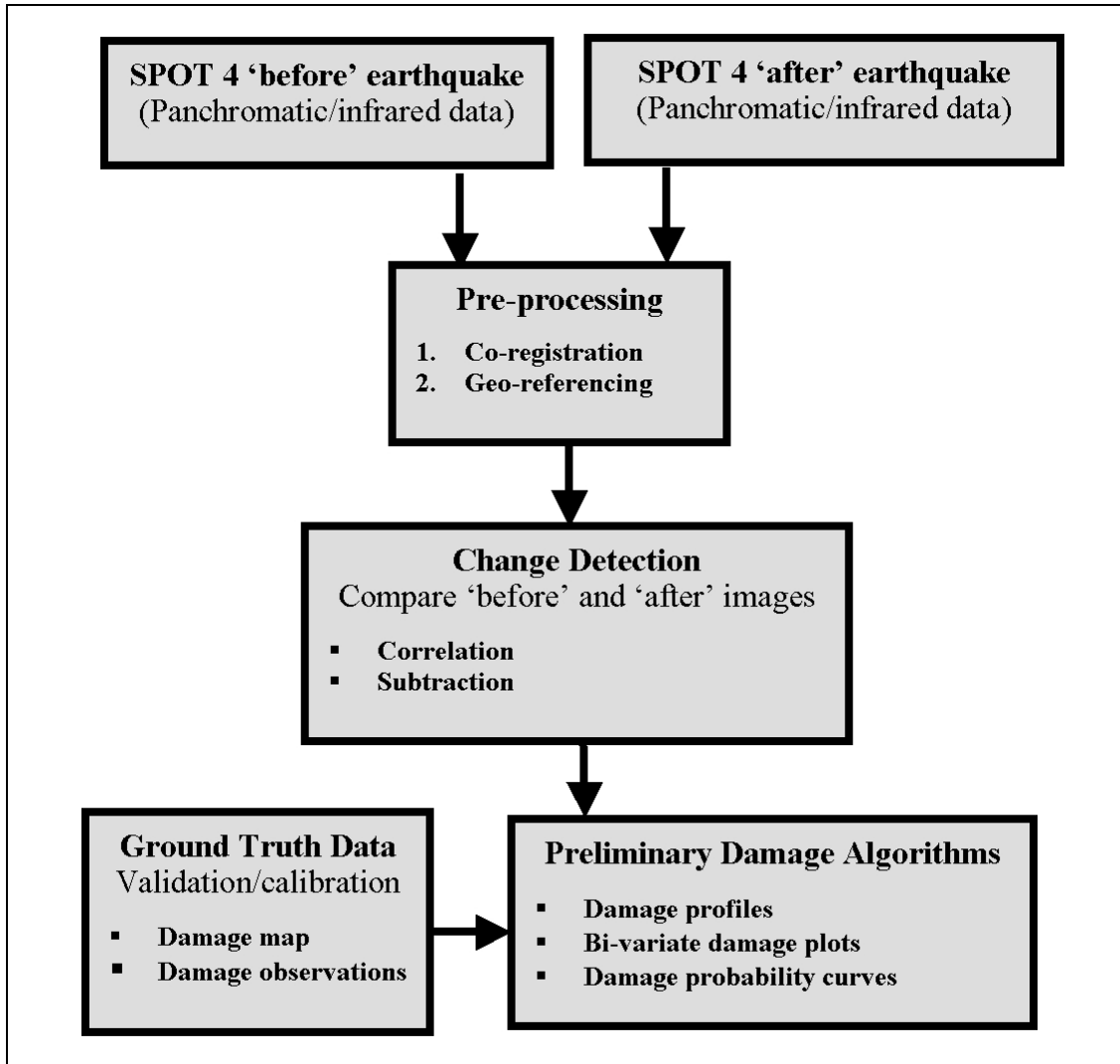


FIGURE 3-23 Flowchart summarizing stages involved in damage detection using high-resolution optical imagery acquired by the SPOT 4 sensor.

3.4.1 Pre-processing

Optical data are subject to a range of geometric distortions, which unless addressed, may compromise the accuracy of changes detected between multi-temporal pairs of images. When acquired, the 'before' and 'after' scenes had already been pre-processed at source, with systematic geometric errors arising from factors such as mirror scan-velocity variance, panoramic distortion, earth rotation/curvature, and variations in platform velocity rectified, prior to delivery. This coarse level of processing relies on internal system data and does not use external GCPs.

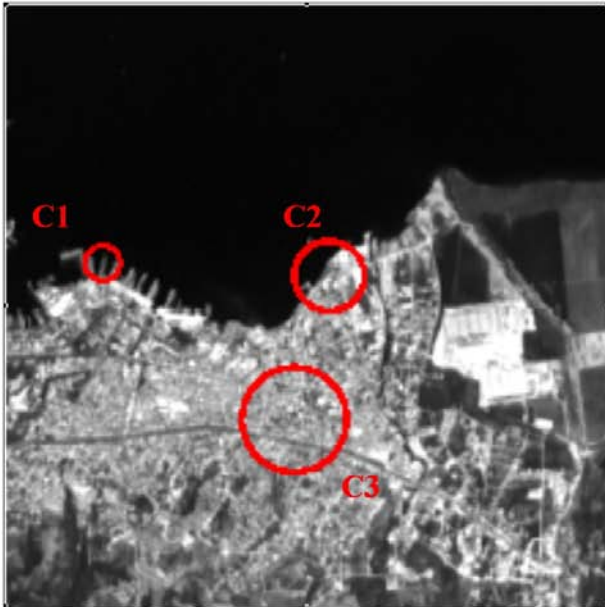
To fine tune the rectification by removing any non-systematic errors such as altitude variance and translation bias, and ensure that the SPOT 4 scenes relate to corresponding areas of the earth's surface, the images were co-registered against the Landsat coverage depicted in Figure 3-1. This dataset had already been fully geo-corrected and projected to UTM zone 36 by the USGS. Registration was performed manually, using a grid of 36 GCPs concentrated around the city center. The warping process was completed using a 1st order polynomial geometric transformation and cubic convolution resampling. To achieve consistency in data display with the SAR ERS coverage, the resulting images were displayed at a 4x4m pixel resolution and geo-referenced using the same projection (UTM zone 36) and datum (WGS 84).

3.4.2 Intensity

Basic intensity data, relating to panchromatic and infrared bands, is employed here as the input to the damage detection algorithms (Section 4). The panchromatic band was selected for its high-resolution 10m coverage, and because it provides a useful overview of reflectance characteristics in the visible part of the spectrum. Although coarser in spatial resolution, the 20m infrared band is also assessed, since it may encapsulate additional features of interest at slightly longer wavelengths.

Figure 3-24 shows the pair [B1,A1] of SPOT 4 panchromatic images acquired for Golcuk. The images are annotated to provide a focus for change detection by visual comparison between the 'before' and 'after' scenes. A rudimentary visual comparison reveals a number of obvious changes arising from the earthquake event. In Figure 3-24a, circle one (C1) identifies a stretch of the shore where several wharf structures were located prior to the earthquake. Circle two (C2) demarcates an area of the coastline where significant ground subsidence was observed. Circle three (C3) encompasses part of Golcuk that was populated with 3-4 story buildings. In Figure 3-24b, which shows the post-earthquake image of Golcuk, the major wharf structure associated with C1 is no longer present. Around C2 there is a marked decrease in reflectance where a large parcel of land has subsided. Finally, significant building collapse is evident in C3, with this area appearing brighter and less well defined on the 'after' scene. Notably, these images also show disruption to the major roadway running west-east through the city, which was obstructed by the debris from collapsed buildings.

(a) B1: Panchromatic (7/15/99)



(b) A1: Panchromatic (8/20/99)

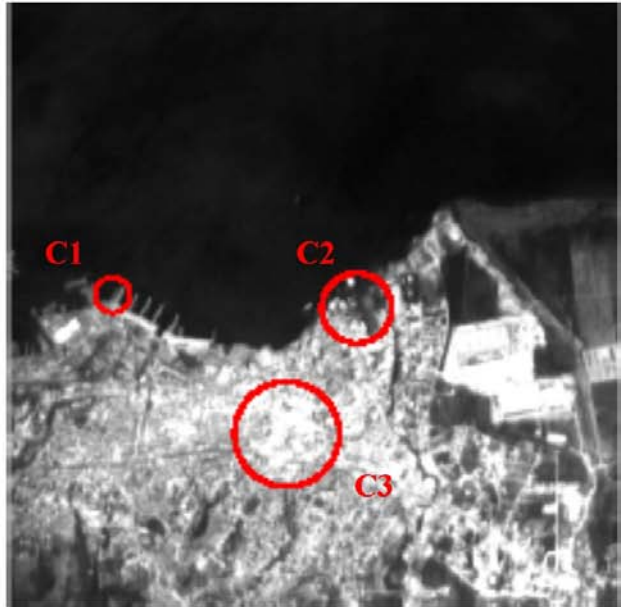


FIGURE 3-24 Panchromatic SPOT 4 coverage of Golcuk. (Data courtesy of NIK). See text for explanation of symbols C1-C3.

(a) B1: Infrared (7/15/99)



(b) A1: Infrared (8/20/99)



FIGURE 3-25 Near-infrared (band 4) SPOT 4 coverage of Golcuk. (Data courtesy of NIK). See text for explanation of symbols C1-C3.

Figure 3-25 shows the middle infrared SPOT 4 scenes for Golcuk, acquired ‘before’ and ‘after’ the earthquake event. As expected, a reduction in spatial resolution is evident compared with the panchromatic data. The urban fabric lacks the distinct boundaries commensurate with 10m pixels, instead exhibiting a blurred appearance. From a temporal perspective, the ‘after’ scene exhibits a lower level of reflectance throughout urban and rural areas to the west of Golcuk, which may be due to smoke in the upper atmosphere emanating from the burning Tupras oil refinery. The false color composite in Figure 3-26 illustrates this effect (see also Figure 3-2j). Although Golcuk is not obscured, the presence of smoke will clearly influence the DN values of pixels falling within the plume. The impact of this distortion, in terms of change detection, becomes evident in the following evaluation of difference and correlation.

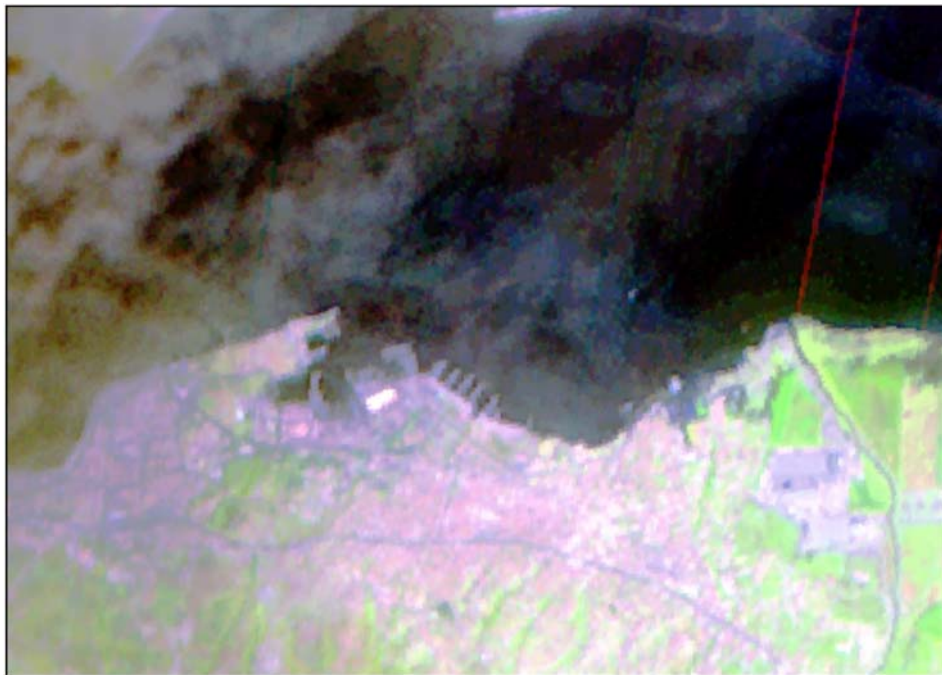


FIGURE 3-26 False color composite (blue = band 2; green = band 3; and red = band 4) for SPOT data acquired ‘after’ the Marmara earthquake on 8/20/99. Western regions of Golcuk are clearly affected by the presence of smoke in the upper atmosphere, which is detected at near/middle infrared wavelengths.

In addition to smoke-induced variations within the city, other temporal changes present in Figure 3-25 are linked to the earthquake event. As for the panchromatic data, symbol C1 highlights the location where a pier has collapsed, and C2 the zone of acute subsidence. C3 again demarcates increased reflectance around the city center, where building damage was concentrated.

3.4.3 Difference

The pre-processed intensity images provide a basis for computing difference values, which constitute the input to quantitative damage detection algorithms (see Section 4). Differences were calculated for panchromatic and middle infrared bands acquired 'before' and 'after' the 1999 Marmara event, using simple subtraction on a per pixel basis (see Figure 2-7).

The resulting scenes are color-coded in Figure 3-27, to highlight regions of Golcuk exhibiting pronounced differences in reflectance, which may be related to earthquake damage. Changes between the panchromatic bands (Figure 3-27a) are concentrated in the central urban area of the city. Reduced differences to the west of the city, where considerable building damage was also sustained, may be due to suppressed reflectance values where smoke from the burning Tupras oil refinery was present in the upper atmosphere (see Figure 3-26). Strongly negative values arise where there is a marked increase in reflectance between the 'before' and 'after' scene. With reference to the damage map in Figure 3-5, these areas clearly correspond with zones exhibiting severe building damage (D-E). This result agrees with the tendency for debris piles associated with collapsed structures, to exhibit a higher spectral return. Positive differences are limited to the coastal stretch that experienced subsidence, where reflectance values have fallen following widespread inundation.

Figure 3-27b depicts the results for infrared wavelengths. The slightly blocky appearance of this image reflects the degradation in pixel size from 10m to 20m resolution. Compared with results obtained using panchromatic data, difference values remain positive for the inundated area, signifying a decrease in reflectance between the 'before' and 'after' scenes. In other areas, infrared results vary where the change between pixel values has been distorted by smoke. In the central region of Golcuk, where building collapse was particularly severe, difference values are now limited to the range $10 < \text{Dif}[B,A] < 50$. The concentration of amplified responses in surrounding areas is again due to the obscuring effect of smoke in the upper atmosphere arising from the burning Tupras oil refinery.

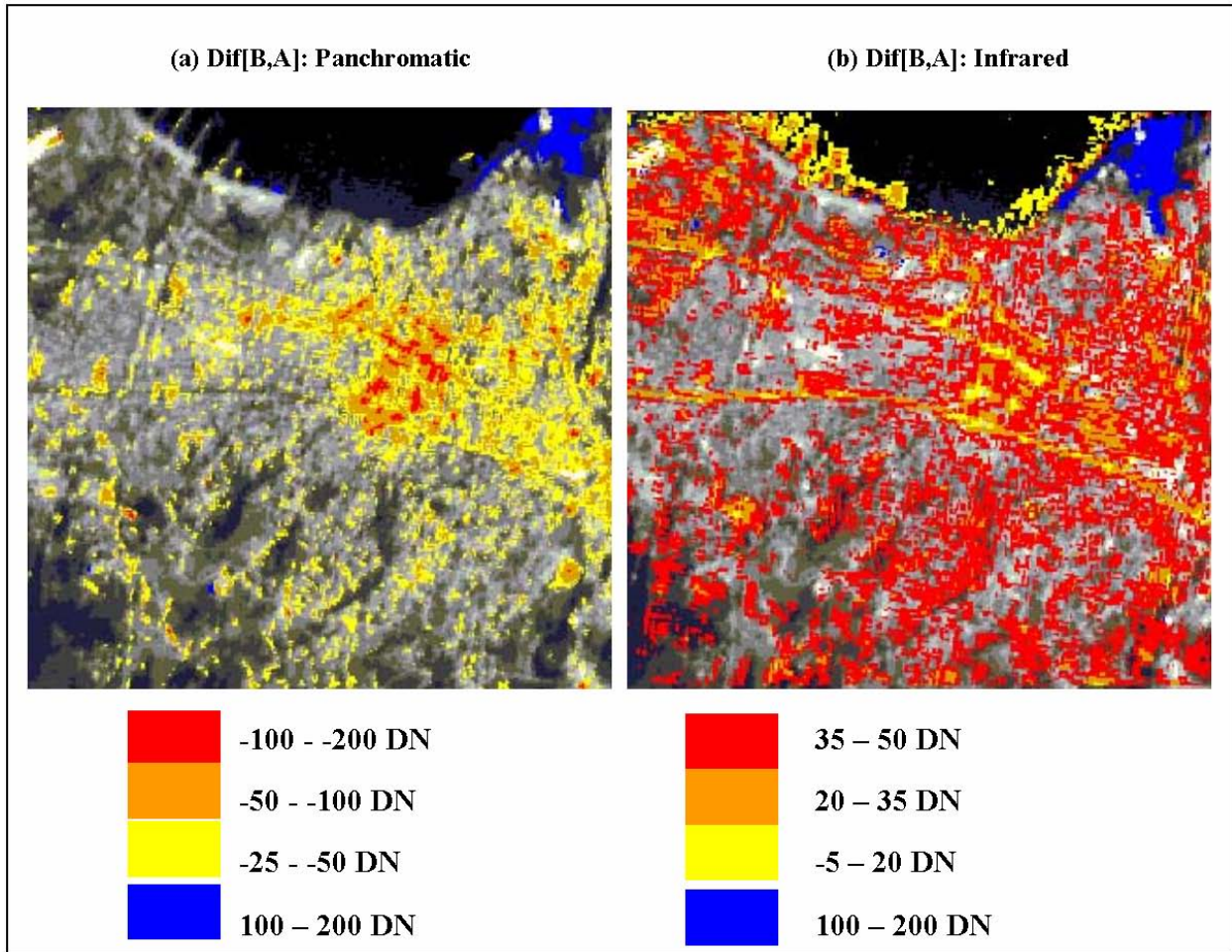


FIGURE 3-27 Color-coded difference values for Golcuk, computed using pre-processed SPOT 4 (a) panchromatic and (b) infrared coverage of Golcuk, acquired on 7/15/99 and 8/20/99. Results are overlaid with the ‘after’ panchromatic image.

3.4.4 Correlation

The correlation between ‘before’ and ‘after’ datasets was computed for panchromatic and middle infrared bands using: (a) a sliding window-based approach and (b) block statistics (for methodological details, see Figure 2-7). The sliding window-based approach employed a 15x15 pixel grid, producing a smaller effective sample area of 60x60m. For the block statistics, preliminary tests were carried out to assess the influence of various block sizes, ranging from 5x5 to 50x50 pixels. In terms of visualization and ability to distinguish between damage states, a 25x25 pixel area yielded the most promising results. Since the pre-processed data had been resampled to 4x4m resolution, this window size produces an aggregated block of 100x100m.

Results for the block- and window-based correlation are overlaid with a base map of Golcuk in Figure 3-28 and Figure 3-29. Since the magnitude rather than the direction of change between B and A is of interest for visualization purposes, the modulus was taken for all values.

Areas exhibiting low levels of correlation are of particular interest for damage detection, because they are synonymous with pronounced changes between the images. For the panchromatic coverage (Figure 3-28a and Figure 3-29a), these areas (displayed in red) are concentrated in central Golcuk (see symbol C1). Comparison with the damage map in Section 3.2.2 confirms that building collapse was widespread throughout this region of the city. As such, panchromatic correlation appears to be a useful measure for locating building damage.

A similar pattern of response is evident for infrared wavelengths, although the level of decorrelation in central areas is less extreme than for the panchromatic band due to the distorting effect of smoke. Elsewhere, low levels of correlation are recorded in the subsided and inundated area (C2). The other main occurrence of low correlation is offshore within the Izmit Bay (C3). In this case, change in reflectance is probably due to the random or chaotic patterns of surface reflectance associated with wind-driven wave action.

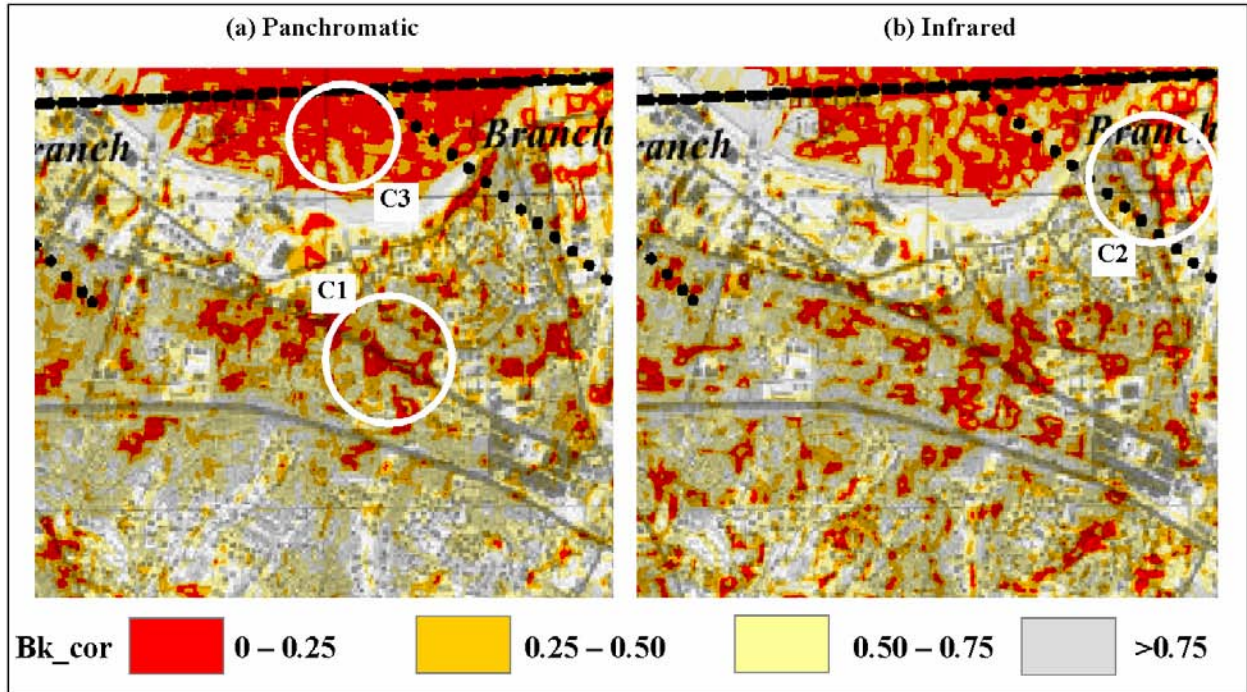


FIGURE 3-28 Optical sliding window-based correlation statistics, computed using: (a) panchromatic; and (b) infrared3 SPOT 4 images acquired on 7/15/99 and 8/20/99. See text for explanation of symbols C1-C3.

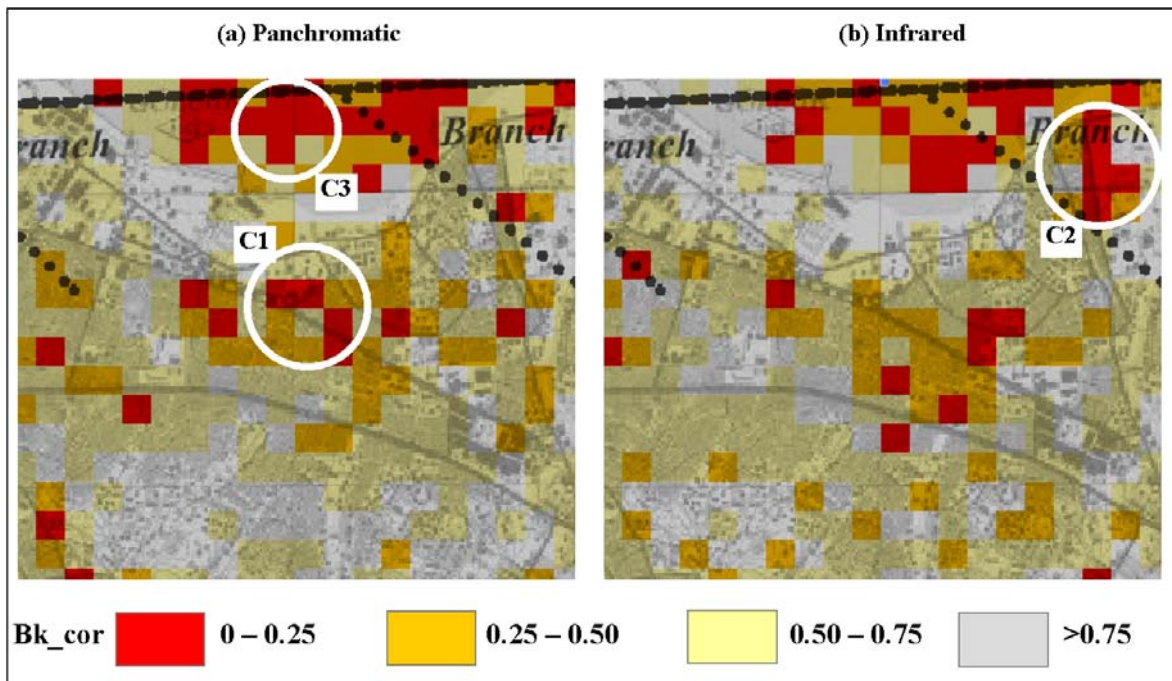


FIGURE 3-29 Optical block correlation statistics for Golcuk computed using: (a) panchromatic; and (b) infrared SPOT 4 images acquired on 7/15/99 and 8/20/99. See text for explanation of symbols C1-C3.

3.5 Summary of Key Findings

The key findings from Section 3 of this report may be summarized as follows:

- ❖ Visual inspection of the correspondence between remotely sensed indices of change and ground truth damage observations suggests that the general *location* of damaged buildings in Golcuk and Adapazari can be determined from analysis of optical and SAR imagery acquired before and after the Marmara earthquake.
- ❖ Based on visual assessment of indices derived from pre- (7/15/99) and post-earthquake (8/20/99) SPOT 4 imagery, the location of building damage in Golcuk coincides with:
 - ✓ SPOT panchromatic ‘after’ imagery = *high* DN values
 - ✓ SPOT panchromatic difference (B-A) = *strongly negative* difference values
- ❖ Based on visual assessment of indices derived from ERS SAR imagery acquired ‘before’ (3/20/99 and 4/24/99) and ‘after’ (9/10/99 and 9/11/99) the Marmara earthquake, the location of building damage in Golcuk and Adapazari coincides with:
 - ✓ ERS sliding window correlation = *low* correlation values
 - ✓ ERS block correlation = *low* correlation values
- ❖ Associations between the remote sensing measures of change and building damage were more difficult to discern from SAR difference and coherence values. Patterns of response for SPOT infrared data were deemed less reliable, due to the obscuring effect of smoke.
- ❖ The availability of baseline ‘before’-‘before’ and ‘after’-‘after’ image pairings for the ERS SAR coverage proved useful for comparing earthquake-related versus extraneous environmental and systematic changes. On a scene-wide basis, correspondence between baseline scenarios appears higher than for ‘before’-‘after’ permutations.
- ❖ Compared with optical coverage, visual inspection of SAR indices of change is problematic, due to high levels of speckle/noise. Building damage appears to be more readily distinguished through the use of spatial averaging techniques, such as block correlation statistics.

SECTION 4

PRELIMINARY DAMAGE ALGORITHMS

The damage algorithms presented in this Section of the report extend the qualitative characterization undertaken in Section 3, which suggested that building damage can be located through analyzing a temporal sequence of remotely sensed images. Returning to Objective 1b as defined by the logistical framework diagram in Table 1-1, these algorithms will demonstrate if, in addition to location, the *severity* or concentration of building damage can be determined. Damage severity is judged on the scale of A-E (see Figure 3-5 and Figure 3-7), in terms of the percentage of collapsed buildings. Comparing damage algorithms for both Golcuk and Adapazari will, in turn, address Objective 1c; whether spatial consistency is inherent, enabling the *extent* of damage to be determined across a wide geographic area.

The algorithms are ‘preliminary’ in the sense that they are empirically-based, and applied to a single earthquake. Subsequent research may enable further development of the theoretical basis underpinning the empirical models, and more widespread application of the approaches presented here to other earthquakes and natural disasters.

Returning to the summary flow diagrams in Figure 3-9 and Figure 3-23, three damage detection algorithms are presented. These graphical approaches include:

- (1) Damage profiles
- (2) Bi-variate damage plots
- (3) Damage probability curves.

Damage profiles are an exploratory tool, used to quantify broad trends between damage states and the magnitude of change on the remote sensing coverage. They are particularly useful when characteristics are studied at an extended zone rather than pixel-based scale. In the latter case, straightforward classification techniques (see, for example, Lillesand and Keifer, 1994) may be employed. From this fundamental demonstration of tendency, bi-variate damage plots indicate whether distinguishing power (and thereby classification accuracy) improves when indices for change are combined or ‘fused’. Lastly, damage probability curves demonstrate the predictive capacity of this methodology, suggesting how remotely sensed indices of change could be used to predict the concentration of various damage states.

In each case, damage algorithms are presented for both optical and SAR coverage. For the optical dataset, results are produced using straightforward difference, sliding window and block correlation techniques. However, given the availability of multiple 'before' and 'after' images for SAR, the algorithms are presented for the optimum permutation of 'before' and 'after', in terms of ability to distinguish between damage states A-E recorded in the field (see Section 3.2.1). The SAR correlation analysis is also extended to compare results with the baseline scenarios, which in theory, isolate extraneous changes from earthquake-related damage.

4.1 SAR Damage Profiles

Damage profiles are employed here to quantify broad trends between levels of damage sustained by buildings in Golcuk and Adapazari during the Marmara earthquake and accompanying changes on the remote sensing coverage (see also EDM, 2000). The performance of several indices of change is assessed: (1) intensity difference; (2) intensity correlation computed using sliding window and block statistics; and (3) coherence. In all cases, results are shown for the image pairing [B2,A1]. Preliminary examination of all possible 'before'-'after' permutations indicates that this pairing provides the optimal distinction between building damage states. From a temporal perspective, this combination of images falls closest to the earthquake event. The [B2,A1] damage profiles are also compared with baseline scenarios [B1,B2] and [A1,A2], to distinguish between earthquake damage and subordinate environmental and systematic effects. Details of procedures used to generate the profiles are given in the following sections, together with an evaluation of the results obtained.

4.1.1 Intensity Difference

The damage profiles in Figure 4-1 and Figure 4-2 depict the difference in intensity between SAR images acquired 'before' and 'after' the 1999 Marmara earthquake (see also Section 3.3.3). Having been pre-processed, resampled to 4x4m resolution and the difference ('before' minus 'after') computed on a per pixel basis, a central measure of tendency for each damage state is presented for the Golcuk and Adapazari datasets. The class centroid was calculated in two steps. First, a zone-based average difference was computed for each of the 70 zones in Golcuk and 16 zones in Adapazari. Based on the damage state recorded for each zone, these averages were then

grouped, and finally aggregated to yield a mean and standard deviation (shown as error bars) for classes A-E and ‘Sunk’. For comparative purposes, difference values were calculated in a similar manner for the baseline cases $\text{dif}[B1,B2]$ and $\text{dif}[A1,A2]$.

In theory, the reduction in radar return when buildings collapse and corner reflectors are destroyed should yield a positive intensity difference, as the ‘after’ scene becomes darker than ‘before’. However, the damage profile for Golcuk in Figure 4-1a deviates from the expected trend in both the absolute and relative magnitude of response. Contrary to expectation, values for $\text{dif}[B2,A1]$ that were expected to be positive, are small and negative for classes A-D, and tend towards zero for class E. This discrepancy arises from a false assumption that DN values in the original intensity images have the same frequency distribution. Visual inspection in Section 3.3.2 instead suggests the presence of scene-wide intensity offset due to factors such as gain setting and look angle. Image B1 (acquired on 3/20/99) is brighter than B2 (4/24/99), while the histograms for A1 (9/10/99) and A2 (9/11/99) in Figure 3-11g,h peak at a higher frequency, indicating that scenes acquired after the earthquake are brighter still. This fundamental intensity offset dominates the difference damage profiles for both the ‘before’-‘after’ and baseline pairings (see Figure 4-1b). Exploratory tests show that the mean difference across all 70 zones in baseline images $\text{dif}[B1,B2] = 0.47\text{DN}$ and $\text{dif}[A1,A2] = 0.16\text{DN}$. Where the ‘after’ image is brighter than ‘before’, the mean difference for $\text{dif}[B2,A1] = -0.15\text{DN}$. Figure 4-1c shows the result of subtracting these zone-wide averages from the class means for damage states A-E. The profiles are now centered around zero, with $\text{dif}[B2,A1]$ showing a tendency for differences to increase with the level of building damage. This adjustment procedure highlights the need for image normalization during the initial data processing routine. Where difference values are required, histogram matching should be incorporated into the methodological procedure.

Over and above this absolute offset, it is important to note that in relative terms, the mean intensity difference for damage states A-E in the adjusted profile (Figure 4-1c) span a very narrow range of values, from $\text{dif}[B2,A1] \sim 0\text{DN}$ for class A to $\text{dif}[B2,A1] \sim 0.2\text{DN}$ for class E. Although the damage profiles for Adapazari in Figure 4-2 are truncated, due to the absence of categories A-B from the subset of sample zones, the remaining difference values are of a similar magnitude and follow a comparable trend. Section 3.3.3 observed the limited sensitivity of this measure on a ‘per pixel’ basis to changes between the SAR images.

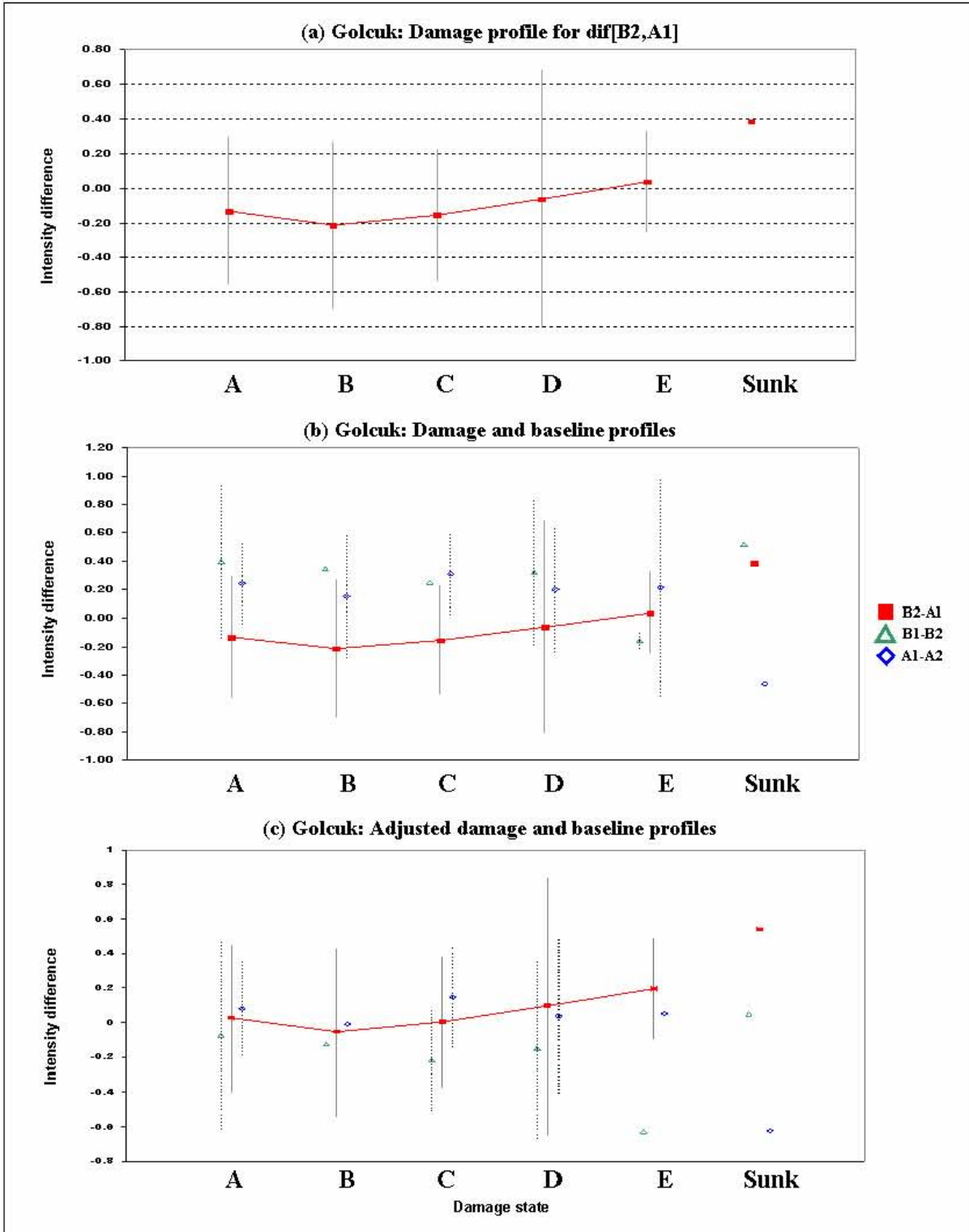


FIGURE 4-1 Damage profiles for Golcuk, showing: (a) the mean difference in SAR intensity values dif[B2,A1] as a function of building damage state (A-E); (b) Comparison between damage profile dif[B2,A1] and baseline profiles dif[B1,B2] and dif[A1,A2]; (c) damage profiles adjusted for radiometric offset.

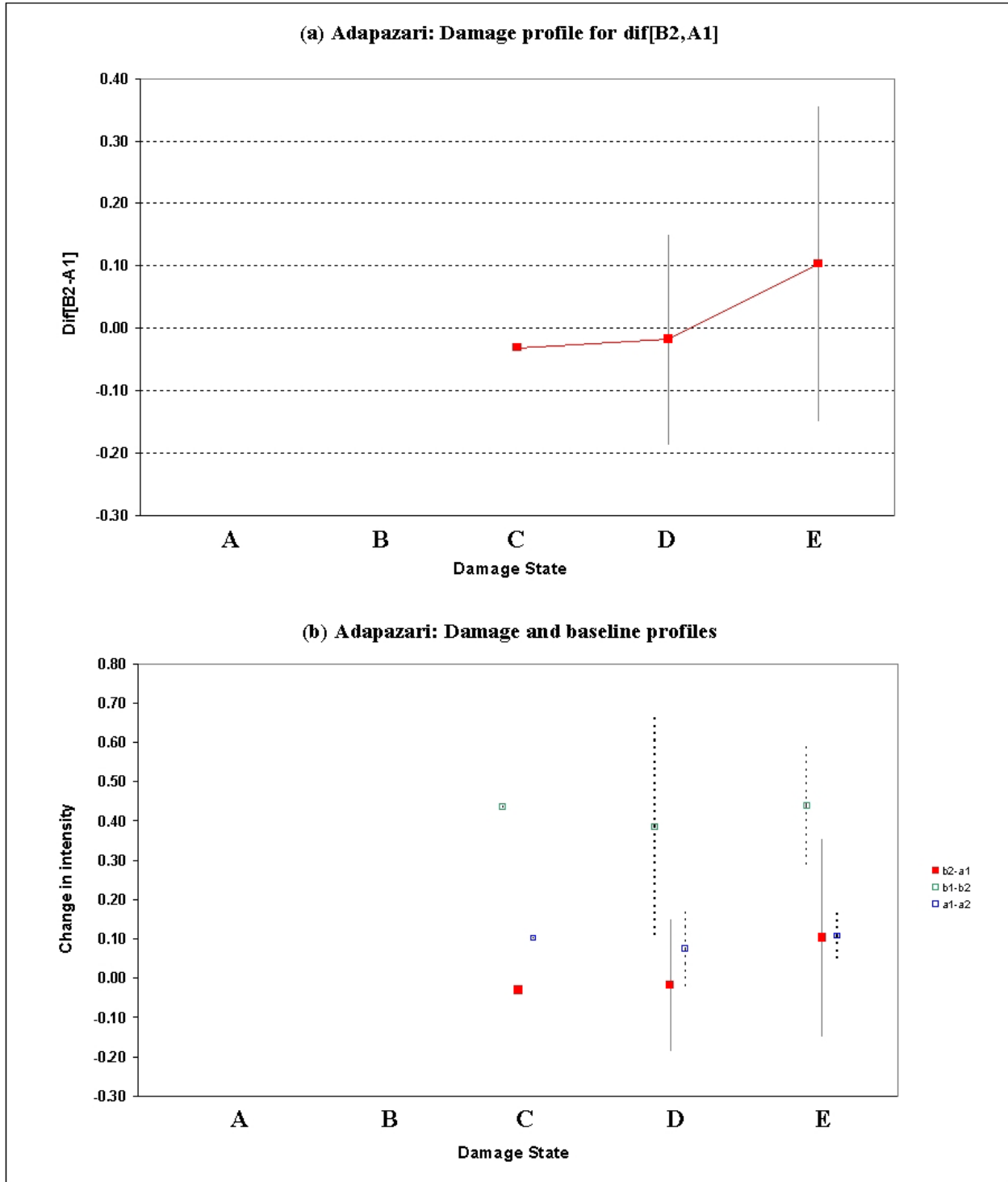


FIGURE 4-2 (a) Damage profile for Adapazari, showing the mean difference in SAR intensity values $dif[B2,A1]$ as a function of building damage state (A-E); (b) Comparison between damage profile $dif[B2,A1]$ and baseline profiles $dif[B1,B2]$ and $dif[A1,A2]$. Error bars represent 1 standard deviation about the mean.

Once again, the aggregated mean statistics in these damage profiles are dominated by the high frequency of values around zero (see the image histograms in Figure 3-15g,h). This suggests that pixel- and zone-based analysis of SAR intensity difference is of limited value for locating building damage in Golcuk and Adapazari, and determining its severity.

4.1.2 Correlation

In order to determine the approach yielding optimal distinguishing power between building damage states, the following analysis investigates the performance of: (1) sliding window; and (2) block correlation techniques. The resulting damage profiles are also compared with baseline scenarios, to distinguish between earthquake damage and subordinate environmental and systematic effects.

The input intensity datasets for Golcuk and Adapazari had been pre-processed and posted at a 4x4m spatial resolution (see Section 3.3.2). For each pixel in the scene, sliding-window based correlation values were computed across an effective 60x60m area. A class centroid was calculated for each damage state (A-E and 'Sunk') using mean correlation values for the Golcuk and Adapazari ground truth zones (Figure 3-5 and Figure 3-7). The zonal averages were then aggregated into a single measure of tendency and standard deviation reading. These statistics were used to produce the damage profiles in Figure 4-3a and Figure 4-4a. The profile for Adapazari is truncated, since all 16 zones fall into classes C-E. As with intensity difference, a suite of profiles may be generated from the sequence of 'before' and 'after' scenes. The permutation $\text{cor}[B2,A1]$ offers the most promising trend between damage state and change, for both study areas.

Correlation readings of $r_c \sim 0.25$ in Figure 4-3 and Figure 4-4 reflect the high levels of speckle or noise inherent in the SAR data. Despite this subdued level of association, in both areas there is a clear tendency for mean correlation values to decrease as building damage escalates (see also Aoki *et al.*, 1998). Correspondence between the before and after scenes is equally limited for the subsided zone in Golcuk, where the pattern of return was affected by inundation.

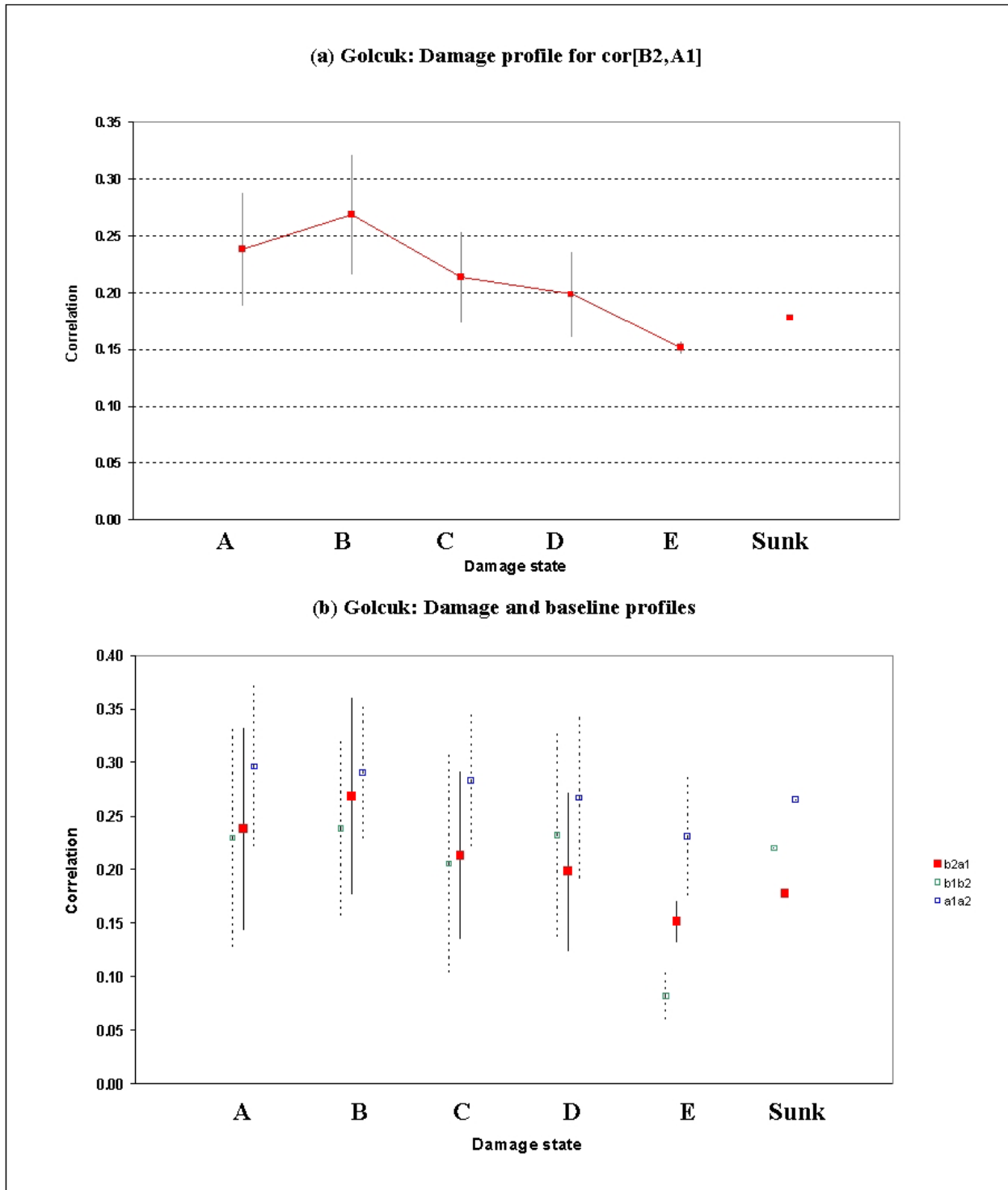


FIGURE 4-3 (a) Damage profile for Golcuk, showing mean sliding window correlation values $\text{cor}[B2,A1]$ as a function of building damage state (A-E); (b) Comparison between damage profile $\text{cor}[B2,A1]$ and baseline profiles $\text{cor}[B1,B2]$ and $\text{cor}[A1,A2]$. Error bars represent 1 standard deviation about the mean.

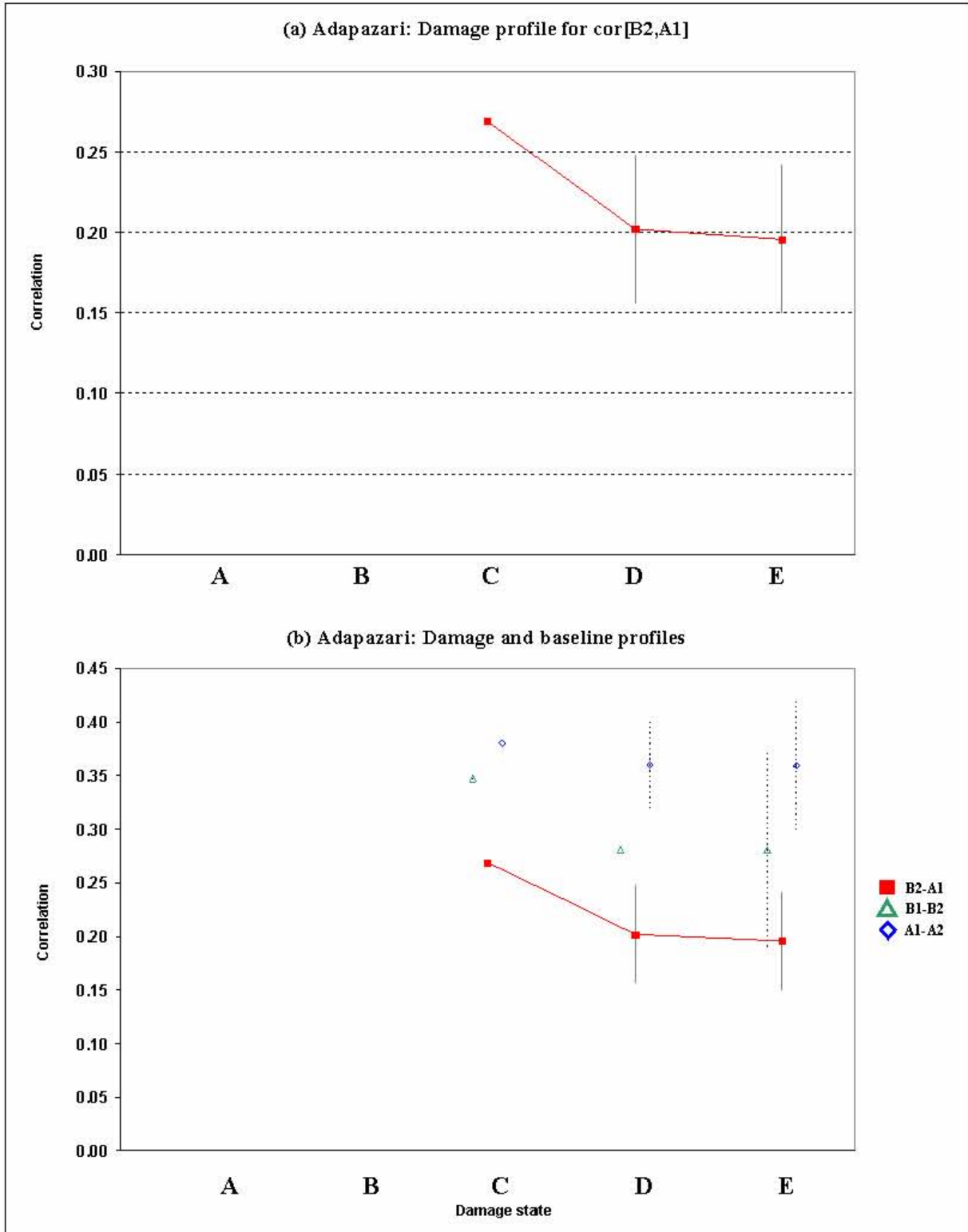


FIGURE 4-4 (a) Damage profile for Adapazari, showing mean sliding window correlation values $\text{cor}[B2,A1]$ as a function of building damage state (A-E); (b) Comparison between damage profile $\text{cor}[B2,A1]$ and baseline profiles $\text{cor}[B1,B2]$ and $\text{cor}[A1,A2]$. Error bars represent 1 standard deviation about the mean.

For comparative purposes, the baseline scenarios are included in Figure 4-3b and Figure 4-4b. The ‘after’ pairings for Golcuk and Adapazari behave as expected, lacking any obvious trend with the extent of building collapse. The amplified correlation values of $r_c \sim 0.35$ reflect the short time lapse between data acquisition. Values for $\text{cor}[B1,B2]$ are somewhat lower, due to the increase in time interval to ~ 1 month.

The performance of block correlation statistics was assessed for window sizes ranging from 20x20 to 60x60 pixels. For each of these scenarios, an average value was computed for the Golcuk and Adapazari ground truth zones, and the respective series aggregated to produce class centroids for damage states A-E and ‘Sunk’. Using the same $\text{bk_cor}[B2,A1]$ permutation as above, the 40x40 pixel scenario (equivalent to 160x160m on the ground) provides the best distinction for both study sites.

Block correlation values in Golcuk span a range of $0.2 < r_b < 0.4$. Slightly higher levels of association, compared with the sliding-window based approach, may be attributed to the increased sample area, which suppresses or ‘smoothes’ speckle/noise. A progressive decrease in correlation is apparent on damage profile for both Golcuk and Adapazari (Figure 4-5a and Figure 4-6a), as the degree of building damage increases from minor to severe (A to E). Correlation values of a similar magnitude for the ‘Sunk’ category, confirms the distinct signature accompanying inundation. For Golcuk, the addition of baseline profiles in Figure 4-5b also reveals a pronounced distinction between earthquake-related damage $\text{bk_cor}[B2,A1]$ and residual changes between the ‘before’ and ‘after’ pairings. These latter cases lack any systematic trend between block correlation and building damage state. Notably, the smoothing effect of an increased sample window has mitigated the reduction in return that was evident in $\text{dif}[B1,B2]$ and $\text{cor}[B1,B2]$ for category E. Baseline $\text{bk_cor}[A1,A2]$ behaves in a similar manner for Adapazari. However, from the partial profile, it is difficult to determine whether $\text{bk_cor}[B1,B2]$ significantly decreases with damage state.

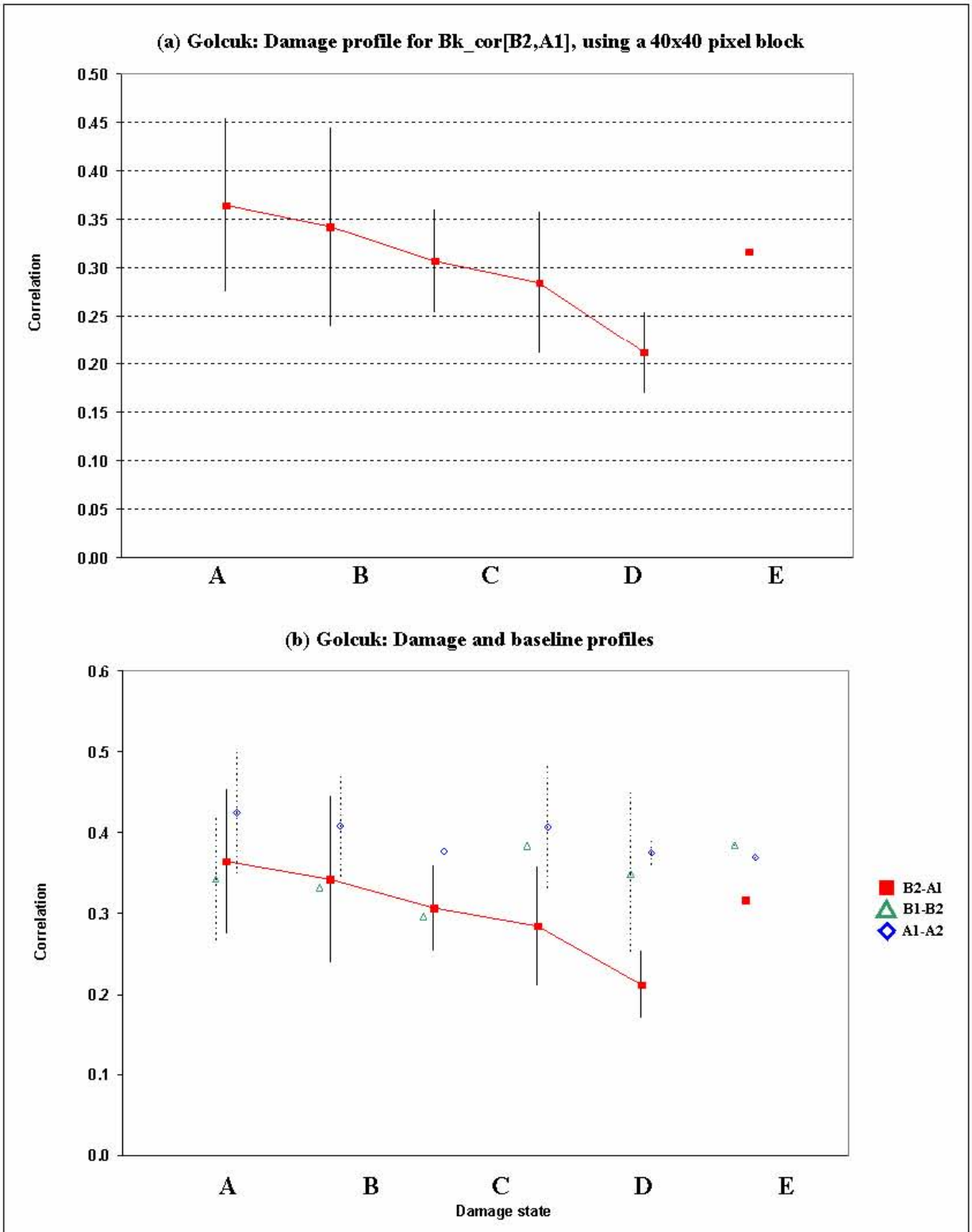


Figure 4-5 (a) Damage profile for Golcuk, showing mean block correlation values $bk_cor[B2,A1]$ as a function of building damage state (A-E); (b) Comparison between damage profile $bk_cor[B2,A1]$ and baseline profiles $bk_cor[B1,B2]$ and $bk_cor[A1,A2]$. Error bars represent 1 standard deviation about the mean.

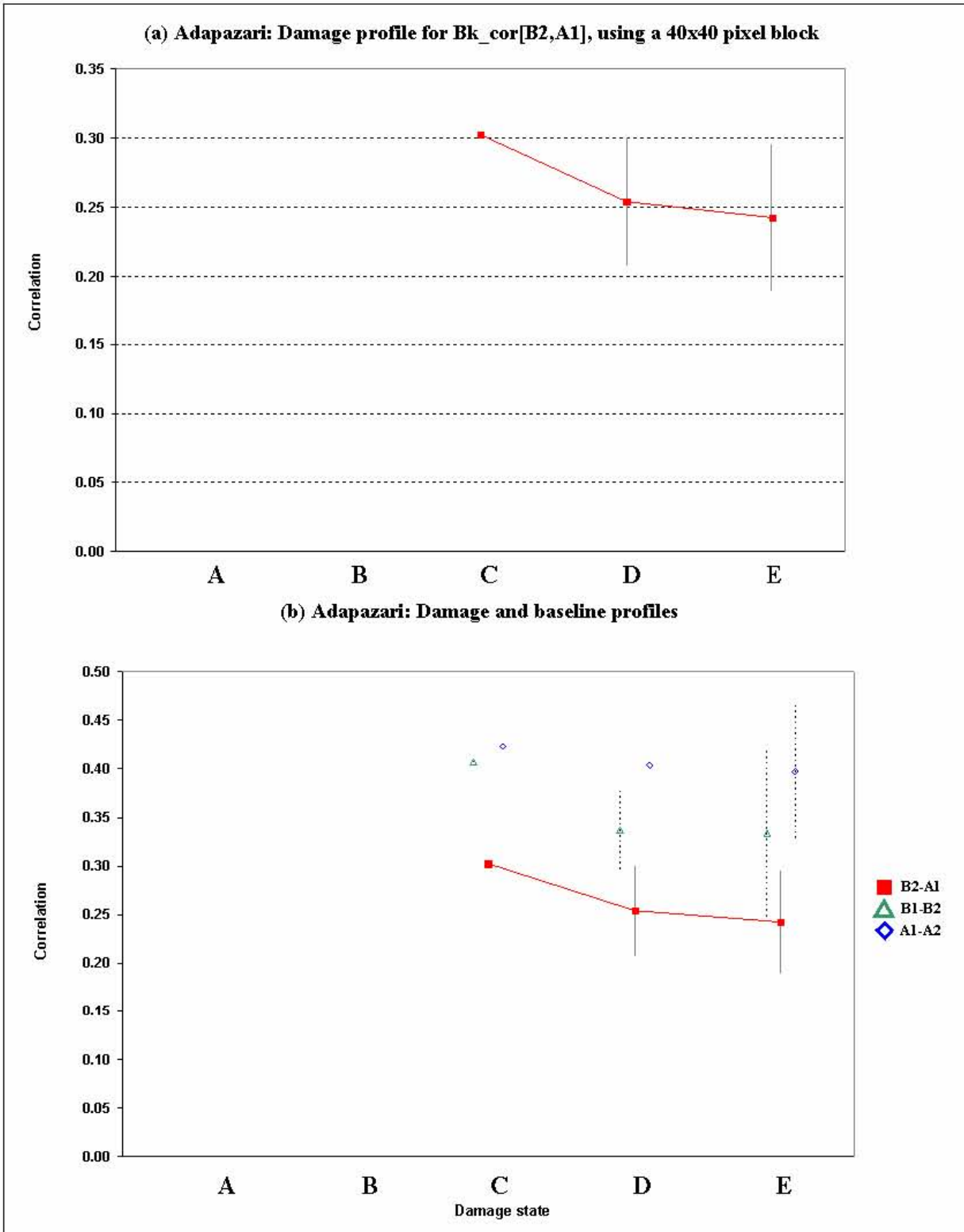


FIGURE 4-6 (a) Damage profile for Adapazari, showing mean block correlation values $bk_cor[B2,A1]$ as a function of building damage state (A-E); (b) Comparison between damage profile $bk_cor[B2,A1]$ and baseline profiles $bk_cor[B1,B2]$ and $bk_cor[A1,A2]$. Error bars represent 1 standard deviation about the mean.

4.1.3 Coherence

The complex correlation or coherence datasets depicted in Figure 3-21 and Figure 3-22 have been pre-processed and posted at a 4x4m spatial resolution. Values were computed from complex imagery, using the sliding-window based approach, based on an effective 60x60m window. For the damage profile, a mean coherence value was calculated for each ground truth zone in Golcuk and Adapazari (Figure 3-5 and Figure 3-7). These averages were then aggregated into a class centroid and standard deviation for damage states A-E and ‘Sunk’. From the sequence of ‘before’ and ‘after’ scenes, $\text{coh}[B2,A1]$ exhibits a promising trend between damage state and coherence for both Golcuk and Adapazari.

The consistently low level of coherence ($r_c \sim 0.25$) recorded for Golcuk and Adapazari in Figure 4-7 and Figure 4-8, reflects the influence of speckle or noise inherent in SAR data. Compared with the correlation datasets, coherence values span a narrow range, suggesting that as with intensity difference, changes in response due to building damage have a subtle manifestation in complex radar return. Nevertheless, the damage profiles in Figure 4-7a and Figure 4-8a reveal a tendency for mean coherence to decrease as the severity of building damage increases. The inclusion of baseline curves in Figure 4-7b and Figure 4-8b demonstrates the level of non-earthquake related change. Near horizontal curves for Golcuk confirm that baseline coherence is indeed independent of damage state. This is perhaps more so, than for either intensity difference, or correlation. The profile $\text{coh}[A1,A2]$ is also near-horizontal for Adapazari, with an amplified value of $r_h \sim 0.37$ reflecting the short time span between image acquisition. Overall, the systematic trend displayed by $\text{coh}[B2,A1]$ therefore appears to reflect the density of collapsed structures rather than natural environmental effects.

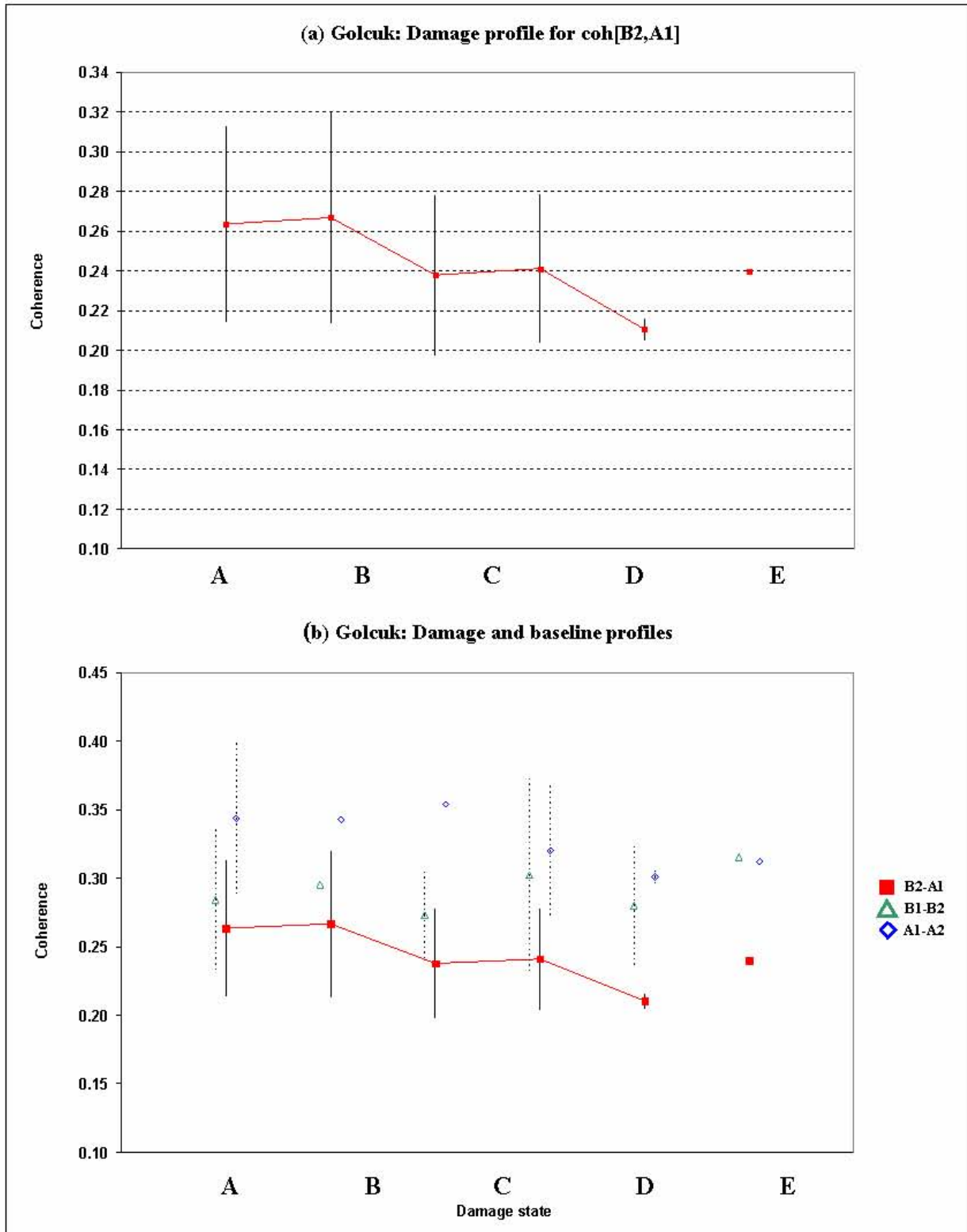


FIGURE 4-7 (a) Damage profile for Golcuk, showing mean coherence values coh[B2,A1] as a function of building damage state (A-E); (b) Comparison between damage profile coh[B2,A1] and baseline profiles coh[B1,B2] and coh[A1,A2]. Error bars represent 1 standard deviation about the mean.

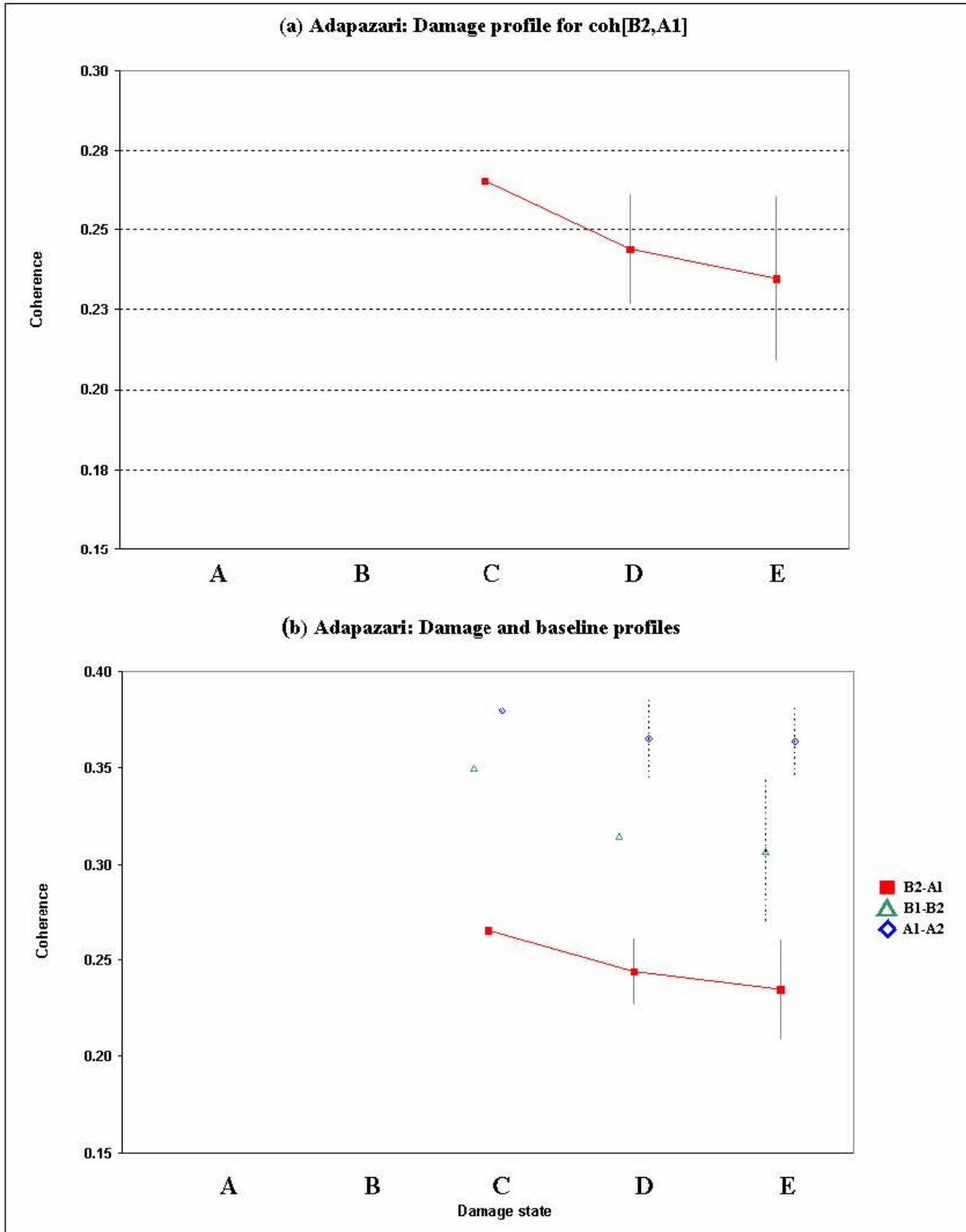


FIGURE 4-8 (a) Damage profile for Adapazari, showing mean coherence values $\text{coh}[B2,A1]$ as a function of building damage state (A-E); (b) Comparison between damage profile $\text{coh}[B2,A1]$ and baseline profiles $\text{coh}[B1,B2]$ and $\text{coh}[A1,A2]$. Error bars represent 1 standard deviation about the mean.

4.2 Optical Damage Profiles

Damage profiles are employed here as an exploratory tool, to determine whether high-resolution SPOT 4 data are a useful tool for determining the severity of damage sustained by buildings during an earthquake. The following sections assess the performance of: (1) difference; and (2) correlation change detection models for the city of Golcuk. Details of procedures used to generate the profiles are given in the following sections, together with an evaluation of the results obtained. Due to the limited spatial extent of SPOT 4 coverage and absence of a temporal sequence of ‘before’ and ‘after’ scenes, optical profiles are unavailable for the city of Adapazari and the general baseline case.

4.2.1 Difference

To generate the damage profiles in Figure 4-9, class centroids were computed for building damage states based on the difference images presented in Section 3.4.3. An average difference and standard deviation (plotted as error bars) were recorded for each of the 70 ground truth zones (see Figure 3-5), and these values aggregated into a central measure of tendency for classes A-E and ‘Sunk’.

Figure 4-9a shows the difference damage profile for 10m resolution SPOT 4 panchromatic data. The negative values for A-E substantiate the observation made in Section 3.4.2, that reflectance in the image acquired ‘after’ the earthquake is consistently higher than ‘before’. This finding is consistent with the idea that building collapse results in increased intensity, as debris piles replace roof structures in the optical coverage. As with the SAR imagery (see Section 4.1.1) extraneous changes between the scenes may be responsible for a degree of the offset. However, in the absence of sequential ‘before’ images to establish a baseline, it is difficult to determine the significance of this effect.

The panchromatic dataset also reveals an encouraging positive trend between difference and damage state. As the percentage of collapsed buildings increases from class A to E, the offset between ‘before’ and ‘after’ scenes is increasingly pronounced. Values for category A, where 0-6.25% of structures collapsed, tend towards zero. In contrast, values for category E, where 50-100% collapsed reach $\text{dif}[B1,A1] \sim -50\text{DN}$. The ‘Sunk’ category relating to inundated coastal

areas behaves differently. Difference values are generally positive suggesting that reflectance in the 'after' scene is lower than 'before'. This result was perhaps to be expected, given that water bodies have a comparatively low return in this region of the electromagnetic spectrum. However, these contrasting responses demonstrate the ability of damage profiles to distinguish between different types of earthquake damage, in this case building damage and subsidence-related inundation. A similar distinction between the signature of liquefaction, burned areas, and building damage is made using Landsat data by Matsuoka and Yamazaki (1998, 2000) for the Hyogoken-Nanbu and Kobe earthquakes.

With the exception of the Sunk' category, the infrared band exhibits a contrasting pattern of response. In the case of urban areas, positive values in Figure 4-9b suggest that reflectance is higher in the 'before', compared with the 'after' scene. As noted previously (Section 3.4.2; also Plate 3.3), reflectance after the earthquake was reduced by the presence of smoke in the upper atmosphere, emanating from fires burning at the Tupras oil refinery. In terms of distinguishing power, the association between damage state and difference is less pronounced than for the panchromatic data, with only a subtle fall in mean values as the percentage of collapsed structures increases from class A-E. Again, the range of values may be suppressed by the obscuring effect of smoke.

On the basis of these damage profiles, panchromatic imagery provides a useful distinction between levels of building damage. Since data for the infrared band is subject to radiometric distortion arising from the smoke plume, assessment of its performance is reserved as a subject for further research.

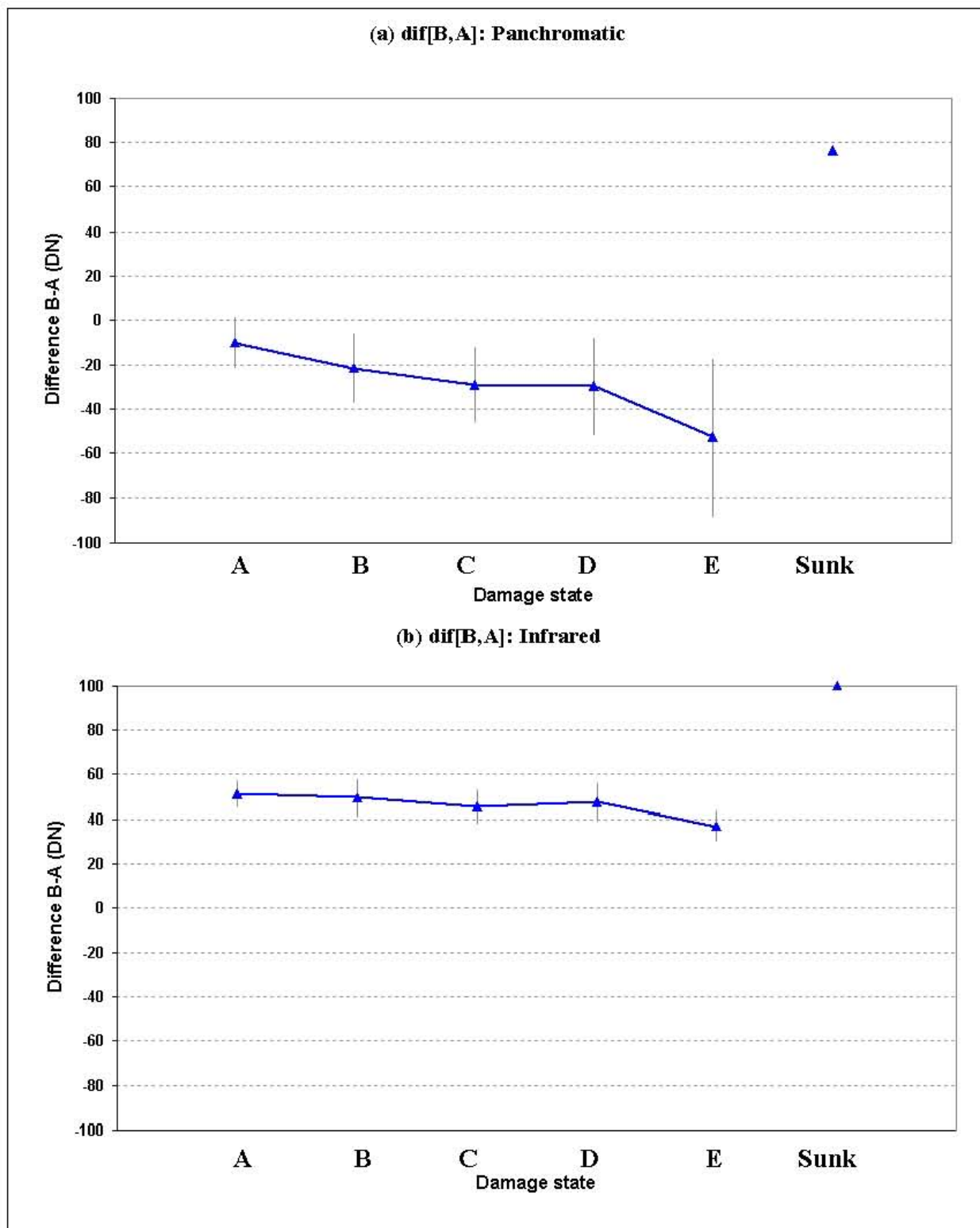


FIGURE 4-9 Damage profiles for Golcuk, showing the association between building damage state (A-E) and average difference between 'before' and 'after' for SPOT 4 (a) panchromatic and (b) infrared bands. Errors bars represent 1 standard deviation about the mean..

4.2.2 Correlation

Correlation statistics were computed for the optical coverage using: (a) sliding window; and (b) block statistical approaches. A 15x15 pixel sliding window was used to compute correlation values, which are assigned on a per pixel basis. Block correlation statistics were generated for panchromatic and infrared bands using a 25x25 pixel sample window. The input data had been pre-processed and resampled to 4x4m resolution, so that all values within the 100x100m block assume the same value (for methodological details see Figure 2-7). In both cases, mean values were output for each of the 70 study zones. A class centroid and standard deviation were then computed for damage states A-E and 'Sunk', as an aggregation of the zonal values. The standard deviation is plotted as error bars, which denote mixed landuse at the sub-zone scale and variability in the spectral response or signature associated with building collapse.

Average sliding-window and block correlation values in Figure 4-10 and Figure 4-11 are markedly higher than those recorded for the SAR coverage. They also reveal a shared tendency towards decreasing levels of correlation as the degree of building damage increases from class A-E. The panchromatic band exhibits a similar response for both correlation measures. However, for the infrared band, block statistics have greater distinguishing potential, with sliding-window-based responses for B-D instead recording a near-constant value of $r_c \sim 0.5$. This general trend confirms that the transition from standing structures ('before') to debris piles ('after') produces a distinct signature throughout visible regions of the spectrum. In most cases, levels of correlation exhibit a further decrease for the category 'Sunk', which relates to the subsided area bordering Izmit Bay. Reduced values of $0.3 < r_c < 0.5$ for panchromatic and infrared are synonymous with a pronounced change in reflectance characteristics with the ensuing inundation.

As noted previously, values for the optical imagery are markedly higher for both block and sliding-window-based techniques, compared with SAR correlation statistics (compare Figure 4-3 and Figure 4-5). This increase in correspondence between 'before' and 'after' is probably due to a combination of factors. First, optical data are subject to a reduced level of noise. Second, the time interval between 'before' and 'after' is substantially smaller for the SPOT coverage, which means that extraneous baseline differences will be mitigated to some extent.

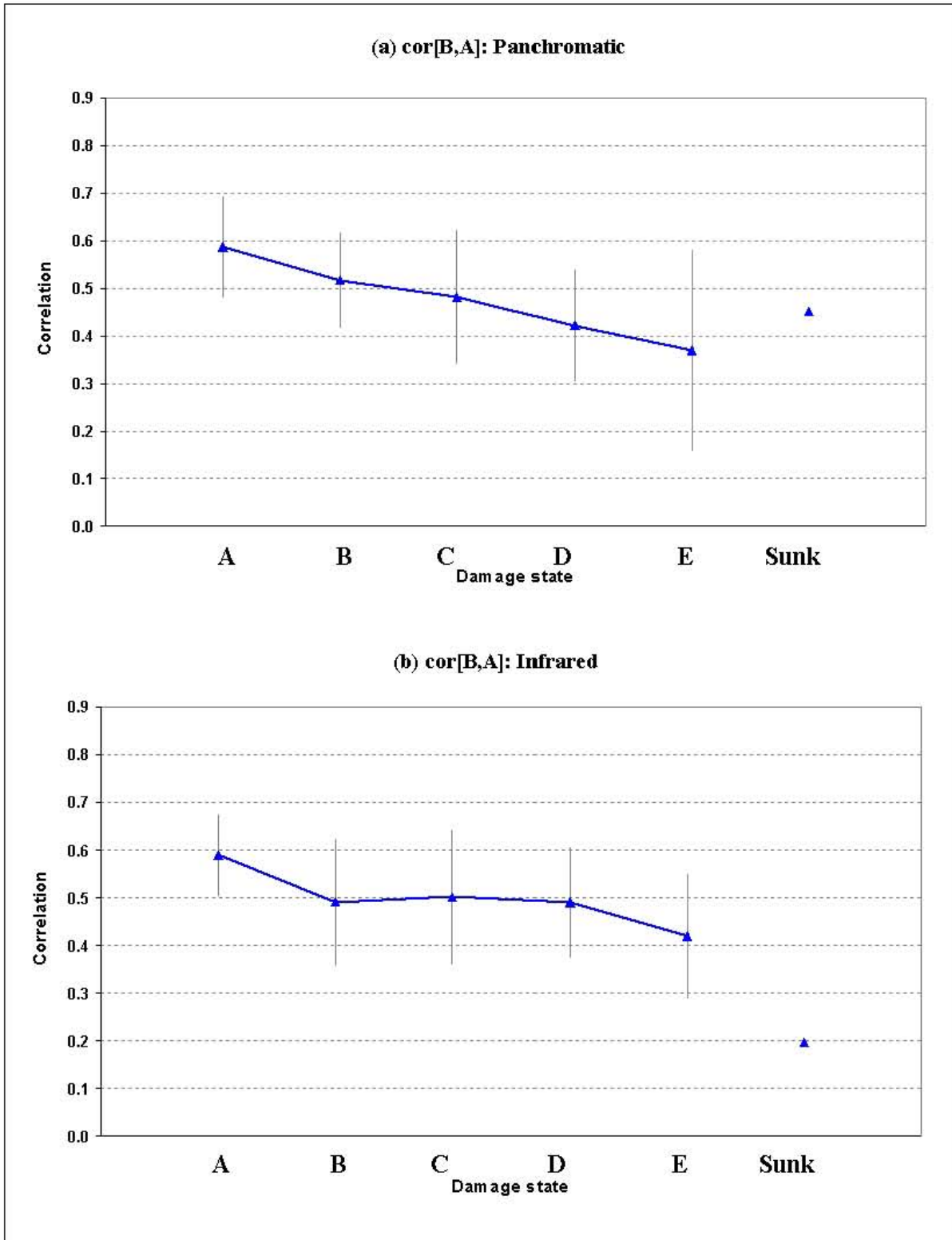


FIGURE 4-10 Damage profiles for Golcuk, showing the association between building damage state (A-E) and average sliding-window-based correlation (computed using a 15x15 pixel window) between 'before' and 'after' for SPOT 4 (a) panchromatic and (b) infrared bands. Errors bars represent 1 standard deviation about the mean.

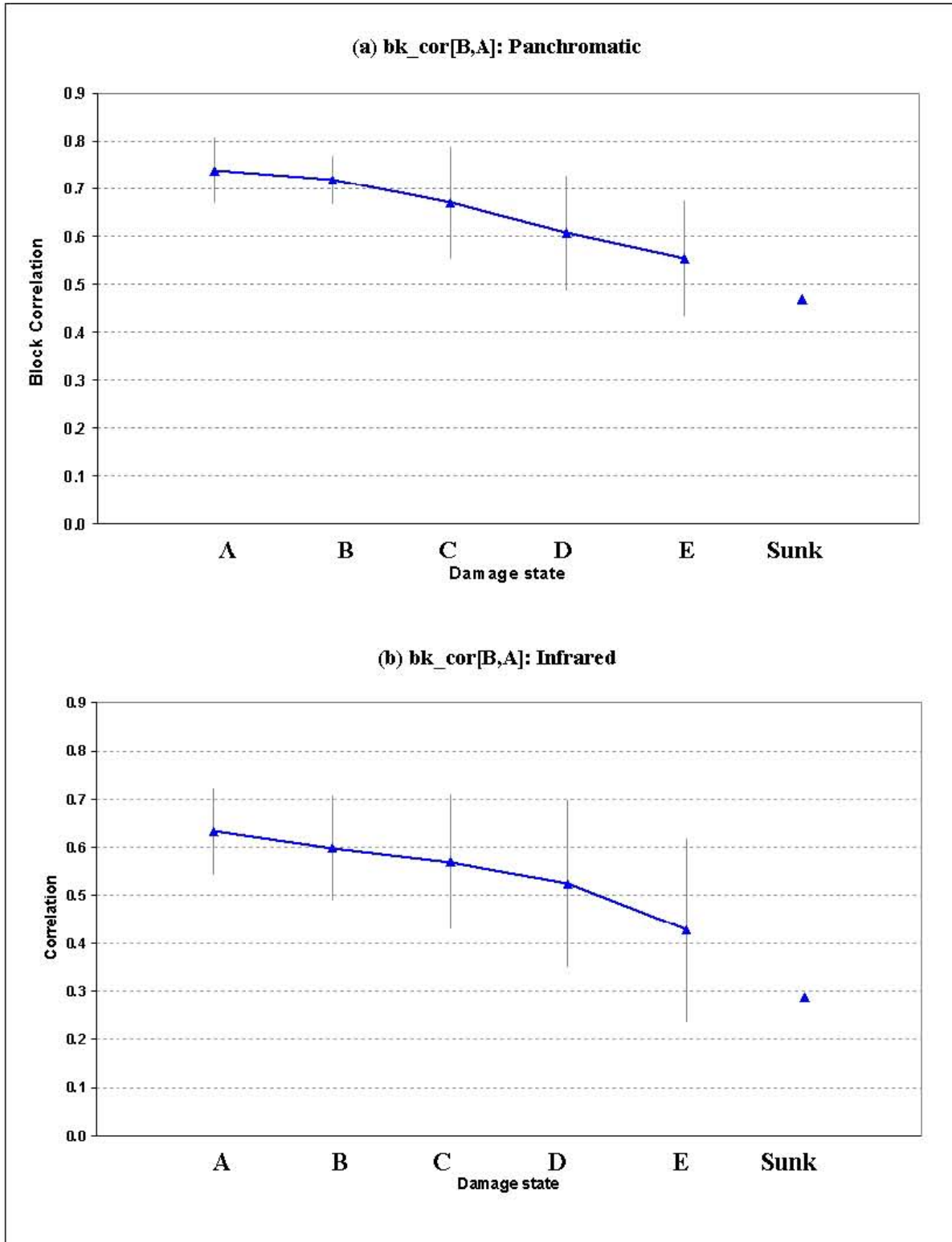


FIGURE 4-11 Damage profiles for Golcuk, showing the association between building damage state (A-E) and average block correlation (computed using a 25x25 window) between 'before' and 'after' for SPOT 4 (a) panchromatic and (b) infrared bands. Errors bars represent 1 standard deviation about the mean.

Together with the difference damage profiles, trends between correlation and damage state point towards an empirical association that warrants further investigation. Damage detection procedures are developed further in the following sections, through advanced methods of graphical display.

4.3 Bi-variate Building Damage Plots

Bi-variate building damage plots simultaneously record the pattern of response for two major indices of change, such as intensity difference and correlation. Aoki *et al.* (1998) employ a similar technique to distinguish damage states arising from the 1995 Kobe earthquake. As with damage profiles, this approach is particularly useful for visualizing class boundaries where the analysis is zone- rather than pixel-based. Class centroids (A-E) recorded in the preceding damage profiles, are graphed together in a scatter plot. The standard deviation about each class is shown as an error bar.

Figure 4-12 and Figure 4-13 show bi-variate plots for the optical remote sensing coverage of Golcuk and Adapazari. The methodology is not applied here to SAR coverage, in view of the limited sensitivity of intensity difference for these study sites. Mean values of difference and block correlation for the Golcuk area are respectively employed as the X,Y series in Figure 4-12. For the SPOT 4 panchromatic band in Figure 4-12a, the bi-variate representation of spectral response provides a promising distinction between damage states. Clustering is evident between the classes. In the case of A-B, where the percentage of building collapse is limited to 0-12.5%, difference values are low and the block correlation high. This result was to be expected, since change due to earthquake damage is limited and consistency between the scenes attains a maximum. As damage level increases, classes C-D cluster in a central position, recording an intermediate difference and block correlation. However category E, where more than 50% of the structures were destroyed, stands somewhat apart. In this latter case, strongly negative difference and subdued correlation is indicative of pronounced changes between the 'before' and 'after' images, where amplified reflectance of debris piles accompanies structural collapse. Comparison with the results for sliding-window based correlation and difference in Figure 4-13 reveals a similar pattern of response, although values of r_b span a slightly higher range due to the smoothing effect of block statistics. However, the same trend towards decreasing correlation and

difference values tending towards zero as the percentage of collapsed structures increases is clearly apparent.

The infrared band (Figure 4-12b and Figure 4-13b) also exhibits clustering of damage states within the graphical space. In terms of absolute values, the block and sliding-window based correlation data span a comparable range to the panchromatic band. However, closer examination of the difference values reveals a reversal in the trend between damage state and magnitude. Zones A-B are now associated with high positive differences of $\text{Dif}[B,A] \sim 50\text{DN}$ and zone E with subdued levels of $\text{Dif}[B,A] \sim 35\text{DN}$. As noted in Section, 4.2.1, this irregular response for the infrared band is attributable to distorted reflectance values, arising from the obscuring effect of smoke in the upper atmosphere, emanating from the burning Tupras oil refinery. Radiometric distortion is a potential limitation of optical data acquired in the aftermath of a disaster. Although the results presented here usefully illustrate the approach, an alternative smoke-free data set is required to establish an indicative damage plot.

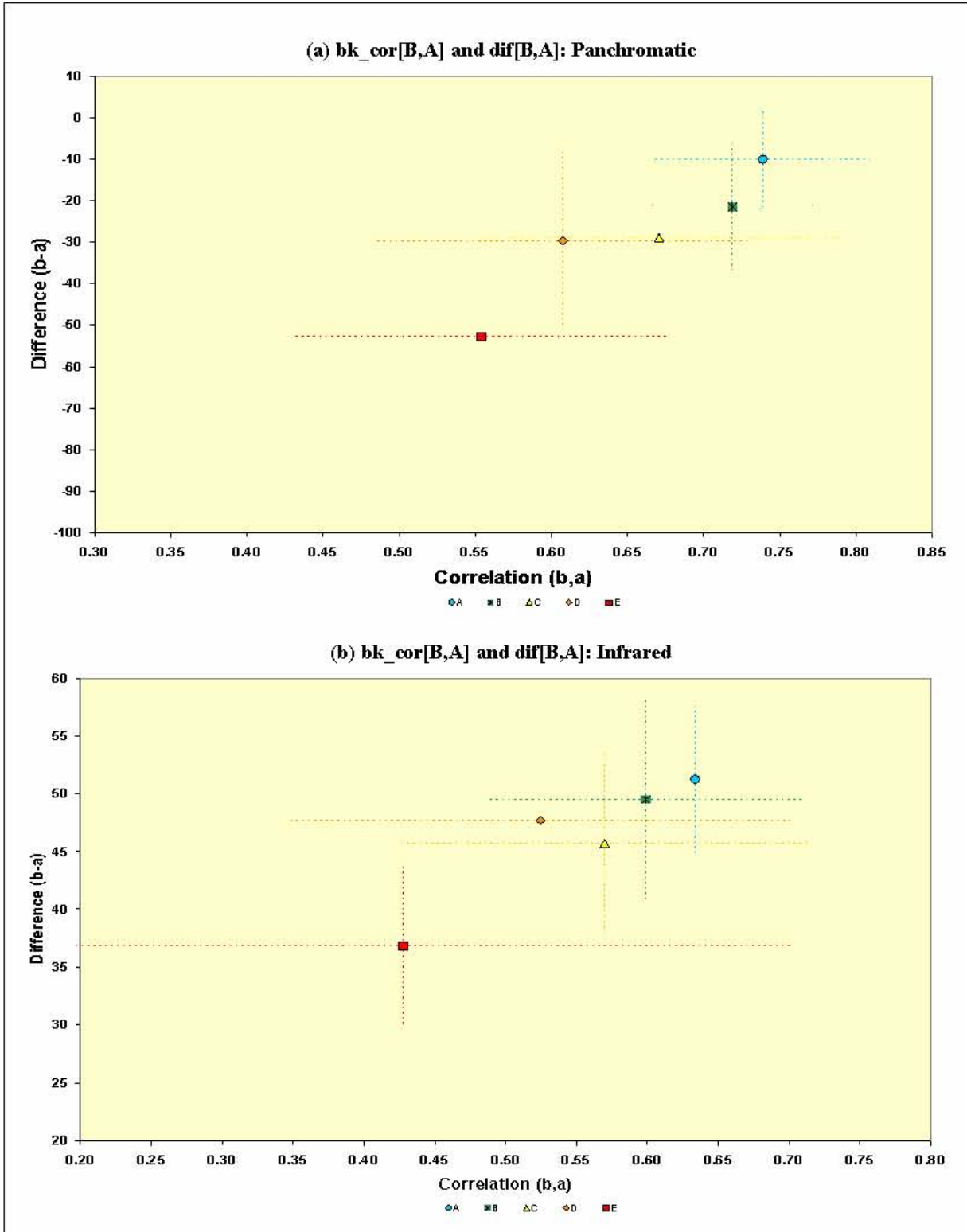


FIGURE 4-12 Bi-variate building damage plots for Golcuk, showing mean and standard deviation in difference and block correlation for: (a) panchromatic; and (b) infrared SPOT 4 data. Damage states A-E correspond with increased concentration of collapsed structures.

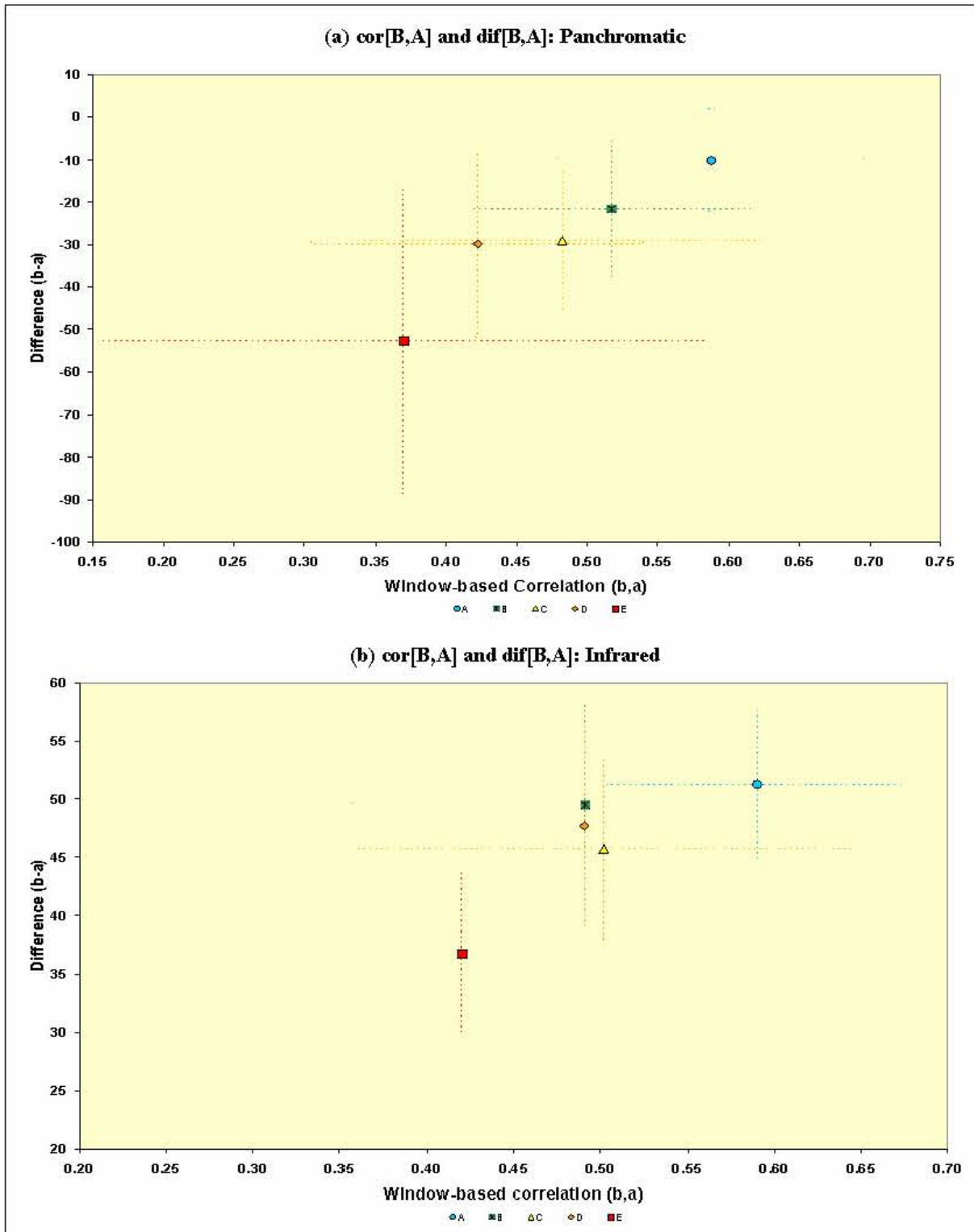


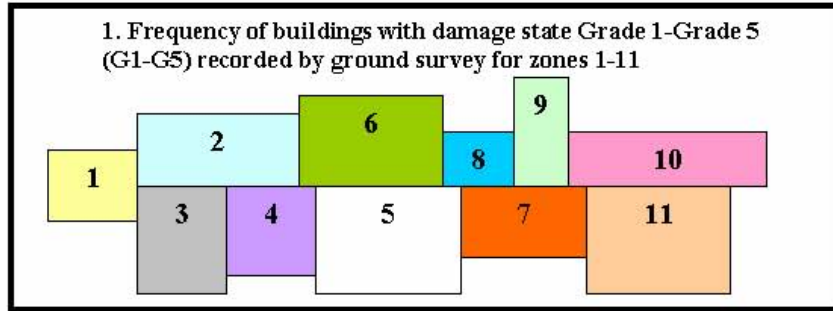
FIGURE 4-13 Bi-variate building damage plots for Golcuk, showing mean and standard deviation in difference and sliding-window based correlation for: (a) panchromatic; and (b) infrared SPOT 4 data. Damage states A-E correspond with increased concentration of collapsed structures.

4.4 Damage Probability Curves

The damage probability curve presented in the following section is introduced as a diagnostic or predictive tool, which may be used to establish the extent of building damage from knowledge of the characteristic response on remote sensing coverage. These empirically-based curves are individualized, relating specifically to the 1999 Marmara event. The development of generic building damage probability curves requires further theoretical advances, and as such remains a key subject for future research (see Section 6).

Whereas the damage profiles and bi-variate plots (Section 4.2-4.3) employ damage classes A-E, damage probability curves return to the original ground truth data, comprising the complete set of observations for all building damage states. As noted in Section 3.2, observations were made on a 4- or 5-level scale, ranging from negligible/slight damage to destruction/collapse. Taking Golcuk as an illustrative example, observations for each of the 70 zones are adjusted to show the percentage of inventoried buildings recorded as Grade 1, Grade 2, Grade 3, Grade 4 and Grade 5 (see Table 3.-2 for definitions), as a percentage of the total number of observations.

Figure 4-14 uses a simplified example to conceptualize the sequence of processing stages generating the probability curves. First, the measure of change (correlation in this case) is ranked for the 11 hypothetical zones. Associated building percentages, which would be recorded during ground truthing, are organized accordingly with a separate series for classes G1-G5. Next, the data are grouped by magnitude of change, and a central measure of tendency computed. For ease of visualization, the results are lastly combined into categories of severe (%G4-G5) and minor damage (%G1-G3) for graphical display. With the series combined in this manner, probability curves are able to diagnose the relative occurrence of severe versus minor damage for a given level of correlation between remote sensing images acquired 'before' and 'after' an earthquake.



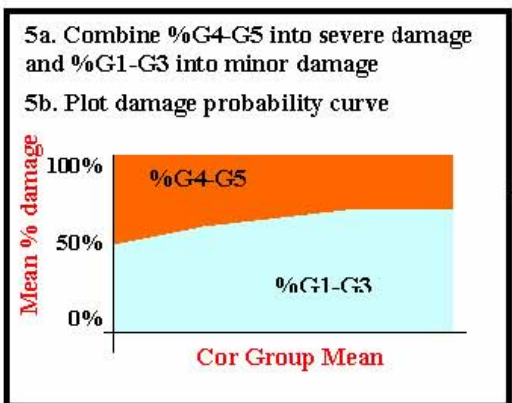
2a. For each zone, occurrences of buildings recording damage state G1-G5 expressed as % of total observations

2b. Associated mean correlation (cor) value from 'before' and 'after' remote sensing coverage is computed for each zone

Zone	Cor	%G1	%G2	%G3	%G4	%G5	Total %
1	0.26	42	17	4	10	27	100
2	0.24	40	15	5	10	30	100
3	0.24	38	16	6	12	28	100
4	0.21	38	14	6	14	28	100
5	0.14	28	10	8	18	36	100
6	0.16	32	9	9	15	35	100
7	0.18	34	13	7	13	33	100
8	0.10	25	9	9	20	37	100
9	0.17	35	11	7	15	32	100
10	0.29	50	18	5	9	18	100
11	0.28	46	17	5	9	23	100

3a. % values (G1-G5) for zones 1-11 ranked by measure of change – in this case correlation.

Zone	Cor	%G1	%G2	%G3	%G4	%G5
8	0.10	25	9	9	20	37
5	0.14	28	10	8	18	36
6	0.16	32	9	9	15	35
9	0.17	35	11	7	15	32
7	0.18	34	13	7	13	33
4	0.21	38	14	6	14	28
3	0.24	38	16	6	12	28
2	0.24	40	15	5	10	30
1	0.26	42	17	4	10	27
11	0.28	46	17	5	9	23
10	0.29	50	18	5	9	18



4a. Devise groupings for change measure (cor)

4b. Compute central measure of tendency for group and for percentage classes G1-G5.

Cor Group	Group Mean	Mean %G1	Mean %G2	Mean %G3	Mean %G4	Mean %G5	Total %
0.10-0.15	0.125	26.5	9.5	8.5	19.0	36.5	100
0.15-0.20	0.175	33.7	11.0	7.7	14.3	33.3	100
0.20-0.25	0.225	38.7	15.0	5.6	12.0	28.7	100
0.25-0.30	0.275	46.0	17.3	4.7	9.3	22.7	100

Figure 4-14 Hypothetical example of building damage observations and change statistics, demonstrating the approach used to generate damage probability curves.

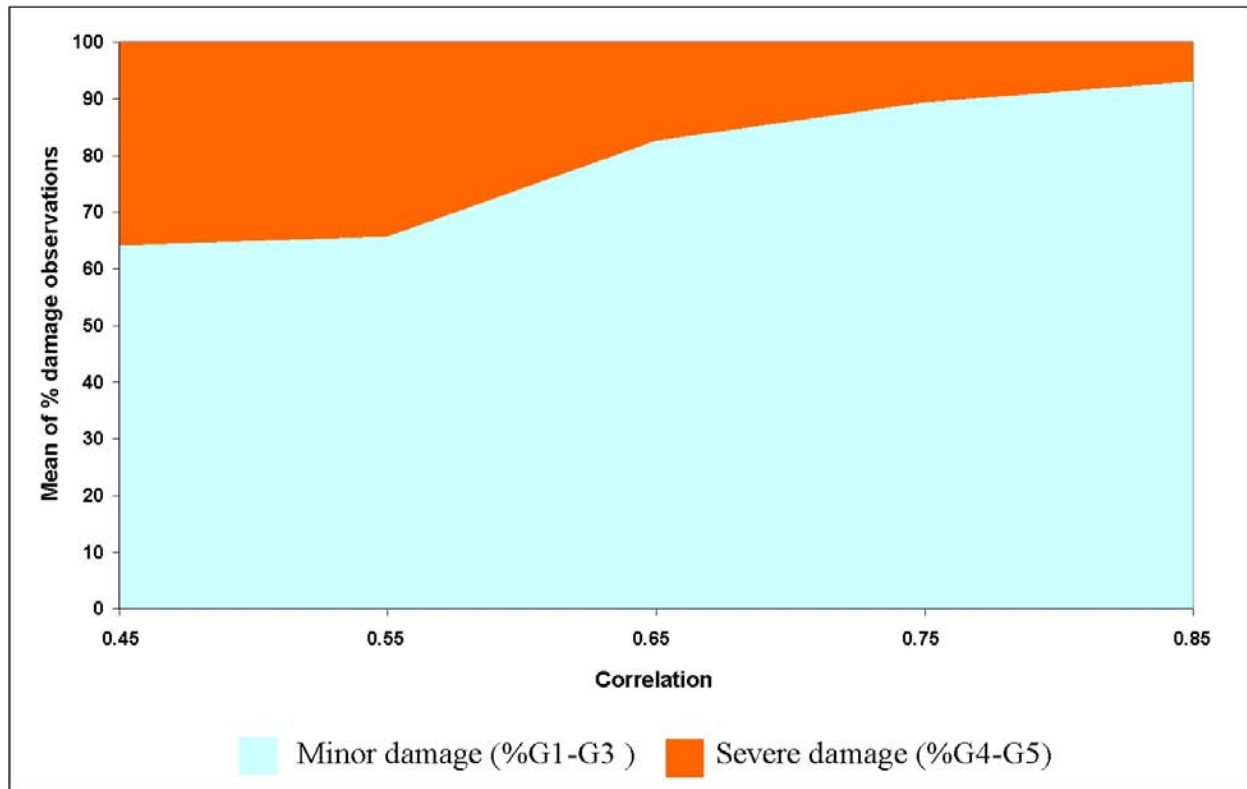


FIGURE 4-15 Damage probability curves, showing association between block correlation recorded on panchromatic SPOT 4 coverage of Golcuk, and mean percentage of damage observations categorized as minor (G1-G3) and severe (G4-G5).

For a damage probability curve to be representative, an alternative approach to sampling building damage is required to that employed by the present study. A high density of observations is required, resulting in values that span the full range of the given index of change. Due to the relatively small number of data points available for Golcuk and Adapazari (70 and 16 respectively), this section of the report only serves to exemplify the approach. It is important to recognize that the predictive capability of the model is limited, with considerable interpolation between readings along the x-axis, due to the limited sample size.

Figure 4-15 illustrates the type of block correlation damage probability curve that can be generated using SPOT 4 panchromatic data. To ensure consistency with the damage probability curves and bi-variate plots, the permutation [B2,A1] was used. First, average bk_cor[B2,A1] statistics were ranked for the 70 zones in Golcuk. The associated percentage of observations for ground truth classes G1-G5 were similarly ranked and the sequence of values aggregated into finite intervals according to natural breaks in the series. For display purposes, results were

divided into broad categories of severe (G4-G5) and minor (G1-G3) damage. The ranked and grouped index of change (x-axis) was then plotted against mean percentage of building damage observations (y-axis). The SPOT 4 panchromatic curve demonstrates how the percentage of severely damaged structures decreases as block correlation increases. For the lowest correlation of $r_b = 0.45$, ~65% of structures were severely damaged. The percentage of buildings with minor damage increases to >90% as correlation values tend towards $r_b = 0.85$.

4.5 Summary of Key Findings

The key findings from Section 4 of this report may be summarized as follows:

❖ Damage profiles generated using optical and SAR indices of change are a useful methodological approach for diagnosing the *severity* of building damage in urban areas of Golcuk and Adapazari. Although general tendencies are apparent for both sensor types, more pronounced trends for SPOT imagery may be attributable to lower levels noise of compared with the SAR coverage.

❖ Optical damage profiles for Golcuk show that as the concentration of collapsed buildings increases from Class A (0-6.25%) to Class E (50-100%), aggregated zonal averages for:

- ✓ SPOT 4 panchromatic *difference widens* from zero to $\text{dif}[B,A] \sim -50\text{DN}$
- ✓ SPOT 4 panchromatic *correlation decreases* from $\text{cor}[B,A] \sim 0.58$ to $\text{cor}[B,A] \sim 0.38$
- ✓ SPOT 4 panchromatic *block correlation decreases* from $\text{bk_cor}[B,A] \sim 0.75$ to $\text{bk_cor}[B,A] \sim 0.55$

❖ SAR damage profiles for Golcuk show that as the concentration of collapsed buildings increases from Class A (0-6.25%) to Class E (50-100%), aggregated zonal averages for:

- ✓ ERS *correlation decreases* from $\text{cor}[B2,A1] \sim 0.25$ to $\text{cor}[B2,A1] \sim 0.15$
- ✓ ERS *block correlation decreases* from $\text{bk_cor}[B2,A1] \sim 0.37$ to $\text{bk_cor}[B2,A1] \sim 0.22$

❖ Despite the truncated results for Adapazari due to the absence of damage state A and state B, consistency in the magnitude and direction of damage profiles obtained for Golcuk suggest that on a regional basis, damage states C-D have a fairly uniform signature within remote sensing coverage. This suggests that the damage profile methodology is a useful tool for tracking the spatial *extent* of severe building damage across a broader regional basis.

- ❖ In general, SAR baseline profiles [B1,B2] and [A1,A2] lack any obvious trend as the concentration of collapsed buildings increases from A-E. This is to be expected, since changes recorded by these profiles are instead related to extraneous environmental and systematic variations between the constituent images.

- ❖ Damage profiles for SAR intensity difference and coherence showed limited ability to distinguish between levels of building damage. Where difference measures are employed as an index of change, image processing should incorporate a histogram matching procedure to alleviate scene-wide offsets in intensity that may cause misleading results.

- ❖ The association between SPOT infrared damage profiles and building damage is less pronounced than for panchromatic bands, due to the obscuring effect of smoke in the upper atmosphere.

- ❖ Introduction of a normalization procedure into the initial data processing routine is necessary to counteract any fundamental offset in intensity that will otherwise dominate difference damage profiles.

- ❖ Bi-variate building damage plots for Golcuk, which integrate several remote sensing indices of change, enhance the distinction between building damage states A-E. The use of data fusion techniques for increasing distinguishing potential warrants further investigation.

- ❖ Empirically-based damage probability curves are a potentially useful predictive tool, which use remote sensing indices of change to indicate the relative distribution of minor (Grade 1 through Grade 3) and severe (Grade 4 and Grade 5) building damage.

SECTION 5

DATA FUSION

5.1 Introduction

Conceptually, the term ‘data fusion’ encompasses ‘*techniques that combine data from multiple sources and related information from associated databases, to achieve improved accuracy and more specific inferences than could be achieved by the use of a single sensor*’ (Hall and Llinas, 1997). A number of other definitions are presented in the literature (see for example, Hall, 1992; DSTO, 1994; and Wald, 1999, 2001), which despite subtle variations in emphasis, all draw attention to data fusion as a methodological framework for the alliance of data originating from a range of different sources, to yield information of greater quality.

In a remote sensing context, previous studies use data fusion to: sharpen the appearance of objects within an image (Pohl and Van Genderen, 1998; Zhang and Blum, 1999; Wang and Lohmann, 2000); enhance information that is poorly presented in a single data source (see Guojin *et al.*, 1998; Hill *et al.*, 1999; Pohl and Touron, 1999; Zhang and Blum, 1999; Achalakul, 2002; Aiazzi *et al.*, 2002; Beauchemin *et al.*, 2002; Dell Acqua *et al.*, 2002; Garzelli, 2002; Huyck and Adams, 2002; Luo *et al.*, 2002); monitor temporal variations and update for changes (Hill *et al.*, 1999; Jeon and Landgrebe, 1999); substitute missing or distorted information with data from another image (Zhang and Blum, 1999; Wang and Lohmann, 2000); and increase the accuracy and efficiency of information extraction (Xiao *et al.*, 1998; Solaiman, 1998; Hellwich, 1999; Hellwich and Wiedemann, 1999; Partington *et al.*, 1999; Le Hegarat-Masclé *et al.*, 1998, 2000, 2003). Application areas range from security purposes (Pohl and Touron, 1999), to flood monitoring (Pohl and van Genderen, 1998), mobile mapping (Paletta and Paar, 2002), land use mapping (Le Hegarat-Masclé *et al.*, 2000), and geological interpretation (see Pohl and Van Genderen, 1998). Increasingly, it is being integrated into operational systems (see Pohl, 1999) such as the DARPA Terrain Feature Generator, the NASA Earth Observing Data and Information System (EOSDIS) (Waltz, 2001), and the processing regime of commercial satellite data providers such as DigitalGlobe (see DigitalGlobe, 2003).

However, it is also important to recognize that remote sensing is just one of many research areas implementing fusion techniques. Data fusion is by nature multidisciplinary (Wang and Lohmann, 2000; Hall and Llinas, 2001; Achalakul, 2002; Luo *et al.*, 2002; Tagarev and Ivanova, 2002), with considerable effort invested in the fields of: military surveillance (Llinas and Hall, 1998; Llinas and Singh, 1998; Wang and Lohmann, 2000; Hall and Llinas, 2001; Luo *et al.*, 2002); medical diagnosis (Wang and Lohmann, 2000); weather forecasting (Trenish, 2001); system diagnostics (Byington and Garga, 2001; Qui *et al.*, 2001; Roemer *et al.*, 2001; Luo *et al.*, 2002); feature recognition (Rahman and Fairhurst, 1998); navigation (Sharma *et al.*, 1999); and robotics (Luo *et al.*, 2002).

Military application driven data fusion architectures documented by Llinas and Hall (1998) emphasize a processing hierarchy comprising: object refinement; situation assessment, threat assessment and process refinement (see also Kokar and Tomasik, 1994; Llinas and Singh, 1998; Joen and Landgrebe, 1999; Hall and Llinas, 2001). However, in the remote sensing domain, a theoretically-based architecture is more widely used (for a useful summary see Achalakul, 2002; Pohl and Van Genderen, 1998; Wald, 1999; also Waltz, 2001), where fusion is undertaken at the following three processing levels:

- (1) Measurement
- (2) Feature
- (3) Decision

The conceptual diagram in Figure 5-1 summarizes key characteristics associated with these major architectural levels (see also Pohl and Van Genderen, 1998; Wang and Lohmann, 2000; Roemer *et al.*, 2001; Waltz, 2001). The fundamental difference between them relates to the processing stage at which fusion occurs. It is important to note that the models are not application specific, applying to both remote sensing and outside applications. In selected instances the processing sequence may be interrupted. For example, measurement fusion may be used for visualization purposes, in which case feature extraction may not occur. Additional scene- and multiple-level fusion techniques are mentioned in the literature, but receive considerably less attention.

Measurement level data fusion is a low-level fusion process, where the input data comprises raw signals that are typically geophysical information output from some type of sensor (Wald, 1999),

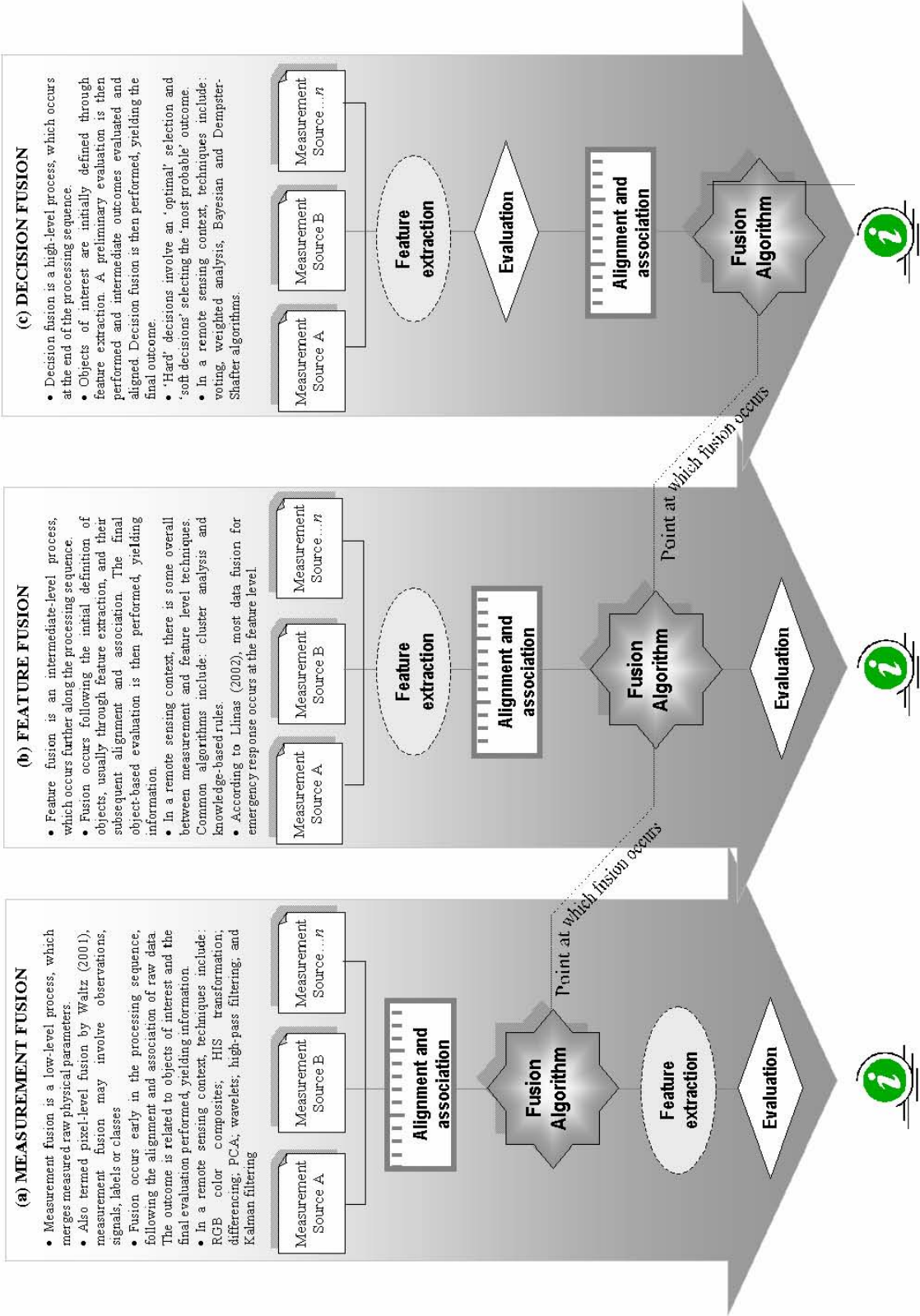


FIGURE 5-1 Conceptual representation of the generic data fusion processing architecture, comprising measurement, feature and decision level approaches.

topographic maps, or GPS coordinates. In the remote sensing field, this is often referred to as image' fusion (see, for example Pohl and Van Genderen, 1998; Pohl and Touron, 1999; Wang and Lohmann, 2000; Achalakul, 2002; Bretschneider and Kao, 2000). Whereas Waltz (2001) emphasizes the 'pixel' as the fundamental measurement unit, other studies recognize the need for generic terminology (see for example Wald, 1999). In these latter cases, the 2D raster image-based unit is exchanged for an observation, signal, category, class, taxon or label. From Figure 5-1, fusion occurs early in the processing sequence, following initial pre-processing to align and associate data within a common frame of reference (see Pinz, 1995; Pohl and Van Genderen, 1998; Wald, 1999; also Thepaut *et al.*, 2000). Working from the original raw signals, the *alignment* process establishes a common frame of reference through standardization of the coordination system and units, sensor calibration, and radiometric correction. *Association* has a specific spatial connotation, relating to the registration of readings so that they correspond with a common object (Wald, 1999).

Feature or medium-level data fusion combines an array of attributes relating to a designated and often purposely recognizable object, to generate new or improved information. In this instance, data fusion occurs further along the processing sequence. The input measurements have already been aligned and associated, and feature extraction techniques (see for example Dell Acqua *et al.*, 2002) used to delineate the target of interest. In a remote sensing context, features typically relate to the edges, corners and lines (Wang and Lohmann, 2000) comprising segmented regions or objects such as buildings, fields, or roads (Aplin *et al.*, 1999; Dell Acqua *et al.*, 2002; Hellwich and Wiedemann, 1999). The suite of attributes associated with the given object may be derived from measurement level techniques, or mono-source classification (see Farag *et al.*, 2002). They are referred to as its 'state vector' (Wald, 1999).

High-level *decision* fusion is also referred to as 'post-detection' fusion (Waltz, 2001). It occurs at the end of the data processing sequence, after the location, identity or attributes have been established for a given measurement or feature, and a preliminary inference made. These intermediate outcomes, termed *sensor* decisions by Waltz (2001), are typically obtained through feature level fusion techniques or mono-source classification (Le Hegarat-Masclé *et al.*, 2003). They are fused to reach the final decision.

Waltz (2001) proposes lesser documented ‘scene-level’ methods as a supplement to the three-tier data fusion architecture. In this case, information obtained from a low-resolution sensing device is used to cue a search and confirm process by a high-resolution sensor. This process could involve commercial satellite systems, such lower resolution SPOT coupled with the detailed coverage offered by IKONOS or Quickbird.

Building on the observation by Wald (1999) that ‘*inputs of a fusion process can be any of the [three major] levels..., in a mixed way, and outputs can be any of these levels*’, multiple-level or ‘hybrid’ approaches integrate measurement-, feature- and decision-based approaches (see also Waltz, 2001). Beugnon *et al.* (2000) further stress the importance of practical gain. Their ‘adaptive’ fusion involves selecting the most appropriate fusion technique, based on decision logic, which may include the ‘no fusion’ option if there is a computational burden without significant analytical gain.

Having introduced the data fusion architecture, Table 5-1 summarizes details of common algorithms employed at the measurement, feature, and decision processing level. The widest range of techniques is documented for the measurement level. Within this category, Pohl and Van Genderen (1998) observe a two-way split between: (1) color related; and (2) numerical and statistical approaches (see also Pohl and Touron, 1999). The former entails some permutation of the three-channel color space. This may, for *example*, involve straightforward red-blue-green (RGB) color composites, or a more complex hue-saturation-intensity (HSI) substitution. Numeric approaches comprise mathematical combinations and transformations. They range from simple spatially-based arithmetic operations of addition, subtraction, ratio and multiplication, to sophisticated multi-resolution transformations in the frequency domain. Associated techniques, such as wavelets and pyramids, are selection based, and as such, are of limited use for multi-temporal analysis. Statistical techniques manipulate and substitute measurement values through principal components analysis (PCA), regression variables, correlation and filtering. In addition to these well established categories of measurement fusion, review of the literature suggests that a further ‘probabilistic’ category warrants inclusion. These operators optimize the fused product through neural networks and random markov fields.

Feature level approaches operate on the concatenated state vector, which relates to selected objects of interest. The diagnosis of segmented attributes is typically performed using knowledge based rules (see Table 5-1), or neural networks. However, the literature also documents a degree of overlap between fusion techniques employed at measurement and feature levels. As shown in Table 5-1, techniques such as cluster analysis and parametric templates operate on either pixel or object-based units. In a military context, target recognition may utilize model-based matching to distinguish objects of interest. Byington and Garga (2001) document a similar ‘training’ mechanism for electromechanical system diagnostics.

At the decision level, techniques are mostly inference based, employing a Boolean (AND/OR), or heuristic approach. Waltz (2001) further distinguishes between ‘hard’ and ‘soft’ algorithms (see also Tagarev and Ivanova, 2002), where a single ‘optimum’, or ‘most probable’ decision is made. Hard algorithms use voting techniques or a priori knowledge of performance to score a judgment. These voted may be weighted according to various performance based measures, including cost. Soft algorithms are instead probabilistic, based on probability rather than performance. Algorithms include Dempster-Shafer evidence theory and Bayesian inference. For these latter techniques, there is some cross-over with the measurement level, as the same theoretical principle is applicable for processing pixels and decisions (see for example, Sharma *et al.*, 1999; Le Hegarat-Masclé *et al.*, 2000; also Wang and Lohmann, 2000).

In terms of application, it is increasingly recognized that data fusion has a central role to play in emergency management. For example, Tagarev and Ivanova (2002) propose fusion techniques for the early warning of potential security situations. Trenish (2001) outlines the use of data fusion in planning for weather-related catastrophes. Experiences from the World Trade Center attacks further demonstrate the value of fused remote sensing coverage for damage assessment, response and recovery (Huyck and Adams, 2002). For identifying specific obstacles to emergency operations, multi-source damage detection algorithms have also shown potential as an early warning of highway bridge collapse (Adams *et al.*, 2002). Importantly, techniques such as these could feed into loss estimation models, for a rapid assessment of the potential economic impact following a natural disaster or terrorist attack.

TABLE 5-1 Characterization of measurement, feature, and decision level data fusion.

	TECHNIQUE	DESCRIPTION	REFERENCES
Measurement-level	RGB color composite	<ul style="list-style-type: none"> • Color mapping where three image-based sources of measurement are assigned to red, green and blue color channels, forming a color composite. • Band selection may be customized for the application. Non-standard bands constitute a 'false' color composite. 	Pohl and Van Genderen (1998) Rockinger and Fechner (1998) Pohl (1999) Wang and Lohmann (2000)
	HSI	<ul style="list-style-type: none"> • A standard RGB image can also be expressed in terms of hue, saturation and intensity (HIS) channels. This separates color (H,S) from brightness (I). • One channel (usually I) is replaced by a new band, followed by an inverse transformation back to RGB format. 	Pohl and Van Genderen (1998) Pohl (1999) Pohl and Touron (1999) Bretschneider and Kao (2000)
	YIQ	<ul style="list-style-type: none"> • Another version of the RGB transformation, Y (luminance) is the brightness of a panchromatic scene; I is red-cyan; and Q is magenta-green. 	Pohl and Van Genderen (1998)
	Addition & multiplication	<ul style="list-style-type: none"> • Addition or multiplication of measurements of the same object, obtained from different sensors. Input bands may be weighted. • This numeric technique is widely used to combine high- and low-resolution images. 	Pohl and Van Genderen (1998) Pohl (1999) Pohl and Touron (1999) Achalakul (2002) Bretschneider and Kao (2000)
	Difference & ratio	<ul style="list-style-type: none"> • Difference or ratio of measurements of the same object, obtained at different times or at different wavelengths. • This numeric technique is widely used for change detection. • The Bovey ratio is a transformation that normalizes bands used for RGB display and substitutes the brightness component with a different high-resolution scene. 	Pohl and Van Genderen (1998) Pohl (1999) Pohl and Touron (1999) Achalakul (2002)
	Wavelet decomposition	<ul style="list-style-type: none"> • Follows the concept of a multi-resolution analysis, where fusion occurs in the frequency domain. • Image frequencies are structured hierarchically by scale and direction. Wavelet coefficients are merged according to an optimal decision rule, and the fused image synthesized with an inverse transformation. • The fused image may include substitute wavelets in selected areas of interest, or where <i>data are</i> otherwise poor. Application is limited for multi-temporal analysis. 	Korona and Kokar (1997) Rockinger (1997) Guojin <i>et al.</i> (1998) Pohl and Van Genderen (1998) Rockinger and Fechner (1998) Pohl (1999) Zhang and Elum (1999) Wang and Lohmann (2000) Aiazzi <i>et al.</i> (2002) Beauchemin <i>et al.</i> (2002) Garzelli (2002) Hill <i>et al.</i> (2002)
	Image Pyramids	<ul style="list-style-type: none"> • The pyramid comprises low-pass copies of the original image, where the sample density, or resolution, is reduced in regular steps or levels. • Potential low-pass operators include Laplacian, Gaussian, gradient, morphological and a ratio-of-low pass. • A fused pyramid is constructed using a coefficient selection rule, such as the local maxima or weighted average. An inverse transformation is then performed. • Application is limited for multi-temporal analysis. 	Rockinger and Fechner (1998) Sharma <i>et al.</i> (1999) Wang and Lohmann (2000) Aiazzi <i>et al.</i> (2002)
	Regression variable substitution	<ul style="list-style-type: none"> • This statistical approach involves the linear combination of image channels, which then replace a single band. • It is suitable for bands where the global correlation is high 	Pohl and Van Genderen (1998) Hill <i>et al.</i> (1999) Pohl (1999) Pohl and Touron (1999) Bretschneider and Kao (2000)

TABLE 5-1 (cont.) Characterization of measurement, feature, and decision level data fusion.

	TECHNIQUE	DESCRIPTION	REFERENCES
Measurement-level	Averaging &	<ul style="list-style-type: none"> • For this estimation method, a statistical average is taken of corresponding measurement values within a series of associated and aligned source images. 	Pohl and Van Genderen (1998) Wang and Lohmann (2000) Luo <i>et al.</i> (2002)
	Weighted average or PCA	<ul style="list-style-type: none"> • Principal components analysis (otherwise know as the Karhunen Loeve approach) transforms multi-band measurements into uncorrelated ‘orthogonal’ variables. • Weightings of input images or bands are derived from eigenvalues. Pixel values may be weighted accordingly. 	Pohl and Van Genderen (1998) Rockinger and Fechner (1998) Pohl (1999) Pohl and Touron (1999) Wang and Lohmann (2000) Achalakul (2002)
	Local correlation modeling	<ul style="list-style-type: none"> • Correlation readings are computed between multiple input scenes or bands, within a local window. • Coefficients and residuals of an associated regression function guide the substitution of more detailed imagery, while retaining radiometric accuracy. 	Hill <i>et al.</i> (1999)
	High-pass filtering	<ul style="list-style-type: none"> • High-pass filtering of detailed imagery captures high spatial frequency, often textural features of the scene. • This is merged with multispectral bands of high spectral but lower spatial resolution, through arithmetic operations such as averaging or subtraction. 	Pohl and Van Genderen (1998) Bretschneider and Kao (2000)
	Kalman filtering	<ul style="list-style-type: none"> • An estimation algorithm, employing a recursive method of least squares analysis, minimizing covariance (average estimation error) to yield an optimal fused solution. • Requires inputs of system response/equation and system error/covariance matrices (e.g. sensor models which record variance). • Kalman filtering assumes a linear system model and Gaussian noise. Extended Kalman filtering accommodates non-linearity. 	Slatton <i>et al.</i> (2001) Luo <i>et al.</i> (2002)
	Neural network classification	<ul style="list-style-type: none"> • Multi-layered perceptron, pulse coupled, or bimodal neuron-based neural network techniques are trained to generate an optimal fused image. • This is an artificial intelligence (AI) black box function, which learns the most likely outcome by ‘remembering’ prior associations. 	Rockinger and Fechner (1998) Xiao <i>et al.</i> (1998) Wang and Lohmann (2000)
	Markov random field	<ul style="list-style-type: none"> • The fusion task is expressed as an optimization problem. • The Markov random field (in this case comprising input images) defines a cost function, based on homogenous regions with congruent edges. This is input to a global optimization strategy. 	Rockinger and Fechner (1998) Wang and Lohmann (2000)
	Bayesian optimization	<ul style="list-style-type: none"> • A Bayesian maximum a posteriori framework estimates true scene characteristics from noisy sensor images. 	Sharma <i>et al.</i> (1999) Wang and Lohmann (2000)

TABLE 5-1 (cont.) Characterization of measurement, feature, and decision level data fusion.

	TECHNIQUE	DESCRIPTION	REFERENCES
Measurement/Feature	Cluster analysis	<ul style="list-style-type: none"> • Classification technique comprising hierarchical agglomerative, hierarchical divisive and iterative partitioning. • Based on data samples or 'training sets', classes are derived for features of interest. The multisensor state vector is then classified in terms of correspondence with these classes. 	Achalakul (2002) Luo <i>et al.</i> (2002)
	Parametric templates	<ul style="list-style-type: none"> • The n-dimensional state vector is compared with geometrical or statistically defined classes. The class usually has a centroid and associated uncertainty. • A similarity measurement determines the final class membership or identity. 	Achalakul (2002) Luo <i>et al.</i> (2002)
Feature level	Knowledge-based rules	<ul style="list-style-type: none"> • Also termed rule base reasoning, state vector constituents (measurements and classes) are input to simple conditional statements to determine the fused result. • Feature-based diagnostic indicators may be fused using fuzzy logic, to determine if significant variations are present between scenes. 	Stassopoulou <i>et al.</i> (1998) Xiao <i>et al.</i> (1998) Hellwich and Wiedemann (1999) Roemer <i>et al.</i> (2001) Achalakul (2002) Luo <i>et al.</i> (2002)
	Neural networks	<ul style="list-style-type: none"> • Neurons are trained to recognize associations between combinations of state vector measurements and fused outcomes. 	Roemer <i>et al.</i> (2001) Achalakul (2002) Luo <i>et al.</i> (2002)
Decision level	Voting	<ul style="list-style-type: none"> • Simplest approach to fusing multiple estimates. 'Hard' decision is typically based on a majority verdict, where most votes (M-of-N) 'wins'. • Variations include weighted voting, plurality and consensus methods. 	Giacinto and Roli (1997) Llinas (1997) Rahman & Fairhurst (1998) Byington and Garga (2001) Roemer <i>et al.</i> (2001)
	Weighted analysis	<ul style="list-style-type: none"> • Sensor estimates are weighted based on <i>a priori</i> knowledge or assumptions of reliability. The 'hard' decision is based on a score function. • Assumption of equal reliability is the equivalent of voting. 	Byington and Garga (2001) Roemer <i>et al.</i> (2001)
	Cost-based	<ul style="list-style-type: none"> • Costs are assigned to each sensor estimate. The final decision is made according to a conditional rule, such as minimization. 	Llinas (1997) Jeon and Landgrebe (1999)
	Bayesian inference	<ul style="list-style-type: none"> • The final 'soft' decision is reached using Bayes rule to combine probabilities. • The <i>a posteriori</i> probability of a given sensor outcome or event is inferred, based on a priori estimates of outcome probability and the likelihood of sensor prediction. • For image fusion, a Bayesian framework may also provide a maximum likelihood <i>a posteriori</i> estimate of a true scene, based on noisy input images. 	Giacinto and Roli (1997) Stassopoulou <i>et al.</i> (1998) Byington and Garga (2001) Roemer <i>et al.</i> (2001) Farang <i>et al.</i> (2002) Paletta and Pare (2002)
	Dempster-Shafer evidence theory	<ul style="list-style-type: none"> • A 'soft' decision is reached from considering sensor imprecision and uncertainty. This comprises sensor <i>belief</i> and <i>plausibility</i> functions. • Method is particularly useful for unreliable or imprecise data. 	Le Hegara-Masclé <i>et al.</i> (1998, 2000) Roemer <i>et al.</i> (2001)
	Conditional probability	<ul style="list-style-type: none"> • Most likely decision is chosen on the basis of a conditional probability rule, such a minimization of misclassified pixels. 	Farang <i>et al.</i> (2002)
	Metaclassifier	<ul style="list-style-type: none"> • Output from primary measurement or feature level classifiers forms the input to a secondary classification. 	Giacinto and Roli (1997)

In an effort to formalize procedures for addressing post-earthquake and post-chemical attack scenarios, Llinas (2002) highlights: analysis problem encoding; design and development of a synthetic task environment; and *review of candidate fusion algorithms* (see also Llinas, 1997), as key steps towards developing a robust methodology. With respect to the final step, Objective 2 of this report sets out *'to determine whether multi-sensor data fusion improves the performance of building damage detection methodologies'* (see Section 1, also Table 1-1). The following sections address this objective, by demonstrating the potential of data fusion techniques to generate enhanced information concerning earthquake damage in Golcuk. Examples are based on fusing optical and SAR imagery, a research area receiving increasing attention in the literature (Korona and Kokar, 1997; Le Hegarat-Masclé *et al.*, 1998, 2000; Pohl and Van Genderen, 1998; Xiao *et al.*, 1998; Pohl and Touron, 1999; Waltz, 2001). If implemented as part of an operational system, it is envisaged that these results will significantly enhance emergency response efforts in future events. Section 5.2 and Section 5.3 summarize measurement and feature level techniques incorporated into the analysis presented in Section 3 and Section 4. Section 5.4 presents an innovative new performance-weighted decision fusion approach to identifying city-wide variations in the extent of building damage. It is important to note that this research is exploratory by nature, with a focus on methodological development, rather than widespread application.

5.2 Measurement Level Fusion

In context of the present study, measurement level techniques of data fusion have already been employed for visualization (see Section 3.3.2) and the spectral characterization of zone-based damage states (Section 4.1). Color-related and numerical approaches have been employed at the measurement level, with coverage from several sensors combined on a per pixel basis, producing a single output image. In Figure 3-10 and Figure 3-12, a HSI transformation was performed (for details see Table 5-1). SPOT panchromatic data determines the saturation or brightness of the image, while SAR intensity modifies the hue. In Figure 3-15 and Figure 3-16, a similar procedure employs a standard city map for the saturation, and results of the block correlation analysis for the hue. The results are clearly beneficial. It becomes easier to interpret the SAR response when combined with more familiar optical coverage, and success of the change detection algorithm is more readily assessed once combined with the city map.

Numeric fusion was performed through the calculation of difference and correlation measures using images acquired before and after the earthquake. From Figure 3-22 through Figure 3-24, these measures were computed on a per pixel- or correlation window-basis for visualization purposes. The following section describes their subsequent manipulation using a feature level approach, to generate descriptive statistics for object-orientated zones.

5.3 Feature Level Fusion

For the present study, feature level fusion is distinguished from measurement level operations by the role of *zones*, rather than pixels, as the basic spatial unit. During Section 3, vector-based ground truth data were fused with both input images (see Figure 3-9 and Figure 3-11), and derived difference and correlation measures (see Figure 3-3, Figure 3-14, Figure 3-17 and Figure 3-18). The introduction of these zones aids viewer orientation, thereby enhancing visualization. In terms of spectral characterization, the damage profiles in Section 4 were produced using descriptive feature level statistics. This form of abstraction converted pixel-based measurements into a central measure of tendency at the object level, followed by zonal aggregation according to damage state.

The bi-variate damage plots in Section 4.3 illustrate the manner in which feature level data fusion may enhance the distinguishing capability of remote sensing datasets (see also Aoki *et al.*, 1998). Although damage profiles indicated that on an individual basis, SAR and optical measures vary with building damage, under certain circumstances, each is problematic. For example, certain bands of the SPOT image were affected by smoke in western regions of Golcuk. This appeared to suppress DN values throughout the area, resulting in radiometrically distorted damage profiles. Since the SAR response is not affected by smoke, the fusion of these datasets should improve the damage state classification. Other distorting effects include: cloud cover, seasonal change, noise, and variable illumination conditions (see also Le Hegarat-Masclé *et al.*, 1998). Data fusion could equally separate features that look similar in some, but not all scenes. For example, concrete buildings and roadways are difficult to distinguish in optical images. However, buildings are often corner reflectors, producing a high return in SAR coverage, while roadways diffuse the signal. The bi-variate example, conceptualized in Figure 5-2, combines damage profiles obtained from optical and SAR sensors. Each zone may be

represented by a state vector comprising a mean value for optical and SAR correlation. The fusion process aggregates both measures by damage state to produce a centroid (and error bars) in 2D feature space. This approach is synonymous with the cluster analysis described in Table 5-1, and could be readily extended incorporate additional measures of change.

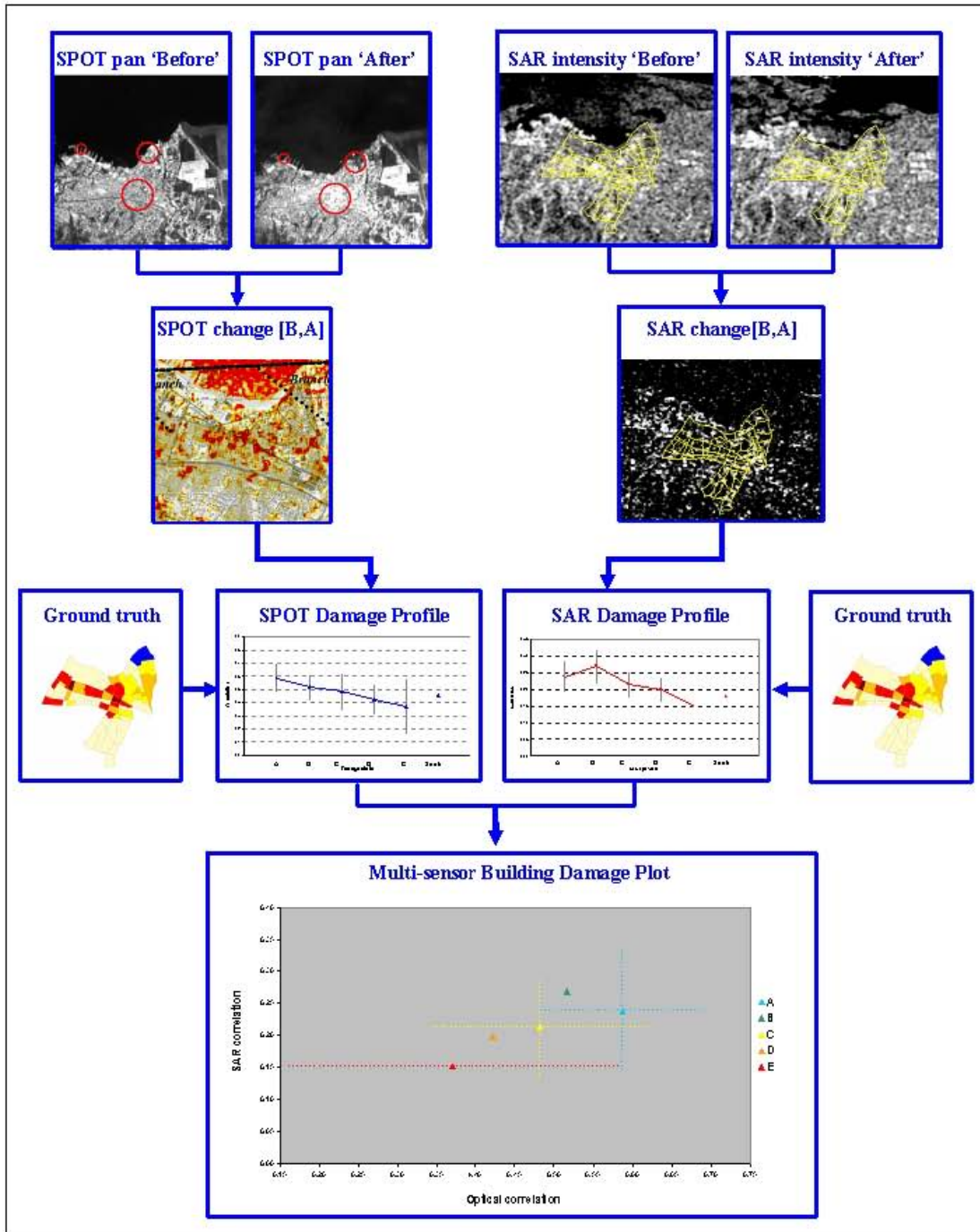


FIGURE 5-2 Schematic representation of bi-variate sensor (SAR and optical) data fusion, for post-earthquake building damage assessment.

5.4 Performance-Weighted Decision Fusion

To further illustrate the value of data fusion in emergency earthquake response, this section of the report introduces a decision fusion approach towards building damage categorization. The fusion process is similar to the weighted approach described in Table 5-1. For the present study, a hard decision is made based on *a priori* knowledge of ‘performance’, which is measured in terms of the reliability and accuracy levels assigned to the various measures of change.

Of the 70 damage zones for Golcuk, the 69 recording building damage states A-E are used to illustrate the methodological process in Figure 5-3 (the category ‘Sunk’ is excluded). Following a similar sampling strategy to Rahman and Fairhurst (1998) and Solberg *et al.* (2002), the ground truth dataset is divided into *calibration* and *validation* components. As shown in Figure 5-4, the former consists of 49 zones. This subset was selected according to an equi-percentage class rule (see also Table 5-2), to ensure that each damage class (A-E) is represented during both the training and test phases. The latter employs the remaining 20 zones to offer a quantitative assessment of fusion-related improvement.

TABLE 5-2 Subdivision of Golcuk zone-based damage observations into calibration and validation datasets (see also Figure 5-4).

Damage class	Total number of zones	Number of zones for Calibration	Number of zones for Validation
A	33	24	9
B	11	8	3
C	9	6	3
D	14	10	4
E	2	1	1

5.4.1 Model Calibration

The calibration phase commences with forging empirical relationships between indices of change recorded on remote sensing coverage, and the extent of building collapse observed in the 49 Golcuk zones. The following ten measures obtained from SPOT and SAR coverage (see Section 4) were employed:

- **SPOT difference** (panchromatic & infrared) – dif_PAN[B,A] and dif_IR[B,A]
- **SPOT correlation** (panchromatic & infrared) – cor_PAN[B,A] and cor_IR[B,A]
- **SPOT block correlation** (panchromatic & infrared) – bk_cor_PAN[B,A] and bk_cor_IR[B,A]
- **SAR difference** (using scenes B2 and A1) - dif [B2,A1]
- **SAR correlation** (using scenes B2 and A1) - cor [B2,A1]
- **SAR block correlation** (using scenes B2 and A1) – bk_cor [B2,A1]
- **SAR complex correlation or coherence** (using scenes B2 and A1) - coh [B2,A1]

A state vector was constructed for every object (zone) in the Golcuk calibration dataset, including a mean value for each of the above indices. Empirical damage models were then plotted, with the relationship between the damage index and percentage of building collapse trained as a linear regression function. The regression function performs a similar role to the classification models adopted by Farag *et al.* (2002). However, the alternative approach employed here is better suited to available ground truth data. Standard classification algorithms are particularly effective when the objective is defining non-continuous classes such as water, urban, and agricultural land uses (see, for example, Aplin *et al.*, 1999; Farag *et al.*, 2002), which occupy disparate locations in the feature space. In contrast, the percentage building damage is an interval dataset, with continuous values allocated to ordered classes. The linear regression model is well suited to these sequential classes, and offers an illustrative representation of the categorization process that is largely absent from pre-programmed classification models.

Figure 5-5 shows the resulting empirical models. In general, these follow a similar tendency to the damage profiles in Section 4, which are based on the full set of zones. Correlation and block correlation levels for both sensors tend towards zero, as the percentage of collapsed structures attains a maximum. Difference measures are somewhat less consistent. In the case of SPOT panchromatic, the difference between ‘before’ and ‘after’ scenes is increasingly pronounced as the building damage level and density of bright debris increases. However, SPOT infrared and ERS regression functions are less straightforward. A tendency towards zero offset as damage level increases is, in the former case, attributable to radiometric distortions caused up smoke emanating from the burning Tupras refinery (see Figure 3-26). In the latter case, the narrow range of dif[B2,A1] values is indicative of limited sensitivity to building collapse.

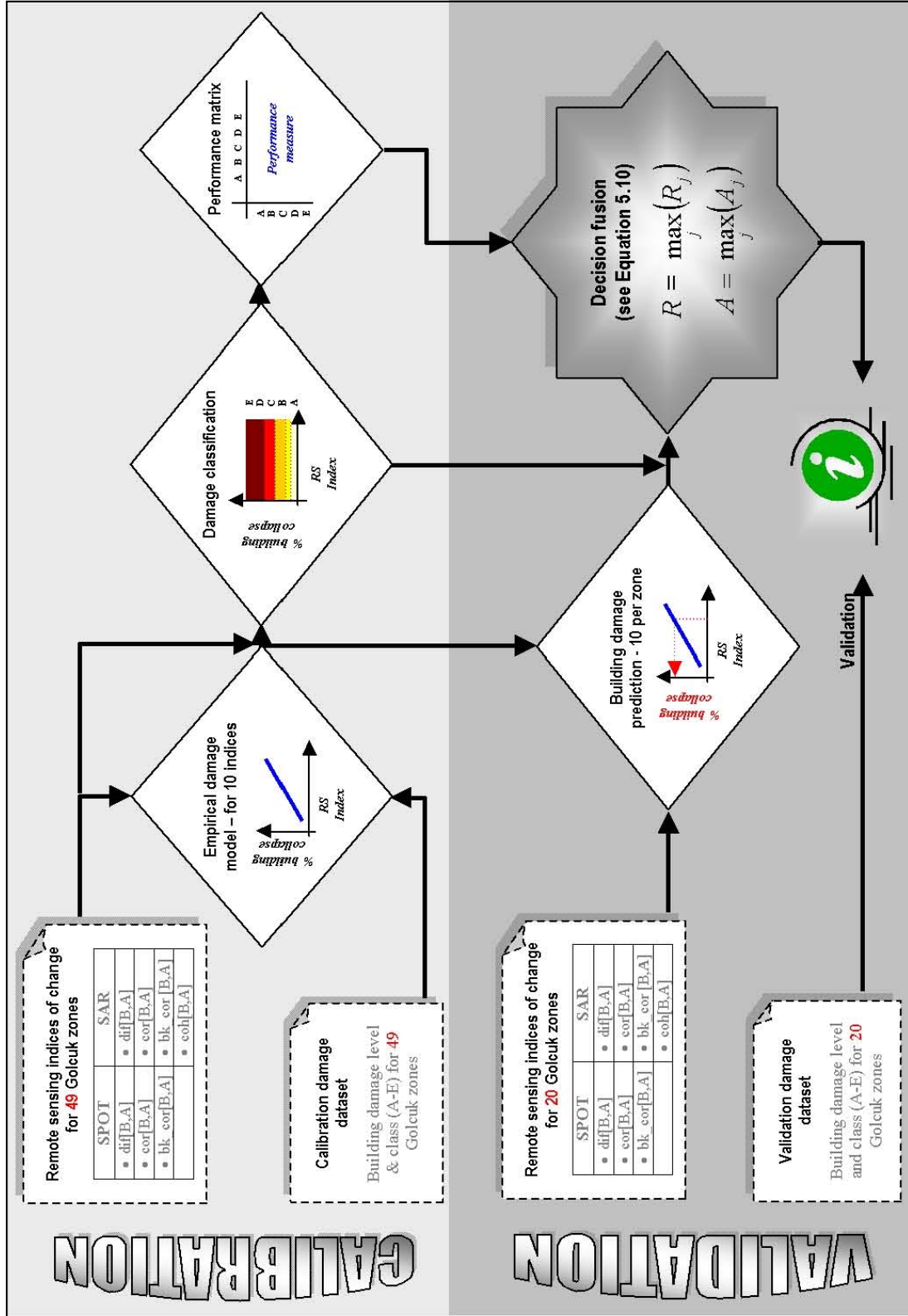


FIGURE 5-3 Schematic representation of calibration and validation phases of an *a priori* performance-weighted decision fusion approach to building damage classification.

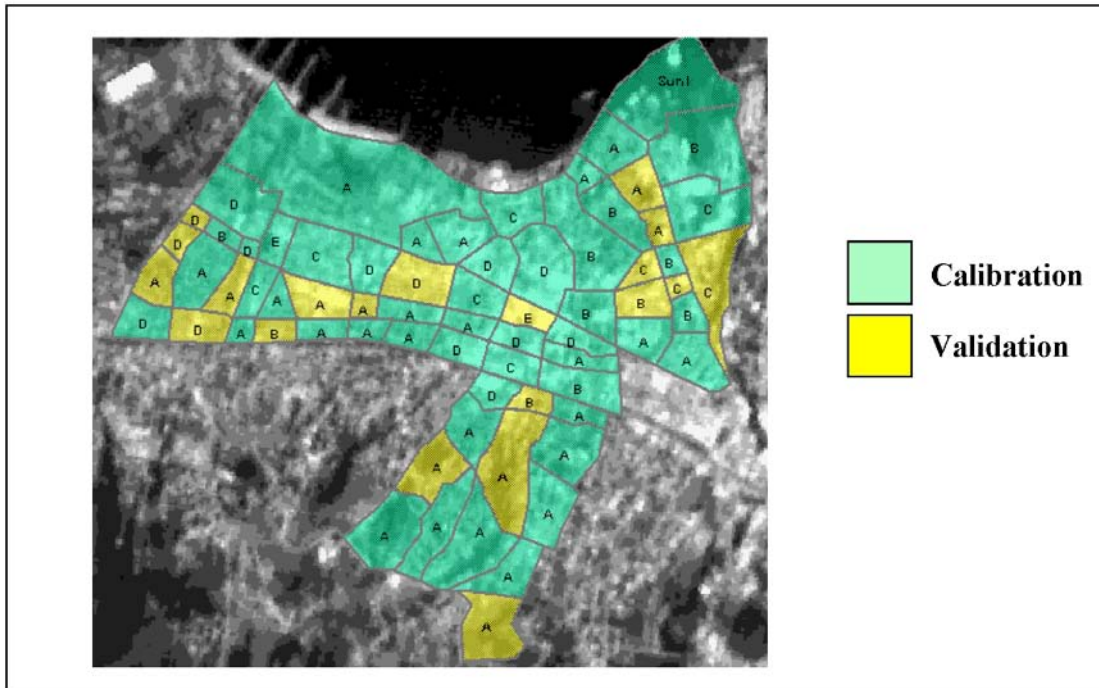


FIGURE 5-4 Division of Golcuk ground truth zones into calibration and validation datasets.

Judging from the R-square (R^2) statistics in Table 5-3, the *individual* predictive capability of the models is somewhat limited. Although R^2 values for dif_PAN[B,A], cor_PAN[B,A], bk_cor_PAN[B,A] and bk_cor[B2,A1] are slightly higher, considerable scatter is still present about these trendlines (see Figure 5-5a,c,e,i). For the present study, scatter about the general tendency may be attributed to the zone-based scale of analysis, which is in turn, a function of the available ground truth observations. While the occurrence of collapsed buildings is expressed as a percentage of total observed structures, the figure fails to consider subordinate factors that may influence radiometric return. Mixed pixel effects may play a significant role, where the density of buildings varies with the concentration of alternative industrial, infrastructure, commercial, or recreational land use. However, in the absence of more detailed ground truth data, it is not possible to scale the sample zones by density of residential land use.

These general observations are borne out by the *performance matrices* in Figure 5-6, the highlighted diagonal of which expresses the degree of correspondence between observed and estimated building collapse. Constructing the matrix is a two stage process, involving training the classifier and calculating a performance function. The initial classification stage (see

Equation 5-1) is performed according to Equation 5-2 and Equation 5-3. Remotely sensed values for the same 49 zones were passed through the previously generated regression functions (see Table 5-3), thereby ‘estimating’ the percentage of building collapse. Damage readings were then converted to the nominal A-E scale, using the grouping scheme g^s .

$$C^s = g^s(E^s) = g^s(h^s(S^s)) = F^s(S^s) \quad (5-1)$$

$$E^s = h^s(S^s) \quad (5-2)$$

$$C^s = g^s(E^s), C^s \in \{A, B, C, D, E\} \quad (5-3)$$

- S^s : Zone-based measurement s (mean for SPOT or SAR index of change)
 E^s : Estimated value associated with measurement s , (in this study, the percentage of collapsed buildings within the zone)
 C^s : Nominal class based on classification index E
 h^s : Established (trained) relationship between measurement and classification index (this study uses simple linear regression)
 g^s : Classification function using the estimated index E , whereby
 A: $0 < E^s \leq 6.25$
 B: $6.25 < E^s \leq 12.5$
 C: $12.5 < E^s \leq 25$
 D: $25 < E^s \leq 50$
 E: $50 < E^s \leq 100$
 F^s : Classifier of measurement s .

For the second stage, performance data for each index of change was generated at this classificatory level. The statistical correspondence between observed and estimated occurrences of classes A-E was computed using Equation 5-4 through Equation 5-6.

$$P_{i,j}^s = P\{i = C^s, j = \bar{C} | S^s\}, i = A...E, j = A...E \quad (5-4)$$

For the present study, $P_{i,j}^s$ denotes the number of members (cardinality) of a set where the classifier of measurement s estimates class- i when the measurement is S^s , while the observed class of the feature is j . For example, in Figure 5-6a when s is dif_PAN, $i=B$ and $j=A$, $P_{i,j}^s=13$. When estimation of i is an independent random event, $P_{i,j}^s$ is represented by a conditional *probability*. For the non-independent case, where the same training dataset is used to develop the regression model and calibrate the matrix, $P_{i,j}^s$ is a instead measure of *performance*.

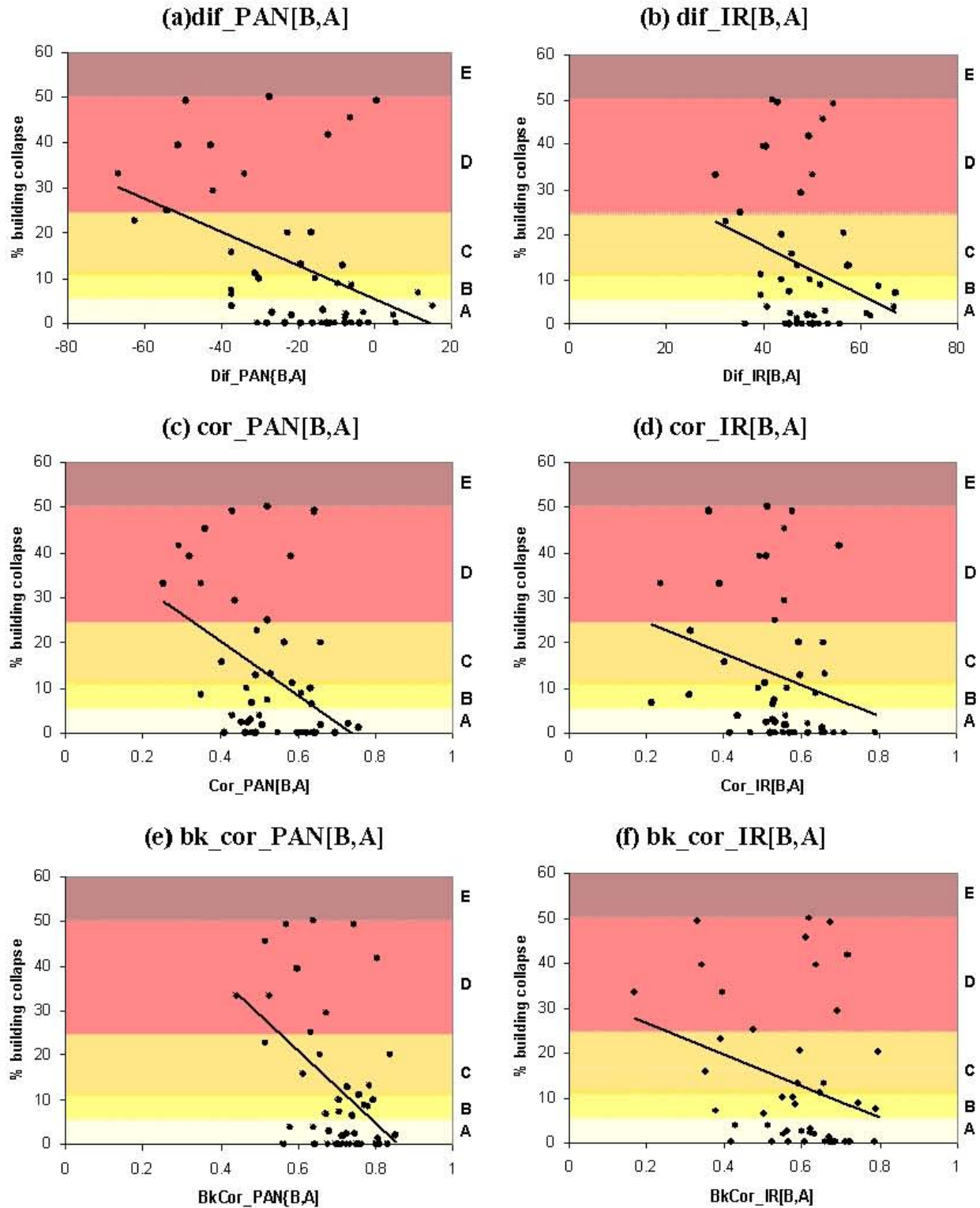


FIGURE 5-5 Damage models for the 10 indices of change recorded using SPOT and SAR remote sensing coverage. Linear regression functions model the relationship with ground truth measurements for the percentage of collapsed buildings in 49 calibration zones. The range and boundaries for corresponding damage classes A-E, are illustrated in color.

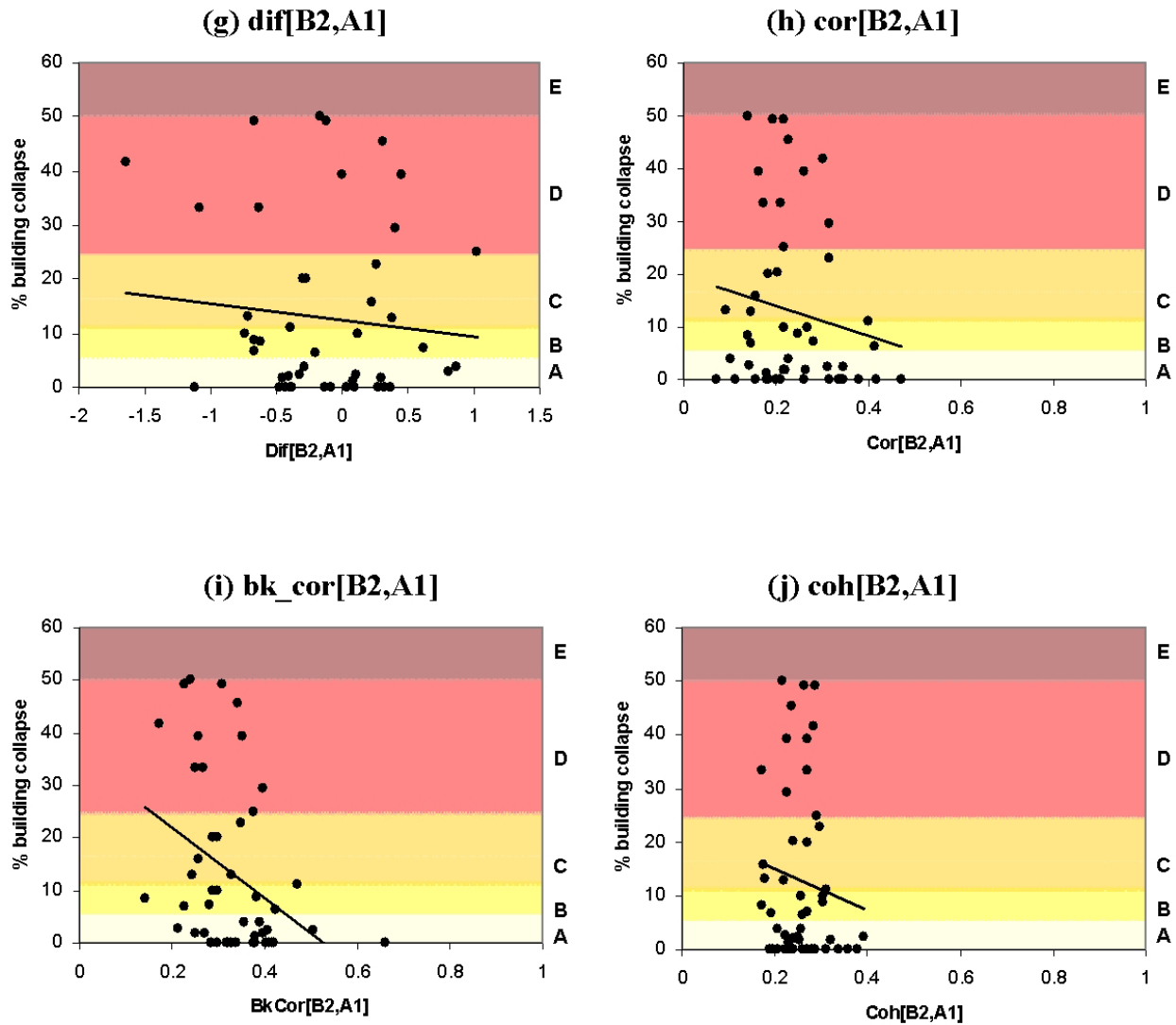


FIGURE 5-5 cont. Damage models for the ten indices of change recorded using optical SPOT and SAR ERS remote sensing coverage. Linear regression functions model the relationship with ground truth measurements for the percentage of collapsed buildings. The range and boundaries for corresponding damage classes A-E, are illustrated in color.

TABLE 5-3 Statistical summary of linear regression functions used to model the relationship between remote sensing indices of change and percentage building collapse.

Sensor	Index	α			β			R^2	F
		Coefficient.	t	p	Coefficient.	t	p		
SPOT	dif_PAN[B,A]	-0.38	-3.32	0.002	5.30	1.72	0.09	0.19	11.06
	dif_IR[B,A]	-0.54	-1.93	0.06	39.47	2.83	0.007	0.07	3.74
	cor_PAN[B,A]	-59.95	-3.27	0.002	44.25	4.50	0.001	0.18	10.70
	cor_IR[B,A]	-34.34	-1.80	0.08	31.34	2.97	0.004	0.06	3.22
	bk_cor_PAN[B,A]	-81.12	-3.72	0.001	69.56	4.53	0.001	0.22	13.85
	bk_cor_IR[B,A]	-35.52	-2.18	0.03	33.89	3.42	0.001	0.09	4.75
ERS	dif[B2,A1]	-3.05	-0.69	0.50	12.43	5.19	0.001	0.01	0.47
	cor[B2,A1]	-28.60	-1.14	0.26	19.63	3.10	0.003	0.03	1.31
	bk_cor[B2,A1]	-66.97	-2.77	0.01	35.21	4.21	0.001	0.14	7.66
	coh[B2,A1]	-38.59	-0.85	0.40	22.79	1.91	0.06	0.02	0.72

Following Farag *et al.* (2002), two possible performance measures are presented, which will be referred to as reliability R (Equation 5-5) and accuracy A (Equation 5-6). R_j^s and A_j^s represent the performance of measurement s in classification of j . This ratio records ‘the number of cases in which the estimated class i matches the observed class j ’, against ‘the number of cases in which the observed class is j ’.

$$R_i^s = \frac{P_{i,i}^s}{\sum_j P_{i,j}^s}; \quad i = A...E, j = A...E \quad (\text{reliability}) \quad (5-5)$$

$$A_j^s = \frac{P_{j,j}^s}{\sum_i P_{i,j}^s}; \quad i = A...E, j = A...E \quad (\text{accuracy}) \quad (5-6)$$

Figure 5-6 shows the derived matrix for each measure of change. As the final step in this calibration phase of the decision fusion process, separate reliability and accuracy matrices were created, summarizing the respective measures by sensor and class. As described in the following section, these provide a statistical weighting for determining the most likely level of building damage within each zone of the validation dataset.

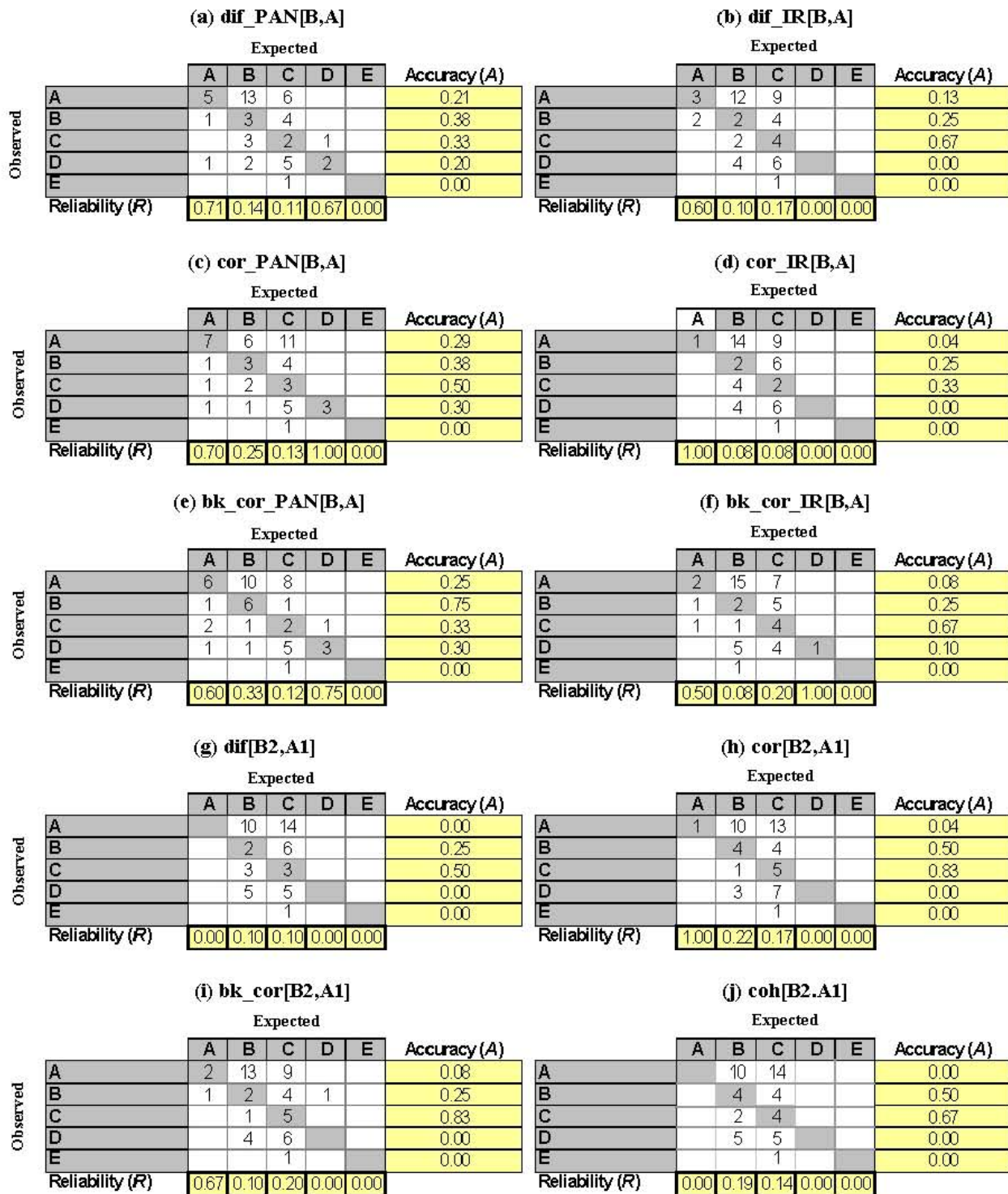


FIGURE 5-6 Performance matrices for the 10 measures of change recorded using SPOT optical and ERS SAR imagery of Golcuk acquired before and after the 1999 Marmara earthquake. Reliability (R) and accuracy (A) indices, based on the 49 calibration zones, are shown for each index (see Equation 5-4 and Equation 5-5).

5.4.2 Model Validation

As shown by the schematic representation of the performance-weighted decision fusion methodology in Figure 5-3, the validation phase was undertaken using a subset of 20 zones within the city of Golcuk (see Figure 5-4; also Table 5-2). A state vector was constructed for every zone, comprising the average for each measure of change recorded from the SPOT and SAR coverage. Following the procedure outlined in Equation 5-1, these values were input to the trained regression functions and an initial estimate of percentage building collapse generated. The ten predictions were then converted to damage classes using Equation 5-7, in preparation for the final phase of decision fusion.

Fusing the individual responses may be conceptualized as a two-step procedure. For a given zone, individual decisions from the ten indices were first assigned to an incidence matrix X_j^s . The matrix was constructed according to Equation 5-8, using a Boolean conditional rule (0,1) to represent each decision. As the second step, the class-wise reliability or accuracy measures (see Section 5.3.1) were aggregated using Equation 5-9a or Equation 5-9b respectively. The maximum aggregated performance of the sensors in Equation 5-10 indicates the most likely state, and was therefore selected as the fused decision.

$$C^s = F^s(S^s), \quad C^s \in \{A, B, C, D, E\} \quad (5-7)$$

$$\text{if } j = Cs \text{ (classified to } j \text{ by measurement } s), X_j^s = 1, \text{ else } X_j^s = 0 \quad (5-8)$$

$$R_j = \sum_s R_j^s \cdot X_j^s; \quad j = A \dots E \quad (\text{reliability}) \quad (5-9a)$$

$$A_j = \sum_s A_j^s \cdot X_j^s; \quad j = A \dots E \quad (\text{accuracy}) \quad (5-9b)$$


$$R = \max_j (R_j); \quad j = A \dots E \quad (\text{reliability}) \quad (5-10a)$$

$$A = \max_j (A_j); \quad j = A \dots E \quad (\text{accuracy}) \quad (5-10b)$$

The *individual* predictive capability of the ten indices of change provides a benchmark for determining whether decision fusion yields superior results. From Table 5-4, these trends follow

the R^2 values associated with the calibration regression functions (see Table 5-3). SPOT panchromatic difference and correlation measures perform the best, recording a maximum agreement of 40% between observed and estimated damage states. Reduced diagnostic capability of 20-30% for infrared wavelengths is attributable to the distorting effect of smoke in the upper atmosphere. Performance for the optical coverage is typically superior to the SAR data. Apart from the 35% agreement level recorded by block correlation, values of 15-25% reaffirm the limited distinguishing capability of ERS difference and coherence measures.

TABLE 5-4 Predictive capability of SPOT and ERS indices of change for damage classification, recorded *individually* and using *performance-weighted* decision fusion.

Sensor	Indices of change	Agreement between observed and expected damage classes (A-E)	
SPOT	dif_PAN[B,A]	40%	
	dif_IR[B,A]	30%	
	cor_PAN[B,A]	40%	
	cor_IR[B,A]	20%	
	bk_cor_PAN[B,A]	40%	
	bk_cor_IR[B,A]	15%	
ERS	dif[B2,A1]	25%	
	cor[B2,A1]	15%	
	bk_cor[B2,A1]	35%	
	coh[B2,A1]	20%	
Decision fusion		Reliability	50%
		Accuracy	15%

In comparison, the reliability-based decision fusion approach yields a higher level of 50% agreement between observed and estimated responses. This suggests that in future earthquakes, performance-weighted decision fusion would be a valuable addition to remote sensing damage detection methodologies determining the location and extent of building collapse.

5.5 Summary of Key Findings

The key findings from Section 5 of this report may be summarized as follows:

- ❖ A review of the literature suggests that increasingly, data fusion techniques are being applied to remote sensing imagery. Their implementation within the emergency management arena is very much in its infancy, with Llinas (2002) highlighting the review of candidate fusion algorithms as a key step towards methodological formalization.
- ❖ In terms of the basic data fusion processing architecture, a fundamental distinction can be made between measurement, feature and decision level approaches. A useful summary is presented of techniques documented in the literature.
- ❖ Objective 2 of this study sets out to determine whether multi-sensor fusion improves the performance of building damage detection methodologies. Exploratory studies undertaken at measurement, feature and decision fusion levels suggest that data fusion augments the building damage detection methodologies presented here, and as such, should be included in future algorithm development.
- ❖ At a ‘measurement’ level, the interpretation of noisy SAR coverage for Golcuk and Adapazari was improved through the use of an HSI transformation. The substitution of optical and map data for brightness values was found to enhance the qualitative assessment of changes between ‘before’ and ‘after’ scenes, which may be related to earthquake building damage.
- ❖ At a ‘measurement’ level, measures of change were obtained through the numeric fusion of remote sensing images recorded before and after the earthquake. The derived indices of difference, correlation and coherence facilitate quantitative analysis of the magnitude and extent of changes, which are used here to ascertain the location, extent and severity of building damage.
- ❖ At a ‘feature’ level, multi-sensor bi-variate damage plots bring together the zone-based characteristics of optical and SAR imagery. The preliminary investigation conducted here suggests that the integration of SPOT damage signatures with changes in texture and geometry captured by ERS imagery, enhances the distinction between levels of building damage. Combining several data sets in this way may prove particularly useful when the distinguishing capability of a single measure is compromised by extraneous effects like smoke or cloud cover.

❖ At the ‘decision’ level, a novel performance-weighted approach to data fusion is presented. A reliability measure was found to increase the prediction of damage state (A-E) from remote sensing data, compared with the performance of individual SPOT and SAR indices of change.

SECTION 6

KEY FINDINGS AND RECOMMENDATIONS

6.1 Overview of Findings

In addressing the general aim identified by the logistical framework diagram in Table 1-1, the research presented here explores how remote sensing technologies can make an important contribution to improving post-earthquake response and recovery activities through characterizing the location, severity and extent of urban building damage.

In characterizing the *location* of building damage (Objective 1a), exploratory visualization suggests that collapsed structures record a distinct signature on remote sensing coverage. By comparing a multi-temporal sequence of optical and SAR scenes, acquired before and after the 1999 Marmara earthquake, the following generalizations can be made:

- ❖ From SPOT 4 panchromatic coverage of Golcuk, areas with a high concentration of collapsed buildings appear *brighter* in the post earthquake image.
- ❖ From the SPOT 4 difference image for Golcuk, values are *strongly negative* in areas with a high concentration of collapsed buildings. This confirms that DN values and brightness levels are generally higher in the ‘after’, compared with the ‘before’ image.
- ❖ From ERS sliding window and block correlation images for Golcuk and Adapazari, correlation values tend to *decrease* as the concentration of collapsed structures increases.

Graph-based damage profiles, bivariate damage plots and damage probability curves are presented as methodological procedures for characterizing the *severity* of earthquake building damage (Objective 1b). Damage profiles express the changing signature of building damage in SPOT and ERS coverage, as the concentration of collapsed structures increases from 0-100%. Based on aggregated responses for the Golcuk and Adapazari study zones:

- ❖ The difference in brightness on SPOT 4 coverage widens from zero to $\text{dif}[B,A] \sim -50\text{DN}$ as the concentration of collapsed structures increases from damage state A-E.

- ❖ SPOT 4 sliding window correlation values decrease from $\text{cor}[B,A] \sim 0.58$ to $\text{cor}[B,A] \sim 0.38$ as the concentration of collapsed structures increases from damage state A-E.
- ❖ SPOT 4 block window correlation values decrease from $\text{bk_cor}[B,A] \sim 0.75$ to $\text{bk_cor}[B,A] \sim 0.55$ as the concentration of collapsed structures increases from damage state A-E.
- ❖ ERS sliding window correlation decreases from $\text{cor}[B2,A1] \sim 0.25$ to $\text{cor}[B2,A1] \sim 0.15$ as the concentration of collapsed structures increases from damage state A-E.
- ❖ ERS block correlation decreases from $\text{bk_cor}[B2,A1] \sim 0.37$ to $\text{bk_cor}[B2,A1] \sim 0.22$ as the concentration of collapsed structures increases from damage state A-E.

In characterizing the location and severity of building damage, certain indices of change proved more useful than others. Associations were difficult to discern from SAR difference and correlation values, which appeared to be subject to considerable noise. For these indices of change, pixel and zone based scales of analysis have limited sensitivity to building damage. The magnitude and pattern of response on SPOT 4 infrared coverage was also deemed less reliable than its panchromatic counterpart, due to the obscuring effect of smoke in the upper atmosphere.

From general consistency in building damage signatures for the cities of Golcuk and Adapazari, the qualitative and quantitative damage detection methodologies presented here could be used to assess damage *extent* at a regional scale (Objective 1c). However, further studies are required to determine whether these empirically-based results vary on a broader international basis, as the building stock changes.

In addressing Objective 2, the investigative research documented here suggests that data fusion undertaken at measurement, feature and decision levels holds considerable promise for improving the performance of building damage detection methodologies. In theoretical terms, the integration of optical and SAR data brings together the benefits of straightforward visual interpretation (optical) with 24/7, all weather viewing (radar).

At the measurement level, the integration of coverage for Golcuk and Adapazari through HIS transformation enhances qualitative assessment. Derived indices of change underpinning the

damage detection process are also obtained through measurement level fusion; in this case the fusion of multi-temporal imagery through subtraction and correlation. At the feature level, multi-sensor bi-variate damage plots demonstrate how remote sensing characteristics co-vary as the severity of damage increases. Compared with the individual measures, this method of fusion offers enhanced distinguishing capability between damage states A-E. At the decision level, a novel performance-weighted approach offers increased reliability of damage state estimation. These illustrative examples go some way towards satisfying the pressing need identified by Llinas (2002) for a ‘review of candidate fusion algorithms’, as a key step towards the widespread implementation of data fusion in post-earthquake response and recovery.

6.2 Recommendations

The research documented in this report demonstrates how remote sensing data can be used to determine the location, severity and extent of earthquake building damage, based on imagery acquired for the 1999 Marmara event. To establish the more widespread applicability of the methodologies presented here, it is vital that the techniques are applied to future earthquakes occurring in other cities around the world. This will determine the extent to which the empirically-based associations reported here can be directly applied to other events, or if a scaling factor is required.

This study employs SPOT 4 and ERS coverage as the principal sources of remote sensing information. When the Marmara earthquake occurred, SPOT 4 was one of the highest resolution sources for commercial imagery captured ‘before’ and ‘after’ the event. Following the recent launch of optical QuickBird and IKONOS satellite sensors, a new generation of very high resolution imagery has become available. These systems offer superior distinguishing capability, together with the possibility of damage assessment on a per building basis (see, for example, Adams *et al.*, 2003). Existing qualitative and quantitative damage detection methodologies should be tested using these additional sources of imagery, and adjustments made accordingly. Based on this more detailed coverage, new approaches to damage detection should also be explored, using techniques such as edge detection and texture analysis.

For remote sensing technology to play an active role in future earthquake reconnaissance, response and recovery efforts, an implementation plan is required that outlines procedures for image acquisition, processing and the dissemination of results. This should include the necessary agreements with data providers, and allocation of responsibilities for ordering and processing the data. Contacts should also be forged with governments and international aid organizations that will be using the data.

SECTION 7

REFERENCES

- Achalakul, T. (2002) A survey of fusion techniques for multi-spectral images, *Proceedings of the International Technical Conference on Circuits/Systems, Computers and Communications*, Thailand.
- Adams, B.J., Huyck, C.K. and Eguchi, R.T. (2003) *The Boumerdes (Algeria) Earthquake of May 21, 2003: Preliminary Reconnaissance Using Remotely Sensed Data*, <http://mceer.buffalo.edu/research/boumerdes/default.asp>.
- Adams, B.J., Huyck, C.K., Mansouri, B., Eguchi, R.T. and Shinozuka, M. (2002) Post-disaster bridge damage assessment, *Proceedings of the Joint ISPRS and TRB Conference*, Denver.
- Aiazzi, B., Alparone, L., Baronti, S., Pippi, I. and Selva, M. (2002) Generalised laplacian pyramid-based fusion of MS + P image data with spectral distortion minimization, *Proceedings of the ISPRS Commission III Symposium on Photogrammetric Computer Vision*, Graz, Austria.
- AIJ, 1999, *Report on the Damage Investigation of the 1999 Kocaeli Earthquake in Turkey*, AIJ: Tokyo.
- Andre, G., Chiroiu, L., Mering, C. and Chopin, F. (2003) Building destruction and damage assessment after earthquake using high resolution optical sensors. The case of the Gujurat earthquake of January 26, 2001, *Proceedings of the IGARSS 03*, Toulouse.
- Aoki, H., Matsuoka, M. and Yamazaki, F., 1998, Characteristics of satellite SAR images in the damaged areas due to the Hyogoken-Nanbu earthquake, *Proceedings of the 1998 Asian Conference on Remote Sensing*, <http://www.gisdevelopment.net/aars/acrs/1998/ts3/ts3007.shtml>.
- Aplin, P., Atkinson, P.M. and Curran, P.J. (1999) Per-field classification of land use using the forthcoming very fine spatial resolution satellite sensors: Problems and potential solutions, *In* Atkinson, P.M. and Tate, N.J. (eds) *Advances in Remote Sensing and GIS Analysis*, Wiley: Chichester, p. 219-241.
- Aschheim, M., 2000, Performance of buildings, *In* Youd, T.I., Bardet., J and Bray, J.D. (eds.) *Earthquake Spectra Supplement A to Volume 16: Kocaeli, Turkey, Earthquake of August 17, 1999 Reconnaissance Report*, 237-279.
- Beauchemin, M., Fung, K.B. and Geng, X. (2002) A method based on local variance for quality assessment of multiresolutional image fusion, *Proceedings of the ISPRS Commission III Symposium on Photogrammetric Computer Vision*, Graz, Austria.
- Beugnon, C., Singh, T., Llinas, J. and Saha, R. (2000) Adaptive track fusion in a multisensor environment, *Proceedings of the 3rd International Conference on Information Fusion*, Paris, France.

Bray, J.D. and Stewart, J.P., 2000, Damage patterns and foundation performance in Adapazari, *In* Youd, T.I., Bardet., J and Bray, J.D. (eds.) *Earthquake Spectra Supplement A to Volume 16: Kocaeli, Turkey, Earthquake of August 17, 1999 Reconnaissance Report*, 163-189.

Bretschneider, T. and Kao, O. (2000) Image fusion in remote sensing, *Proceedings of the 1st Online Symposium of Electronic Engineers*, <http://www.ntu.edu.sg/home/astimo/Publications/OSEE2000.htm>.

Bruneau, M. (2000) Structural damage, *In* Scawthorn, C. (ed.) *The Marmara, Turkey Earthquake of August 17, 1999: Reconnaissance Report, Section 4, Technical Report MCEER-00-0001*, MCEER: Buffalo.

Byington, C.S. and Garga, A.K. (2001) Data fusion for developing predictive diagnostics for electromechanical systems, *In* Hall, D.L. and Llinas, J. (eds.) *Handbook of Multisensor Data Fusion*, CRC: New York, 23.1-23.30.

Campbell, J.B., 1996, *Introduction to Remote Sensing, 2nd ed.*, Taylor and Francis: London.

CEOS (2001) *The Use of Earth Observing Satellites for Hazard Support: Assessments and Scenarios. Final Report of the CEOS Disaster Management Support Group*, http://www.oosa.unvienna.org/SAP/stdm/CEOS_DMSG_Final_Report.pdf.

Chiroiu, L. and Andre, G. (2001) *Damage assessment using high resolution satellite imagery: application to 2001 Bhuj, India earthquake*, www.riskworld.com.

Chiroiu, L., Andre, G., Guillande, R., and Bahoken, F. (2002) Earthquake damage assessment using high resolution satellite imagery, *Proceedings of the 7th U.S. National Conference on Earthquake Engineering*, Boston.

Chiroiu, L., Andre, G. and Bahoken, F. (2003) *Earthquake loss estimation using high resolution satellite imagery*, www.gisdevelopment.net/application/natural_hazards/earthquakes/nheq0005.htm.

Dell Acqua, F., Gamba, P. and Lisini, G. (2002) Extraction and fusion of street networks from fine resolution SAR data, *Data Fusion Special Session IGARSS*, http://dfc.jrc.it/doc/gamba_020624.pdf.

DigitalGlobe (2003) *Quickbird Imagery Products: Product Guide*, <http://www.digitalglobe.com/products/basic.shtml>.

DSTO (1994) *Data Fusion Lexicon*, Data Fusion Special Interest Group. Department of Defense, Australia.

EDM, 2000, *Report on the Kocaeli, Turkey Earthquake of August 17, 1999*, Technical Report Series No. 6, EDM (Riken): Miki.

Eguchi, R.T., Huyck, C.K., Houshmand, B., Mansouri, B., Shinozuka, M., Yamazaki, F. and Matsuoka, M. (2000a) The Marmara Earthquake: A View from Space, In Scawthorn, C. (ed.) *The Marmara, Turkey Earthquake of August 17, 1999: Reconnaissance Report, Section 10, Technical Report MCEER-00-0001*, MCEER: Buffalo.

Eguchi, R.T., Huyck, C.K., Houshmand, B., Mansouri, B., Shinozuka, M., Yamazaki, F. and Matsuoka, M. and Ulgen, S. (2000b) The Marmara, Turkey earthquake: Using advanced technology to conduct earthquake reconnaissance, *MCEER research and Accomplishments 1999-2000*, MCEER: Buffalo.

Eguchi, R.T., Huyck, C.K., Adams, B.J., Mansouri, B., Houshmand, B. and Shinozuka, M. (2003a) Earthquake damage detection algorithms using remotely sensed data – Application to the August 17, 1999 Marmara, Turkey earthquake, *Proceedings of the 7th EERI US/Japan Workshop on Urban Earthquake Hazard Reduction*, Maui.

Eguchi, R.T., Huyck, C.K., Adams, B.J., Mansouri, B., Houshmand, B., and Shinozuka, M. (2003b) Resilient disaster response: Using remote Sensing technologies for post-earthquake damage detection, *MCEER research and Accomplishments 2001-2003*, MCEER: Buffalo.

Elachi, C., 1987, *Introduction to the Physics and Techniques of Remote Sensing*, John Wiley: Chichester.

ESA, 2002, *ERS SAR Toolbox: Overview*, <http://earth.esa.int/services/stbx>.

Estrada, M., Kohiyama, M., Matsuoka, M. and Yamazaki, F. (2001a) Detection of damage due to the 2001 El Salvadore earthquake using Landsat images, *Proceedings of the 22nd Asian Conference on Remote Sensing*, Singapore.

Estrada, M., Matsuoka, M., Yamazaki, F. (2001b) Digital damage detection due to the 1999 Kocaeli, Turkey earthquake, *Bulletin of the Earthquake Resistant Structure Research Center*, 34, 55-66.

Estrada, M., Kohiyama, M. and Yamazaki, F. (2001) *Assessment of satellite imagery capability for damage detection using Landsat 7/ETM+ images for the 2001 Atico, Peru earthquake*, <http://www.ecie.org/sismoatico/semana1/05/003.pdf>.

Farag, A.A., Mohamed, R.M. and Mahdi, H. (2002) Experiments in multimodality image classification and data fusion, *Proceedings of the 5th International Conference on Information Fusion*, Annapolis, Maryland.

Freeman, T., 2000, *What is imaging radar?*, <http://southport.jpl.nasa.gov/desc/imagingradarv3.html>

Gabriel, A.K., Goldstein, R.M. and Zebker, H.A., 1989, Mapping small elevation changes over large areas: differential radar interferometry, *Journal of Geophysical Research*, 94 (B7), 9183-9191.

- Garzelli, A. (2002) Wavelet-based fusion of optical and SAR image data over urban area, *Proceedings of the ISPRS Commission III Symposium on Photogrammetric Computer Vision*, Graz.
- Giacinto, G and Roli, F. (1997) Ensembles of neural networks for soft classification of remote sensing images, *Proceedings of the European Symposium on Intelligent Techniques*, Bari.
- Guojin, H., Kelu, L. and Deyong, H. (1998) A fusion approach of multi-sensor remote sensing data based on wavelet transform, <http://www.gisdevelopment.net/aars/acrs/1998/ts9/ts9004.shtml>
- Hall, D.L. (1992) *Mathematical Techniques in Multisensor Data Fusion*, Artech House, Inc: Norwood.
- Hall, D.L. and Llinas, J. (1997) An introduction to multisensor data fusion, *Proceedings of the IEEE*, 85(1): 6-23.
- Hall, D.L. and Llinas, J. (2001) Multisensor data fusion, In Hall, D.L. and Llinas, J. (eds.) *Handbook of Multisensor Data Fusion*, CRC: New York, 1.1-1.10.
- Hasegawa, H., Aoki, H., Yamazaki, F. and Sekimoto, I. (1999) Attempt for automated detection of damaged buildings using aerial HDTV images, *Proceedings of the 20th Asian Conference on Remote Sensing*, Hong Kong.
- Hasegawa, H., Yamazaki, F., Matsuoka, M. and Seikimoto, I. (2000) Determination of building damage due to earthquakes using aerial television images, *Proceedings of the 12th World Conference on Earthquake Engineering*, Aukland.
- Hashitera, S., Kohiyama, M., Maki, N. and Fujita, H. (1999) Use of DMSP-OLS images for early identification of impacted areas due to the 1999 Marmara earthquake disaster, *Proceedings of the 20th Asian Conference on Remote Sensing*, Hong Kong.
- Hellwich, O. (1999) An alternative paradigm for data evaluation in remote sensing using multisensor data fusion, *IEEE Geoscience and Remote Sensing Symposium IGARSS*, Hamburg.
- Hellwich, O. and Wiedemann, C. (1999) Multisensor data fusion for automated scene interpretation, *SPIE Image and Signal Processing for Remote Sensing V*, 3871: 284-295.
- Hill, J., Diemer, C., Stovre, O. and Udelhoven, Th. (1999) A local correlation approach for the fusion of remote sensing data with different spatial resolutions in forestry applications, *International Archives of Photogrammetry and Remote Sensing*, 32(7-4-3 W6), Valladolid.
- Hill, P., Canagarajah, N. and Bull, D. (2002) Image fusion using complex wavelets, *Proceedings of the British Machine Vision Conference*, Cardiff.
- Homan, J. and Eastwood, W.J., 2001, The 17 August 1999 Kocaeli (Izmit) earthquake: Historical records and seismic culture, *Earthquake Spectra*, 17(4): 617-634.

Huyck, C.K. and Adams, B.J. (2002) *Emergency Response in the Wake of the World Trade center Attack: The Remote Sensing Perspective, MCEER Special Report Series, Volume 3*, MCEER: Buffalo.

Huyck, C.K, Mansouri, B., Eguchi, R.T., Houshmand, B., Castner, L. and Shinozuka, M. (2002) Earthquake damage detection algorithms using optical and ERS-SAR satellite data – Application to the August 17, 1999 Marmara, Turkey earthquake, *Proceedings of the 7th U.S. National Conference on Earthquake Engineering*, Boston.

ISDR (2002) *Living with Risk. A Global View of Disaster Reduction Initiatives*, <http://www.unisdr.org/unisdr/Globalreport.htm>.

Jeon, B. and Landgrebe, D.A. (1999) Decision fusion approach for multi-temporal classification, *IEEE Transactions on Geoscience and Remote Sensing*, 37(3): 1227-1233.

Kokar, K.M. and Tomasik, J. (1994) Towards a formal theory of sensor/data fusion, *Technical Report: COE-ECE-MMK-1/94*, Northeastern University, Boston.

Korona, Z and Kokar, M. M. (1997) Multiresolution Multisensor Target Identification, In Irwin, J. D. (ed.), *The Industrial Electronics Handbook*, CRC Press and IEEE Press: 1627-1632.

Le Hegarat-Masclé, S., Bloch, I. and Vidal-Madjar, D. (1998) Introduction of neighbourhood information in evidence theory and application to data fusion of radar and optical images with partial cloud cover, *Pattern Recognition*, 31(11): 1811-1823.

Le Hegarat-Masclé, S., Quesney, A., Vidal-Madjar, D., Normand, M and Loumagne, C. (2000) Land cover discrimination from multi-temporal ERS images and multispectral Landsat images: a study case in an agricultural area in France, *International Journal of Remote Sensing*, 21(3): 435-456.

Le Hegarat-Masclé, S., Richard, D. and Otle, C. (2003) Multi-scale data fusion using Dempster-Shafer evidence theory, *Integrated Computer-aided Engineering*, 10(1): 9-22.

Lettis, W., Bachhuber, J. and Witter, R., 2000, Surface fault rupture, In Youd, T.I., Bardet., J and Bray, J.D. (eds.) *Earthquake Spectra Supplement A to Volume 16: Kocaeli, Turkey, Earthquake of August 17, 1999 Reconnaissance Report*, 11-53.

Lillesand, T.M. and Keifer, R.W., 1994, *Remote Sensing and Image Interpretation*, 3rd edition, John Wiley: New York.

Llinas, J. (1997) Fusion-based methods for target identification in the absence of quantitative classifier confidence, *Proceedings of the SPIE Conference on Signal Processing, Sensor Fusion and Target Recognition*, Orlando.

Llinas, J. (2002) *Information fusion for natural and man-made disasters*, http://www.infofusion.buffalo.edu/reports/Dr.%20Llinas'%20stuff/papers/info_fusion_natural_man_made_dis.pdf.

Llinas, J. and Hall, D.L. (1998) An introduction to multi-sensor data fusion, *Proceedings of the IEEE International Symposium on Circuits and Systems*, Monterey, 537-540.

Llinas, J and Singh, T. (1998) *Adaptive data fusion processing: thoughts and perspectives*, http://www.infofusion.buffalo.edu/reports/Dr.%20Llinas%20stuff/papers/adap_dt_fusn_pro_thoughts_perspectives.pdf.

Luo, R.C., Yih, C. and Su, K.L. (2002) Multisensor fusion and integration: Approaches, applications and future research directions, *IEEE Sensors Journal*, 2(2): 107-119.

Mansouri, B., Houshmand, B. and Shinozuka, M., 2001, Building change/damage detection in Seymen-Turkey using ERS SAR data, *Proceedings of the 8th Annual International Symposium on Smart Structures and Materials*, Newport Beach.

Massonnet, D., and Rabaute, T., 1993, Radar interferometry: Limits and potential, *IEEE Transactions on Geoscience and Remote Sensing*, 31(2), 455-464.

Matsuoka, M. and Yamazaki, F. (1998) Identification of damaged areas due to the 1995 Hyogoken-Nanbu earthquake using satellite optical images, *Proceedings of the 19th Asian Conference on Remote Sensing*, Manila.

Matsuoka, M and Yamazaki, F. (2000a) Interferometric characterization of areas damaged by the 1995 Kobe earthquake using satellite SAR images, *Proceedings of the 12th World Conference on Earthquake Engineering*, Auckland.

Matsuoka, M. and Yamazaki, F. (2000b) Satellite remote sensing of damaged areas due to the 1995 Kobe earthquake, In Toki, K. (ed.) *Confronting Urban Earthquakes, Report of Fundamental Research on the Mitigation of Urban Disasters Caused by Near-field Earthquakes*, 259-262.

Matsuoka, M. and Yamazaki, F. (2002) Application of the damage detection method using SAR intensity images to recent earthquakes, *Proceedings of the IGARSS*, Toronto.

Matsuoka, M. and Yamazaki, F. (2003) Application of a methodology for detection building-damage area to recent earthquakes using SAR intensity images, *Proceedings of the 7th EERI US Japan Conference on Urban Earthquake Hazard Reduction*, Maui.

MCEER, 2000, *The Marmara, Turkey Earthquake of August 17, 1999: Reconnaissance Report, Technical report MCEER-00-0001*, MCEER: Buffalo.

MCEER (2003) *Overview of MCEER research thrusts*, <http://mceer.buffalo.edu/research/NSFResearch/ResPgrm.asp>.

Mitomi, H., Yamazaki, F. and Matsuoka, M. (2000) Automated detection of building damage due to recent earthquakes using aerial television images, *Proceedings of the 21st Asian Conference on Remote Sensing*, Taipei.

- Mitomi, H., Matsuoka, M. and Yamazaki, F. (2001) Automated detection of buildings from aerial television images of the 2001 Gujarat, India earthquake, *Proceedings of the IEEE International Symposium on Geoscience and Remote Sensing*, Sydney.
- Mitomi, H., Matsuoka, M and Yamazaki, F. (2002) Application of automated damage detection of buildings due to earthquakes by panchromatic television images, *Proceedings of the 7th U.S. National Conference on Earthquake Engineering*, Boston.
- Ogawa, N., Hasegawa, H., Yamazaki, F., Matsuoka, M and Aoki, H. (1999) Earthquake damage survey methods based on airborne HDTV, photography and SAR, *Proceedings of the 5th US Conference on Lifeline Earthquake Engineering*, ASCE, 322-331.
- Ogawa, N. and Yamazaki, F. (2000) Photo-interpretation of buildings damage due to earthquakes using aerial photographs, *Proceedings of the 12th World Conference on Earthquake Engineering*, Auckland.
- Oliver, C. and Quegan, S., 1998, *Understanding Synthetic Aperture Radar Images*, Artech House: Boston.
- Paletta, L. and Paar, G. (2002) Bayesian decision fusion for dynamic multi-cue object detection, *Proceedings of the ICVGIP*, Ahmedabad, India.
- Papageorgiou, A. (2000) Seismology, In Scawthorn, C. (ed.) *The Marmara, Turkey Earthquake of August 17, 1999: Reconnaissance Report, Section 2, Technical Report MCEER-00-0001*, MCEER: Buffalo.
- Partington, K., Keller, M., Seymour, P. and Bertoia, C. (1999) Data fusion for use of passive microwave data in operational sea-ice monitoring, *Proceedings of IGARSS '99*, Hamburg.
- Peltzer, P. and Rosen, P., 1995, Surface displacement of the 17 May 1993 Eureka Valley earthquake observed by SAR interferometry, *Science*, 268: 1333-1336.
- Pinz, A. (1995) Interpretation and fusion – recognition versus reconstruction, In Pinz, A. and Burger, W. (eds.) *Vision Milestones*, OGAI Lecture Series, p. 1-12.
- Pohl, C. (1999) Tools and methods for fusion of images of different spatial resolution, *International Archives of Photogrammetry and Remote Sensing*, 32(7-4-3), Valladolid.
- Pohl, C and Touron, H. (1999) Operational applications of multi-sensor image fusion, *International Archives of Photogrammetry and Remote Sensing*, 32(7-4-3), Valladolid.
- Pohl, C. and Van Genderen, J.L. (1998) Multisensor image fusion in remote sensing: concepts, methods and applications, *International Journal of Remote Sensing*, 19(5): 823-854.
- Qui, S., Agogino, A.M., Song, S., Wu, J. and Sitarama, S. (2001) A fusion of Bayesian and fuzzy analysis for print faults diagnostics, *Proceedings of the 16th International Conference on Computers and Their Applications*, Seattle.

- Rahman, A.F.R. and Fairhurst, M.C. (1998) A novel confidence-based framework for multiple expert decision fusion, *Proceedings of the 9th British Machine Vision Conference*, Southampton.
- Rathje, E., 2000, Strong ground motions and site effects, *In* Youd, T.I., Bardet., J and Bray, J.D. (eds.) *Earthquake Spectra Supplement A to Volume 16: Kocaeli, Turkey, Earthquake of August 17, 1999 Reconnaissance Report*, 65-96.
- Rejaie, S.A. and Shinozuka, M. (2001) *Urban damage assessment from remotely sensed images*, http://mceer.buffalo.edu/publications/sp_pubs/01-SP02/sra_ind/08.pdf.
- Rockinger, O. (1997) Image sequence fusion using a shift-invariant wavelet transform, *Proceedings of the IEEE International Conference on Image Processing*, Washington.
- Rockinger, O. and Fechner, T. (1998) Pixel-level image fusion: the case of image sequences, *SPIE Signal Processing, Sensor Fusion and Target Recognition*, 3374: 378-388.
- Rodriguez, E., and Martin, J.M., 1992, Theory and Design of Interferometric Synthetic Aperture Radars, *IEEE Proceedings-F*, 139(2): 147-159.
- Roemer, M.J., Kacprzynski, G.J. and Orsagh, R.F. (2001) Assessment of data and knowledge fusion strategies for prognostics and health management, *Proceedings of the IEEE Aerospace Conference*, Big Sky.
- Saito, K., Spence, R.J., Going, C. and Markus, M. (2004) Using high-resolution satellite images for post-earthquake building damage assessment: a study following the 26.1.01 Gujarat earthquake, *Earthquake Spectra*, Volume 20: 145-169.
- Sharma, R.K., Leen, T.K. and Pavel, M. (1999) Probabilistic image sensor fusion, *Advances in Neural Information Processing Systems*, 11, MIT Press.
- Slatton, K.C., Crawford, M.M. and Evans, B.L. (2001) Fusing interferometric radar and laser altimeter data to estimate surface topography and vegetation heights, *IEEE Transactions on Geoscience and Remote Sensing*, 39(11): 2470-2482.
- Solaiman, B. (1998) Multisensor/contextual data fusion through membership functions revision. Application to land-cover SAR data classification, *Proceedings of Fusion 98 – International Conference on Multisource-multisensor information fusion*, Las Vegas.
- Solberg, A.S., Storvik, G. and Fjortoft, R. (2002) A comparison of criteria for decision fusion and parameter estimation in statistical multisensor image fusion, <http://www.math.uio.no/~geirs/publications.html>.
- Stassopoulou, A., Petrou, M. and Kittler, J. (1998) Application of a Bayesian network in a GIS based decision making system, *International Journal of Geographical Information Science*, 12(1): 23-46.

- Tagarev, T. and Ivanova, P. (2002) Computational intelligence in multi-source data and information fusion, http://www.isn.ethz.ch/researchpub/publihouse/infosecurity/volume_2/f4/f4_index.htm.
- Thepaut, O., Kpalma, K. and Ronsin, J. (2000) Automatic registration of ERS and SPOT multisensor images in a data fusion context, *Forest Ecology and Management*, 128(1-2): 93-100.
- Trenish, L. (2001) Visual data fusion for decision support applications of numerical weather prediction, *Proceedings of the 17th International Conference on Interactive Information and Processing Systems (IIPS) for Meteorology, Oceanography, and Hydrology*, Albuquerque.
- Wald, L. (1999) Definitions and terms of reference in data fusion, *International Archives of Photogrammetry and Remote Sensing*, 32(7-4-3), Valladolid.
- Wald, L. (2001) *Various unsatisfactory definitions of information fusion*, <http://www.data-fusion.org/article.php?sid=73>.
- Walker, N.P., Gutierrez del Olmo, J. and Laur, H., (1999) *The ERS SAR Toolbox: A Software Package to Help ERS SAR Data Users*, <http://esapub.esrin.esa.it/eoq/eoq64/toolbox.pdf>.
- Waltz, E. (2001) The principle and practice of image and spatial data fusion, In Hall, D.L. and Llinas, J. (eds.) *Handbook of Multisensor Data Fusion*, CRC: New York, 4.1-4.15.
- Wang, Y. and Lohmann, B. (2000) Multisensor image fusion: concept, method and applications, <http://www.iat.uni-bremen.de/lohmann/Papers/wang1.pdf>.
- Webb, G., 2000, Restoration Activities, *The Marmara, Turkey Earthquake of August 17, 1999: Reconnaissance Report, Section 10, Technical Report MCEER-00-0001*, MCEER: Buffalo.
- Xiao, R., Wilson, R. and Carande, R. (1998) Neural network classification with IfSAR and multispectral data fusion, *Proceedings of the IEEE International Symposium on Geoscience and Remote Sensing*, Seattle.
- Yamazaki, F. (2001) Applications of remote sensing and GIS for damage assessment, *Proceedings of the Joint Workshop on Urban Safety Engineering*, Asian Institute of Technology, Bangkok.
- Youd, T.I., Bardet, J. and Bray, J.D., 2000, Kocaeli, Turkey, Earthquake of August 17, 1999 Reconnaissance Report, *Earthquake Spectra Supplement A to Volume 16*, EERI.
- Yusuf, Y., Matsuoka, M. and Yamazaki, F. (2001a) Damage assessment after 2001 Gujarat earthquake using Landsat-7 satellite images, *Journal of the Indian Society of Remote Sensing*, 29(1): 233-239.
- Yusuf, Y., Matsuoka, M. and Yamazaki, F. (2001b) Damage detection from Landsat-7 satellite images for the 2001 Gujarat, India earthquake, *Proceedings of the 22nd Asian Conference on Remote Sensing*, Singapore.

Zhang, Z. and Blum, R.S. (1999) A categorization of multiscale-decomposition-based image fusion schemes with a performance study for a digital camera application, *Proceedings of the IEEE*, 87(8): 1315-1325.

Multidisciplinary Center for Earthquake Engineering Research List of Technical Reports

The Multidisciplinary Center for Earthquake Engineering Research (MCEER) publishes technical reports on a variety of subjects related to earthquake engineering written by authors funded through MCEER. These reports are available from both MCEER Publications and the National Technical Information Service (NTIS). Requests for reports should be directed to MCEER Publications, Multidisciplinary Center for Earthquake Engineering Research, State University of New York at Buffalo, Red Jacket Quadrangle, Buffalo, New York 14261. Reports can also be requested through NTIS, 5285 Port Royal Road, Springfield, Virginia 22161. NTIS accession numbers are shown in parenthesis, if available.

- NCEER-87-0001 "First-Year Program in Research, Education and Technology Transfer," 3/5/87, (PB88-134275, A04, MF-A01).
- NCEER-87-0002 "Experimental Evaluation of Instantaneous Optimal Algorithms for Structural Control," by R.C. Lin, T.T. Soong and A.M. Reinhorn, 4/20/87, (PB88-134341, A04, MF-A01).
- NCEER-87-0003 "Experimentation Using the Earthquake Simulation Facilities at University at Buffalo," by A.M. Reinhorn and R.L. Ketter, to be published.
- NCEER-87-0004 "The System Characteristics and Performance of a Shaking Table," by J.S. Hwang, K.C. Chang and G.C. Lee, 6/1/87, (PB88-134259, A03, MF-A01). This report is available only through NTIS (see address given above).
- NCEER-87-0005 "A Finite Element Formulation for Nonlinear Viscoplastic Material Using a Q Model," by O. Gyebe and G. Dasgupta, 11/2/87, (PB88-213764, A08, MF-A01).
- NCEER-87-0006 "Symbolic Manipulation Program (SMP) - Algebraic Codes for Two and Three Dimensional Finite Element Formulations," by X. Lee and G. Dasgupta, 11/9/87, (PB88-218522, A05, MF-A01).
- NCEER-87-0007 "Instantaneous Optimal Control Laws for Tall Buildings Under Seismic Excitations," by J.N. Yang, A. Akbarpour and P. Ghaemmaghami, 6/10/87, (PB88-134333, A06, MF-A01). This report is only available through NTIS (see address given above).
- NCEER-87-0008 "IDARC: Inelastic Damage Analysis of Reinforced Concrete Frame - Shear-Wall Structures," by Y.J. Park, A.M. Reinhorn and S.K. Kunnath, 7/20/87, (PB88-134325, A09, MF-A01). This report is only available through NTIS (see address given above).
- NCEER-87-0009 "Liquefaction Potential for New York State: A Preliminary Report on Sites in Manhattan and Buffalo," by M. Budhu, V. Vijayakumar, R.F. Giese and L. Baumgras, 8/31/87, (PB88-163704, A03, MF-A01). This report is available only through NTIS (see address given above).
- NCEER-87-0010 "Vertical and Torsional Vibration of Foundations in Inhomogeneous Media," by A.S. Veletsos and K.W. Dotson, 6/1/87, (PB88-134291, A03, MF-A01). This report is only available through NTIS (see address given above).
- NCEER-87-0011 "Seismic Probabilistic Risk Assessment and Seismic Margins Studies for Nuclear Power Plants," by Howard H.M. Hwang, 6/15/87, (PB88-134267, A03, MF-A01). This report is only available through NTIS (see address given above).
- NCEER-87-0012 "Parametric Studies of Frequency Response of Secondary Systems Under Ground-Acceleration Excitations," by Y. Yong and Y.K. Lin, 6/10/87, (PB88-134309, A03, MF-A01). This report is only available through NTIS (see address given above).
- NCEER-87-0013 "Frequency Response of Secondary Systems Under Seismic Excitation," by J.A. HoLung, J. Cai and Y.K. Lin, 7/31/87, (PB88-134317, A05, MF-A01). This report is only available through NTIS (see address given above).
- NCEER-87-0014 "Modelling Earthquake Ground Motions in Seismically Active Regions Using Parametric Time Series Methods," by G.W. Ellis and A.S. Cakmak, 8/25/87, (PB88-134283, A08, MF-A01). This report is only available through NTIS (see address given above).

- NCEER-87-0015 "Detection and Assessment of Seismic Structural Damage," by E. DiPasquale and A.S. Cakmak, 8/25/87, (PB88-163712, A05, MF-A01). This report is only available through NTIS (see address given above).
- NCEER-87-0016 "Pipeline Experiment at Parkfield, California," by J. Isenberg and E. Richardson, 9/15/87, (PB88-163720, A03, MF-A01). This report is available only through NTIS (see address given above).
- NCEER-87-0017 "Digital Simulation of Seismic Ground Motion," by M. Shinozuka, G. Deodatis and T. Harada, 8/31/87, (PB88-155197, A04, MF-A01). This report is available only through NTIS (see address given above).
- NCEER-87-0018 "Practical Considerations for Structural Control: System Uncertainty, System Time Delay and Truncation of Small Control Forces," J.N. Yang and A. Akbarpour, 8/10/87, (PB88-163738, A08, MF-A01). This report is only available through NTIS (see address given above).
- NCEER-87-0019 "Modal Analysis of Nonclassically Damped Structural Systems Using Canonical Transformation," by J.N. Yang, S. Sarkani and F.X. Long, 9/27/87, (PB88-187851, A04, MF-A01).
- NCEER-87-0020 "A Nonstationary Solution in Random Vibration Theory," by J.R. Red-Horse and P.D. Spanos, 11/3/87, (PB88-163746, A03, MF-A01).
- NCEER-87-0021 "Horizontal Impedances for Radially Inhomogeneous Viscoelastic Soil Layers," by A.S. Veletsos and K.W. Dotson, 10/15/87, (PB88-150859, A04, MF-A01).
- NCEER-87-0022 "Seismic Damage Assessment of Reinforced Concrete Members," by Y.S. Chung, C. Meyer and M. Shinozuka, 10/9/87, (PB88-150867, A05, MF-A01). This report is available only through NTIS (see address given above).
- NCEER-87-0023 "Active Structural Control in Civil Engineering," by T.T. Soong, 11/11/87, (PB88-187778, A03, MF-A01).
- NCEER-87-0024 "Vertical and Torsional Impedances for Radially Inhomogeneous Viscoelastic Soil Layers," by K.W. Dotson and A.S. Veletsos, 12/87, (PB88-187786, A03, MF-A01).
- NCEER-87-0025 "Proceedings from the Symposium on Seismic Hazards, Ground Motions, Soil-Liquefaction and Engineering Practice in Eastern North America," October 20-22, 1987, edited by K.H. Jacob, 12/87, (PB88-188115, A23, MF-A01). This report is available only through NTIS (see address given above).
- NCEER-87-0026 "Report on the Whittier-Narrows, California, Earthquake of October 1, 1987," by J. Pantelic and A. Reinhorn, 11/87, (PB88-187752, A03, MF-A01). This report is available only through NTIS (see address given above).
- NCEER-87-0027 "Design of a Modular Program for Transient Nonlinear Analysis of Large 3-D Building Structures," by S. Srivastav and J.F. Abel, 12/30/87, (PB88-187950, A05, MF-A01). This report is only available through NTIS (see address given above).
- NCEER-87-0028 "Second-Year Program in Research, Education and Technology Transfer," 3/8/88, (PB88-219480, A04, MF-A01).
- NCEER-88-0001 "Workshop on Seismic Computer Analysis and Design of Buildings With Interactive Graphics," by W. McGuire, J.F. Abel and C.H. Conley, 1/18/88, (PB88-187760, A03, MF-A01). This report is only available through NTIS (see address given above).
- NCEER-88-0002 "Optimal Control of Nonlinear Flexible Structures," by J.N. Yang, F.X. Long and D. Wong, 1/22/88, (PB88-213772, A06, MF-A01).
- NCEER-88-0003 "Substructuring Techniques in the Time Domain for Primary-Secondary Structural Systems," by G.D. Manolis and G. Juhn, 2/10/88, (PB88-213780, A04, MF-A01).
- NCEER-88-0004 "Iterative Seismic Analysis of Primary-Secondary Systems," by A. Singhal, L.D. Lutes and P.D. Spanos, 2/23/88, (PB88-213798, A04, MF-A01).

- NCEER-88-0005 "Stochastic Finite Element Expansion for Random Media," by P.D. Spanos and R. Ghanem, 3/14/88, (PB88-213806, A03, MF-A01).
- NCEER-88-0006 "Combining Structural Optimization and Structural Control," by F.Y. Cheng and C.P. Pantelides, 1/10/88, (PB88-213814, A05, MF-A01).
- NCEER-88-0007 "Seismic Performance Assessment of Code-Designed Structures," by H.H-M. Hwang, J-W. Jaw and H-J. Shau, 3/20/88, (PB88-219423, A04, MF-A01). This report is only available through NTIS (see address given above).
- NCEER-88-0008 "Reliability Analysis of Code-Designed Structures Under Natural Hazards," by H.H-M. Hwang, H. Ushiba and M. Shinozuka, 2/29/88, (PB88-229471, A07, MF-A01). This report is only available through NTIS (see address given above).
- NCEER-88-0009 "Seismic Fragility Analysis of Shear Wall Structures," by J-W Jaw and H.H-M. Hwang, 4/30/88, (PB89-102867, A04, MF-A01).
- NCEER-88-0010 "Base Isolation of a Multi-Story Building Under a Harmonic Ground Motion - A Comparison of Performances of Various Systems," by F-G Fan, G. Ahmadi and I.G. Tadjbakhsh, 5/18/88, (PB89-122238, A06, MF-A01). This report is only available through NTIS (see address given above).
- NCEER-88-0011 "Seismic Floor Response Spectra for a Combined System by Green's Functions," by F.M. Lavelle, L.A. Bergman and P.D. Spanos, 5/1/88, (PB89-102875, A03, MF-A01).
- NCEER-88-0012 "A New Solution Technique for Randomly Excited Hysteretic Structures," by G.Q. Cai and Y.K. Lin, 5/16/88, (PB89-102883, A03, MF-A01).
- NCEER-88-0013 "A Study of Radiation Damping and Soil-Structure Interaction Effects in the Centrifuge," by K. Weissman, supervised by J.H. Prevost, 5/24/88, (PB89-144703, A06, MF-A01).
- NCEER-88-0014 "Parameter Identification and Implementation of a Kinematic Plasticity Model for Frictional Soils," by J.H. Prevost and D.V. Griffiths, to be published.
- NCEER-88-0015 "Two- and Three- Dimensional Dynamic Finite Element Analyses of the Long Valley Dam," by D.V. Griffiths and J.H. Prevost, 6/17/88, (PB89-144711, A04, MF-A01).
- NCEER-88-0016 "Damage Assessment of Reinforced Concrete Structures in Eastern United States," by A.M. Reinhorn, M.J. Seidel, S.K. Kunnath and Y.J. Park, 6/15/88, (PB89-122220, A04, MF-A01). This report is only available through NTIS (see address given above).
- NCEER-88-0017 "Dynamic Compliance of Vertically Loaded Strip Foundations in Multilayered Viscoelastic Soils," by S. Ahmad and A.S.M. Israil, 6/17/88, (PB89-102891, A04, MF-A01).
- NCEER-88-0018 "An Experimental Study of Seismic Structural Response With Added Viscoelastic Dampers," by R.C. Lin, Z. Liang, T.T. Soong and R.H. Zhang, 6/30/88, (PB89-122212, A05, MF-A01). This report is available only through NTIS (see address given above).
- NCEER-88-0019 "Experimental Investigation of Primary - Secondary System Interaction," by G.D. Manolis, G. Juhn and A.M. Reinhorn, 5/27/88, (PB89-122204, A04, MF-A01).
- NCEER-88-0020 "A Response Spectrum Approach For Analysis of Nonclassically Damped Structures," by J.N. Yang, S. Sarkani and F.X. Long, 4/22/88, (PB89-102909, A04, MF-A01).
- NCEER-88-0021 "Seismic Interaction of Structures and Soils: Stochastic Approach," by A.S. Veletsos and A.M. Prasad, 7/21/88, (PB89-122196, A04, MF-A01). This report is only available through NTIS (see address given above).
- NCEER-88-0022 "Identification of the Serviceability Limit State and Detection of Seismic Structural Damage," by E. DiPasquale and A.S. Cakmak, 6/15/88, (PB89-122188, A05, MF-A01). This report is available only through NTIS (see address given above).

- NCEER-88-0023 "Multi-Hazard Risk Analysis: Case of a Simple Offshore Structure," by B.K. Bhartia and E.H. Vanmarcke, 7/21/88, (PB89-145213, A05, MF-A01).
- NCEER-88-0024 "Automated Seismic Design of Reinforced Concrete Buildings," by Y.S. Chung, C. Meyer and M. Shinozuka, 7/5/88, (PB89-122170, A06, MF-A01). This report is available only through NTIS (see address given above).
- NCEER-88-0025 "Experimental Study of Active Control of MDOF Structures Under Seismic Excitations," by L.L. Chung, R.C. Lin, T.T. Soong and A.M. Reinhorn, 7/10/88, (PB89-122600, A04, MF-A01).
- NCEER-88-0026 "Earthquake Simulation Tests of a Low-Rise Metal Structure," by J.S. Hwang, K.C. Chang, G.C. Lee and R.L. Ketter, 8/1/88, (PB89-102917, A04, MF-A01).
- NCEER-88-0027 "Systems Study of Urban Response and Reconstruction Due to Catastrophic Earthquakes," by F. Kozin and H.K. Zhou, 9/22/88, (PB90-162348, A04, MF-A01).
- NCEER-88-0028 "Seismic Fragility Analysis of Plane Frame Structures," by H.H-M. Hwang and Y.K. Low, 7/31/88, (PB89-131445, A06, MF-A01).
- NCEER-88-0029 "Response Analysis of Stochastic Structures," by A. Kardara, C. Bucher and M. Shinozuka, 9/22/88, (PB89-174429, A04, MF-A01).
- NCEER-88-0030 "Nonnormal Accelerations Due to Yielding in a Primary Structure," by D.C.K. Chen and L.D. Lutes, 9/19/88, (PB89-131437, A04, MF-A01).
- NCEER-88-0031 "Design Approaches for Soil-Structure Interaction," by A.S. Veletsos, A.M. Prasad and Y. Tang, 12/30/88, (PB89-174437, A03, MF-A01). This report is available only through NTIS (see address given above).
- NCEER-88-0032 "A Re-evaluation of Design Spectra for Seismic Damage Control," by C.J. Turkstra and A.G. Tallin, 11/7/88, (PB89-145221, A05, MF-A01).
- NCEER-88-0033 "The Behavior and Design of Noncontact Lap Splices Subjected to Repeated Inelastic Tensile Loading," by V.E. Sagan, P. Gergely and R.N. White, 12/8/88, (PB89-163737, A08, MF-A01).
- NCEER-88-0034 "Seismic Response of Pile Foundations," by S.M. Mamoon, P.K. Banerjee and S. Ahmad, 11/1/88, (PB89-145239, A04, MF-A01).
- NCEER-88-0035 "Modeling of R/C Building Structures With Flexible Floor Diaphragms (IDARC2)," by A.M. Reinhorn, S.K. Kunnath and N. Panahshahi, 9/7/88, (PB89-207153, A07, MF-A01).
- NCEER-88-0036 "Solution of the Dam-Reservoir Interaction Problem Using a Combination of FEM, BEM with Particular Integrals, Modal Analysis, and Substructuring," by C-S. Tsai, G.C. Lee and R.L. Ketter, 12/31/88, (PB89-207146, A04, MF-A01).
- NCEER-88-0037 "Optimal Placement of Actuators for Structural Control," by F.Y. Cheng and C.P. Pantelides, 8/15/88, (PB89-162846, A05, MF-A01).
- NCEER-88-0038 "Teflon Bearings in Aseismic Base Isolation: Experimental Studies and Mathematical Modeling," by A. Mokha, M.C. Constantinou and A.M. Reinhorn, 12/5/88, (PB89-218457, A10, MF-A01). This report is available only through NTIS (see address given above).
- NCEER-88-0039 "Seismic Behavior of Flat Slab High-Rise Buildings in the New York City Area," by P. Weidlinger and M. Ettouney, 10/15/88, (PB90-145681, A04, MF-A01).
- NCEER-88-0040 "Evaluation of the Earthquake Resistance of Existing Buildings in New York City," by P. Weidlinger and M. Ettouney, 10/15/88, to be published.
- NCEER-88-0041 "Small-Scale Modeling Techniques for Reinforced Concrete Structures Subjected to Seismic Loads," by W. Kim, A. El-Attar and R.N. White, 11/22/88, (PB89-189625, A05, MF-A01).

- NCEER-88-0042 "Modeling Strong Ground Motion from Multiple Event Earthquakes," by G.W. Ellis and A.S. Cakmak, 10/15/88, (PB89-174445, A03, MF-A01).
- NCEER-88-0043 "Nonstationary Models of Seismic Ground Acceleration," by M. Grigoriu, S.E. Ruiz and E. Rosenblueth, 7/15/88, (PB89-189617, A04, MF-A01).
- NCEER-88-0044 "SARCF User's Guide: Seismic Analysis of Reinforced Concrete Frames," by Y.S. Chung, C. Meyer and M. Shinozuka, 11/9/88, (PB89-174452, A08, MF-A01).
- NCEER-88-0045 "First Expert Panel Meeting on Disaster Research and Planning," edited by J. Pantelic and J. Stoyke, 9/15/88, (PB89-174460, A05, MF-A01).
- NCEER-88-0046 "Preliminary Studies of the Effect of Degrading Infill Walls on the Nonlinear Seismic Response of Steel Frames," by C.Z. Chrysostomou, P. Gergely and J.F. Abel, 12/19/88, (PB89-208383, A05, MF-A01).
- NCEER-88-0047 "Reinforced Concrete Frame Component Testing Facility - Design, Construction, Instrumentation and Operation," by S.P. Pessiki, C. Conley, T. Bond, P. Gergely and R.N. White, 12/16/88, (PB89-174478, A04, MF-A01).
- NCEER-89-0001 "Effects of Protective Cushion and Soil Compliancy on the Response of Equipment Within a Seismically Excited Building," by J.A. HoLung, 2/16/89, (PB89-207179, A04, MF-A01).
- NCEER-89-0002 "Statistical Evaluation of Response Modification Factors for Reinforced Concrete Structures," by H.H-M. Hwang and J-W. Jaw, 2/17/89, (PB89-207187, A05, MF-A01).
- NCEER-89-0003 "Hysteretic Columns Under Random Excitation," by G-Q. Cai and Y.K. Lin, 1/9/89, (PB89-196513, A03, MF-A01).
- NCEER-89-0004 "Experimental Study of 'Elephant Foot Bulge' Instability of Thin-Walled Metal Tanks," by Z-H. Jia and R.L. Ketter, 2/22/89, (PB89-207195, A03, MF-A01).
- NCEER-89-0005 "Experiment on Performance of Buried Pipelines Across San Andreas Fault," by J. Isenberg, E. Richardson and T.D. O'Rourke, 3/10/89, (PB89-218440, A04, MF-A01). This report is available only through NTIS (see address given above).
- NCEER-89-0006 "A Knowledge-Based Approach to Structural Design of Earthquake-Resistant Buildings," by M. Subramani, P. Gergely, C.H. Conley, J.F. Abel and A.H. Zaghaw, 1/15/89, (PB89-218465, A06, MF-A01).
- NCEER-89-0007 "Liquefaction Hazards and Their Effects on Buried Pipelines," by T.D. O'Rourke and P.A. Lane, 2/1/89, (PB89-218481, A09, MF-A01).
- NCEER-89-0008 "Fundamentals of System Identification in Structural Dynamics," by H. Imai, C-B. Yun, O. Maruyama and M. Shinozuka, 1/26/89, (PB89-207211, A04, MF-A01).
- NCEER-89-0009 "Effects of the 1985 Michoacan Earthquake on Water Systems and Other Buried Lifelines in Mexico," by A.G. Ayala and M.J. O'Rourke, 3/8/89, (PB89-207229, A06, MF-A01).
- NCEER-89-R010 "NCEER Bibliography of Earthquake Education Materials," by K.E.K. Ross, Second Revision, 9/1/89, (PB90-125352, A05, MF-A01). This report is replaced by NCEER-92-0018.
- NCEER-89-0011 "Inelastic Three-Dimensional Response Analysis of Reinforced Concrete Building Structures (IDARC-3D), Part I - Modeling," by S.K. Kunnath and A.M. Reinhorn, 4/17/89, (PB90-114612, A07, MF-A01). This report is available only through NTIS (see address given above).
- NCEER-89-0012 "Recommended Modifications to ATC-14," by C.D. Poland and J.O. Malley, 4/12/89, (PB90-108648, A15, MF-A01).
- NCEER-89-0013 "Repair and Strengthening of Beam-to-Column Connections Subjected to Earthquake Loading," by M. Corazao and A.J. Durrani, 2/28/89, (PB90-109885, A06, MF-A01).

- NCEER-89-0014 "Program EXKAL2 for Identification of Structural Dynamic Systems," by O. Maruyama, C-B. Yun, M. Hoshiya and M. Shinozuka, 5/19/89, (PB90-109877, A09, MF-A01).
- NCEER-89-0015 "Response of Frames With Bolted Semi-Rigid Connections, Part I - Experimental Study and Analytical Predictions," by P.J. DiCorso, A.M. Reinhorn, J.R. Dickerson, J.B. Radzinski and W.L. Harper, 6/1/89, to be published.
- NCEER-89-0016 "ARMA Monte Carlo Simulation in Probabilistic Structural Analysis," by P.D. Spanos and M.P. Mignolet, 7/10/89, (PB90-109893, A03, MF-A01).
- NCEER-89-P017 "Preliminary Proceedings from the Conference on Disaster Preparedness - The Place of Earthquake Education in Our Schools," Edited by K.E.K. Ross, 6/23/89, (PB90-108606, A03, MF-A01).
- NCEER-89-0017 "Proceedings from the Conference on Disaster Preparedness - The Place of Earthquake Education in Our Schools," Edited by K.E.K. Ross, 12/31/89, (PB90-207895, A012, MF-A02). This report is available only through NTIS (see address given above).
- NCEER-89-0018 "Multidimensional Models of Hysteretic Material Behavior for Vibration Analysis of Shape Memory Energy Absorbing Devices, by E.J. Graesser and F.A. Cozzarelli, 6/7/89, (PB90-164146, A04, MF-A01).
- NCEER-89-0019 "Nonlinear Dynamic Analysis of Three-Dimensional Base Isolated Structures (3D-BASIS)," by S. Nagarajaiah, A.M. Reinhorn and M.C. Constantinou, 8/3/89, (PB90-161936, A06, MF-A01). This report has been replaced by NCEER-93-0011.
- NCEER-89-0020 "Structural Control Considering Time-Rate of Control Forces and Control Rate Constraints," by F.Y. Cheng and C.P. Pantelides, 8/3/89, (PB90-120445, A04, MF-A01).
- NCEER-89-0021 "Subsurface Conditions of Memphis and Shelby County," by K.W. Ng, T-S. Chang and H-H.M. Hwang, 7/26/89, (PB90-120437, A03, MF-A01).
- NCEER-89-0022 "Seismic Wave Propagation Effects on Straight Jointed Buried Pipelines," by K. Elhadi and M.J. O'Rourke, 8/24/89, (PB90-162322, A10, MF-A02).
- NCEER-89-0023 "Workshop on Serviceability Analysis of Water Delivery Systems," edited by M. Grigoriu, 3/6/89, (PB90-127424, A03, MF-A01).
- NCEER-89-0024 "Shaking Table Study of a 1/5 Scale Steel Frame Composed of Tapered Members," by K.C. Chang, J.S. Hwang and G.C. Lee, 9/18/89, (PB90-160169, A04, MF-A01).
- NCEER-89-0025 "DYNA1D: A Computer Program for Nonlinear Seismic Site Response Analysis - Technical Documentation," by Jean H. Prevost, 9/14/89, (PB90-161944, A07, MF-A01). This report is available only through NTIS (see address given above).
- NCEER-89-0026 "1:4 Scale Model Studies of Active Tendon Systems and Active Mass Dampers for Aseismic Protection," by A.M. Reinhorn, T.T. Soong, R.C. Lin, Y.P. Yang, Y. Fukao, H. Abe and M. Nakai, 9/15/89, (PB90-173246, A10, MF-A02). This report is available only through NTIS (see address given above).
- NCEER-89-0027 "Scattering of Waves by Inclusions in a Nonhomogeneous Elastic Half Space Solved by Boundary Element Methods," by P.K. Hadley, A. Askar and A.S. Cakmak, 6/15/89, (PB90-145699, A07, MF-A01).
- NCEER-89-0028 "Statistical Evaluation of Deflection Amplification Factors for Reinforced Concrete Structures," by H.H.M. Hwang, J-W. Jaw and A.L. Ch'ng, 8/31/89, (PB90-164633, A05, MF-A01).
- NCEER-89-0029 "Bedrock Accelerations in Memphis Area Due to Large New Madrid Earthquakes," by H.H.M. Hwang, C.H.S. Chen and G. Yu, 11/7/89, (PB90-162330, A04, MF-A01).
- NCEER-89-0030 "Seismic Behavior and Response Sensitivity of Secondary Structural Systems," by Y.Q. Chen and T.T. Soong, 10/23/89, (PB90-164658, A08, MF-A01).
- NCEER-89-0031 "Random Vibration and Reliability Analysis of Primary-Secondary Structural Systems," by Y. Ibrahim, M. Grigoriu and T.T. Soong, 11/10/89, (PB90-161951, A04, MF-A01).

- NCEER-89-0032 "Proceedings from the Second U.S. - Japan Workshop on Liquefaction, Large Ground Deformation and Their Effects on Lifelines, September 26-29, 1989," Edited by T.D. O'Rourke and M. Hamada, 12/1/89, (PB90-209388, A22, MF-A03).
- NCEER-89-0033 "Deterministic Model for Seismic Damage Evaluation of Reinforced Concrete Structures," by J.M. Bracci, A.M. Reinhorn, J.B. Mander and S.K. Kunnath, 9/27/89, (PB91-108803, A06, MF-A01).
- NCEER-89-0034 "On the Relation Between Local and Global Damage Indices," by E. DiPasquale and A.S. Cakmak, 8/15/89, (PB90-173865, A05, MF-A01).
- NCEER-89-0035 "Cyclic Undrained Behavior of Nonplastic and Low Plasticity Silts," by A.J. Walker and H.E. Stewart, 7/26/89, (PB90-183518, A10, MF-A01).
- NCEER-89-0036 "Liquefaction Potential of Surficial Deposits in the City of Buffalo, New York," by M. Budhu, R. Giese and L. Baumgrass, 1/17/89, (PB90-208455, A04, MF-A01).
- NCEER-89-0037 "A Deterministic Assessment of Effects of Ground Motion Incoherence," by A.S. Veletsos and Y. Tang, 7/15/89, (PB90-164294, A03, MF-A01).
- NCEER-89-0038 "Workshop on Ground Motion Parameters for Seismic Hazard Mapping," July 17-18, 1989, edited by R.V. Whitman, 12/1/89, (PB90-173923, A04, MF-A01).
- NCEER-89-0039 "Seismic Effects on Elevated Transit Lines of the New York City Transit Authority," by C.J. Costantino, C.A. Miller and E. Heymsfield, 12/26/89, (PB90-207887, A06, MF-A01).
- NCEER-89-0040 "Centrifugal Modeling of Dynamic Soil-Structure Interaction," by K. Weissman, Supervised by J.H. Prevost, 5/10/89, (PB90-207879, A07, MF-A01).
- NCEER-89-0041 "Linearized Identification of Buildings With Cores for Seismic Vulnerability Assessment," by I-K. Ho and A.E. Aktan, 11/1/89, (PB90-251943, A07, MF-A01).
- NCEER-90-0001 "Geotechnical and Lifeline Aspects of the October 17, 1989 Loma Prieta Earthquake in San Francisco," by T.D. O'Rourke, H.E. Stewart, F.T. Blackburn and T.S. Dickerman, 1/90, (PB90-208596, A05, MF-A01).
- NCEER-90-0002 "Nonnormal Secondary Response Due to Yielding in a Primary Structure," by D.C.K. Chen and L.D. Lutes, 2/28/90, (PB90-251976, A07, MF-A01).
- NCEER-90-0003 "Earthquake Education Materials for Grades K-12," by K.E.K. Ross, 4/16/90, (PB91-251984, A05, MF-A05). This report has been replaced by NCEER-92-0018.
- NCEER-90-0004 "Catalog of Strong Motion Stations in Eastern North America," by R.W. Busby, 4/3/90, (PB90-251984, A05, MF-A01).
- NCEER-90-0005 "NCEER Strong-Motion Data Base: A User Manual for the GeoBase Release (Version 1.0 for the Sun3)," by P. Friberg and K. Jacob, 3/31/90 (PB90-258062, A04, MF-A01).
- NCEER-90-0006 "Seismic Hazard Along a Crude Oil Pipeline in the Event of an 1811-1812 Type New Madrid Earthquake," by H.H.M. Hwang and C-H.S. Chen, 4/16/90, (PB90-258054, A04, MF-A01).
- NCEER-90-0007 "Site-Specific Response Spectra for Memphis Sheahan Pumping Station," by H.H.M. Hwang and C.S. Lee, 5/15/90, (PB91-108811, A05, MF-A01).
- NCEER-90-0008 "Pilot Study on Seismic Vulnerability of Crude Oil Transmission Systems," by T. Ariman, R. Dobry, M. Grigoriu, F. Kozin, M. O'Rourke, T. O'Rourke and M. Shinozuka, 5/25/90, (PB91-108837, A06, MF-A01).
- NCEER-90-0009 "A Program to Generate Site Dependent Time Histories: EQGEN," by G.W. Ellis, M. Srinivasan and A.S. Cakmak, 1/30/90, (PB91-108829, A04, MF-A01).
- NCEER-90-0010 "Active Isolation for Seismic Protection of Operating Rooms," by M.E. Talbott, Supervised by M. Shinozuka, 6/8/9, (PB91-110205, A05, MF-A01).

- NCEER-90-0011 "Program LINEARID for Identification of Linear Structural Dynamic Systems," by C-B. Yun and M. Shinozuka, 6/25/90, (PB91-110312, A08, MF-A01).
- NCEER-90-0012 "Two-Dimensional Two-Phase Elasto-Plastic Seismic Response of Earth Dams," by A.N. Yiagos, Supervised by J.H. Prevost, 6/20/90, (PB91-110197, A13, MF-A02).
- NCEER-90-0013 "Secondary Systems in Base-Isolated Structures: Experimental Investigation, Stochastic Response and Stochastic Sensitivity," by G.D. Manolis, G. Juhn, M.C. Constantinou and A.M. Reinhorn, 7/1/90, (PB91-110320, A08, MF-A01).
- NCEER-90-0014 "Seismic Behavior of Lightly-Reinforced Concrete Column and Beam-Column Joint Details," by S.P. Pessiki, C.H. Conley, P. Gergely and R.N. White, 8/22/90, (PB91-108795, A11, MF-A02).
- NCEER-90-0015 "Two Hybrid Control Systems for Building Structures Under Strong Earthquakes," by J.N. Yang and A. Danielians, 6/29/90, (PB91-125393, A04, MF-A01).
- NCEER-90-0016 "Instantaneous Optimal Control with Acceleration and Velocity Feedback," by J.N. Yang and Z. Li, 6/29/90, (PB91-125401, A03, MF-A01).
- NCEER-90-0017 "Reconnaissance Report on the Northern Iran Earthquake of June 21, 1990," by M. Mehrain, 10/4/90, (PB91-125377, A03, MF-A01).
- NCEER-90-0018 "Evaluation of Liquefaction Potential in Memphis and Shelby County," by T.S. Chang, P.S. Tang, C.S. Lee and H. Hwang, 8/10/90, (PB91-125427, A09, MF-A01).
- NCEER-90-0019 "Experimental and Analytical Study of a Combined Sliding Disc Bearing and Helical Steel Spring Isolation System," by M.C. Constantinou, A.S. Mokha and A.M. Reinhorn, 10/4/90, (PB91-125385, A06, MF-A01). This report is available only through NTIS (see address given above).
- NCEER-90-0020 "Experimental Study and Analytical Prediction of Earthquake Response of a Sliding Isolation System with a Spherical Surface," by A.S. Mokha, M.C. Constantinou and A.M. Reinhorn, 10/11/90, (PB91-125419, A05, MF-A01).
- NCEER-90-0021 "Dynamic Interaction Factors for Floating Pile Groups," by G. Gazetas, K. Fan, A. Kaynia and E. Kausel, 9/10/90, (PB91-170381, A05, MF-A01).
- NCEER-90-0022 "Evaluation of Seismic Damage Indices for Reinforced Concrete Structures," by S. Rodriguez-Gomez and A.S. Cakmak, 9/30/90, PB91-171322, A06, MF-A01).
- NCEER-90-0023 "Study of Site Response at a Selected Memphis Site," by H. Desai, S. Ahmad, E.S. Gazetas and M.R. Oh, 10/11/90, (PB91-196857, A03, MF-A01).
- NCEER-90-0024 "A User's Guide to Strongmo: Version 1.0 of NCEER's Strong-Motion Data Access Tool for PCs and Terminals," by P.A. Friberg and C.A.T. Susch, 11/15/90, (PB91-171272, A03, MF-A01).
- NCEER-90-0025 "A Three-Dimensional Analytical Study of Spatial Variability of Seismic Ground Motions," by L-L. Hong and A.H.-S. Ang, 10/30/90, (PB91-170399, A09, MF-A01).
- NCEER-90-0026 "MUMOID User's Guide - A Program for the Identification of Modal Parameters," by S. Rodriguez-Gomez and E. DiPasquale, 9/30/90, (PB91-171298, A04, MF-A01).
- NCEER-90-0027 "SARCF-II User's Guide - Seismic Analysis of Reinforced Concrete Frames," by S. Rodriguez-Gomez, Y.S. Chung and C. Meyer, 9/30/90, (PB91-171280, A05, MF-A01).
- NCEER-90-0028 "Viscous Dampers: Testing, Modeling and Application in Vibration and Seismic Isolation," by N. Makris and M.C. Constantinou, 12/20/90 (PB91-190561, A06, MF-A01).
- NCEER-90-0029 "Soil Effects on Earthquake Ground Motions in the Memphis Area," by H. Hwang, C.S. Lee, K.W. Ng and T.S. Chang, 8/2/90, (PB91-190751, A05, MF-A01).

- NCEER-91-0001 "Proceedings from the Third Japan-U.S. Workshop on Earthquake Resistant Design of Lifeline Facilities and Countermeasures for Soil Liquefaction, December 17-19, 1990," edited by T.D. O'Rourke and M. Hamada, 2/1/91, (PB91-179259, A99, MF-A04).
- NCEER-91-0002 "Physical Space Solutions of Non-Proportionally Damped Systems," by M. Tong, Z. Liang and G.C. Lee, 1/15/91, (PB91-179242, A04, MF-A01).
- NCEER-91-0003 "Seismic Response of Single Piles and Pile Groups," by K. Fan and G. Gazetas, 1/10/91, (PB92-174994, A04, MF-A01).
- NCEER-91-0004 "Damping of Structures: Part 1 - Theory of Complex Damping," by Z. Liang and G. Lee, 10/10/91, (PB92-197235, A12, MF-A03).
- NCEER-91-0005 "3D-BASIS - Nonlinear Dynamic Analysis of Three Dimensional Base Isolated Structures: Part II," by S. Nagarajaiah, A.M. Reinhorn and M.C. Constantinou, 2/28/91, (PB91-190553, A07, MF-A01). This report has been replaced by NCEER-93-0011.
- NCEER-91-0006 "A Multidimensional Hysteretic Model for Plasticity Deforming Metals in Energy Absorbing Devices," by E.J. Graesser and F.A. Cozzarelli, 4/9/91, (PB92-108364, A04, MF-A01).
- NCEER-91-0007 "A Framework for Customizable Knowledge-Based Expert Systems with an Application to a KBES for Evaluating the Seismic Resistance of Existing Buildings," by E.G. Ibarra-Anaya and S.J. Fenves, 4/9/91, (PB91-210930, A08, MF-A01).
- NCEER-91-0008 "Nonlinear Analysis of Steel Frames with Semi-Rigid Connections Using the Capacity Spectrum Method," by G.G. Deierlein, S-H. Hsieh, Y-J. Shen and J.F. Abel, 7/2/91, (PB92-113828, A05, MF-A01).
- NCEER-91-0009 "Earthquake Education Materials for Grades K-12," by K.E.K. Ross, 4/30/91, (PB91-212142, A06, MF-A01). This report has been replaced by NCEER-92-0018.
- NCEER-91-0010 "Phase Wave Velocities and Displacement Phase Differences in a Harmonically Oscillating Pile," by N. Makris and G. Gazetas, 7/8/91, (PB92-108356, A04, MF-A01).
- NCEER-91-0011 "Dynamic Characteristics of a Full-Size Five-Story Steel Structure and a 2/5 Scale Model," by K.C. Chang, G.C. Yao, G.C. Lee, D.S. Hao and Y.C. Yeh," 7/2/91, (PB93-116648, A06, MF-A02).
- NCEER-91-0012 "Seismic Response of a 2/5 Scale Steel Structure with Added Viscoelastic Dampers," by K.C. Chang, T.T. Soong, S-T. Oh and M.L. Lai, 5/17/91, (PB92-110816, A05, MF-A01).
- NCEER-91-0013 "Earthquake Response of Retaining Walls; Full-Scale Testing and Computational Modeling," by S. Alampalli and A-W.M. Elgamal, 6/20/91, to be published.
- NCEER-91-0014 "3D-BASIS-M: Nonlinear Dynamic Analysis of Multiple Building Base Isolated Structures," by P.C. Tsopelas, S. Nagarajaiah, M.C. Constantinou and A.M. Reinhorn, 5/28/91, (PB92-113885, A09, MF-A02).
- NCEER-91-0015 "Evaluation of SEAOC Design Requirements for Sliding Isolated Structures," by D. Theodossiou and M.C. Constantinou, 6/10/91, (PB92-114602, A11, MF-A03).
- NCEER-91-0016 "Closed-Loop Modal Testing of a 27-Story Reinforced Concrete Flat Plate-Core Building," by H.R. Somaprasad, T. Toksoy, H. Yoshiyuki and A.E. Aktan, 7/15/91, (PB92-129980, A07, MF-A02).
- NCEER-91-0017 "Shake Table Test of a 1/6 Scale Two-Story Lightly Reinforced Concrete Building," by A.G. El-Attar, R.N. White and P. Gergely, 2/28/91, (PB92-222447, A06, MF-A02).
- NCEER-91-0018 "Shake Table Test of a 1/8 Scale Three-Story Lightly Reinforced Concrete Building," by A.G. El-Attar, R.N. White and P. Gergely, 2/28/91, (PB93-116630, A08, MF-A02).
- NCEER-91-0019 "Transfer Functions for Rigid Rectangular Foundations," by A.S. Veletsos, A.M. Prasad and W.H. Wu, 7/31/91, to be published.

- NCEER-91-0020 "Hybrid Control of Seismic-Excited Nonlinear and Inelastic Structural Systems," by J.N. Yang, Z. Li and A. Daniellians, 8/1/91, (PB92-143171, A06, MF-A02).
- NCEER-91-0021 "The NCEER-91 Earthquake Catalog: Improved Intensity-Based Magnitudes and Recurrence Relations for U.S. Earthquakes East of New Madrid," by L. Seeber and J.G. Armbruster, 8/28/91, (PB92-176742, A06, MF-A02).
- NCEER-91-0022 "Proceedings from the Implementation of Earthquake Planning and Education in Schools: The Need for Change - The Roles of the Changemakers," by K.E.K. Ross and F. Winslow, 7/23/91, (PB92-129998, A12, MF-A03).
- NCEER-91-0023 "A Study of Reliability-Based Criteria for Seismic Design of Reinforced Concrete Frame Buildings," by H.H.M. Hwang and H-M. Hsu, 8/10/91, (PB92-140235, A09, MF-A02).
- NCEER-91-0024 "Experimental Verification of a Number of Structural System Identification Algorithms," by R.G. Ghanem, H. Gavin and M. Shinozuka, 9/18/91, (PB92-176577, A18, MF-A04).
- NCEER-91-0025 "Probabilistic Evaluation of Liquefaction Potential," by H.H.M. Hwang and C.S. Lee, 11/25/91, (PB92-143429, A05, MF-A01).
- NCEER-91-0026 "Instantaneous Optimal Control for Linear, Nonlinear and Hysteretic Structures - Stable Controllers," by J.N. Yang and Z. Li, 11/15/91, (PB92-163807, A04, MF-A01).
- NCEER-91-0027 "Experimental and Theoretical Study of a Sliding Isolation System for Bridges," by M.C. Constantinou, A. Kartoum, A.M. Reinhorn and P. Bradford, 11/15/91, (PB92-176973, A10, MF-A03).
- NCEER-92-0001 "Case Studies of Liquefaction and Lifeline Performance During Past Earthquakes, Volume 1: Japanese Case Studies," Edited by M. Hamada and T. O'Rourke, 2/17/92, (PB92-197243, A18, MF-A04).
- NCEER-92-0002 "Case Studies of Liquefaction and Lifeline Performance During Past Earthquakes, Volume 2: United States Case Studies," Edited by T. O'Rourke and M. Hamada, 2/17/92, (PB92-197250, A20, MF-A04).
- NCEER-92-0003 "Issues in Earthquake Education," Edited by K. Ross, 2/3/92, (PB92-222389, A07, MF-A02).
- NCEER-92-0004 "Proceedings from the First U.S. - Japan Workshop on Earthquake Protective Systems for Bridges," Edited by I.G. Buckle, 2/4/92, (PB94-142239, A99, MF-A06).
- NCEER-92-0005 "Seismic Ground Motion from a Haskell-Type Source in a Multiple-Layered Half-Space," A.P. Theoharis, G. Deodatis and M. Shinozuka, 1/2/92, to be published.
- NCEER-92-0006 "Proceedings from the Site Effects Workshop," Edited by R. Whitman, 2/29/92, (PB92-197201, A04, MF-A01).
- NCEER-92-0007 "Engineering Evaluation of Permanent Ground Deformations Due to Seismically-Induced Liquefaction," by M.H. Baziar, R. Dobry and A-W.M. Elgamel, 3/24/92, (PB92-222421, A13, MF-A03).
- NCEER-92-0008 "A Procedure for the Seismic Evaluation of Buildings in the Central and Eastern United States," by C.D. Poland and J.O. Malley, 4/2/92, (PB92-222439, A20, MF-A04).
- NCEER-92-0009 "Experimental and Analytical Study of a Hybrid Isolation System Using Friction Controllable Sliding Bearings," by M.Q. Feng, S. Fujii and M. Shinozuka, 5/15/92, (PB93-150282, A06, MF-A02).
- NCEER-92-0010 "Seismic Resistance of Slab-Column Connections in Existing Non-Ductile Flat-Plate Buildings," by A.J. Durrani and Y. Du, 5/18/92, (PB93-116812, A06, MF-A02).
- NCEER-92-0011 "The Hysteretic and Dynamic Behavior of Brick Masonry Walls Upgraded by Ferrocement Coatings Under Cyclic Loading and Strong Simulated Ground Motion," by H. Lee and S.P. Prawl, 5/11/92, to be published.
- NCEER-92-0012 "Study of Wire Rope Systems for Seismic Protection of Equipment in Buildings," by G.F. Demetriades, M.C. Constantinou and A.M. Reinhorn, 5/20/92, (PB93-116655, A08, MF-A02).

- NCEER-92-0013 "Shape Memory Structural Dampers: Material Properties, Design and Seismic Testing," by P.R. Witting and F.A. Cozzarelli, 5/26/92, (PB93-116663, A05, MF-A01).
- NCEER-92-0014 "Longitudinal Permanent Ground Deformation Effects on Buried Continuous Pipelines," by M.J. O'Rourke, and C. Nordberg, 6/15/92, (PB93-116671, A08, MF-A02).
- NCEER-92-0015 "A Simulation Method for Stationary Gaussian Random Functions Based on the Sampling Theorem," by M. Grigoriu and S. Balopoulou, 6/11/92, (PB93-127496, A05, MF-A01).
- NCEER-92-0016 "Gravity-Load-Designed Reinforced Concrete Buildings: Seismic Evaluation of Existing Construction and Detailing Strategies for Improved Seismic Resistance," by G.W. Hoffmann, S.K. Kunnath, A.M. Reinhorn and J.B. Mander, 7/15/92, (PB94-142007, A08, MF-A02).
- NCEER-92-0017 "Observations on Water System and Pipeline Performance in the Limón Area of Costa Rica Due to the April 22, 1991 Earthquake," by M. O'Rourke and D. Ballantyne, 6/30/92, (PB93-126811, A06, MF-A02).
- NCEER-92-0018 "Fourth Edition of Earthquake Education Materials for Grades K-12," Edited by K.E.K. Ross, 8/10/92, (PB93-114023, A07, MF-A02).
- NCEER-92-0019 "Proceedings from the Fourth Japan-U.S. Workshop on Earthquake Resistant Design of Lifeline Facilities and Countermeasures for Soil Liquefaction," Edited by M. Hamada and T.D. O'Rourke, 8/12/92, (PB93-163939, A99, MF-E11).
- NCEER-92-0020 "Active Bracing System: A Full Scale Implementation of Active Control," by A.M. Reinhorn, T.T. Soong, R.C. Lin, M.A. Riley, Y.P. Wang, S. Aizawa and M. Higashino, 8/14/92, (PB93-127512, A06, MF-A02).
- NCEER-92-0021 "Empirical Analysis of Horizontal Ground Displacement Generated by Liquefaction-Induced Lateral Spreads," by S.F. Bartlett and T.L. Youd, 8/17/92, (PB93-188241, A06, MF-A02).
- NCEER-92-0022 "IDARC Version 3.0: Inelastic Damage Analysis of Reinforced Concrete Structures," by S.K. Kunnath, A.M. Reinhorn and R.F. Lobo, 8/31/92, (PB93-227502, A07, MF-A02).
- NCEER-92-0023 "A Semi-Empirical Analysis of Strong-Motion Peaks in Terms of Seismic Source, Propagation Path and Local Site Conditions, by M. Kamiyama, M.J. O'Rourke and R. Flores-Berrones, 9/9/92, (PB93-150266, A08, MF-A02).
- NCEER-92-0024 "Seismic Behavior of Reinforced Concrete Frame Structures with Nonductile Details, Part I: Summary of Experimental Findings of Full Scale Beam-Column Joint Tests," by A. Beres, R.N. White and P. Gergely, 9/30/92, (PB93-227783, A05, MF-A01).
- NCEER-92-0025 "Experimental Results of Repaired and Retrofitted Beam-Column Joint Tests in Lightly Reinforced Concrete Frame Buildings," by A. Beres, S. El-Borgi, R.N. White and P. Gergely, 10/29/92, (PB93-227791, A05, MF-A01).
- NCEER-92-0026 "A Generalization of Optimal Control Theory: Linear and Nonlinear Structures," by J.N. Yang, Z. Li and S. Vongchavalitkul, 11/2/92, (PB93-188621, A05, MF-A01).
- NCEER-92-0027 "Seismic Resistance of Reinforced Concrete Frame Structures Designed Only for Gravity Loads: Part I - Design and Properties of a One-Third Scale Model Structure," by J.M. Bracci, A.M. Reinhorn and J.B. Mander, 12/1/92, (PB94-104502, A08, MF-A02).
- NCEER-92-0028 "Seismic Resistance of Reinforced Concrete Frame Structures Designed Only for Gravity Loads: Part II - Experimental Performance of Subassemblages," by L.E. Aycaardi, J.B. Mander and A.M. Reinhorn, 12/1/92, (PB94-104510, A08, MF-A02).
- NCEER-92-0029 "Seismic Resistance of Reinforced Concrete Frame Structures Designed Only for Gravity Loads: Part III - Experimental Performance and Analytical Study of a Structural Model," by J.M. Bracci, A.M. Reinhorn and J.B. Mander, 12/1/92, (PB93-227528, A09, MF-A01).

- NCEER-92-0030 "Evaluation of Seismic Retrofit of Reinforced Concrete Frame Structures: Part I - Experimental Performance of Retrofitted Subassemblages," by D. Choudhuri, J.B. Mander and A.M. Reinhorn, 12/8/92, (PB93-198307, A07, MF-A02).
- NCEER-92-0031 "Evaluation of Seismic Retrofit of Reinforced Concrete Frame Structures: Part II - Experimental Performance and Analytical Study of a Retrofitted Structural Model," by J.M. Bracci, A.M. Reinhorn and J.B. Mander, 12/8/92, (PB93-198315, A09, MF-A03).
- NCEER-92-0032 "Experimental and Analytical Investigation of Seismic Response of Structures with Supplemental Fluid Viscous Dampers," by M.C. Constantinou and M.D. Symans, 12/21/92, (PB93-191435, A10, MF-A03). This report is available only through NTIS (see address given above).
- NCEER-92-0033 "Reconnaissance Report on the Cairo, Egypt Earthquake of October 12, 1992," by M. Khater, 12/23/92, (PB93-188621, A03, MF-A01).
- NCEER-92-0034 "Low-Level Dynamic Characteristics of Four Tall Flat-Plate Buildings in New York City," by H. Gavin, S. Yuan, J. Grossman, E. Pekelis and K. Jacob, 12/28/92, (PB93-188217, A07, MF-A02).
- NCEER-93-0001 "An Experimental Study on the Seismic Performance of Brick-Infilled Steel Frames With and Without Retrofit," by J.B. Mander, B. Nair, K. Wojtkowski and J. Ma, 1/29/93, (PB93-227510, A07, MF-A02).
- NCEER-93-0002 "Social Accounting for Disaster Preparedness and Recovery Planning," by S. Cole, E. Pantoja and V. Razak, 2/22/93, (PB94-142114, A12, MF-A03).
- NCEER-93-0003 "Assessment of 1991 NEHRP Provisions for Nonstructural Components and Recommended Revisions," by T.T. Soong, G. Chen, Z. Wu, R-H. Zhang and M. Grigoriu, 3/1/93, (PB93-188639, A06, MF-A02).
- NCEER-93-0004 "Evaluation of Static and Response Spectrum Analysis Procedures of SEAOC/UBC for Seismic Isolated Structures," by C.W. Winters and M.C. Constantinou, 3/23/93, (PB93-198299, A10, MF-A03).
- NCEER-93-0005 "Earthquakes in the Northeast - Are We Ignoring the Hazard? A Workshop on Earthquake Science and Safety for Educators," edited by K.E.K. Ross, 4/2/93, (PB94-103066, A09, MF-A02).
- NCEER-93-0006 "Inelastic Response of Reinforced Concrete Structures with Viscoelastic Braces," by R.F. Lobo, J.M. Bracci, K.L. Shen, A.M. Reinhorn and T.T. Soong, 4/5/93, (PB93-227486, A05, MF-A02).
- NCEER-93-0007 "Seismic Testing of Installation Methods for Computers and Data Processing Equipment," by K. Kosar, T.T. Soong, K.L. Shen, J.A. HoLung and Y.K. Lin, 4/12/93, (PB93-198299, A07, MF-A02).
- NCEER-93-0008 "Retrofit of Reinforced Concrete Frames Using Added Dampers," by A. Reinhorn, M. Constantinou and C. Li, to be published.
- NCEER-93-0009 "Seismic Behavior and Design Guidelines for Steel Frame Structures with Added Viscoelastic Dampers," by K.C. Chang, M.L. Lai, T.T. Soong, D.S. Hao and Y.C. Yeh, 5/1/93, (PB94-141959, A07, MF-A02).
- NCEER-93-0010 "Seismic Performance of Shear-Critical Reinforced Concrete Bridge Piers," by J.B. Mander, S.M. Waheed, M.T.A. Chaudhary and S.S. Chen, 5/12/93, (PB93-227494, A08, MF-A02).
- NCEER-93-0011 "3D-BASIS-TABS: Computer Program for Nonlinear Dynamic Analysis of Three Dimensional Base Isolated Structures," by S. Nagarajaiah, C. Li, A.M. Reinhorn and M.C. Constantinou, 8/2/93, (PB94-141819, A09, MF-A02).
- NCEER-93-0012 "Effects of Hydrocarbon Spills from an Oil Pipeline Break on Ground Water," by O.J. Helweg and H.H.M. Hwang, 8/3/93, (PB94-141942, A06, MF-A02).
- NCEER-93-0013 "Simplified Procedures for Seismic Design of Nonstructural Components and Assessment of Current Code Provisions," by M.P. Singh, L.E. Suarez, E.E. Matheu and G.O. Maldonado, 8/4/93, (PB94-141827, A09, MF-A02).
- NCEER-93-0014 "An Energy Approach to Seismic Analysis and Design of Secondary Systems," by G. Chen and T.T. Soong, 8/6/93, (PB94-142767, A11, MF-A03).

- NCEER-93-0015 "Proceedings from School Sites: Becoming Prepared for Earthquakes - Commemorating the Third Anniversary of the Loma Prieta Earthquake," Edited by F.E. Winslow and K.E.K. Ross, 8/16/93, (PB94-154275, A16, MF-A02).
- NCEER-93-0016 "Reconnaissance Report of Damage to Historic Monuments in Cairo, Egypt Following the October 12, 1992 Dahshur Earthquake," by D. Sykora, D. Look, G. Croci, E. Karaesmen and E. Karaesmen, 8/19/93, (PB94-142221, A08, MF-A02).
- NCEER-93-0017 "The Island of Guam Earthquake of August 8, 1993," by S.W. Swan and S.K. Harris, 9/30/93, (PB94-141843, A04, MF-A01).
- NCEER-93-0018 "Engineering Aspects of the October 12, 1992 Egyptian Earthquake," by A.W. Elgamal, M. Amer, K. Adalier and A. Abul-Fadl, 10/7/93, (PB94-141983, A05, MF-A01).
- NCEER-93-0019 "Development of an Earthquake Motion Simulator and its Application in Dynamic Centrifuge Testing," by I. Krstelj, Supervised by J.H. Prevost, 10/23/93, (PB94-181773, A-10, MF-A03).
- NCEER-93-0020 "NCEER-Taisei Corporation Research Program on Sliding Seismic Isolation Systems for Bridges: Experimental and Analytical Study of a Friction Pendulum System (FPS)," by M.C. Constantinou, P. Tsopelas, Y-S. Kim and S. Okamoto, 11/1/93, (PB94-142775, A08, MF-A02).
- NCEER-93-0021 "Finite Element Modeling of Elastomeric Seismic Isolation Bearings," by L.J. Billings, Supervised by R. Shepherd, 11/8/93, to be published.
- NCEER-93-0022 "Seismic Vulnerability of Equipment in Critical Facilities: Life-Safety and Operational Consequences," by K. Porter, G.S. Johnson, M.M. Zadeh, C. Scawthorn and S. Eder, 11/24/93, (PB94-181765, A16, MF-A03).
- NCEER-93-0023 "Hokkaido Nansei-oki, Japan Earthquake of July 12, 1993, by P.I. Yanev and C.R. Scawthorn, 12/23/93, (PB94-181500, A07, MF-A01).
- NCEER-94-0001 "An Evaluation of Seismic Serviceability of Water Supply Networks with Application to the San Francisco Auxiliary Water Supply System," by I. Markov, Supervised by M. Grigoriu and T. O'Rourke, 1/21/94, (PB94-204013, A07, MF-A02).
- NCEER-94-0002 "NCEER-Taisei Corporation Research Program on Sliding Seismic Isolation Systems for Bridges: Experimental and Analytical Study of Systems Consisting of Sliding Bearings, Rubber Restoring Force Devices and Fluid Dampers," Volumes I and II, by P. Tsopelas, S. Okamoto, M.C. Constantinou, D. Ozaki and S. Fujii, 2/4/94, (PB94-181740, A09, MF-A02 and PB94-181757, A12, MF-A03).
- NCEER-94-0003 "A Markov Model for Local and Global Damage Indices in Seismic Analysis," by S. Rahman and M. Grigoriu, 2/18/94, (PB94-206000, A12, MF-A03).
- NCEER-94-0004 "Proceedings from the NCEER Workshop on Seismic Response of Masonry Infills," edited by D.P. Abrams, 3/1/94, (PB94-180783, A07, MF-A02).
- NCEER-94-0005 "The Northridge, California Earthquake of January 17, 1994: General Reconnaissance Report," edited by J.D. Goltz, 3/11/94, (PB94-193943, A10, MF-A03).
- NCEER-94-0006 "Seismic Energy Based Fatigue Damage Analysis of Bridge Columns: Part I - Evaluation of Seismic Capacity," by G.A. Chang and J.B. Mander, 3/14/94, (PB94-219185, A11, MF-A03).
- NCEER-94-0007 "Seismic Isolation of Multi-Story Frame Structures Using Spherical Sliding Isolation Systems," by T.M. Al-Hussaini, V.A. Zayas and M.C. Constantinou, 3/17/94, (PB94-193745, A09, MF-A02).
- NCEER-94-0008 "The Northridge, California Earthquake of January 17, 1994: Performance of Highway Bridges," edited by I.G. Buckle, 3/24/94, (PB94-193851, A06, MF-A02).
- NCEER-94-0009 "Proceedings of the Third U.S.-Japan Workshop on Earthquake Protective Systems for Bridges," edited by I.G. Buckle and I. Friedland, 3/31/94, (PB94-195815, A99, MF-A06).

- NCEER-94-0010 "3D-BASIS-ME: Computer Program for Nonlinear Dynamic Analysis of Seismically Isolated Single and Multiple Structures and Liquid Storage Tanks," by P.C. Tsopelas, M.C. Constantinou and A.M. Reinhorn, 4/12/94, (PB94-204922, A09, MF-A02).
- NCEER-94-0011 "The Northridge, California Earthquake of January 17, 1994: Performance of Gas Transmission Pipelines," by T.D. O'Rourke and M.C. Palmer, 5/16/94, (PB94-204989, A05, MF-A01).
- NCEER-94-0012 "Feasibility Study of Replacement Procedures and Earthquake Performance Related to Gas Transmission Pipelines," by T.D. O'Rourke and M.C. Palmer, 5/25/94, (PB94-206638, A09, MF-A02).
- NCEER-94-0013 "Seismic Energy Based Fatigue Damage Analysis of Bridge Columns: Part II - Evaluation of Seismic Demand," by G.A. Chang and J.B. Mander, 6/1/94, (PB95-18106, A08, MF-A02).
- NCEER-94-0014 "NCEER-Taisei Corporation Research Program on Sliding Seismic Isolation Systems for Bridges: Experimental and Analytical Study of a System Consisting of Sliding Bearings and Fluid Restoring Force/Damping Devices," by P. Tsopelas and M.C. Constantinou, 6/13/94, (PB94-219144, A10, MF-A03).
- NCEER-94-0015 "Generation of Hazard-Consistent Fragility Curves for Seismic Loss Estimation Studies," by H. Hwang and J-R. Huo, 6/14/94, (PB95-181996, A09, MF-A02).
- NCEER-94-0016 "Seismic Study of Building Frames with Added Energy-Absorbing Devices," by W.S. Pong, C.S. Tsai and G.C. Lee, 6/20/94, (PB94-219136, A10, A03).
- NCEER-94-0017 "Sliding Mode Control for Seismic-Excited Linear and Nonlinear Civil Engineering Structures," by J. Yang, J. Wu, A. Agrawal and Z. Li, 6/21/94, (PB95-138483, A06, MF-A02).
- NCEER-94-0018 "3D-BASIS-TABS Version 2.0: Computer Program for Nonlinear Dynamic Analysis of Three Dimensional Base Isolated Structures," by A.M. Reinhorn, S. Nagarajaiah, M.C. Constantinou, P. Tsopelas and R. Li, 6/22/94, (PB95-182176, A08, MF-A02).
- NCEER-94-0019 "Proceedings of the International Workshop on Civil Infrastructure Systems: Application of Intelligent Systems and Advanced Materials on Bridge Systems," Edited by G.C. Lee and K.C. Chang, 7/18/94, (PB95-252474, A20, MF-A04).
- NCEER-94-0020 "Study of Seismic Isolation Systems for Computer Floors," by V. Lambrou and M.C. Constantinou, 7/19/94, (PB95-138533, A10, MF-A03).
- NCEER-94-0021 "Proceedings of the U.S.-Italian Workshop on Guidelines for Seismic Evaluation and Rehabilitation of Unreinforced Masonry Buildings," Edited by D.P. Abrams and G.M. Calvi, 7/20/94, (PB95-138749, A13, MF-A03).
- NCEER-94-0022 "NCEER-Taisei Corporation Research Program on Sliding Seismic Isolation Systems for Bridges: Experimental and Analytical Study of a System Consisting of Lubricated PTFE Sliding Bearings and Mild Steel Dampers," by P. Tsopelas and M.C. Constantinou, 7/22/94, (PB95-182184, A08, MF-A02).
- NCEER-94-0023 "Development of Reliability-Based Design Criteria for Buildings Under Seismic Load," by Y.K. Wen, H. Hwang and M. Shinozuka, 8/1/94, (PB95-211934, A08, MF-A02).
- NCEER-94-0024 "Experimental Verification of Acceleration Feedback Control Strategies for an Active Tendon System," by S.J. Dyke, B.F. Spencer, Jr., P. Quast, M.K. Sain, D.C. Kaspari, Jr. and T.T. Soong, 8/29/94, (PB95-212320, A05, MF-A01).
- NCEER-94-0025 "Seismic Retrofitting Manual for Highway Bridges," Edited by I.G. Buckle and I.F. Friedland, published by the Federal Highway Administration (PB95-212676, A15, MF-A03).
- NCEER-94-0026 "Proceedings from the Fifth U.S.-Japan Workshop on Earthquake Resistant Design of Lifeline Facilities and Countermeasures Against Soil Liquefaction," Edited by T.D. O'Rourke and M. Hamada, 11/7/94, (PB95-220802, A99, MF-E08).

- NCEER-95-0001 “Experimental and Analytical Investigation of Seismic Retrofit of Structures with Supplemental Damping: Part I - Fluid Viscous Damping Devices,” by A.M. Reinhorn, C. Li and M.C. Constantinou, 1/3/95, (PB95-266599, A09, MF-A02).
- NCEER-95-0002 “Experimental and Analytical Study of Low-Cycle Fatigue Behavior of Semi-Rigid Top-And-Seat Angle Connections,” by G. Pekcan, J.B. Mander and S.S. Chen, 1/5/95, (PB95-220042, A07, MF-A02).
- NCEER-95-0003 “NCEER-ATC Joint Study on Fragility of Buildings,” by T. Anagnos, C. Rojahn and A.S. Kiremidjian, 1/20/95, (PB95-220026, A06, MF-A02).
- NCEER-95-0004 “Nonlinear Control Algorithms for Peak Response Reduction,” by Z. Wu, T.T. Soong, V. Gattulli and R.C. Lin, 2/16/95, (PB95-220349, A05, MF-A01).
- NCEER-95-0005 “Pipeline Replacement Feasibility Study: A Methodology for Minimizing Seismic and Corrosion Risks to Underground Natural Gas Pipelines,” by R.T. Eguchi, H.A. Seligson and D.G. Honegger, 3/2/95, (PB95-252326, A06, MF-A02).
- NCEER-95-0006 “Evaluation of Seismic Performance of an 11-Story Frame Building During the 1994 Northridge Earthquake,” by F. Naeim, R. DiSulio, K. Benuska, A. Reinhorn and C. Li, to be published.
- NCEER-95-0007 “Prioritization of Bridges for Seismic Retrofitting,” by N. Basöz and A.S. Kiremidjian, 4/24/95, (PB95-252300, A08, MF-A02).
- NCEER-95-0008 “Method for Developing Motion Damage Relationships for Reinforced Concrete Frames,” by A. Singhal and A.S. Kiremidjian, 5/11/95, (PB95-266607, A06, MF-A02).
- NCEER-95-0009 “Experimental and Analytical Investigation of Seismic Retrofit of Structures with Supplemental Damping: Part II - Friction Devices,” by C. Li and A.M. Reinhorn, 7/6/95, (PB96-128087, A11, MF-A03).
- NCEER-95-0010 “Experimental Performance and Analytical Study of a Non-Ductile Reinforced Concrete Frame Structure Retrofitted with Elastomeric Spring Dampers,” by G. Pekcan, J.B. Mander and S.S. Chen, 7/14/95, (PB96-137161, A08, MF-A02).
- NCEER-95-0011 “Development and Experimental Study of Semi-Active Fluid Damping Devices for Seismic Protection of Structures,” by M.D. Symans and M.C. Constantinou, 8/3/95, (PB96-136940, A23, MF-A04).
- NCEER-95-0012 “Real-Time Structural Parameter Modification (RSPM): Development of Innervated Structures,” by Z. Liang, M. Tong and G.C. Lee, 4/11/95, (PB96-137153, A06, MF-A01).
- NCEER-95-0013 “Experimental and Analytical Investigation of Seismic Retrofit of Structures with Supplemental Damping: Part III - Viscous Damping Walls,” by A.M. Reinhorn and C. Li, 10/1/95, (PB96-176409, A11, MF-A03).
- NCEER-95-0014 “Seismic Fragility Analysis of Equipment and Structures in a Memphis Electric Substation,” by J-R. Huo and H.H.M. Hwang, 8/10/95, (PB96-128087, A09, MF-A02).
- NCEER-95-0015 “The Hanshin-Awaji Earthquake of January 17, 1995: Performance of Lifelines,” Edited by M. Shinozuka, 11/3/95, (PB96-176383, A15, MF-A03).
- NCEER-95-0016 “Highway Culvert Performance During Earthquakes,” by T.L. Youd and C.J. Beckman, available as NCEER-96-0015.
- NCEER-95-0017 “The Hanshin-Awaji Earthquake of January 17, 1995: Performance of Highway Bridges,” Edited by I.G. Buckle, 12/1/95, to be published.
- NCEER-95-0018 “Modeling of Masonry Infill Panels for Structural Analysis,” by A.M. Reinhorn, A. Madan, R.E. Valles, Y. Reichmann and J.B. Mander, 12/8/95, (PB97-110886, MF-A01, A06).
- NCEER-95-0019 “Optimal Polynomial Control for Linear and Nonlinear Structures,” by A.K. Agrawal and J.N. Yang, 12/11/95, (PB96-168737, A07, MF-A02).

- NCEER-95-0020 “Retrofit of Non-Ductile Reinforced Concrete Frames Using Friction Dampers,” by R.S. Rao, P. Gergely and R.N. White, 12/22/95, (PB97-133508, A10, MF-A02).
- NCEER-95-0021 “Parametric Results for Seismic Response of Pile-Supported Bridge Bents,” by G. Mylonakis, A. Nikolaou and G. Gazetas, 12/22/95, (PB97-100242, A12, MF-A03).
- NCEER-95-0022 “Kinematic Bending Moments in Seismically Stressed Piles,” by A. Nikolaou, G. Mylonakis and G. Gazetas, 12/23/95, (PB97-113914, MF-A03, A13).
- NCEER-96-0001 “Dynamic Response of Unreinforced Masonry Buildings with Flexible Diaphragms,” by A.C. Costley and D.P. Abrams, 10/10/96, (PB97-133573, MF-A03, A15).
- NCEER-96-0002 “State of the Art Review: Foundations and Retaining Structures,” by I. Po Lam, to be published.
- NCEER-96-0003 “Ductility of Rectangular Reinforced Concrete Bridge Columns with Moderate Confinement,” by N. Wehbe, M. Saiidi, D. Sanders and B. Douglas, 11/7/96, (PB97-133557, A06, MF-A02).
- NCEER-96-0004 “Proceedings of the Long-Span Bridge Seismic Research Workshop,” edited by I.G. Buckle and I.M. Friedland, to be published.
- NCEER-96-0005 “Establish Representative Pier Types for Comprehensive Study: Eastern United States,” by J. Kulicki and Z. Prucz, 5/28/96, (PB98-119217, A07, MF-A02).
- NCEER-96-0006 “Establish Representative Pier Types for Comprehensive Study: Western United States,” by R. Imbsen, R.A. Schamber and T.A. Osterkamp, 5/28/96, (PB98-118607, A07, MF-A02).
- NCEER-96-0007 “Nonlinear Control Techniques for Dynamical Systems with Uncertain Parameters,” by R.G. Ghanem and M.I. Bujakov, 5/27/96, (PB97-100259, A17, MF-A03).
- NCEER-96-0008 “Seismic Evaluation of a 30-Year Old Non-Ductile Highway Bridge Pier and Its Retrofit,” by J.B. Mander, B. Mahmoodzadegan, S. Bhadra and S.S. Chen, 5/31/96, (PB97-110902, MF-A03, A10).
- NCEER-96-0009 “Seismic Performance of a Model Reinforced Concrete Bridge Pier Before and After Retrofit,” by J.B. Mander, J.H. Kim and C.A. Ligozio, 5/31/96, (PB97-110910, MF-A02, A10).
- NCEER-96-0010 “IDARC2D Version 4.0: A Computer Program for the Inelastic Damage Analysis of Buildings,” by R.E. Valles, A.M. Reinhorn, S.K. Kunnath, C. Li and A. Madan, 6/3/96, (PB97-100234, A17, MF-A03).
- NCEER-96-0011 “Estimation of the Economic Impact of Multiple Lifeline Disruption: Memphis Light, Gas and Water Division Case Study,” by S.E. Chang, H.A. Seligson and R.T. Eguchi, 8/16/96, (PB97-133490, A11, MF-A03).
- NCEER-96-0012 “Proceedings from the Sixth Japan-U.S. Workshop on Earthquake Resistant Design of Lifeline Facilities and Countermeasures Against Soil Liquefaction, Edited by M. Hamada and T. O’Rourke, 9/11/96, (PB97-133581, A99, MF-A06).
- NCEER-96-0013 “Chemical Hazards, Mitigation and Preparedness in Areas of High Seismic Risk: A Methodology for Estimating the Risk of Post-Earthquake Hazardous Materials Release,” by H.A. Seligson, R.T. Eguchi, K.J. Tierney and K. Richmond, 11/7/96, (PB97-133565, MF-A02, A08).
- NCEER-96-0014 “Response of Steel Bridge Bearings to Reversed Cyclic Loading,” by J.B. Mander, D-K. Kim, S.S. Chen and G.J. Premus, 11/13/96, (PB97-140735, A12, MF-A03).
- NCEER-96-0015 “Highway Culvert Performance During Past Earthquakes,” by T.L. Youd and C.J. Beckman, 11/25/96, (PB97-133532, A06, MF-A01).
- NCEER-97-0001 “Evaluation, Prevention and Mitigation of Pounding Effects in Building Structures,” by R.E. Valles and A.M. Reinhorn, 2/20/97, (PB97-159552, A14, MF-A03).
- NCEER-97-0002 “Seismic Design Criteria for Bridges and Other Highway Structures,” by C. Rojahn, R. Mayes, D.G. Anderson, J. Clark, J.H. Hom, R.V. Nutt and M.J. O’Rourke, 4/30/97, (PB97-194658, A06, MF-A03).

- NCEER-97-0003 "Proceedings of the U.S.-Italian Workshop on Seismic Evaluation and Retrofit," Edited by D.P. Abrams and G.M. Calvi, 3/19/97, (PB97-194666, A13, MF-A03).
- NCEER-97-0004 "Investigation of Seismic Response of Buildings with Linear and Nonlinear Fluid Viscous Dampers," by A.A. Seleemah and M.C. Constantinou, 5/21/97, (PB98-109002, A15, MF-A03).
- NCEER-97-0005 "Proceedings of the Workshop on Earthquake Engineering Frontiers in Transportation Facilities," edited by G.C. Lee and I.M. Friedland, 8/29/97, (PB98-128911, A25, MR-A04).
- NCEER-97-0006 "Cumulative Seismic Damage of Reinforced Concrete Bridge Piers," by S.K. Kunnath, A. El-Bahy, A. Taylor and W. Stone, 9/2/97, (PB98-108814, A11, MF-A03).
- NCEER-97-0007 "Structural Details to Accommodate Seismic Movements of Highway Bridges and Retaining Walls," by R.A. Imbsen, R.A. Schamber, E. Thorkildsen, A. Kartoum, B.T. Martin, T.N. Rosser and J.M. Kulicki, 9/3/97, (PB98-108996, A09, MF-A02).
- NCEER-97-0008 "A Method for Earthquake Motion-Damage Relationships with Application to Reinforced Concrete Frames," by A. Singhal and A.S. Kiremidjian, 9/10/97, (PB98-108988, A13, MF-A03).
- NCEER-97-0009 "Seismic Analysis and Design of Bridge Abutments Considering Sliding and Rotation," by K. Fishman and R. Richards, Jr., 9/15/97, (PB98-108897, A06, MF-A02).
- NCEER-97-0010 "Proceedings of the FHWA/NCEER Workshop on the National Representation of Seismic Ground Motion for New and Existing Highway Facilities," edited by I.M. Friedland, M.S. Power and R.L. Mayes, 9/22/97, (PB98-128903, A21, MF-A04).
- NCEER-97-0011 "Seismic Analysis for Design or Retrofit of Gravity Bridge Abutments," by K.L. Fishman, R. Richards, Jr. and R.C. Divito, 10/2/97, (PB98-128937, A08, MF-A02).
- NCEER-97-0012 "Evaluation of Simplified Methods of Analysis for Yielding Structures," by P. Tsopelas, M.C. Constantinou, C.A. Kircher and A.S. Whittaker, 10/31/97, (PB98-128929, A10, MF-A03).
- NCEER-97-0013 "Seismic Design of Bridge Columns Based on Control and Repairability of Damage," by C-T. Cheng and J.B. Mander, 12/8/97, (PB98-144249, A11, MF-A03).
- NCEER-97-0014 "Seismic Resistance of Bridge Piers Based on Damage Avoidance Design," by J.B. Mander and C-T. Cheng, 12/10/97, (PB98-144223, A09, MF-A02).
- NCEER-97-0015 "Seismic Response of Nominally Symmetric Systems with Strength Uncertainty," by S. Balopoulou and M. Grigoriu, 12/23/97, (PB98-153422, A11, MF-A03).
- NCEER-97-0016 "Evaluation of Seismic Retrofit Methods for Reinforced Concrete Bridge Columns," by T.J. Wipf, F.W. Klaiber and F.M. Russo, 12/28/97, (PB98-144215, A12, MF-A03).
- NCEER-97-0017 "Seismic Fragility of Existing Conventional Reinforced Concrete Highway Bridges," by C.L. Mullen and A.S. Cakmak, 12/30/97, (PB98-153406, A08, MF-A02).
- NCEER-97-0018 "Loss Assessment of Memphis Buildings," edited by D.P. Abrams and M. Shinozuka, 12/31/97, (PB98-144231, A13, MF-A03).
- NCEER-97-0019 "Seismic Evaluation of Frames with Infill Walls Using Quasi-static Experiments," by K.M. Mosalam, R.N. White and P. Gergely, 12/31/97, (PB98-153455, A07, MF-A02).
- NCEER-97-0020 "Seismic Evaluation of Frames with Infill Walls Using Pseudo-dynamic Experiments," by K.M. Mosalam, R.N. White and P. Gergely, 12/31/97, (PB98-153430, A07, MF-A02).
- NCEER-97-0021 "Computational Strategies for Frames with Infill Walls: Discrete and Smeared Crack Analyses and Seismic Fragility," by K.M. Mosalam, R.N. White and P. Gergely, 12/31/97, (PB98-153414, A10, MF-A02).

- NCEER-97-0022 "Proceedings of the NCEER Workshop on Evaluation of Liquefaction Resistance of Soils," edited by T.L. Youd and I.M. Idriss, 12/31/97, (PB98-155617, A15, MF-A03).
- MCEER-98-0001 "Extraction of Nonlinear Hysteretic Properties of Seismically Isolated Bridges from Quick-Release Field Tests," by Q. Chen, B.M. Douglas, E.M. Maragakis and I.G. Buckle, 5/26/98, (PB99-118838, A06, MF-A01).
- MCEER-98-0002 "Methodologies for Evaluating the Importance of Highway Bridges," by A. Thomas, S. Eshenaur and J. Kulicki, 5/29/98, (PB99-118846, A10, MF-A02).
- MCEER-98-0003 "Capacity Design of Bridge Piers and the Analysis of Overstrength," by J.B. Mander, A. Dutta and P. Goel, 6/1/98, (PB99-118853, A09, MF-A02).
- MCEER-98-0004 "Evaluation of Bridge Damage Data from the Loma Prieta and Northridge, California Earthquakes," by N. Basoz and A. Kiremidjian, 6/2/98, (PB99-118861, A15, MF-A03).
- MCEER-98-0005 "Screening Guide for Rapid Assessment of Liquefaction Hazard at Highway Bridge Sites," by T. L. Youd, 6/16/98, (PB99-118879, A06, not available on microfiche).
- MCEER-98-0006 "Structural Steel and Steel/Concrete Interface Details for Bridges," by P. Ritchie, N. Kaulh and J. Kulicki, 7/13/98, (PB99-118945, A06, MF-A01).
- MCEER-98-0007 "Capacity Design and Fatigue Analysis of Confined Concrete Columns," by A. Dutta and J.B. Mander, 7/14/98, (PB99-118960, A14, MF-A03).
- MCEER-98-0008 "Proceedings of the Workshop on Performance Criteria for Telecommunication Services Under Earthquake Conditions," edited by A.J. Schiff, 7/15/98, (PB99-118952, A08, MF-A02).
- MCEER-98-0009 "Fatigue Analysis of Unconfined Concrete Columns," by J.B. Mander, A. Dutta and J.H. Kim, 9/12/98, (PB99-123655, A10, MF-A02).
- MCEER-98-0010 "Centrifuge Modeling of Cyclic Lateral Response of Pile-Cap Systems and Seat-Type Abutments in Dry Sands," by A.D. Gadre and R. Dobry, 10/2/98, (PB99-123606, A13, MF-A03).
- MCEER-98-0011 "IDARC-BRIDGE: A Computational Platform for Seismic Damage Assessment of Bridge Structures," by A.M. Reinhorn, V. Simeonov, G. Mylonakis and Y. Reichman, 10/2/98, (PB99-162919, A15, MF-A03).
- MCEER-98-0012 "Experimental Investigation of the Dynamic Response of Two Bridges Before and After Retrofitting with Elastomeric Bearings," by D.A. Wendichansky, S.S. Chen and J.B. Mander, 10/2/98, (PB99-162927, A15, MF-A03).
- MCEER-98-0013 "Design Procedures for Hinge Restrainers and Hinge Sear Width for Multiple-Frame Bridges," by R. Des Roches and G.L. Fenves, 11/3/98, (PB99-140477, A13, MF-A03).
- MCEER-98-0014 "Response Modification Factors for Seismically Isolated Bridges," by M.C. Constantinou and J.K. Quarshie, 11/3/98, (PB99-140485, A14, MF-A03).
- MCEER-98-0015 "Proceedings of the U.S.-Italy Workshop on Seismic Protective Systems for Bridges," edited by I.M. Friedland and M.C. Constantinou, 11/3/98, (PB2000-101711, A22, MF-A04).
- MCEER-98-0016 "Appropriate Seismic Reliability for Critical Equipment Systems: Recommendations Based on Regional Analysis of Financial and Life Loss," by K. Porter, C. Scawthorn, C. Taylor and N. Blais, 11/10/98, (PB99-157265, A08, MF-A02).
- MCEER-98-0017 "Proceedings of the U.S. Japan Joint Seminar on Civil Infrastructure Systems Research," edited by M. Shinozuka and A. Rose, 11/12/98, (PB99-156713, A16, MF-A03).
- MCEER-98-0018 "Modeling of Pile Footings and Drilled Shafts for Seismic Design," by I. PoLam, M. Kapuskar and D. Chaudhuri, 12/21/98, (PB99-157257, A09, MF-A02).

- MCEER-99-0001 "Seismic Evaluation of a Masonry Infilled Reinforced Concrete Frame by Pseudodynamic Testing," by S.G. Buonopane and R.N. White, 2/16/99, (PB99-162851, A09, MF-A02).
- MCEER-99-0002 "Response History Analysis of Structures with Seismic Isolation and Energy Dissipation Systems: Verification Examples for Program SAP2000," by J. Scheller and M.C. Constantinou, 2/22/99, (PB99-162869, A08, MF-A02).
- MCEER-99-0003 "Experimental Study on the Seismic Design and Retrofit of Bridge Columns Including Axial Load Effects," by A. Dutta, T. Kokorina and J.B. Mander, 2/22/99, (PB99-162877, A09, MF-A02).
- MCEER-99-0004 "Experimental Study of Bridge Elastomeric and Other Isolation and Energy Dissipation Systems with Emphasis on Uplift Prevention and High Velocity Near-source Seismic Excitation," by A. Kasalanati and M. C. Constantinou, 2/26/99, (PB99-162885, A12, MF-A03).
- MCEER-99-0005 "Truss Modeling of Reinforced Concrete Shear-flexure Behavior," by J.H. Kim and J.B. Mander, 3/8/99, (PB99-163693, A12, MF-A03).
- MCEER-99-0006 "Experimental Investigation and Computational Modeling of Seismic Response of a 1:4 Scale Model Steel Structure with a Load Balancing Supplemental Damping System," by G. Pekcan, J.B. Mander and S.S. Chen, 4/2/99, (PB99-162893, A11, MF-A03).
- MCEER-99-0007 "Effect of Vertical Ground Motions on the Structural Response of Highway Bridges," by M.R. Button, C.J. Cronin and R.L. Mayes, 4/10/99, (PB2000-101411, A10, MF-A03).
- MCEER-99-0008 "Seismic Reliability Assessment of Critical Facilities: A Handbook, Supporting Documentation, and Model Code Provisions," by G.S. Johnson, R.E. Sheppard, M.D. Quilici, S.J. Eder and C.R. Scawthorn, 4/12/99, (PB2000-101701, A18, MF-A04).
- MCEER-99-0009 "Impact Assessment of Selected MCEER Highway Project Research on the Seismic Design of Highway Structures," by C. Rojahn, R. Mayes, D.G. Anderson, J.H. Clark, D'Appolonia Engineering, S. Gloyd and R.V. Nutt, 4/14/99, (PB99-162901, A10, MF-A02).
- MCEER-99-0010 "Site Factors and Site Categories in Seismic Codes," by R. Dobry, R. Ramos and M.S. Power, 7/19/99, (PB2000-101705, A08, MF-A02).
- MCEER-99-0011 "Restrainer Design Procedures for Multi-Span Simply-Supported Bridges," by M.J. Randall, M. Saiidi, E. Maragakis and T. Isakovic, 7/20/99, (PB2000-101702, A10, MF-A02).
- MCEER-99-0012 "Property Modification Factors for Seismic Isolation Bearings," by M.C. Constantinou, P. Tsopelas, A. Kasalanati and E. Wolff, 7/20/99, (PB2000-103387, A11, MF-A03).
- MCEER-99-0013 "Critical Seismic Issues for Existing Steel Bridges," by P. Ritchie, N. Kauh and J. Kulicki, 7/20/99, (PB2000-101697, A09, MF-A02).
- MCEER-99-0014 "Nonstructural Damage Database," by A. Kao, T.T. Soong and A. Vender, 7/24/99, (PB2000-101407, A06, MF-A01).
- MCEER-99-0015 "Guide to Remedial Measures for Liquefaction Mitigation at Existing Highway Bridge Sites," by H.G. Cooke and J. K. Mitchell, 7/26/99, (PB2000-101703, A11, MF-A03).
- MCEER-99-0016 "Proceedings of the MCEER Workshop on Ground Motion Methodologies for the Eastern United States," edited by N. Abrahamson and A. Becker, 8/11/99, (PB2000-103385, A07, MF-A02).
- MCEER-99-0017 "Quindío, Colombia Earthquake of January 25, 1999: Reconnaissance Report," by A.P. Asfura and P.J. Flores, 10/4/99, (PB2000-106893, A06, MF-A01).
- MCEER-99-0018 "Hysteretic Models for Cyclic Behavior of Deteriorating Inelastic Structures," by M.V. Sivaselvan and A.M. Reinhorn, 11/5/99, (PB2000-103386, A08, MF-A02).

- MCEER-99-0019 "Proceedings of the 7th U.S.- Japan Workshop on Earthquake Resistant Design of Lifeline Facilities and Countermeasures Against Soil Liquefaction," edited by T.D. O'Rourke, J.P. Bardet and M. Hamada, 11/19/99, (PB2000-103354, A99, MF-A06).
- MCEER-99-0020 "Development of Measurement Capability for Micro-Vibration Evaluations with Application to Chip Fabrication Facilities," by G.C. Lee, Z. Liang, J.W. Song, J.D. Shen and W.C. Liu, 12/1/99, (PB2000-105993, A08, MF-A02).
- MCEER-99-0021 "Design and Retrofit Methodology for Building Structures with Supplemental Energy Dissipating Systems," by G. Pekcan, J.B. Mander and S.S. Chen, 12/31/99, (PB2000-105994, A11, MF-A03).
- MCEER-00-0001 "The Marmara, Turkey Earthquake of August 17, 1999: Reconnaissance Report," edited by C. Scawthorn; with major contributions by M. Bruneau, R. Eguchi, T. Holzer, G. Johnson, J. Mander, J. Mitchell, W. Mitchell, A. Papageorgiou, C. Scaethorn, and G. Webb, 3/23/00, (PB2000-106200, A11, MF-A03).
- MCEER-00-0002 "Proceedings of the MCEER Workshop for Seismic Hazard Mitigation of Health Care Facilities," edited by G.C. Lee, M. Ettouney, M. Grigoriu, J. Hauer and J. Nigg, 3/29/00, (PB2000-106892, A08, MF-A02).
- MCEER-00-0003 "The Chi-Chi, Taiwan Earthquake of September 21, 1999: Reconnaissance Report," edited by G.C. Lee and C.H. Loh, with major contributions by G.C. Lee, M. Bruneau, I.G. Buckle, S.E. Chang, P.J. Flores, T.D. O'Rourke, M. Shinozuka, T.T. Soong, C-H. Loh, K-C. Chang, Z-J. Chen, J-S. Hwang, M-L. Lin, G-Y. Liu, K-C. Tsai, G.C. Yao and C-L. Yen, 4/30/00, (PB2001-100980, A10, MF-A02).
- MCEER-00-0004 "Seismic Retrofit of End-Sway Frames of Steel Deck-Truss Bridges with a Supplemental Tendon System: Experimental and Analytical Investigation," by G. Pekcan, J.B. Mander and S.S. Chen, 7/1/00, (PB2001-100982, A10, MF-A02).
- MCEER-00-0005 "Sliding Fragility of Unrestrained Equipment in Critical Facilities," by W.H. Chong and T.T. Soong, 7/5/00, (PB2001-100983, A08, MF-A02).
- MCEER-00-0006 "Seismic Response of Reinforced Concrete Bridge Pier Walls in the Weak Direction," by N. Abo-Shadi, M. Saiidi and D. Sanders, 7/17/00, (PB2001-100981, A17, MF-A03).
- MCEER-00-0007 "Low-Cycle Fatigue Behavior of Longitudinal Reinforcement in Reinforced Concrete Bridge Columns," by J. Brown and S.K. Kunnath, 7/23/00, (PB2001-104392, A08, MF-A02).
- MCEER-00-0008 "Soil Structure Interaction of Bridges for Seismic Analysis," I. PoLam and H. Law, 9/25/00, (PB2001-105397, A08, MF-A02).
- MCEER-00-0009 "Proceedings of the First MCEER Workshop on Mitigation of Earthquake Disaster by Advanced Technologies (MEDAT-1), edited by M. Shinozuka, D.J. Inman and T.D. O'Rourke, 11/10/00, (PB2001-105399, A14, MF-A03).
- MCEER-00-0010 "Development and Evaluation of Simplified Procedures for Analysis and Design of Buildings with Passive Energy Dissipation Systems," by O.M. Ramirez, M.C. Constantinou, C.A. Kircher, A.S. Whittaker, M.W. Johnson, J.D. Gomez and C. Chrysostomou, 11/16/01, (PB2001-105523, A23, MF-A04).
- MCEER-00-0011 "Dynamic Soil-Foundation-Structure Interaction Analyses of Large Caissons," by C-Y. Chang, C-M. Mok, Z-L. Wang, R. Settgast, F. Waggoner, M.A. Ketchum, H.M. Gonnermann and C-C. Chin, 12/30/00, (PB2001-104373, A07, MF-A02).
- MCEER-00-0012 "Experimental Evaluation of Seismic Performance of Bridge Restrainers," by A.G. Vlassis, E.M. Maragakis and M. Saiid Saiidi, 12/30/00, (PB2001-104354, A09, MF-A02).
- MCEER-00-0013 "Effect of Spatial Variation of Ground Motion on Highway Structures," by M. Shinozuka, V. Saxena and G. Deodatis, 12/31/00, (PB2001-108755, A13, MF-A03).
- MCEER-00-0014 "A Risk-Based Methodology for Assessing the Seismic Performance of Highway Systems," by S.D. Werner, C.E. Taylor, J.E. Moore, II, J.S. Walton and S. Cho, 12/31/00, (PB2001-108756, A14, MF-A03).

- MCEER-01-0001 “Experimental Investigation of P-Delta Effects to Collapse During Earthquakes,” by D. Vian and M. Bruneau, 6/25/01, (PB2002-100534, A17, MF-A03).
- MCEER-01-0002 “Proceedings of the Second MCEER Workshop on Mitigation of Earthquake Disaster by Advanced Technologies (MEDAT-2),” edited by M. Bruneau and D.J. Inman, 7/23/01, (PB2002-100434, A16, MF-A03).
- MCEER-01-0003 “Sensitivity Analysis of Dynamic Systems Subjected to Seismic Loads,” by C. Roth and M. Grigoriu, 9/18/01, (PB2003-100884, A12, MF-A03).
- MCEER-01-0004 “Overcoming Obstacles to Implementing Earthquake Hazard Mitigation Policies: Stage 1 Report,” by D.J. Alesch and W.J. Petak, 12/17/01, (PB2002-107949, A07, MF-A02).
- MCEER-01-0005 “Updating Real-Time Earthquake Loss Estimates: Methods, Problems and Insights,” by C.E. Taylor, S.E. Chang and R.T. Eguchi, 12/17/01, (PB2002-107948, A05, MF-A01).
- MCEER-01-0006 “Experimental Investigation and Retrofit of Steel Pile Foundations and Pile Bents Under Cyclic Lateral Loadings,” by A. Shama, J. Mander, B. Blabac and S. Chen, 12/31/01, (PB2002-107950, A13, MF-A03).
- MCEER-02-0001 “Assessment of Performance of Bolu Viaduct in the 1999 Duzce Earthquake in Turkey” by P.C. Roussis, M.C. Constantinou, M. Erdik, E. Durukal and M. Dicleli, 5/8/02, (PB2003-100883, A08, MF-A02).
- MCEER-02-0002 “Seismic Behavior of Rail Counterweight Systems of Elevators in Buildings,” by M.P. Singh, Rildova and L.E. Suarez, 5/27/02. (PB2003-100882, A11, MF-A03).
- MCEER-02-0003 “Development of Analysis and Design Procedures for Spread Footings,” by G. Mylonakis, G. Gazetas, S. Nikolaou and A. Chauncey, 10/02/02, (PB2004-101636, A13, MF-A03, CD-A13).
- MCEER-02-0004 “Bare-Earth Algorithms for Use with SAR and LIDAR Digital Elevation Models,” by C.K. Huyck, R.T. Eguchi and B. Houshmand, 10/16/02, (PB2004-101637, A07, CD-A07).
- MCEER-02-0005 “Review of Energy Dissipation of Compression Members in Concentrically Braced Frames,” by K.Lee and M. Bruneau, 10/18/02, (PB2004-101638, A10, CD-A10).
- MCEER-03-0001 “Experimental Investigation of Light-Gauge Steel Plate Shear Walls for the Seismic Retrofit of Buildings” by J. Berman and M. Bruneau, 5/2/03, (PB2004-101622, A10, MF-A03, CD-A10).
- MCEER-03-0002 “Statistical Analysis of Fragility Curves,” by M. Shinozuka, M.Q. Feng, H. Kim, T. Uzawa and T. Ueda, 6/16/03, (PB2004-101849, A09, CD-A09).
- MCEER-03-0003 “Proceedings of the Eighth U.S.-Japan Workshop on Earthquake Resistant Design of Lifeline Facilities and Countermeasures Against Liquefaction,” edited by M. Hamada, J.P. Bardet and T.D. O’Rourke, 6/30/03, (PB2004-104386, A99, CD-A99).
- MCEER-03-0004 “Proceedings of the PRC-US Workshop on Seismic Analysis and Design of Special Bridges,” edited by L.C. Fan and G.C. Lee, 7/15/03, (PB2004-104387, A14, CD-A14).
- MCEER-03-0005 “Urban Disaster Recovery: A Framework and Simulation Model,” by S.B. Miles and S.E. Chang, 7/25/03, (PB2004-104388, A07, CD-A07).
- MCEER-03-0006 “Behavior of Underground Piping Joints Due to Static and Dynamic Loading,” by R.D. Meis, M. Maragakis and R. Siddharthan, 11/17/03.
- MCEER-03-0007 “Seismic Vulnerability of Timber Bridges and Timber Substructures,” by A.A. Shama, J.B. Mander, I.M. Friedland and D.R. Allicock, 12/15/03.
- MCEER-04-0001 “Experimental Study of Seismic Isolation Systems with Emphasis on Secondary System Response and Verification of Accuracy of Dynamic Response History Analysis Methods,” by E. Wolff and M. Constantinou, 1/16/04.

- MCEER-04-0002 “Tension, Compression and Cyclic Testing of Engineered Cementitious Composite Materials,” by K. Kesner and S.L. Billington, 3/1/04.
- MCEER-04-0003 “Cyclic Testing of Braces Laterally Restrained by Steel Studs to Enhance Performance During Earthquakes,” by O.C. Celik, J.W. Berman and M. Bruneau, 3/16/04.
- MCEER-04-0004 “Methodologies for Post Earthquake Building Damage Detection Using SAR and Optical Remote Sensing: Application to the August 17, 1999 Marmara, Turkey Earthquake,” by C.K. Huyck, B.J. Adams, S. Cho, R.T. Eguchi, B. Mansouri and B. Houshmand, 6/15/04.



MULTIDISCIPLINARY CENTER FOR EARTHQUAKE ENGINEERING RESEARCH

A National Center of Excellence in Advanced Technology Applications

University at Buffalo, State University of New York

Red Jacket Quadrangle ■ Buffalo, New York 14261

Phone: (716) 645-3391 ■ Fax: (716) 645-3399

E-mail: mceer@mceermail.buffalo.edu ■ WWW Site <http://mceer.buffalo.edu>



University at Buffalo *The State University of New York*

ISSN 1520-295X